A.D. 1308
unipg
UNIVERSITÀ DEGLI STUDI
DI PERUGIA

First observation and branching fraction measurement of the $\Sigma^+ \to p\mu^+\mu^-$ decay at LHCb

CERN-THESIS-2024-372
29/04/2024

Dipartimento di Fisica e Geologia
PhD in Physics (XXXVI cycle)

Gabriele Martelli
ID number 337275

Advisor
Dr. Monica Pepe

Co-Advisor
Dr. Mauro Piccini

Academic Year 2023/2024

Thesis defended on 29/04/2024
in front of a Board of Examiners composed by:

Prof. Simone Pacetti (chairman)

Prof. Claudio Luci

Prof. Angela Papa

First observation and branching fraction measurement of the $\Sigma^+ \to p\mu^+\mu^-$ decay at LHCb

PhD thesis. Università degli Studi di Perugia

This thesis has been typeset by LaTeX.

Author's email: gabriele.martelli@cern.ch

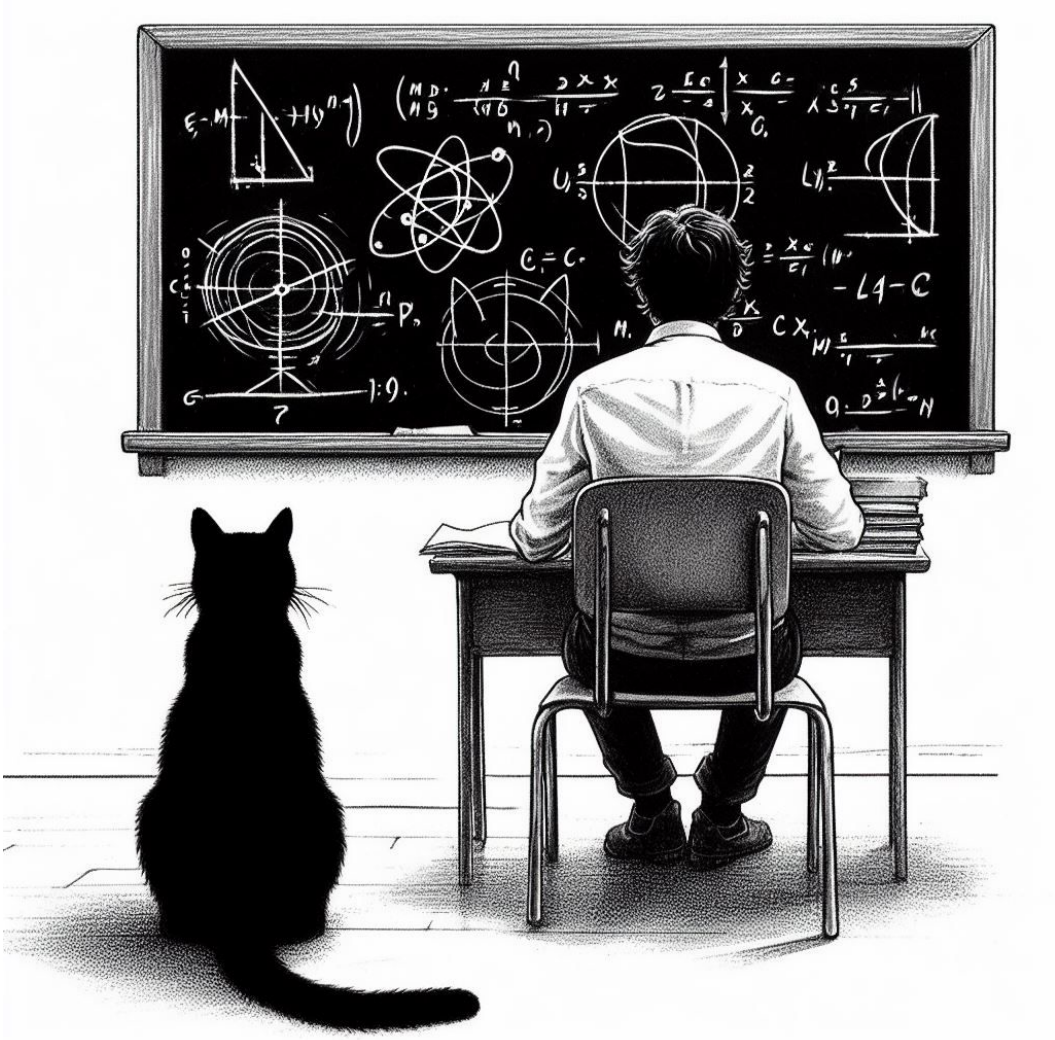

Acknowledgments

Firstly, I would like to express my sincere gratitude to my family. Their continuous support, despite the physical distance, has always encouraged me and kept me motivated during my PhD.

I am extremely grateful to my advisors, Monica Pepe and Mauro Piccini, for teaching me a lot and for their guidance in my activities within the LHCb collaboration. I would also like to extend my sincere thanks to the other members of the LHCb/NA62 Perugia group, Giuseppina Anzivino, Francesco Brizioli, Patrizia Cenci, Viacheslav Duk and Pasquale Lubrano, for believing in me. In addition, I would like to mention Francesco Dettori and Francesca Dordei from the Σ^+ group. Their unlimited feedback has been invaluable during the analysis.

Last but not least, I would like to thank my old and new friends for supporting me throughout the last three years.

Contents

List of Tables

List of Figures

Introduction

The Standard Model has achieved its maximum success as a quantum field theory able to describe the interactions between fundamental particles with the observation of the Higgs boson. However, despite its confirmation, the Model remains incomplete and leaves open questions without answers.

It has been shown that only 5% of the total energy density in the Universe is described by the Standard Model. The largest part, accounting for 68% of the total, seems to consist of the so-called dark energy, an unknown form of energy introduced to explain the accelerated rate of expansion of the Universe. The remaining 27% appears to be made of non-baryonic and non-luminous matter, denoted as dark matter. Cosmological observations also reveal an excessive asymmetry in Nature between matter and antimatter that cannot be sufficiently accounted for by the observed CP symmetry violation, well explained by the Model. Furthermore, the experimental results on the neutrino mass are inconsistent with the minimal formulation of the Standard Model, in which neutrinos are described as massless. From a theoretical perspective, the primary unexplained phenomena that need to be addressed are the hierarchy problem, the non-inclusion of the gravitational interaction and the presence of several free parameters in the Model.

The quark flavour sector, the physics area that delves into the properties and interactions of different quark flavours, may be explored to study most of the open problems of the Standard Model. Using the Large Hadron Collider at CERN, the LHCb experiment has proven to be an ideal setting for investigating flavour physics. Within LHCb, an indirect search of New Physics is possible with precision measurements of observables in processes highly suppressed in the Model. In this context, Flavour Changing Neutral Current processes are a promising field of interest as they necessitate high-order diagrams to be described, being heavily suppressed. These processes are potentially sensitive to contributions from New Physics sources, such as weakly interacting and undiscovered low-mass particles, which could appear as resonances.

The $\Sigma^+ \to p\mu^+\mu^-$ decay is the rarest baryon decay ever predicted within the Standard Model, with an estimated branching fraction of

$$1.6 \times 10^{-8} < \mathcal{B}(\Sigma^+ \to p\mu^+\mu^-) < 9.0 \times 10^{-8}. \tag{0.1}$$

Evidence of this decay was reported by the HyperCP experiment, based on the observation of three candidates. The measured branching fraction was

$$\mathcal{B}(\Sigma^+ \to p\mu^+\mu^-) = (8.6^{+6.6}_{-5.4} \pm 5.5) \times 10^{-8}, \tag{0.2}$$

compatible with the Standard Model prediction. The curious feature of this evidence is that the three observed candidates have a dimuon invariant mass consistent with each other. The average value was measured to be

$$m_{X^0} = 214.3 \pm 0.5 \text{ MeV}/c^2. \tag{0.3}$$

Such a result, if confirmed, would point towards a decay with an intermediate particle X^0 coming from the Σ^+ baryon and decaying in two muons, i.e. a $\Sigma^+ \to pX^0(\to \mu^+\mu^-)$ decay, which would constitute evidence of New Physics beyond the Standard Model. Various hypotheses have been proposed to explain this evidence. The intermediate particle could be a light pseudoscalar Higgs boson in the Next-to-Minimal Supersymmetric Standard Model extension or a sgoldstino in various supersymmetric models. In general, a pseudoscalar particle is favoured over a scalar one to describe the HyperCP result and a lifetime of the order of 10^{-14} s is estimated. Attempts to confirm this new particle have been performed by many experiments in various initial and final states, without finding any sign of New Physics.

Within LHCb, a direct search of the rare decay $\Sigma^+ \to p\mu^+\mu^-$ was performed using proton-proton collision data recorded at centre-of-mass energies $\sqrt{s} = 7$ and 8 TeV, corresponding to an integrated luminosity of 3 fb^{-1}. An evidence for this decay was reported with $10.2^{+3.9}_{-3.5}$ signal candidates, corresponding to a significance of 4.1σ. The measured branching fraction was

$$\mathcal{B}(\Sigma^+ \to p\mu^+\mu^-) = (2.2^{+1.8}_{-1.3}) \times 10^{-8}, \tag{0.4}$$

consistent with the Standard Model prediction. The spectrum of the dimuon invariant mass was compatible with the phase space distribution, i.e. no significant sign of a resonant contribution was observed, in contrast with the previous result from the HyperCP experiment. An upper limit on the branching fraction of the resonant channel has been set at $\mathcal{B}(\Sigma^+ \to pX^0(\to \mu^+\mu^-)) < 1.4 \times 10^{-8}(1.7 \times 10^{-8})$ at 90% (95%) confidence level, which would exclude the HyperCP signal in the resonant hypothesis.

In this thesis, the first significant observation of the $\Sigma^+ \to p\mu^+\mu^-$ decay and the measurement of the branching fraction are presented. The analysis has been performed within the LHCb experiment using proton-proton collision data recorded at centre-of-mass energies $\sqrt{s} = 13$ TeV, corresponding to an integrated luminosity of 5.4 fb^{-1}. In Chapter 1, the theoretical framework of the $\Sigma^+ \to p\mu^+\mu^-$ decay is presented, including its phenomenology and state-of-the-art. In Chapter 2, the LHCb experiment and its detectors are illustrated. In Chapter 3, the main steps of the analysis are shown with the $\Sigma^+ \to p\mu^+\mu^-$ selection strategy, which is optimised in Chapter 4. In Chapter 5, the fit strategy and the first observation of the decay are reported. In Chapter 6, the normalisation for the branching fraction measurement is presented, using the $\Sigma^+ \to p\pi^0$ decay. In Chapter 7, the systematics uncertainties, affecting the measurement of the branching fraction, are discussed. In Chapter 8, the measurement of the $\Sigma^+ \to p\mu^+\mu^-$ branching fraction is illustrated and studies on the dimuon invariant mass are reported. Conclusions and future prospects are illustrated in the final pages of this work.

During my PhD, in addition to the analysis of the $\Sigma^+ \to p\mu^+\mu^-$ decay, I was also involved in the test beam campaigns dedicated to the future upgrades of the

LHCb RICH detector, in view of the high-luminosity phase of the Large Hadron Collider. In Appendix C, studies on the single-photon time resolution, using the data collected with the SPS charged particle beam facility at CERN, are presented.

Chapter 1

Theoretical framework and experimental state-of-the-art

The rare hyperon decays offer a unique opportunity to delve into the properties of the fundamental interactions. These processes are characterized by branching fractions of the order of 10^{-5} or smaller and may provide insights on possible New Physics effects.

In this chapter, after a brief introduction to the Standard Model and its unexplained phenomena, the theoretical framework of the current study is presented. In details, the phenomenology of both signal $\Sigma^+ \to p\mu^+\mu^-$ and normalisation $\Sigma^+ \to p\pi^0$ decay modes is illustrated. Furthermore, an up-to-date overview on the advancements in studying the $\Sigma^+ \to p\mu^+\mu^-$ decay is reported.

1.1 The Standard Model

The Standard Model of particle physics (SM) is a quantum field theory able to describe the fundamental interactions between elementary particles in Nature. Its origins can be traced back to the early 20th century with the discovery of the electron by J.J. Thomson (1897) [1] and the proton by Ernest Rutherford (1917) [2], setting the foundation for the understanding of the atomic structure. In the 1930s and 1940s, Enrico Fermi formulated the initial theory of the weak force, which evolved into the Fermi theory of β decay [3]. This idea was later incorporated into the electroweak theory, the unification of the weak and electromagnetic interactions, developed by Glashow (1961) [4], Salam (1964) [5] and Weinberg (1967) [6]. The 1960s and 1970s witnessed the independent proposals by Murray Gell-Mann [7] and George Zweig [8] of the quarks theory and the development of the Quantum ElectroDynamics (QED) and ChromoDynamics (QCD). Finally, the SM achieved its maximum success with the introduction of the Higgs boson. This particle was initially proposed by Peter Higgs [9] (1964) and it was observed for the first time at the Large Hadron Collider of CERN by the ATLAS [10] and CMS [11] collaborations (2012).

In the current view of the SM, ordinary matter is composed of elementary particles, also known as fundamental particles. The Model is composed of 12 fermions, divided into two groups: leptons and quarks. These groups are further divided into generations. Particles of different generations have different flavours,

defined by the flavour quantum number. These flavours are grouped in the three generations of quarks: (u, d), (c, s) and (t, b). The (u, c, t) quarks are the up-type while the (d, s, b) quarks denote the down-type of each generation.

The electromagnetic, weak and strong interactions are well described within the SM. The electromagnetic interaction is a long-range force, described by the QED, which defines the interaction between light and matter. It is mediated by the massless and electrically neutral photon γ and it is coupled to the particle electric charge. The weak interaction is responsible for specific types of radioactive processes, such as the β decay. The term "weak" denotes its several orders of magnitude lower field strength, compared to the other forces. Its unification with the electromagnetic interaction forms the electroweak sector. Within this theory, three weak gauge bosons play the role of mediators for the charged and neutral current interactions: the $W^{\pm}$ and Z^0 bosons. The strong interaction is a short-range force that acts through the exchange of gluons g between quarks, binding them together to form non-fundamental particles. It acts solely between quarks and gluons as they are the only fundamental particles with a non-vanishing colour charge. The strong interaction finds its description in the QCD, which precisely defines the interaction between quarks and gluons.

An overview of the SM fundamental particles is provided in Tab. 1.1. Here, the listed properties are taken from the Particle Data Group (PDG) [12].

Particle	Symbol	Q	s	Mass [MeV/c^2]
Leptons				
Electron	e^-	-1	1/2	0.511
Electron neutrino	ν_e	0	1/2	$< 1.0 \times 10^{-6}$
Muon	μ^-	-1	1/2	105.66
Muon neutrino	ν_μ	0	1/2	< 0.17
Tau	τ^-	-1	1/2	1.7768×10^3
Tau neutrino	ν_τ	0	1/2	< 18.2
Quarks				
Up	u	$+2/3$	1/2	2.16
Down	d	$-1/3$	1/2	4.67
Charm	c	$+2/3$	1/2	1.27×10^3
Strange	s	$-1/3$	1/2	93.4
Top	t	$+2/3$	1/2	172.69×10^3
Bottom	b	$-1/3$	1/2	4.18×10^3
Gauge Bosons				
Photon	γ	0	1	0
Gluon	g	0	1	0
W Boson	$W^{\pm}$	± 1	1	80.377×10^3
Z Boson	Z^0	0	1	91.1876×10^3
Higgs				
Higgs Boson	H	0	0	125.25×10^3

Table 1.1. Fundamental particles of the SM. For each particle, the electric charge Q, the spin s and the mass value in MeV/c^2 are reported.

The fundamental interactions are formulated through field theories, also known as gauge theories, which are invariant under local gauge transformations. Within a gauge theory, the interactions are defined by a Lagrangian density $\mathcal{L}$, which is invariant under the appropriate symmetries. According to the Noether theorem, these symmetries denote the conservation laws which control the interactions. The Lagrangian density of the SM, describing the dynamics of the physics fields and the elementary particles, is

$$\mathcal{L}_{\text{SM}} = \mathcal{L}_{\text{gauge}} + \mathcal{L}_{\text{kin}} + \mathcal{L}_{\text{Yukawa}} + \mathcal{L}_{\text{Higgs}}, \tag{1.1}$$

where

- $\mathcal{L}_{\text{gauge}} = -\frac{1}{4} F_{\mu\nu} F^{\mu\nu}$ is the gauge bosons kinetic term, defining the free field, the interaction and auto-interaction terms through the definition of the field stress tensors $F_{\mu\nu}$;

- $\mathcal{L}_{\text{kin}} = \bar{Q}^j \, i\not{D}_{q,L} Q^j + \bar{u}_R^j \, i\not{D}_{q,R} u_R^j + \bar{d}_R^j \, i\not{D}_{q,R} d_R^j + \bar{L}^j \, i\not{D}_L L^j + \bar{l}_R^j \, i\not{D}_R l_R^j$ is the kinetic term of the Dirac fermions, expressing the interaction with the gauge bosons through the covariant derivatives $\not{D}$;

- $\mathcal{L}_{\text{Yukawa}} = -Y_d^{ij} \overline{Q}^i \, \phi \, d_R^j - Y_u^{ij} \overline{Q}^i \, \widetilde{\phi} \, u_R^j - Y_l^{ij} \overline{L}^i \, \phi \, l_R^j - \text{h.c.}$ is the term which describes the couplings between the Dirac fermions and the Higgs field ϕ;

- $\mathcal{L}_{\text{Higgs}} = D^\mu \phi^\dagger D_\mu \phi - V(\phi^\dagger \phi)$ is the term which describes the Higgs field ϕ, defined as a $SU(2)$ doublet composed of two complex scalar fields. It contains the kinetic and interaction terms with the gauge bosons and the potential to which ϕ is subject.

The fundamental interactions are defined by the unbroken gauge symmetry group $SU(3)_C \times SU(2)_L \times U(1)_Y$, where $SU(3)_C$ represents the strong interaction, while $SU(2)_L \times U(1)_Y$ denotes the electroweak sector. For any theory that incorporates the electroweak sector, it is crucial to eliminate logical and mathematical inconsistencies. Mathematically, the theory must be renormalizable, i.e. it must have a valid procedure to eliminate the infinities that may arise in the calculations of the physical observables. To achieve this, $\mathcal{L}_{\text{SM}}$ must not include any explicit mass term. Therefore, both gauge bosons and fermions are considered massless at the Lagrangian level. The proof of renormalizability was given by G.'t Hooft and Veltman (1971) [13], which subsequently earned them the Nobel Prize in 1999. In order to introduce masses without putting at risk the renormalizability, the theory makes use of spontaneous symmetry breaking, also known as the Higgs mechanism. This idea was proposed in 1964 by Englert and Brout [14], Peter Higgs [9], and Guralnik, Hagen, and Kibble [15]. The Higgs mechanism predicts the existence of the Higgs boson and allows the spontaneous symmetry breaking of the $SU(2)_L \times U(1)_Y$ group and the mixing of the gauge bosons into the three massive bosons, responsible for the weak interaction.

1.2 The quark electroweak interactions

In charged weak interactions, the $W^{\pm}$ bosons couple to leptons belonging to a specific generation and no cross-generational coupling is allowed, due to the conservation of the lepton numbers L_i. According to the Feynman rules, the weak vertex factor is

$$\frac{-ig_w}{2\sqrt{2}}\,\gamma^{\mu}(1-\,\gamma^5), \tag{1.2}$$

where $g_w = \sqrt{4\pi\alpha_w}$ denotes the weak coupling constant. The factor $\gamma^{\mu}(1-\gamma^5)$ is the combination of the vector coupling and an axial current, given by γ^{μ} and $\gamma^{\mu}\gamma^5$, respectively. Such a combination implies the violation of the Parity symmetry P in weak interactions.

In neutral weak interactions, the coupling to the Z^0 boson assumes different forms. In particular, the weak vertex factor is

$$\frac{-ig_z}{2}\,\gamma^{\mu}(c_{\nu}^{f}-c_{A}^{f}\gamma^5), \tag{1.3}$$

where g_z is the neutral coupling constant and c_{ν}^{f} and c_{A}^{f} depends on the fermion f involved in the interaction. All these coefficients are determined by the weak mixing angle θ_w, also known as the Weinberg angle, and are reported in Tab. 1.2.

Fermion	c_v	c_A
ν_e, ν_μ, ν_τ	$1/2$	$+1/2$
e, μ, τ	$-1/2 + 2\sin\theta_w$	$-1/2$
u, c, t	$1/2 - 4/3\sin^2\theta_w$	$+1/2$
d, s, b	$-1/3 + 2/3\sin^2\theta_w$	$-1/2$

Table 1.2. Neutral and axial vector couplings of the weak vertex factor.

The Feynman diagrams of both leptonic and fermion vertices in charged and neutral weak interactions are illustrated in Fig. 1.1 (left and right).

The coupling of the $W^{\pm}$ bosons to quarks, contrary to leptons, is cross-generational, as observed in the $\Lambda \to pe\bar{\nu}_e$ decay. In 1963, Nicola Cabibbo suggested that the $d \to u + W^-$ and $s \to u + W^-$ weak factors, illustrated in Fig. 1.1 (bottom), are directly proportional to the sine and cosine of an angle, denoted as Cabibbo angle θ_C. Within this idea, the quark weak vertices become

$$\frac{-ig_w}{2\sqrt{2}}\gamma^{\mu}(1-\gamma^5)\cos\,\theta_C, \qquad \frac{-ig_w}{2\sqrt{2}}\gamma^{\mu}(1-\gamma^5)\sin\theta_C. \tag{1.4}$$

Any process involving the change in strangeness $s \to u + W^-$ is noticeably weaker compared to the one which conserves strangeness $d \to u + W^-$. Therefore, it became evident that θ_c is relatively small. Experimentally, θ_c has been measured to be $\theta_c = 13.1^{\circ}$ [16]. This measurement serves as the foundation of the Cabibbo quark-mixing theory.

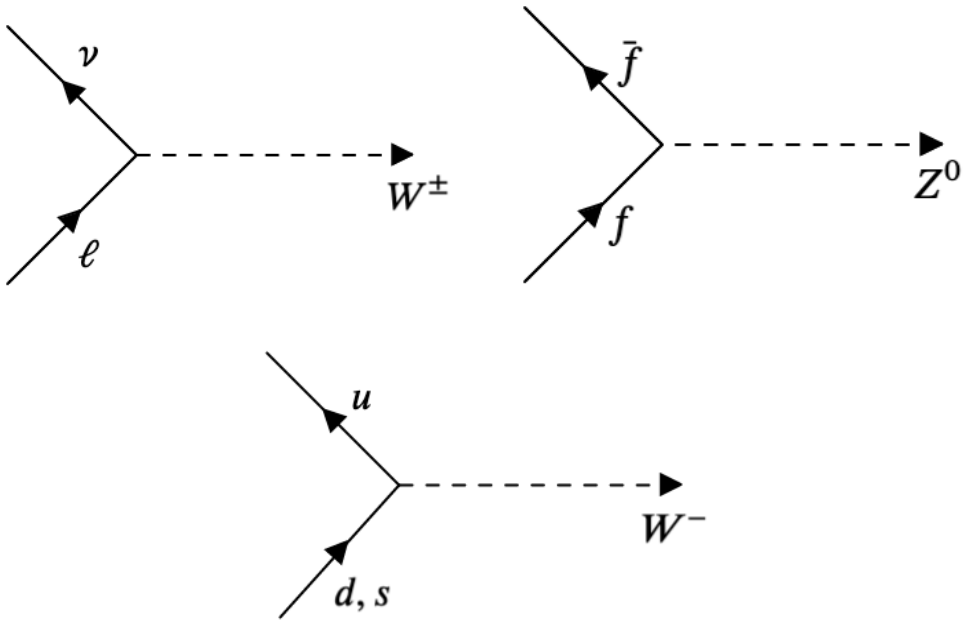

Figure 1.1. Feynman diagrams of the leptonic vertex in charged weak interactions (left), fermion vertex in neutral weak interactions (right) and quark vertex in charged weak interactions (bottom).

1.2.1 The GIM mechanism

The Cabibbo quark-mixing theory found difficulties when attempting to describe the $K^0 \to \mu^+\mu^-$ decay. The corresponding Feynman diagram is illustrated in Fig. 1.2 (left). According to the theory, the amplitude of the $K^0 \to \mu^+\mu^-$ decay should be proportional to $\sin\theta_c \cos\theta_c$. However, the predicted theoretical rate far exceeded the experimental measurement.

This discrepancy was addressed by Glashow, Iliopoulos, and Maiani [17] with the GIM mechanism, introducing a new up-like quark, known as charm c quark. This addition was prompted by indirect experimental results, indicating that the $\Delta S = 2$ transitions were strongly suppressed, compared to the $\Delta S = 1$ ones. The c quark is coupled to both s and d quarks, as illustrated in Fig. 1.2 (bottom), with the coupling factors $\cos\theta_c$ and $-\sin\theta_c$. In the GIM mechanism, the weak vertex factors are written as

$$\frac{-ig_w}{2\sqrt{2}}\,\gamma^\mu(1 - \gamma^5)(-\sin\theta_C), \qquad \frac{-ig_w}{2\sqrt{2}}\,\gamma^\mu(1 - \gamma^5)\cos\theta_C. \tag{1.5}$$

In the proposed solution, the Feynman diagram in Fig. 1.2 (left) is cancelled by the new one with the c quark replacing the u quark, illustrated in Fig. 1.2 (right), with a decay amplitude proportional to $-sin\theta_c cos\theta_c$.

In this new scheme, the weak eigenstates of the quarks with charge $Q = -1/3$ are not the mass eigenstates d and s, but a linear combination of them rotated by the angle θ_C. Such combination is expressed in the following matrix form:

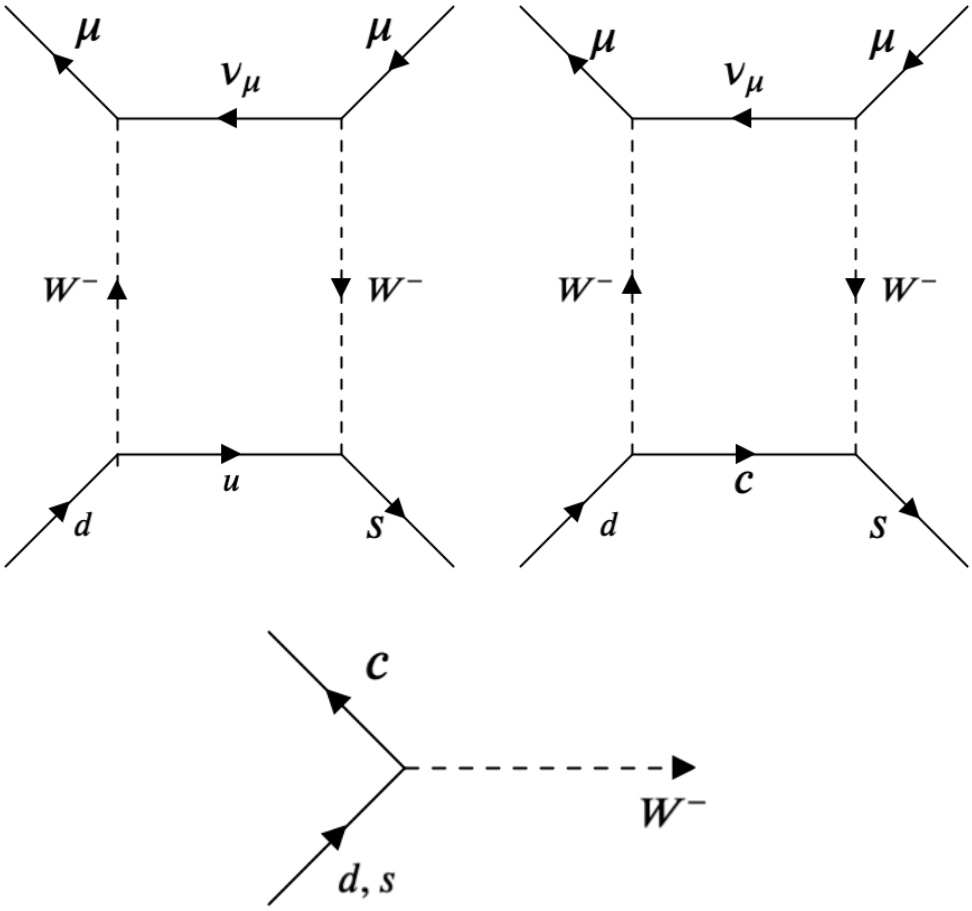

Figure 1.2. Feynman diagrams of the $K^0(d\bar{s}) \to \mu^+\mu^-$ decay in the Cabibbo quark-mixing theory (left) and according to the GIM mechanism (right). Feynman diagram of the quark vertex in charged weak interactions according to GIM mechanism (bottom).

$$\begin{pmatrix} d \\ s' \end{pmatrix} = \begin{pmatrix} \cos\theta_C & \sin\theta_C \\ -\sin\theta_C & \cos\theta_C \end{pmatrix} \begin{pmatrix} d \\ s \end{pmatrix}. \tag{1.6}$$

The GIM mechanism explains the suppression of the Flavour Changing Neutral Current (FCNC) processes. Within the GIM mechanism, the FCNC tree-level interactions disappear as they become accessible only at higher perturbation orders, like box or penguin diagrams, through the exchange of multiple $W^{\pm}$ bosons. Examples of such transitions are the $b \to sl^+l^-$, $b \to dl^+l^-$, $c \to ul^+l^-$ and $s \to dl^+l^-$ interactions, where l^+l^- denotes a pair of leptons with opposite charges.

At the time of the GIM mechanism, the theory of the c quark didn't have any experimental proof. The confirmation of its existence came with the discovery of the $J/\psi(c\bar{c})$ particle by Richter [18] and Ting [19] in 1974. This result provided the much-needed experimental evidence for supporting the GIM mechanism and the presence of the c quark in the quark-mixing theory.

1.2.2 The CKM matrix

Kobayashi and Maskawa extended the Cabibbo theory to take into account the proposed third generation of quarks and explain the observed CP violation [20]. The Cabibbo-Kobayashi-Maskawa (CKM) matrix [21] establishes a connection between the quark flavour eigenstates and those associated with the weak interactions. The CKM matrix is reported in Eq. 1.7. Here, the element of the matrix V_{ij} denotes the coupling between different quark flavours.

$$\left(\begin{array}{c} d' \\ s' \\ b' \end{array} \right)_{weak} = \left(\begin{array}{ccc} V_{ud} & V_{us} & V_{ub} \\ V_{cd} & V_{cs} & V_{cb} \\ V_{td} & V_{ts} & V_{tb} \end{array} \right) \left(\begin{array}{c} d \\ s \\ b \end{array} \right)_{flavour}. \tag{1.7}$$

Another way to express the CKM matrix is the canonical form, in which only three generalized $\theta_{C_i} (i = 1, 2, 3)$ and one phase space factor δ are present:

$$V_{\mathrm{CKM}} = \left(\begin{array}{ccc} c_1 & s_1 c_3 & s_1 s_3 \\ -s_1 c_2 & c_1 c_2 c_3 - s_2 s_3 \, e^{i\delta} & c_1 c_2 s_3 + s_2 c_3 e^{i\delta} \\ -s_1 s_2 & c_1 s_2 c_3 + c_2 s_3 e^{i\delta} & c_1 s_2 s_3 - c_2 c_3 e^{i\delta} \end{array} \right), \tag{1.8}$$

where c_i stands for $cos\theta_{C_i}$ and s_i denotes $sin\theta_{C_i}$. For $\theta_{C_2} = \theta_{C_3} = 0$, the third generation of quark does not mix with the rest and the GIM mechanism is recovered.

Another form of the CKM matrix is the Wolfenstein parametrisation [22]. Here, the matrix is defined by four parameters: λ, A, ρ and η, where $\lambda = |V_{us}| = \sin\theta_c \simeq 0.22$ and η represents the CP violating phase. Expanding the CKM matrix up to $\mathcal{O}(\lambda^4)$ the following form is found:

$$V_{\mathrm{CKM}} = \left(\begin{array}{ccc} 1 - \lambda^2/2 & \lambda & A\lambda^3(\rho - i\eta) \\ -\lambda & 1 - \lambda/2 & A\lambda^2 \\ A\lambda^3(1 - \rho - i\eta) & -A\lambda^2 & 1 \end{array} \right) + \mathcal{O}(\lambda^4), \tag{1.9}$$

where it becomes clear that the CKM matrix is almost diagonal, with small off-diagonal terms. The transitions within a generation are preferred, with couplings of $\mathcal{O}(1)$, while transitions between other generations are suppressed by powers of λ.

At the present time, the V_{CKM} magnitudes for the CKM matrix elements, evaluated from experiments [12], are

$$|V_{\mathrm{CKM}}| = \left(\begin{array}{ccc} 0.97435 \pm 0.00016 & 0.22500 \pm 0.00067 & 0.00369 \pm 0.00011 \\ 0.22486 \pm 0.00067 & 0.97349 \pm 0.00016 & 0.04182^{+0.00085}_{-0.00074} \\ 0.00857^{+0.00020}_{-0.00018} & 0.04110^{+0.00083}_{-0.00072} & 0.999118^{+0.000031}_{-0.000036} \end{array} \right). \tag{1.10}$$

Most of the elements can be studied experimentally from tree-level processes, except for the V_{td} and V_{ts} elements which are extracted from the $B^0 - \bar{B}^0$ and $B_s^0 - \bar{B}_s^0$ oscillations, dominated by box diagrams. The off-diagonal elements in the third row and column turn out to be very small, as learned from the surprisingly long lifetime of the B meson (10^{-12} s).

1.3 Unexplained phenomena in the Standard Model

The SM stands as a remarkable achievement in the understanding of the fundamental particles and their interactions. However, there are still open questions without an answer and numerous unexplained phenomena persist. In the following, some of the SM open problems are reported.

Dark matter, a non-interacting form of matter, constitutes approximately 27% of the Universe mass-energy content and its existence is inferred solely through its gravitational effects on the visible matter and cosmic structures. Candidates for dark matter include Weakly Interacting Massive Particles (WIMPs), axions, and sterile neutrinos, but its true identity remains elusive. Examples of dark matter experiments are XENON1T [23] and DarkSide [24], trying to detect the scattering of dark matter candidates with the nuclei of the target material.

Accounting for approximately 68% of the Universe energy density, the dark energy poses another challenge for the SM. It is a form of energy that permeates the space and drives the accelerated expansion of the Universe. Its physical properties are poorly understood and the cosmological constant, introduced by Einstein in his equations of General Relativity, may be used to understand them.

Neutrinos have become a fine enigma within the SM. Experimental observations from the neutrino oscillation experiments have unequivocally demonstrated that neutrinos possess a non-zero mass value. The SM cannot account for this result, prompting the inclusion of additional terms and interactions to accommodate the neutrino mass generation. Extensions involving heavy right-handed neutrinos, like the seesaw mechanism, have been proposed to explain the neutrino mass and offer prospects for probing New Physics (NP) beyond the SM through specific experiments, such as Super-Kamiokande [25].

The matter-antimatter asymmetry, known as baryogenesis, challenges the SM capability to explain the observed preponderance of matter over antimatter in the Universe. According to the theory, the early Universe should have produced equal amounts of matter and antimatter during the Big Bang. However, through CP violation, a small asymmetry emerged, leading to an excess of matter that eventually formed galaxies, stars, and planets. The understanding of this asymmetry involves the behaviour of quarks, leptons, and their interactions at high energies and temperature regimes, potentially implicating the presence of NP. The CP violation was first observed in Kaons experiments, such as NA31, NA48 [26] and KTeV [27]. The LHCb [28] and Belle II [29] collaborations joined the quest to understand this effect by studying the B mesons. They provide valuable data on the CP violation in the SM and help to establish the Kobayashi-Maskawa mechanism as the source of CP violation in quarks.

The SM offers no explanation for the distinct hierarchy of masses observed among the elementary particles. The mass of the top quark significantly surpasses the rest of the particles, raising questions about the origin of these disparities and the underlying physics driving these variations. Proposed solutions, such as the Yukawa coupling hierarchy, involve studying the interactions with the Higgs field to understand the origin of mass hierarchies.

1.4 The $\Sigma^+ \to p\mu^+\mu^-$ decay

The $\Sigma^+ \to p\mu^+\mu^-$ decay can be described as proceeding to a $s \to d$ quark-FCNC interaction and by internal conversion, as illustrated in Fig. 1.3.

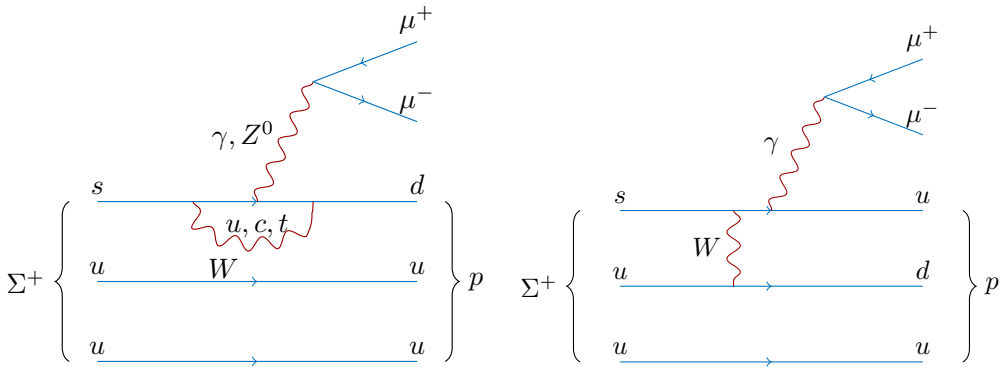

Figure 1.3. Feynman diagrams for the $\Sigma^+ \to p\mu^+\mu^-$ decay proceeding to a $s \to d$ quark-FCNC interaction (left) and by internal conversion (right).

The primary interest in this decay comes from the recent experimental results. The HyperCP experiment reported an evidence for this decay with a possible NP structure in the dimuon invariant mass distribution [30]. Evidence for the $\Sigma^+ \to p\mu^+\mu^-$ decay was also published by the LHCb collaboration, without observing a NP signal [31].

Within the SM, the amplitude of the $\Sigma^+ \to p\mu^+\mu^-$ decay receives contributions from both Short-Distance (SD) and Long-Distance (LD) components. In the next subsections, the theoretical predictions of the $\Sigma^+ \to p\mu^+\mu^-$ branching fraction, depending on these contributions, are presented. Furthermore, the observables of interest, which could be measured by experiments, are reported.

1.4.1 Short-Distance contribution

The SD contribution arises from the Z-penguin, box diagrams and electromagnetic-penguin processes. In this scenario, the $\Sigma^+ \to p\mu^+\mu^-$ decay is described by the following effective Hamiltonian:

$$\mathcal{H}_{\text{eff}} = \frac{G_{\text{F}}}{\sqrt{2}} \bar{d}\gamma^\kappa (1-\gamma_5)\, s\bar{\mu}\gamma_\kappa \left(\lambda_u z_{7V} - \lambda_t y_{7V} - \gamma_5 \lambda_t y_{7A}\right) \mu + \text{ h.c. }, \tag{1.11}$$

where G_F is the Fermi constant, z_{7V} and $y_{7V,7A}$ are the Wilson coefficients and $\lambda_q = V_{qd}^* V_{qs}$ with V_{kl} denoting the CKM matrix elements.

The corresponding decay amplitude is estimated using the baryonic matrix elements, derived from the leading-order strong Lagrangian in chiral perturbation theory (χPT) [32] [33]:

$$\begin{aligned} \left\langle p \left| \bar{d}\gamma^\kappa s \right| \Sigma^+ \right\rangle &= -\bar{u}_p \gamma^\kappa u_\Sigma \\ \left\langle p \left| \bar{d}\gamma^\nu \gamma_5 s \right| \Sigma^+ \right\rangle &= (D-F) \left(\bar{u}_p \gamma^\nu \gamma_5 u_\Sigma + \frac{m_\Sigma + m_p}{q^2 - m_K^2} \bar{u}_p \gamma_5 u_\Sigma q^\nu \right). \end{aligned} \tag{1.12}$$

Here, D and F are constants and $q = p_\Sigma - p_p$ is the difference between the four-momenta of the Σ^+ and p particles. Thus, the SD amplitude for $\Sigma^+ \to p\mu^+\mu^-$ decay is

$$\mathcal{M}_{\rm SM}^{\rm SD} = \frac{G_{\rm F}}{\sqrt{2}} \{-\bar{u}_p\gamma^\nu \left[1+\gamma_5(D-F)\right] u_\Sigma \bar{u}_\mu\gamma_\nu \left(\lambda_u z_{7V} - \lambda_t y_{7V} - \gamma_5\lambda_t y_{7A}\right) v_{\bar{\mu}} + 2(D-F)\frac{m_\Sigma + m_p}{q^2 - m_K^2}\lambda_t y_{7A} m_\mu \bar{u}_p\gamma_5 u_\Sigma \bar{u}_\mu\gamma_5 v_{\bar{\mu}}\Big\}. \tag{1.13}$$

Using the latest results for the variables for which the amplitude depends on [12], the branching fraction is predicted to be $\mathcal{O}(10^{-12})$ [32]. This value is way below the reported results from both the HyperCP and LHCb collaborations, of the order of $\mathcal{O}(10^{-8})$, and the errors on the Wilson coefficients, baryonic and CKM matrix elements do not explain the discrepancy between the theoretical prediction and the measured values. Therefore, the SD contribution is not found to be the dominant component of the $\Sigma^+ \to p\mu^+\mu^-$ amplitude of decay.

1.4.2 Long-Distance contribution

The LD contribution arises mainly from the $\Sigma^+ \to p\gamma^* \to p\mu^+\mu^-$ decays [34]. The corresponding decay amplitude is estimated from the weak nonleptonic $\Sigma^+ \to (N\pi)^+ \to p\gamma^*$ decays, where N represents either a proton or a neutron:

$$\mathcal{M}_{\rm SM}^{\rm LD} = \left\{-iq_\alpha\bar{u}_p\left[a\left(q^2\right) + \gamma_5 b\left(q^2\right)\right]\sigma^{\alpha\beta}u_\Sigma - \bar{u}_p\gamma^\beta\left[c\left(q^2\right) + \gamma_5 d\left(q^2\right)\right]u_\Sigma\right\}\bar{u}_\mu\gamma_\beta v_{\bar{\mu}}, \tag{1.14}$$

with a, b, c and d being the form factors, as functions of $q^2 = m^2_{\mu^+\mu^-}$.

The form factors have been investigated in the χPT with the relativistic [35] and heavy baryon [36] approaches[1]. Their imaginary parts are shown in Fig. 1.4.

The real components of these form factors are experimentally driven. However, compromises must be made as experiments have not yet reached the required accuracy. By assuming that the real parts of a and b have the same dependency in q^2 as their imaginary components, they can be taken as constants, calculated at $q^2 = 0$. From this assumption, a four-fold degeneracy emerges in each χPT method, as reported in Tab. 1.3.

Even if the LD contribution does not produce a unique theoretical value to compare to the experimental results, the order of magnitude in Tab. 1.3 reflects the ones reported by both the HyperCP and LHCb collaborations. Therefore, the LD contribution is confirmed to be the dominant component in the $\Sigma^+ \to p\mu^+\mu^-$ amplitude of decay.

1.4.3 Observables

The observables reported below are related to the decay amplitude estimated in the LD scenario [34].

[1]The results in this subsection are obtained following Ref. [32] with the updated parameters of Ref. [34] from the same authors.

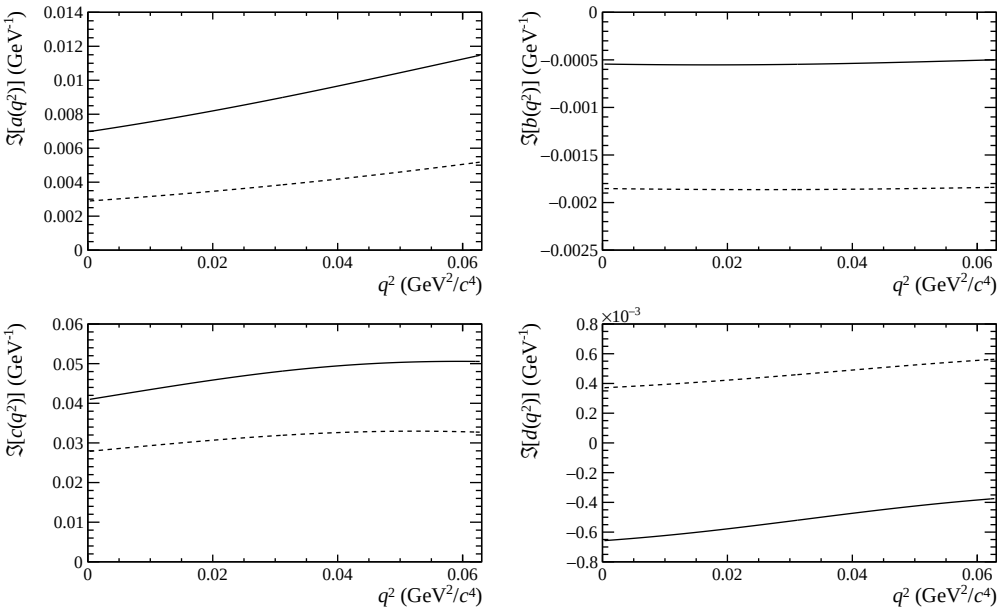

Figure 1.4. Imaginary parts of the a, b, c and d form factors, depending on $q^2 = m^2_{\mu^+\mu^-}$. The solid and dashed lines represent the heavy and relativistic baryon χPT approaches, respectively.

Solution	$\Re[a(0)]\left(\text{GeV}^{-1}\right)$	$\Re[b(0)]\left(\text{GeV}^{-1}\right)$	$\mathcal{B}\left(10^{-8}\right)$
Relativistic baryon			
1	$+0.0133$	-0.0060	1.6
2	-0.0133	$+0.0060$	3.5
3	$+0.0060$	-0.0133	5.1
4	-0.0060	$+0.0133$	9.1
Heavy baryon			
1	$+0.0110$	-0.0074	2.4
2	-0.0110	$+0.0074$	4.7
3	$+0.0074$	-0.0110	4.0
4	-0.0074	$+0.0110$	7.4

Table 1.3. Solutions for the real parts of the a and b form factors and their corresponding $\Sigma^+ \to p\mu^+\mu^-$ branching fraction predictions in the relativistic and heavy baryon χPT approaches.

The double-differential decay rate is obtained after averaging and summing $|\mathcal{M}|^2$ over the initial and final spins:

$$\frac{d^2\Gamma\left(\Sigma^+ \to p\mu^+\mu^-\right)}{dq^2 dt} = \frac{\overline{|\mathcal{M}|^2}}{4\left(4\pi m_\Sigma\right)^3} \tag{1.15}$$

where $t = (p_\Sigma - p_-)^2 = (p_+ + p_p)^2$ and

$$
\begin{aligned}
\overline{|\mathcal{M}|^2} =& 4\left[\left(f_- \mathrm{M}_+^2 + 2fq^2\right)|\tilde{\mathrm{A}}|^2 + \left(f_+ \mathrm{M}_-^2 + 2fq^2\right)|\tilde{\mathrm{B}}|^2 + (f_- - 2f)\,|\tilde{\mathrm{C}}|^2 + (f_+ - 2f)\,|\tilde{\mathrm{D}}|^2\right] \\
&+ 4\left[\left(\beta^2 \hat{m}_-^2 q^2 + 2\hat{m}_+^2 m_\mu^2 - 2f\right)|\tilde{\mathrm{E}}|^2 + \left(\beta^2 \hat{m}_+^2 q^2 + 2\hat{m}_-^2 m_\mu^2 - 2f\right)|\tilde{\mathrm{F}}|^2\right] \\
&+ 2\left(\beta^2 |\tilde{\mathrm{G}}|^2 \hat{m}_+^2 + \beta^2 |\tilde{\mathrm{H}}|^2 \hat{m}_-^2 + |\tilde{\mathrm{J}}|^2 \hat{m}_+^2 + |\tilde{\mathrm{K}}|^2 \hat{m}_-^2\right) q^2 \\
&+ 8\,\mathrm{Re}\left[\tilde{\mathrm{A}}^* \tilde{\mathrm{C}} f_- \mathrm{M}_+ - \tilde{\mathrm{B}}^* \tilde{\mathrm{D}} f_+ \mathrm{M}_- + \left(\tilde{\mathrm{E}}^* \tilde{\mathrm{J}} \hat{m}_+^2 \mathrm{M}_- - \tilde{\mathrm{F}}^* \tilde{\mathrm{K}} \hat{m}_-^2 \mathrm{M}_+\right) m_\mu\right] \\
&+ 4\left(4m_\mu^2 + \hat{m}_-^2 + \hat{m}_+^2 - 4t\right)\mathrm{Re}\left[\left(\tilde{\mathrm{A}}^* \tilde{\mathrm{G}} q^2 + \tilde{\mathrm{B}}^* \tilde{\mathrm{H}} q^2 + \tilde{\mathrm{C}}^* \tilde{\mathrm{G}}_+ \mathrm{M}_+ - \tilde{\mathrm{D}}^* \tilde{\mathrm{H}} \mathrm{M}_-\right) m_\mu\right. \\
&\left. - \left(\tilde{\mathrm{A}}^* \tilde{\mathrm{F}} \mathrm{M}_+ - \tilde{\mathrm{B}}^* \tilde{\mathrm{E}} \mathrm{M}_- + \tilde{\mathrm{C}}^* \tilde{\mathrm{F}} + \tilde{\mathrm{D}}^* \tilde{\mathrm{E}}\right) q^2\right],
\end{aligned}
\tag{1.16}
$$

with

$$
\begin{aligned}
f_\pm &= \left(2m_\mu^2 + q^2\right)\hat{m}_\pm^2, \quad \hat{m}_\pm^2 = \mathrm{M}_\pm^2 - q^2, \quad \mathrm{M}_\pm = m_\Sigma \pm m_p, \quad \beta = \sqrt{1 - \frac{4m_\mu^2}{q^2}} \\
f &= \left(m_\Sigma^2 + m_p^2 + m_\mu^2 - q^2 - t\right)\left(m_\mu^2 - t\right) + m_\Sigma^2 m_p^2.
\end{aligned}
\tag{1.17}
$$

The allowed range of t is given by

$$
t_{\mathrm{max,min}} = \frac{1}{2}\left(m_\Sigma^2 + m_p^2 + 2m_\mu^2 - q^2 \pm \beta\sqrt{\bar{\lambda}}\right), \tag{1.18}
$$

with $\bar{\lambda} = \hat{m}_-^2 \hat{m}_+^2$.

For $\tilde{\mathrm{A}}, \tilde{\mathrm{B}}, \ldots\ \tilde{\mathrm{K}}$ being independent from t, the time integration of the double-differential decay rate leads to

$$
\begin{aligned}
&\frac{d\Gamma\left(\Sigma^+ \to p\mu^+\mu^-\right)}{dq^2} = \\
&\frac{\left(3\beta - \beta^3\right) q^2 \sqrt{\bar{\lambda}}}{64\pi^3 m_\Sigma^3}\left\{\left[\frac{\hat{m}_+^2}{3} + \frac{q^2}{2}\right]|\tilde{\mathrm{A}}|^2 + \left[1 + \frac{\hat{m}_+^2}{3q^2}\right]\frac{|\tilde{\mathrm{C}}|^2}{2} + \mathrm{M}_+\,\mathrm{Re}\left(\tilde{\mathrm{A}}^* \tilde{\mathrm{C}}\right)\right\}\hat{m}_-^2 \\
&+\frac{\left(3\beta - \beta^3\right) q^2 \sqrt{\bar{\lambda}}}{64\pi^3 m_\Sigma^3}\left\{\left[\frac{\hat{m}_-^2}{3} + \frac{q^2}{2}\right]|\tilde{\mathrm{B}}|^2 + \left[1 + \frac{\hat{m}_-^2}{3q^2}\right]\frac{|\tilde{\mathrm{D}}|^2}{2} - \mathrm{M}_-\,\mathrm{Re}\left(\tilde{\mathrm{B}}^* \tilde{\mathrm{D}}\right)\right\}\hat{m}_+^2 \\
&+\frac{\beta\sqrt{\bar{\lambda}}}{32\pi^3 m_\Sigma^3}\left\{\left[\frac{3 - \beta^2}{12}\bar{\lambda} + \frac{\beta^2}{2}\hat{m}_-^2 q^2 + \hat{m}_+^2 m_\mu^2\right]|\tilde{\mathrm{E}}|^2 + \left[\beta^2|\tilde{\mathrm{G}}|^2 + |\tilde{\mathrm{J}}|^2\right]\frac{\hat{m}_+^2 q^2}{4}\right. \\
&\quad + \left[\frac{3 - \beta^2}{12}\bar{\lambda} + \frac{\beta^2}{2}\hat{m}_+^2 q^2 + \hat{m}_-^2 m_\mu^2\right]|\tilde{\mathrm{F}}|^2 + \left[\beta^2|\tilde{\mathrm{H}}|^2 + |\tilde{\mathrm{K}}|^2\right]\frac{\hat{m}_-^2 q^2}{4} \\
&\quad \left. + \hat{m}_+^2 m_\mu \mathrm{M}_-\,\mathrm{Re}\left(\tilde{\mathrm{E}}^* \tilde{\mathrm{J}}\right) - \hat{m}_-^2 m_\mu \mathrm{M}_+\,\mathrm{Re}\left(\tilde{\mathrm{F}}^* \tilde{\mathrm{K}}\right)\right\}.
\end{aligned}
\tag{1.19}
$$

The $\Sigma^+ \to p\mu^+\mu^-$ branching fraction and the dimuon invariant mass are the only quantities that have been explored so far. With a good amount of data, other observables may become accessible, such as the forward-backward asymmetry $\mathcal{A}_{\mathrm{FB}}$ of the muon:

$$A_{\rm FB} \;=\; \frac{\int_{-1}^{1} dc_\theta\, {\rm sgn}(c_\theta)\, \Gamma''}{\int_{-1}^{1} dc_\theta\, \Gamma''}\,, \qquad \Gamma'' \;\equiv\; \frac{d^2\Gamma(\Sigma^+ \to p\mu^+\mu^-)}{dq^2\, dc_\theta}\,, \qquad c_\theta \;\equiv\; \cos\theta\,, \tag{1.20}$$

where θ is the angle between the directions of μ and p in the rest frame of the dimuon system. The forward-backward asymmetry in the decay may provide hints on possible NP effects, which may modify the measured SM decay amplitude with respect to the theoretical expectation.

The integrated forward-backward asymmetry takes the following form:

$$\tilde{A}_{\rm FB} = \frac{1}{\Gamma\left(\Sigma^+ \to p\mu^+\mu^-\right)} \int_{q^2_{\rm min}}^{q^2_{\rm max}} dq^2 \int_{-1}^{1} dc_\theta\, {\rm sgn}\left(c_\theta\right) \Gamma'', \tag{1.21}$$

where

$$\Gamma\left(\Sigma^+ \to p\mu^+\mu^-\right) = \int_{q^2_{\rm min}}^{q^2_{\rm max}} dq^2 \Gamma', \quad q^2_{\rm min} = 4m^2_\mu, \quad q^2_{\rm max} = \left(m_\Sigma - m_p\right)^2. \tag{1.22}$$

The polarization asymmetries of the muons in the final state may also become accessible. When μ^- is polarized, the differential rate becomes

$$\frac{d\Gamma^-\left(\varsigma^-_x, \varsigma^-_y, \varsigma^-_z\right)}{dq^2} = \frac{\Gamma'}{2}\left(1 + \mathcal{P}^-_{\rm T}\varsigma^-_x + \mathcal{P}^-_{\rm N}\varsigma^-_y + \mathcal{P}^-_{\rm L}\varsigma^-_z\right), \tag{1.23}$$

where the subscripts L, N, and T denote the longitudinal, normal, and transverse polarizations of the muon. The corresponding polarization asymmetries $\mathcal{P}^-_{\rm L,N,T}$ are

$$\begin{aligned}
\mathcal{P}^-_{\rm L} &= \frac{\beta^2\sqrt{\bar{\lambda}}}{192\pi^3\Gamma' m^3_\Sigma}\,{\rm Re}\Big\{\Big[-3\left(2{\rm M}_+\tilde{\rm A}^*\tilde{\rm E} + \tilde{\rm H}^*\tilde{\rm K}\right)q^2 - 2\left(\hat{m}^2_+ + 3q^2\right)\tilde{\rm C}^*\tilde{\rm E} + 6m_\mu{\rm M}_+\tilde{\rm F}^*\tilde{\rm H}\Big]\hat{m}^2_- \\
&+ \Big[3\left(2{\rm M}_-\tilde{\rm B}^*\tilde{\rm F} - \tilde{\rm G}^*\tilde{\rm J}\right)q^2 - 2\left(\hat{m}^2_- + 3q^2\right)\tilde{\rm D}^*\tilde{\rm F} - 6m_\mu{\rm M}_-\tilde{\rm E}^*\tilde{\rm G}\Big]\hat{m}^2_+\Big\}\,, \\
\mathcal{P}^-_{\rm N} &= \frac{\beta^2\bar{\lambda}\sqrt{q^2}}{256\pi^2\Gamma' m^3_\Sigma}\,{\rm Im}\Big\{2\Big[\left({\rm M}_+\tilde{\rm A} + \tilde{\rm C}\right)^*\tilde{\rm F} + \left(\tilde{\rm D} - {\rm M}_-\tilde{\rm B}\right)^*\tilde{\rm E}\Big]m_\mu - \left(\tilde{\rm A}^*\tilde{\rm G} + \tilde{\rm B}^*\tilde{\rm H}\right)q^2 \\
&- \left(\tilde{\rm C}^*\tilde{\rm G} - \tilde{\rm E}^*\tilde{\rm J}\right){\rm M}_+ + \left(\tilde{\rm D}^*\tilde{\rm H} - \tilde{\rm F}^*\tilde{\rm K}\right){\rm M}_-\Big\}\,, \\
\mathcal{P}^-_{\rm T} &= \frac{\beta\bar{\lambda}\sqrt{q^2}}{256\pi^2\Gamma' m^3_\Sigma}\,{\rm Re}\Big\{2\Big[2\left({\rm M}_+\tilde{\rm A} + \tilde{\rm C}\right)^*\left(\tilde{\rm D} - {\rm M}_-\tilde{\rm B}\right) - {\rm M}_-\tilde{\rm A}^*\tilde{\rm E} + {\rm M}_+\tilde{\rm B}^*\tilde{\rm F}\Big]m_\mu \\
&-{\rm M}_+\tilde{\rm C}^*\tilde{\rm J} + {\rm M}_-\tilde{\rm D}^*\tilde{\rm K} + \beta^2\left({\rm M}_+\tilde{\rm E}^*\tilde{\rm G} - {\rm M}_-\tilde{\rm F}^*\tilde{\rm H}\right)\Big\} \\
&- \frac{\beta\bar{\lambda}\,{\rm Re}\Big[\left(\tilde{\rm A}^*\tilde{\rm J} + \tilde{\rm B}^*\tilde{\rm K}\right)q^4 + 2\left(\tilde{\rm C}^*\tilde{\rm E} + \tilde{\rm D}^*\tilde{\rm F}\right){\rm M}_+{\rm M}_- m_\mu\Big]}{256\pi^2\Gamma' m^3_\Sigma\sqrt{q^2}}.
\end{aligned} \tag{1.24}$$

If μ^+ is polarized, the resulting polarization asymmetries are

$$\begin{aligned}
\mathcal{P}_{\mathrm{L}}^{+} &= \mathcal{P}_{\mathrm{L}}^{-} + \frac{\beta^2\sqrt{\bar{\lambda}}\,\mathrm{Re}\left[2\left(\hat{m}_{+}^{2}\mathrm{M}_{-}\tilde{\mathrm{E}}^{*}\tilde{\mathrm{G}} - \hat{m}_{-}^{2}\mathrm{M}_{+}\tilde{\mathrm{F}}^{*}\tilde{\mathrm{H}}\right)m_{\mu} + \left(\hat{m}_{+}^{2}\tilde{\mathrm{G}}^{*}\tilde{\mathrm{J}} + \hat{m}_{-}^{2}\tilde{\mathrm{H}}^{*}\tilde{\mathrm{K}}\right)q^2\right]}{32\pi^3\Gamma' m_{\Sigma}^{3}}, \\
\mathcal{P}_{\mathrm{N}}^{+} &= \mathcal{P}_{\mathrm{N}}^{-} + \frac{\beta^2\bar{\lambda}\,\mathrm{Im}\left(\mathrm{M}_{-}\tilde{\mathrm{F}}^{*}\tilde{\mathrm{K}} - \mathrm{M}_{+}\tilde{\mathrm{E}}^{*}\tilde{\mathrm{J}}\right)\sqrt{q^2}}{128\pi^2\Gamma' m_{\Sigma}^{3}}, \\
\mathcal{P}_{\mathrm{T}}^{+} &= \mathcal{P}_{\mathrm{T}}^{-} + \frac{\beta\bar{\lambda}\,\mathrm{Re}\left[\left(\tilde{\mathrm{A}}q^2 + \mathrm{M}_{+}\tilde{\mathrm{C}}\right)^{*}\left(2m_{\mu}\mathrm{M}_{-}\tilde{\mathrm{E}} + \tilde{\mathrm{J}}q^2\right) - \left(\tilde{\mathrm{B}}q^2 - \mathrm{M}_{-}\tilde{\mathrm{D}}\right)^{*}\left(2m_{\mu}\mathrm{M}_{+}\tilde{\mathrm{F}} - \tilde{\mathrm{K}}q^2\right)\right]}{128\pi^2\Gamma' m_{\Sigma}^{3}\sqrt{q^2}}.
\end{aligned} \tag{1.25}$$

The polarisations $\mathcal{P}_{\mathrm{L}}^{\pm}$ probe the P violation in the leptonic contributions of the amplitude while $\mathcal{P}_{\mathrm{T}}^{\pm}$ are sensitive to the P violation in both the hadronic and leptonic components. The polarisations $\mathcal{P}_{\mathrm{N}}^{\pm}$, on the other hand, may be induced by the CP violation, generated from the presence of NP effects. Similar to the forward-backward asymmetry, the integrated polarization asymmetries are defined as

$$\tilde{P}_{\mathrm{L,N,T}}^{\mp} = \frac{1}{\Gamma\left(\Sigma^{+} \to p\mu^{+}\mu^{-}\right)}\int_{q_{\mathrm{min}}^2}^{q_{\mathrm{max}}^2} dq^2\Gamma'\mathcal{P}_{\mathrm{L,N,T}}^{\mp}. \tag{1.26}$$

1.5 The $\Sigma^+ \to p\pi^0$ decay

The $\Sigma^+ \to p\pi^0$ decay is the Σ^+ mode with the largest value of branching fraction, being $\mathcal{B}\left(\Sigma^+ \to p\pi^0\right) = (51.57 \pm 0.30)\,\%$ [12]. It is a nonleptonic process, which is the primary decay mode for a hyperon particle [37].

In the nonleptonic decay, the hyperon B decays into a lighter baryon B' and a charged or neutral pion π. The corresponding decay amplitude is

$$\mathcal{M}_{B\to B'\pi} = \bar{u}(\mathbf{p}')\left[A + B\gamma_5\right]u(\mathbf{p}), \tag{1.27}$$

where A and B denote the parity-violating and parity-conserving amplitudes. If CP is conserved, the phase in the partial wave amplitudes A and B is evaluated with the strong $B'\pi$ scattering phase shifts in the final-state S and P waves, respectively:

$$A = A_0\exp\left(i\delta_{B'\pi}^{S}\right), \qquad B = B_0\exp\left(i\delta_{B'\pi}^{p}\right), \tag{1.28}$$

with A_0 and B_0 being real parameters.

Using A and B, the decay rate is expressed as

$$\Gamma_{B\to B'\pi} = \frac{|\mathbf{q}|\left(E' + m_{B'}\right)}{4\pi m_B}\left(|A|^2 + |\bar{B}|^2\right), \qquad \bar{B} = \sqrt{\frac{E' - m_{B'}}{E' + m_{B'}}}B, \tag{1.29}$$

where $\mathbf{q}$ is the momentum of π in the rest frame of the decaying hyperon.

The decay distribution assumes the form in Eq. 1.30 while the polarization of the baryon in the final state is expressed in Eq. 1.31.

$$W(\theta) = 1 + \alpha \mathbf{P}_B \cdot \hat{\mathbf{p}}_{B'}, \qquad \alpha = \frac{2\mathrm{Re}\,(A^*\,\bar{B})}{|A|^2 + |\bar{B}|^2}. \tag{1.30}$$

$$\langle \mathbf{P}_{B'} \rangle = \frac{(\alpha + \mathbf{P}_B \cdot \hat{\mathbf{p}}_{B'})\,\hat{\mathbf{p}}_{B'} + \beta\,(\mathbf{P}_B \times \hat{\mathbf{p}}_{B'}) + \gamma\,[\hat{\mathbf{p}}_{B'} \times (\mathbf{P}_B \times \hat{\mathbf{p}}_{B'})]}{W(\theta)}, \tag{1.31}$$

with $\mathbf{P}_B$ being the polarization of the initial decaying hyperon and $\hat{\mathbf{p}}_{B'}$ a unit vector in the direction of B'. The parameters β and γ are written as follows:

$$\beta = \frac{2\mathrm{Im}(A^*\bar{B})}{|A|^2 + |\bar{B}|^2}, \qquad \gamma = \frac{|A|^2 - |\bar{B}|^2}{|A|^2 + |\bar{B}|^2} = \pm\sqrt{1 - \alpha^2 - \beta^2}. \tag{1.32}$$

The measured and theoretical values for the A and B amplitudes are listed in Tab.1.4.

Modes	A Amplitudes (10^{-7})		B Amplitudes (10^{-7})	
	Measured	Theoretical	Measured	Theoretical
$\Lambda \to p\pi^-$	$+3.25$	$+3.38$	$+22.1$	$+23.0$
$\Lambda \to n\pi^0$	-2.37	-2.39	-15.8	-16.0
$\Sigma \to n\pi^+$	$+0.13$	0.00	$+42.2$	$+4.30$
$\Sigma \to p\pi^0$	-3.27	-3.18	$+26.6$	$+10.0$
$\Sigma^- \to n\pi^-$	$+4.27$	$+4.50$	-1.44	-10.0
$\Xi^0 \to \Lambda\pi^0$	$+3.43$	-3.14	-12.3	$+3.30$
$\Xi^- \to \Lambda\pi^-$	-4.51	-4.45	$+16.6$	-4.70

Table 1.4. Measured and theoretical values for the A and B amplitudes.

In the lowest-order chiral $SU(3)$ analysis, the A amplitude for the $\Sigma^+ \to p\pi^0$ decay is found to be

$$iA_{\Sigma^+ \to p\pi^0} = \frac{\sqrt{6}}{2F_\pi}(D - F), \tag{1.33}$$

depending of the parameters D and F [37].

The A amplitude, together with the strong $BB'\pi$ vertex, determine the baryon pole contribution to the B amplitude, wich is estimated to be

$$B_{\Sigma^+ \to p\pi^0} = -\frac{m_N + m_\Sigma}{2m_N F_\pi} \cdot \frac{(D - F)\mathcal{M}_{\Sigma^+ p}}{m_\Sigma - m_N}. \tag{1.34}$$

In conclusion, the $\Sigma^+ \to p\pi^0$ decay amplitude [37] can be written as

$$\mathcal{M}_{\Sigma^+ \to p\pi^0} = \frac{2f}{F_\pi}\bar{u}\gamma_\mu\gamma_5 u\, q^\mu = \frac{g_A^{\Sigma^+\Sigma^+}}{F_\pi}\bar{u}\gamma_\mu\gamma_5 u\, q^\mu = \frac{2g_{\pi NN}}{2m_N}\,\frac{f}{f+d}\bar{u}\gamma_\mu\gamma_5 u\; q^\mu. \tag{1.35}$$

Taking $D + F = 1.27$ and $D/F = 1.8$ [37], the P-wave predictions listed in Tab.1.4 are found. The failure in simultaneously fitting the S and P waves is a deficiency of the lowest-order chiral analysis. This is not too surprising as the chiral expansion converges slower in baryons than in mesons [38].

1.6 Overview on the search of the $\Sigma^+ \to p\mu^+\mu^-$ decay

Due to the lack of experiments with large hyperon production rates and to the experimental difficulty in reconstructing soft and long-lived hadrons, only the HyperCP and the LHCb collaborations have searched for the $\Sigma^+ \to p\mu^+\mu^-$ decay.

In the next subsections, the reported results from these experiments are presented. Recent updates on the theoretical branching fraction predictions are also illustrated, coming from the 2023 analysis on the $\Sigma^+ \to p\gamma$ decay of the BESIII collaboration.

1.6.1 The $\Sigma^+ \to p\mu^+\mu^-$ decay at HyperCP

The HyperCP experiment aimed to study asymmetries between matter and antimatter in hyperon and kaon decays. The experiment was conducted at the Fermi National Accelerator Laboratory (Fermilab) and was located at the Meson Center beam line. A schematic view of the HyperCP spectrometer is illustrated in Fig. 1.5 [39].

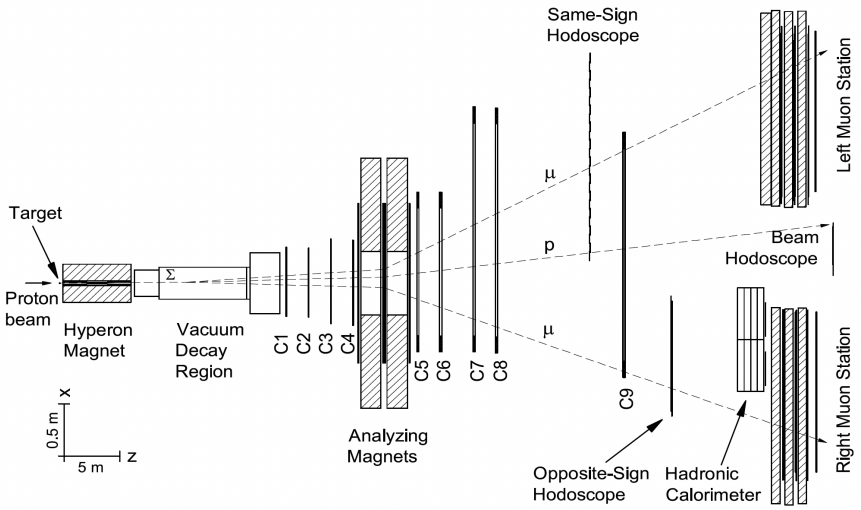

Figure 1.5. Schematic view of the HyperCP spectrometer.

A proton beam with $p \sim 800$ GeV/c was exploited to produce a large rate of hyperons. The target was able to produce a charged secondary beam, by interacting with the primary one, with $p \sim 160$ GeV/c, which in turn was bent by a collimator. The collimator was designed to allow only particles within a specific momentum range to pass through, while a magnet was employed to bend the path of the charged particles. The spectrometer comprised nine Multi Wire Proportional Chambers and magnets with sufficient strength to ensure that the proton and pions from the hyperon decays were always well separated from each other as well as from the charged beam exiting the collimator. On the proton side, a hadronic calorimeter was used to make the trigger blind to muons. A simple muon system at the end of the spectrometer was installed to access rare hyperon decays with muons in the final state.

The first evidence for the $\Sigma^+ \to p\mu^+\mu^-$ decay was reported by the HyperCP collaboration [30] in 2005. The decay was reconstructed with two opposite sign muon tracks and a proton track, originating from a common vertex. The $\Sigma^+ \to p\mu^+\mu^-$ invariant mass from the HyperCP analysis is shown in Fig. 1.6.

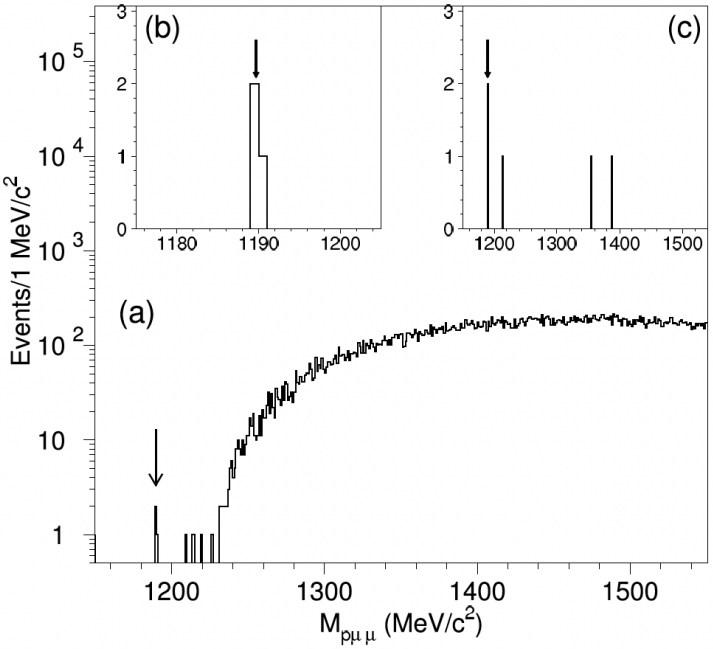

Figure 1.6. Distribution of the $\Sigma^+ \to p\mu^+\mu^-$ invariant mass distribution after a first preselection (a), within ± 15 MeV/c^2 from the Σ^+ mass value (b) and after the final selection (c). The arrow points to the Σ^+ mass value.

The evidence is based on the observation of three signal candidates, corresponding to the following measured branching fraction:

$$\mathcal{B}(\Sigma^+ \to p\mu^+\mu^-) = (8.6^{+6.6}_{-5.4} \pm 5.5) \times 10^{-8}, \tag{1.36}$$

which is compatible with the SM prediction. In the reported result, the first uncertainty is statistical and the second one is systematic.

The reconstructed candidates have almost the same dimuon invariant mass. In details, they present the following values: 214.7, 214.3, and 213.7 MeV/c^2, lying within the expected dimuon mass resolution of ~ 0.5 MeV/c^2. The distribution of the dimuon invariant mass is reported in Fig. 1.7. The unexpectedly narrow distribution suggests that the decay may have an intermediate state, with a particle X^0 decaying into a muon pair. This would indicate an intermediate two-body decay $\Sigma^+ \to pX^0(\to \mu^+\mu^-)$, different from the expected three-body decay in the SM, with $m_{X^0} = 214.3 \pm 0.5$ MeV/c^2.

The branching fraction for this hypothetical NP decay was estimated to be $\mathcal{B}(\Sigma^+ \to pX^0(\to \mu^+\mu^-)) = [3.1^{+2.4}_{-1.9}(\text{stat}) \pm 1.5(\text{syst})] \times 10^{-8}$ [40]. In the scenario in which the three candidates were assumed to be a background component, coming from an unknown source, the upper limit was set at $\mathcal{B}(\Sigma^+ \to p\mu^+\mu^-) < 3.4 \times 10^{-7}$ at 90% confidence level [41].

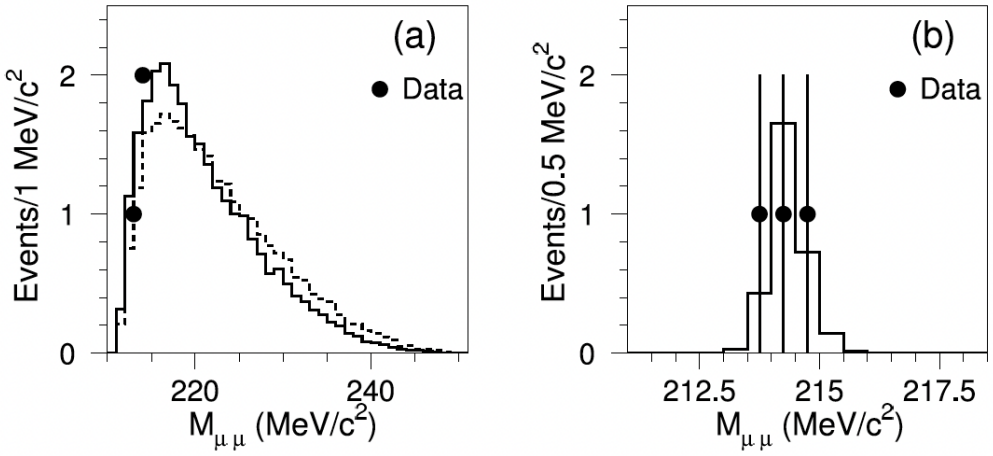

Figure 1.7. Dimuon invariant mass distribution for signal $\Sigma^+ \to p\mu^+\mu^-$ candidates. The distribution is shown superimposed with two MC distributions (phase space and form-factor) (a) and with a MC including a resonant structure decaying into the dimuon pair (b).

1.6.2 The $\Sigma^+ \to p\mu^+\mu^-$ decay at LHCb during Run 1

Many theories Beyond the Standard Model (BSM) have been proposed to explain the HyperCP result. The intermediate X^0 particle could be a light pseudoscalar Higgs boson in the Next-to-Minimal Supersymmetric SM extension [42] [43] or a sgoldstino particle in various supersymmetric models [44] [45]. In general, a pseudoscalar particle is favoured over a scalar one to describe the HyperCP result and a lifetime of the order of 10^{-14} s is estimated for the former case [46] [47] [48] [49] [50].

Various initial and final states were investigated by many experiments to confirm the HyperCP result [51] [52] [53] [54]. Searches for the X^0 particle were also conducted at LHCb by investigating the $B^0_{(s)} \to \mu^+\mu^-\mu^+\mu^-$ [55] and $B^0 \to K^{0*}\mu^+\mu^-$ [56] decays and by searching for photon-like particles [57]. No sign of NP, compatible with the HyperCP result, was ever detected.

The search for the $\Sigma^+ \to p\mu^+\mu^-$ decay has been repeated at LHCb with the data collected at centre-of-mass energies $\sqrt{s} = 7$ and 8 TeV, corresponding to an integrated luminosity of 3 fb^{-1}, during the Run 1 data-taking period of the Large Hadron Collider [31]. The distribution of the $\Sigma^+ \to p\mu^+\mu^-$ invariant mass from the LHCb Run 1 analysis is shown in Fig. 1.8, superimposed with the fit.

Evidence for this decay was reported with the observation of $10.2^{+3.9}_{-3.5}$ signal candidates, corresponding to a signal significance of 4.1σ. The branching fraction was measured to be

$$\mathcal{B}(\Sigma^+ \to p\mu^+\mu^-) = \left(2.2^{+0.9+1.5}_{-0.8-1.1}\right) \times 10^{-8}, \tag{1.37}$$

consistent with the SM prediction, where the first uncertainty is statistical and the second one is systematic.

The distribution of the dimuon invariant mass was also investigated for a possible NP structure, as shown in Fig. 1.9.

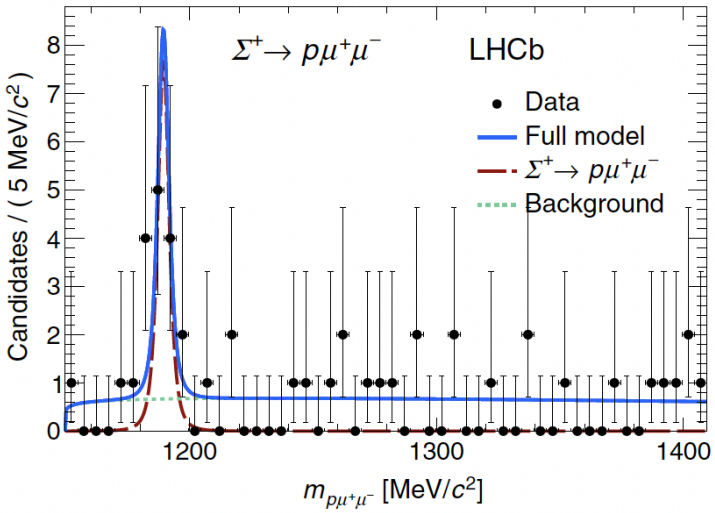

Figure 1.8. Distribution of $\Sigma^+ \to p\mu^+\mu^-$ invariant mass in data and superimposed with the fit (blue). The signal (red) and background (green) components of the fit are also illustrated.

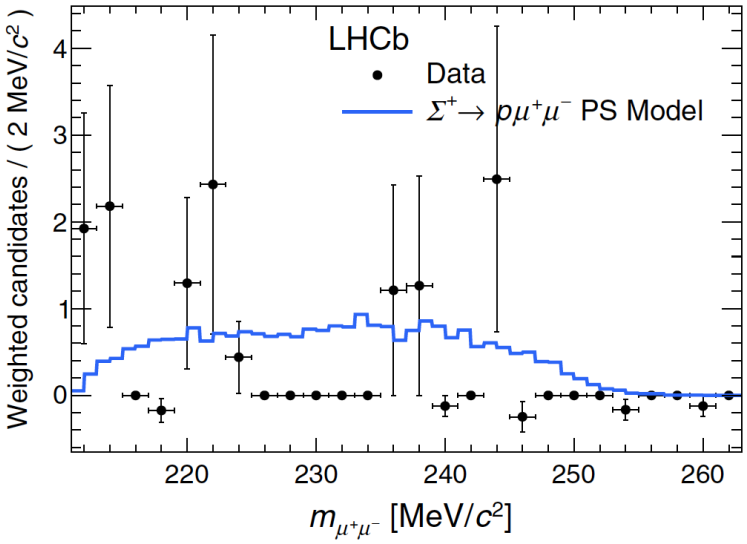

Figure 1.9. Background-subtracted distribution of the dimuon invariant mass for the $\Sigma^+ \to p\mu^+\mu^-$ observed candidates, superimposed with the simulated phase-space (PS) model. Uncertainties on data points are calculated as the square root of the sum of squared weights.

The spectrum in data was compatible with the phase space distribution, i.e. no significant NP structure was observed in the dimuon invariant mass, in contrast with the HyperCP result. An upper limit on the branching fraction of the resonant channel was set at $\mathcal{B}(\Sigma^+ \to pX^0(\to \mu^+\mu^-)) < 1.4 \times 10^{-8} (1.7 \times 10^{-8})$ at 90% (95%) confidence level.

1.6.3 Update on the $\Sigma^+ \to p\mu^+\mu-$ branching fraction prediction

New results on the branching fraction and polarisation asymmetry of the $\Sigma^+ \to p\gamma$ decay were reported by the BESIII collaboration [58] in May 2023, marking the newest study on this decay mode since 1995. These measurements are compared with the PDG values [12] in Tab. 1.5. The single measurement is statistically superior to the world average value, even if the branching fraction is found to be lower by 4.2σ.

Parameter	BESIII	PDG
$\mathcal{B}\,(10^{-3})$	$0.996 \pm 0.021 \pm 0.018$	1.23 ± 0.05
α	$-0.651 \pm 0.056 \pm 0.020$	-0.76 ± 0.08

Table 1.5. Branching fraction and polarisation asymmetry of the $\Sigma^+ \to p\gamma$ decay from the latest BESIII results and the PDG.

The $\Sigma^+ \to p\mu^+\mu-$ and $\Sigma^+ \to p\gamma$ decay amplitudes share the same a and b form factors, which can be extrapolated from the $\Sigma^+ \to p\gamma$ experimental results. Given this, the SM prediction of the $\Sigma^+ \to p\mu^+\mu^-$ branching fraction will change, depending on the latest BESIII input.

The effective Lagrangian of the radiative $\Sigma^+ \to p\gamma$ decay is written as

$$\mathcal{L} \equiv \frac{eG_F}{2}\bar{u}_p[a(0) + b(0)\gamma_5]\sigma^{\mu\nu}u_\Sigma F_{\mu\nu}, \tag{1.38}$$

and $a(0)$ and $b(0)$, with $q^2 = 0$, are related to its decay rate and polarisation asymmetry:

$$\Gamma = \frac{G_F^2 e^2}{\pi}(|a(0)|^2 + |b(0)|^2)E_\gamma^3, \tag{1.39}$$

$$\alpha = \frac{2\Re[a(0)b(0)^*]}{|a(0)|^2 + |b(0)|^2}. \tag{1.40}$$

Taking the imaginary parts of $a(0)$ and $b(0)$ in Fig. 1.4 and converting the measured branching fraction into the decay rate, the real parts $\Re[a(0)]$ and $\Re[b(0)]$ are obtained by solving the system of equations above. A scan on the $\Re[a(0)]$ and $\Re[b(0)]$ space is performed in the relativistic [35] and heavy baryon [36] χPT approaches, as shown in Fig. 1.10. The PDG average values reproduce exactly the results in Tab. 1.3, while the BESIII input gives new predictions, listed in Tab. 1.6.

The overall prediction range, coming from the BESIII input, becomes

$$\mathcal{B}(\Sigma^+ \to p\mu^+\mu^-) = [1.2, 7.9] \times 10^{-8}. \tag{1.41}$$

The newest $\Sigma^+ \to p\mu^+\mu^-$ branching fraction predictions are still compatible with the previous results from the HyperCP and LHCb collaborations. The 8-fold discrepancy between the relativistic and heavy χPT methods is still present and it can be solved only by the experimental results.

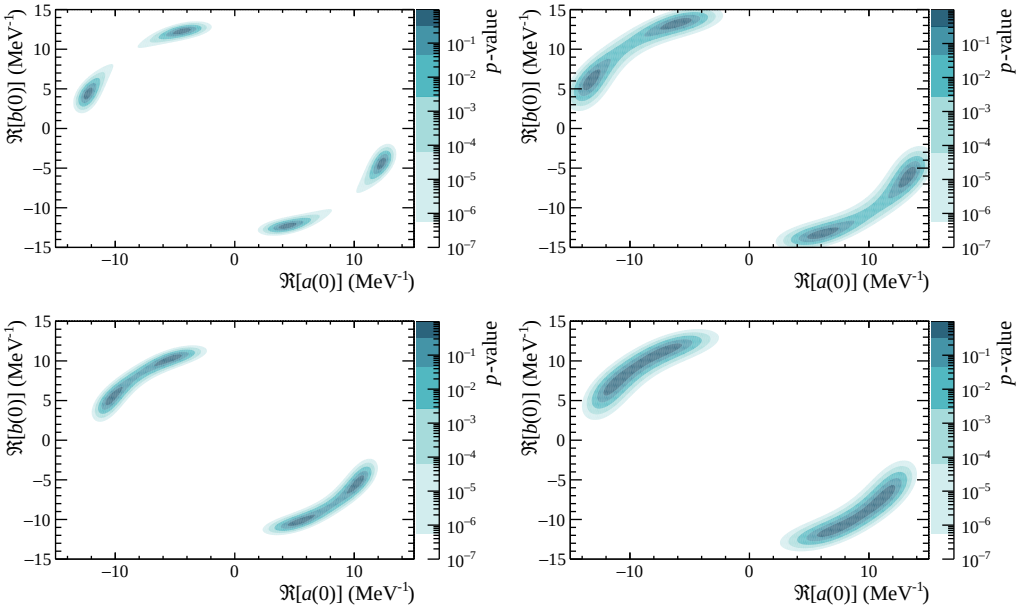

Figure 1.10. Scan of the $\Re[a(0)]$ and $\Re[b(0)]$ space with the BESIII (left) and PDG (right) results in the relativistic (top) and heavy (bottom) baryon χPT approaches.

Solution	$\Re[a(0)]\left(\text{GeV}^{-1}\right)$	$\Re[b(0)]\left(\text{GeV}^{-1}\right)$	$\mathcal{B}\,(10^{-8})$
Relativistic baryon			
1	$+0.0123$	-0.0044	1.2
2	-0.0123	$+0.0044$	2.5
3	$+0.0044$	-0.0123	4.3
4	-0.0044	$+0.0123$	7.9
Heavy baryon			
1	$+0.0103$	-0.0054	1.7
2	-0.0103	$+0.0054$	3.4
3	$+0.0054$	-0.0103	3.4
4	-0.0054	$+0.0103$	6.5

Table 1.6. Solutions for the real parts of the a and b form factors and their corresponding $\Sigma^+ \to p\mu^+\mu^-$ branching fraction predictions in the relativistic and heavy χPT approaches with the BESIII input.

Chapter 2

The LHCb experiment at CERN

The *Conseil Européen pour la Recherche Nucléaire* (CERN) hosts the Large Hadron Collider and the LHCb experiment. The primary goal of LHCb is to study rare decays in particles containing beauty and charm quarks, focusing on the CP violation and all the open questions within the flavour physics, with the aim of searching indirectly for NP beyond the SM. The experiment, having a high hyperon production cross-section, is also able to investigate rare hyperon decays and to perform world-leading measurements in this sector.

In this chapter, after a brief introduction to the Large Hadron Collider, the LHCb detector is presented. In particular, its subsystems and performances are illustrated. The described experimental setup denotes the one employed during the Run 2 data-taking period, between 2015 and 2018, in which the $\Sigma^+ \to p\mu^+\mu^-$ dataset of the analysis presented in this thesis has been collected. Furthermore, upgrades for the Run 3 campaign, which began in July 2022, are reported.

2.1 The Large Hadron Collider

The Large Hadron Collider (LHC) [59] is the world largest particle collider, situated within the underground circular tunnel that once hosted the Large Electron-Positron (LEP) collider [60]. In the tunnel, which is 26.7 km long, 3.8 m wide and ranges from a depth of 50 to 175 m, two beams of protons and/or heavy ions travel in opposite directions within the vacuum pipes. These particles are organized in bunches and collide at centre-of-mass energy on the TeV scale.

The CERN accelerator complex [61] is shown in Fig. 2.1. Protons are produced by removing electrons from hydrogen atoms with an electric field. These are accelerated up to 50 MeV, using the linear particle accelerator LINAC 4 [62]. Furthermore, protons are accelerated again up to 1.4 GeV within the Proton Synchrotron Booster (PSB) [63]. At this point, they are introduced into the Proton Synchrotron (PS) [64], reaching energies up to 26 GeV. These values are later increased up to 450 GeV in the Super Proton Synchrotron (SPS) [65]. Finally, bunches up to 1.15×10^{11} protons are injected in the LHC and set to reach energies on the TeV scale. These bunches, separated from each other by 25 ns, collide at different points with a frequency rate between 30 and 40 MHz. A total of 1232 superconductive dipole magnets and 392 quadrupole magnets are used to keep the beams in a circular trajectory and focused.

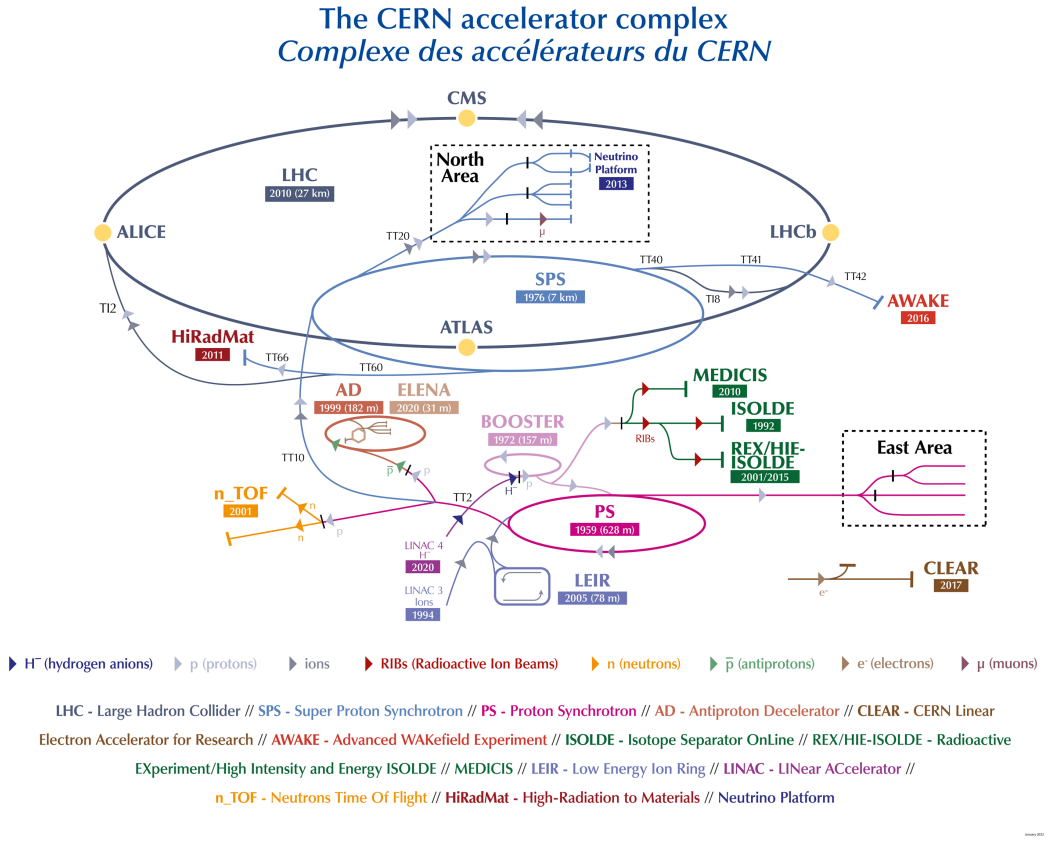

Figure 2.1. The CERN accelerator complex.

The LHC experiments are positioned in the tunnel, near or around the collision points. At the present time, four main experiments are recording data at LHC. The ATLAS [66] and CMS [67] experiments explore the SM electroweak and Higgs sectors and are oriented to the direct search of NP. The ALICE [68] experiment investigates the heavy ion physics and the properties of Quark Gluon Plasma. The LHCb [28] experiment is dedicated to the study of flavour physics and performs indirect searches of NP. The four major LHC experiments are reported in Fig. 2.1.

The first operational phase of LHC, known as Run 1, was conducted between 2010 and 2012. In its initial stage, it operated at $\sqrt{s} = 7$ TeV while in the final months of Run 1 the centre-of-mass energy was increased up to 8 TeV [69]. Following a long shutdown period, dedicated to the upgrades of both the accelerator and detectors to operate at $\sqrt{s} = 13$ TeV, the second operational phase, known as Run 2, started in 2015 until 2018 [70]. The third operational phase, denoted as Run 3, began in July 2022 and it is projected to last until 2026. In this data-taking period, the centre-of-mass energy is set to reach 13.6 TeV.

2.2 The LHCb detector

The Large Hadron Collider beauty (LHCb) experiment investigates the heavy flavour physics in the beauty and charm sectors, given the high production cross-sections of both $b\bar{b}$ and $c\bar{c}$ pairs, corresponding to 72(144) μb and 1.4(2.6) mb at $\sqrt{s} = 7(13)$ TeV within the LHCb acceptance [71] [72].

The LHCb detector is a single-arm spectrometer [73] [74], positioned in the forward region relative to the proton-proton (pp) collision point. This configuration is chosen as heavy-quark hadrons are primarily generated in the forward and backward regions, with respect to the interaction point. This is evident at high energies, where the production of $b\bar{b}$ pairs is mainly governed by gluon-gluon interactions [75]. Both gluons typically possess different momenta and the resulting longitudinal component, along the beam direction, becomes dominant. Simulations on the $b\bar{b}$ pairs production are shown in Fig. 2.2.

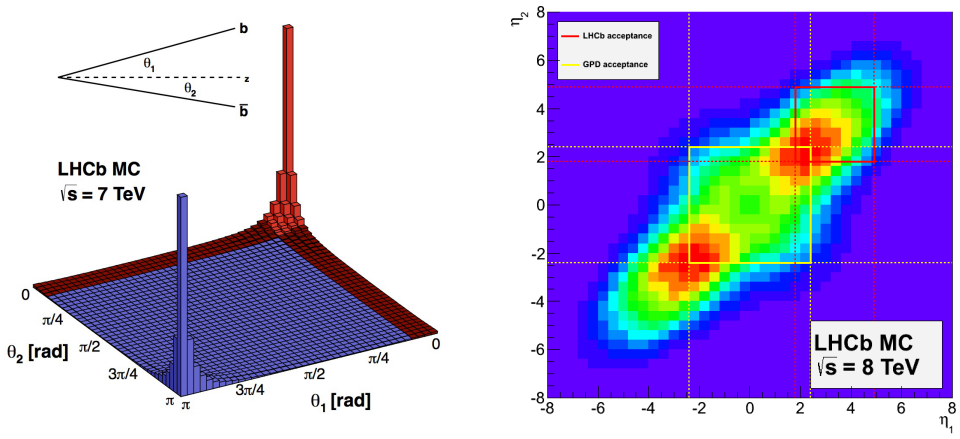

Figure 2.2. Simulation of the $b\bar{b}$ pair production cross-section as a function of their polar angles with respect to the beam axis at $\sqrt{s} = 14$ TeV (left). Two-dimensional pseudorapidity plot of the $b\bar{b}$ pair production phase space in simulated pp collisions at $\sqrt{s} = 14$ TeV. The LHCb acceptance is highlighted in red while the General Purpose Detector (GDP), such as ATLAS and CMS, acceptance is shown in yellow.

A schematic view of the LHCb experiment is illustrated in Fig. 2.3. The coordinate system (O, x, y, z) is centred at the collision point. The z-axis is defined along the beam direction and points to the right, while the y-axis is vertical and points upwards. The decay vertex of the particles, produced in the pp interactions, is reconstructed by the Vertex Locator, surrounding the interacting region. Upstream of the magnet, the particles pass through the first Ring Imaging Cherenkov (RICH1) detector and the Tracker Turicensis (TT). The trajectories of the charged particles are bent by the dipole magnet, before reaching the tracking stations T1, T2 and T3. The magnetic field lines follow the direction of the y-axis, defining the bending x-z and non-bending y-z planes. The angular coverage of the experiment ranges from 10 to 300 mrad in the bending plane and from 10 to 250 mrad in the non-bending plane, corresponding to a pseudorapidity coverage of $2 < \eta < 5$, evaluated as $\eta = -\ln[\tan(\theta/2)]$, where θ defines the angle with respect to the z-axis.

Downstream of the magnet, the particles find the RICH2 detector and the calorimeters system, composed of the Scintillating Pad Detector (SPD), the Pre-Shower detector (PS), the electromagnetic (ECAL) and hadronic (HCAL) calorimeters. At the end of the LHCb detector lies the muon system, composed of five muon stations M1-M5. Details on the LHCb subdetectors and performances will be given in the next sections.

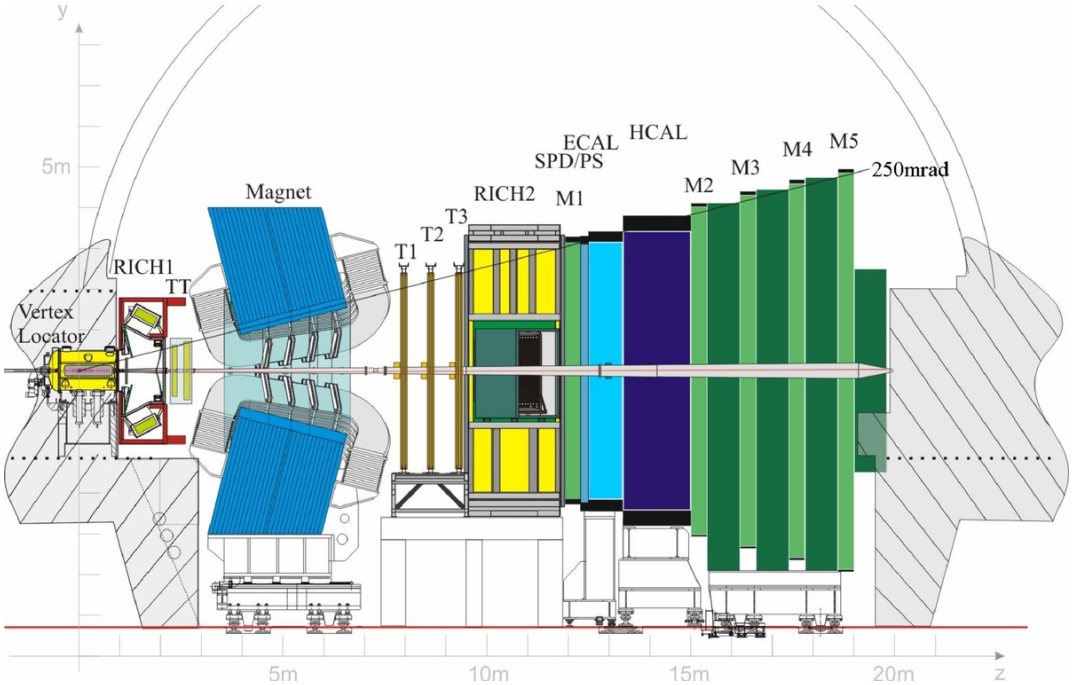

Figure 2.3. Schematic view of the LHCb detector in the y-z non-bending plane.

The instantaneous luminosity of a particle collider can be defined as

$$\mathcal{L} = \frac{N_1 N_2 n_b f_{rev}}{4\pi\sigma_x\sigma_y}, \tag{2.1}$$

where $N_i (i = 1, 2)$ denotes the number of protons in a single bunch in each beam, n_b is the number of colliding bunches, f_{rev} is the revolution frequency, $\sigma_{x,y}$ define the widths of the bunch Gaussian shape in the transverse plane and $4\pi\sigma_x\sigma_y$ represents the effective transverse colliding area [76].

At LHCb, the luminosity is kept, as much as possible, stable during a full LHC fill of bunches. This is achieved by tuning the transverse separation of the beams, thus adjusting the effective colliding area [77]. This method allows to decrease the number of events with many primary decay vertices, simplifying the reconstruction of secondary vertices from the decay of heavy hadrons.

The LHCb experiment ran at an instantaneous luminosity of 4×10^{32} cm^{-2}s^{-1} during the Run 1 and Run 2 data-taking periods. This value is one order of magnitude lower than the ones at the ATLAS and CMS experiments, as shown in Fig. 2.4 for a long LHC fill of bunches during Run 1 [78].

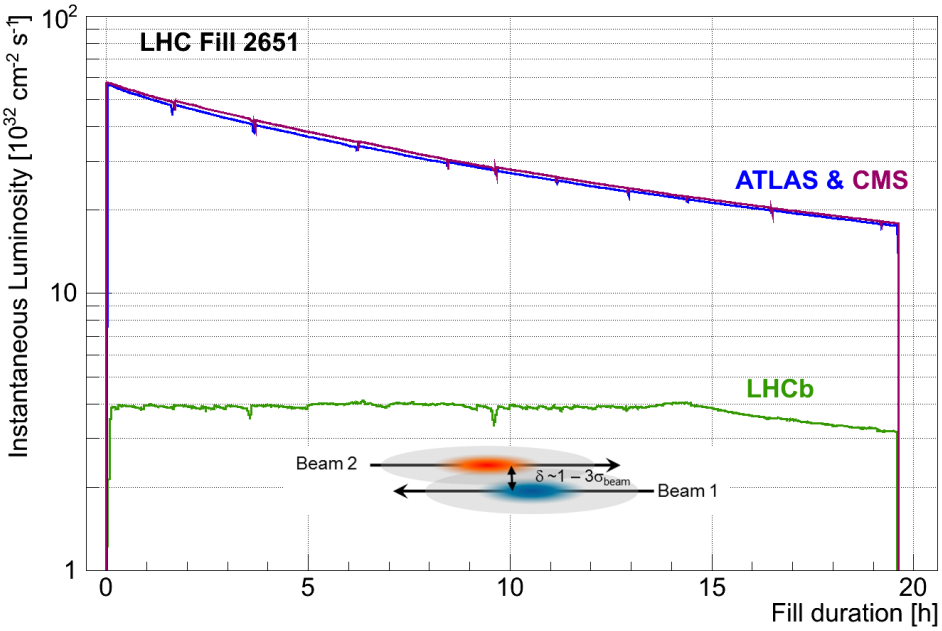

Figure 2.4. Instantaneous luminosity for the ATLAS, CMS and LHCb experiments for a long LHC fill of bunches during Run 1. Once the desired value of 4×10^{32} cm^{-2}s^{-1} is reached at LHCb, the luminosity is kept stable in a range of 5% for about 15 hours.

2.3 The tracking system

The tracking system provides information on the passage of the charged particles through LHCb, with its subsystems positioned both downstream and upstream of the magnet.

The first tracking detector that the particles encounter is the Vertex Locator. Furthermore, they proceed through the Tracker Turicensis, positioned upstream of the dipole magnet. As the charged particles pass through the magnetic field, their trajectories are curved according to their charges and momenta. Downstream of the magnet, they reach the T-stations. Particles with small angles, with respect to the beam direction, pass through the Inner Tracker, situated in the central parts of the T-stations. On the other hand, particles with wider angles pass through the Outer Tracker, positioned in the outer sections of the T-stations.

2.3.1 The Vertex Locator

The Vertex Locator (VELO) [79] is positioned around the *pp* interaction region and measures the particles hit coordinates to reconstruct the Primary Vertices (PV), from *pp* interactions, and the Secondary Vertices (SV), from long-lived hadrons decays. This information allows to discriminate the heavy-flavour decays from the background sources. Measurements of other quantities, such as the time of decay of the hadrons, are also possible with the data coming from the VELO detector.

The VELO is made of two sets of 21 stations, positioned along the beam axis.

Each station is composed of two semi-circular silicon micro-strip sensors, denoted as Φ and R sensors. These sensors measure the azimuthal and radial coordinates of the hit position of the passing particle, respectively. Together with the coordinate of the beam axis, the 3D hit position is estimated. Upstream of the sensors, supplementary modules are integrated to form the pile-up veto system. During the injection of the LHC beams, the stations are moved away from the beam pipe in the horizontal direction to reduce the amount of radiation interacting with the sensors. Once the LHC beams found a stable condition, the VELO is fully closed and the closest active strip is at 8.2 mm from the beam axis. The entire subsystem is installed in a vacuum vessel, which is separated from the Ultra High Vacuum of LHC by a 300 μm thick layer of aluminium, denoted as RF foil. This separation protects the sensors from the radio-frequency waves, produced by the beam, and minimises the material traversed by the charged particles before they reach the sensors. An illustration of the VELO layout is shown in Fig. 2.5.

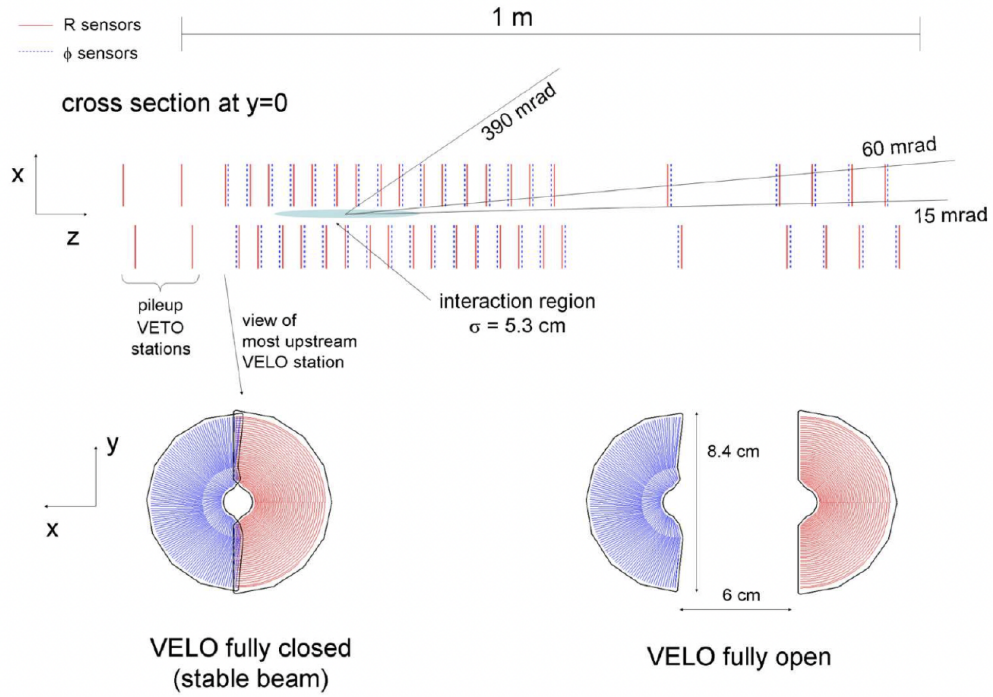

Figure 2.5. Illustration of the VELO layout, including the Φ (red) and R (blue) sensors.

The resolution on the PV is estimated to be 13 μm in the transverse direction and 71 μm in the longitudinal one [80]. The longitudinal resolution decreases to $\sim$ 150 μm for the SVs, due to the smaller number of tracks. The Impact Parameter (IP), defined as the minimum distance between a reconstructed track and its PV, is measured with a resolution of $\sim$ 35 μm for particles with a p_T of 1 GeV. This resolution decreases to 15 μm for larger transverse momentum, as reported in Fig. 2.6. At high p_T, the IP resolution is dominated by the PV resolution rather than the track reconstruction one as particles with high p_T undergo multiple scattering while the PV reconstruction depends on the number of tracks associated with it.

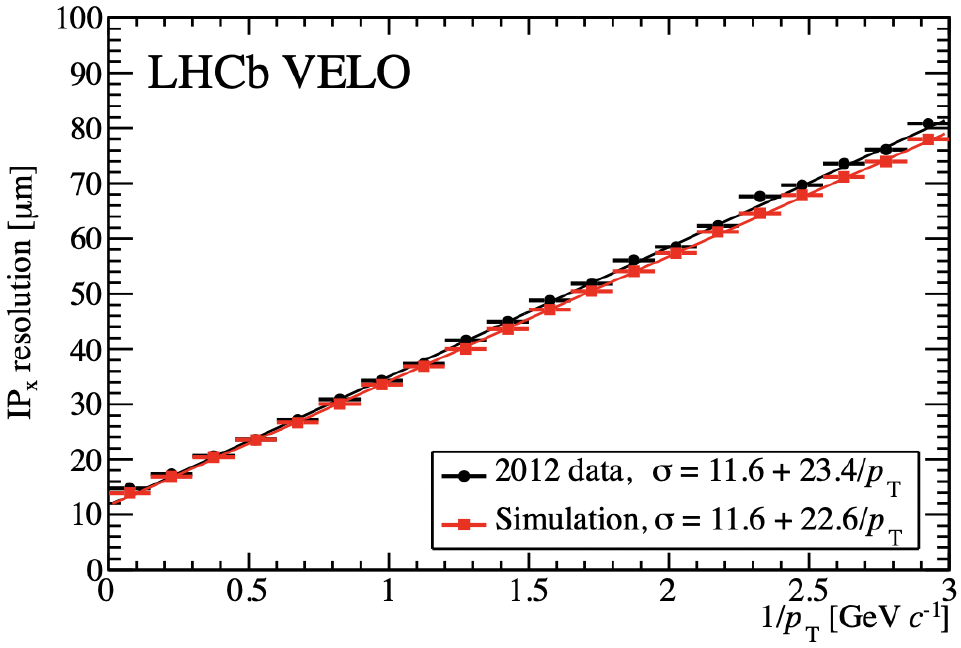

Figure 2.6. Resolution of the Impact Parameter on the x-axis as a function of $1/p_T$ for the 2012 LHCb data (black) and simulation (red).

2.3.2 The dipole magnet

The LHCb dipole magnet [81] is made of two saddle-shaped coils, arranged symmetrically within an iron window frame, as shown in Fig. 2.7. These coils, built with 50 tons of Al-99.7 conductor cables, are bent at 45° with respect to the horizontal plane and are included in a yoke to get the return flow of the field, consisting of steel plates. The opening angle is ±250 mrad vertically and ±300 mrad horizontally.

The nominal current running through the magnet is 5.85 kA, with a total resistance of 130 mΩ at 20° C. The resulting magnetic field has a maximum strength of 1.1 T and an integrated value of 4 T·m. This field covers a significant region along the z-axis, approximately ranging from 2.5 m to 7.95 m. The polarity of the magnetic field is reversed frequently during the data-taking to keep under control systematic effects on the tracking and charge asymmetries in the CP violation measurements. This leads to two distinct recorded datasets: MagDown and MagUp. The evolution of the magnetic field profile along the z-axis is shown in Fig. 2.8 (top).

The LHCb tracking system is designed to reconstruct different types of tracks. The most relevant tracks are the so-called long tracks, which originate from a vertex in the VELO and pass through the whole tracking system. Downstream tracks are very important for long-lived particle studies, such as Λ particles. They are produced from a vertex, downstream of the VELO, and leave hits in the Tracker Turicensis and T-stations. Furthermore, the LHCb detector is able to reconstruct upstream tracks, leaving hits only in the VELO and the Tracker Turicensis, and T tracks, with signatures only in the T-stations. A graphical representation of the LHCb tracks is shown in Fig. 2.8 (bottom).

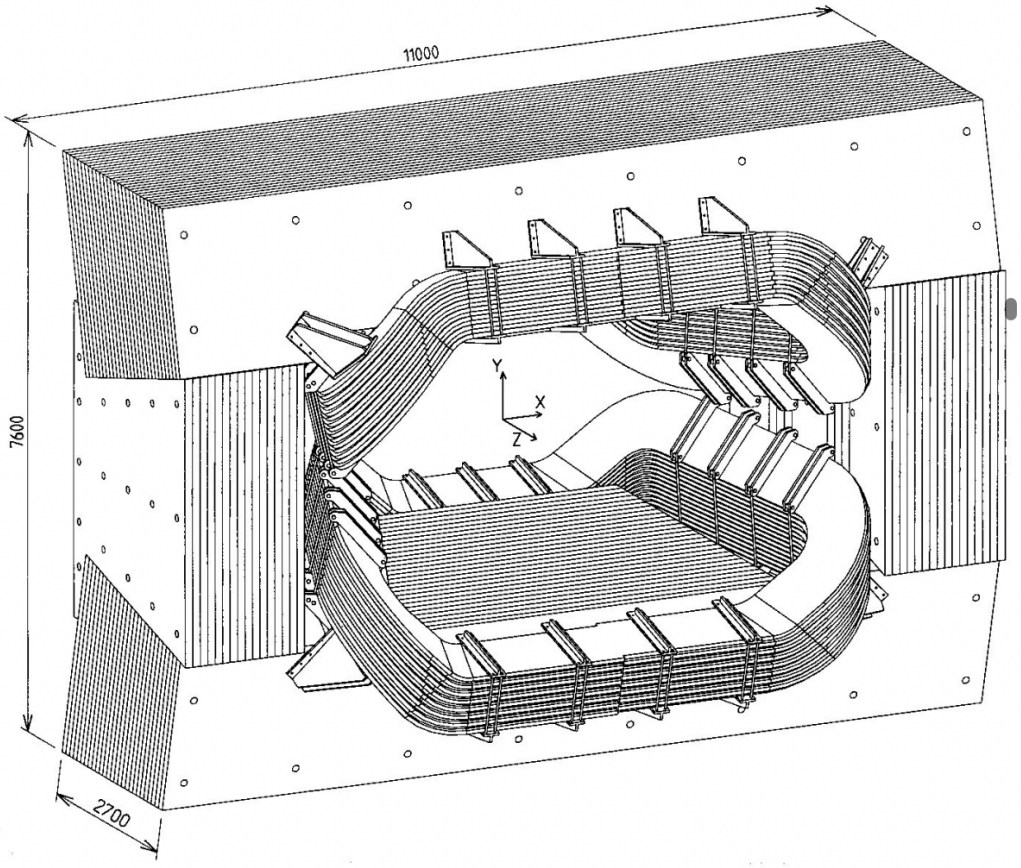

Figure 2.7. Schematic view of the LHCb dipole magnet.

2.3.3 The tracking stations

The tracking stations include the Tracker Turicensis (TT), situated between the RICH1 and the magnet, and the T1-T3 stations, positioned beyond the magnet. The TT and the inner part of the T1-T3 stations, called Inner Tracker (IT) [82], form the Silicon Tracker (ST) [83]. The remaining outer regions of the T-stations form the Outer Tracker (OT) [84].

The TT is made of four 150 cm $\times$ 130 cm planar layers of silicon microstrips, separated by 27 cm along the z-axis and arranged in the two pairs TTa and TTb. A total of 143 thousand strips are employed, with a length of 10-40 cm and pitch of 183 μm, achieving a position resolution of $\sim$ 50 μm in the bending plane. The sensors are organized in a specific configuration in each layer to precisely measure the coordinates of the tracks, denoted as x-u-v-x geometry. In the x-u-v-x geometry, the first and fourth x layers are vertically aligned while the central u and v layers are rotated by $\pm 5^{\circ}$. The combination of the u and v measurements allows to extrapolate the y position of the track and provides the 3D information needed for the full reconstruction. A schematic view of the TT is shown in Fig. 2.9. The TT is essential to reconstruct downstream tracks and helps the long track reconstruction by providing hit measurements before the magnet.

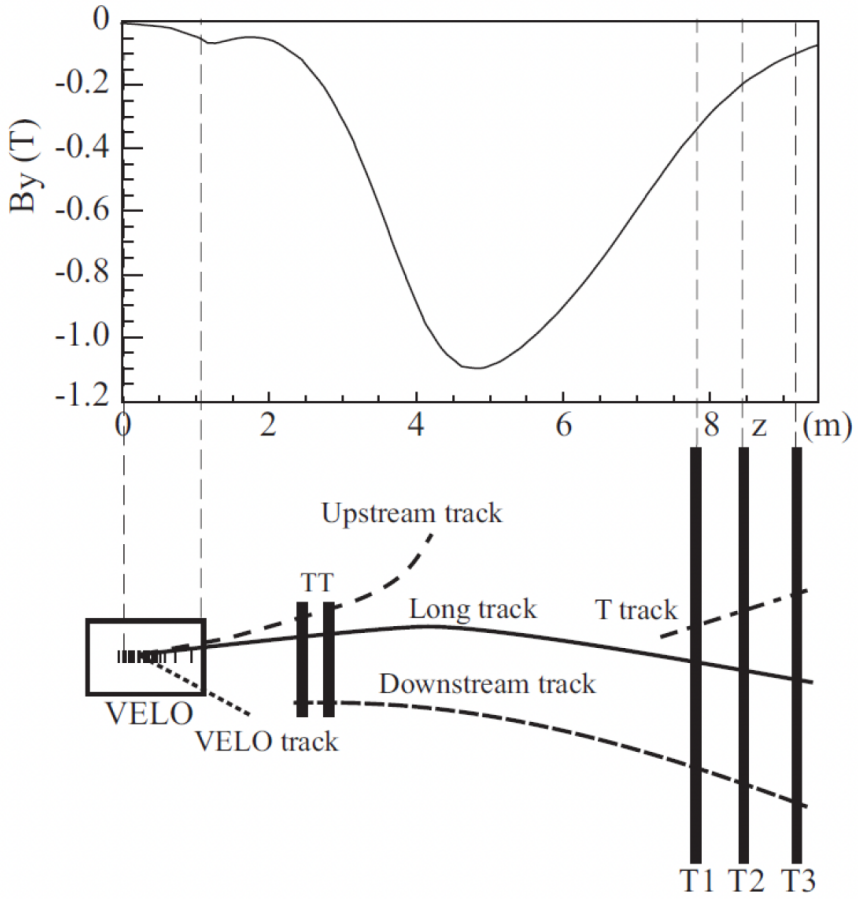

Figure 2.8. Evolution of the magnetic field profile along the z-axis (top) and graphical representation of the LHCb tracks (bottom).

The IT is positioned downstream of the magnet, covering the central region where the particle occupancy is significantly higher. It has a cross-shaped configuration, with a width of 125.6 cm and a height of 41.4 cm. Each station of the IT is made of four detector boxes, surrounding the beam pipe, each containing four layers of sensors arranged in the x-u-v-x geometry. The IT covers only the 2% of the LHCb acceptance but $\sim$ 20% of all the produced tracks in the *pp* collisions pass through this subsystem. A schematic view of the x-layer of the IT is shown in Fig. 2.10.

The OT is a drift chamber detector, designed as an array of 200 gas-tight straw tube modules. It covers the outer regions of the T-stations and serves a crucial role in the detection of charged particles within the low-density region of the tracking system. Each station is made of four layers, arranged in the x-u-v-x geometry, covering an active area of $\sim$ 30 m^2. Each layer contains two monolayers of drift tubes, vertically oriented, with an inner diameter of 4.9 mm and filled with a gas mixture of 70% Argon, 28.5% CO2, and 1.5% O2. At the core of each straw lies a 25 μm thick anode wire. The drift time across the tube is less than 50 ns and the spatial resolution is $\sim$ 200 μm. A schematic view of the OT is shown in Fig. 2.11.

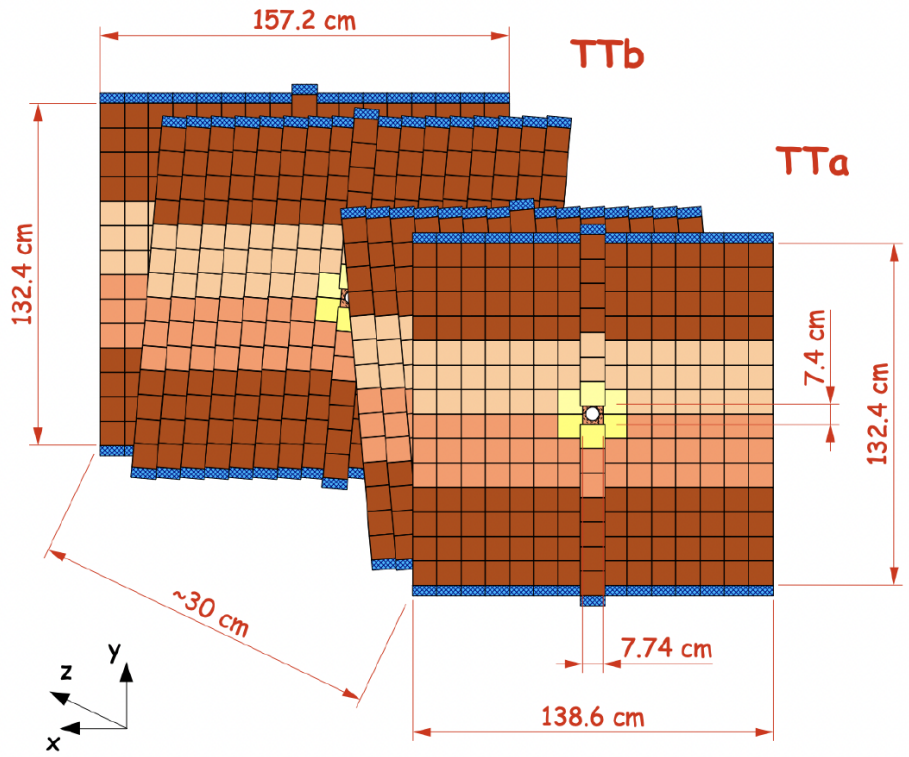

Figure 2.9. Schematic view of the TT detector.

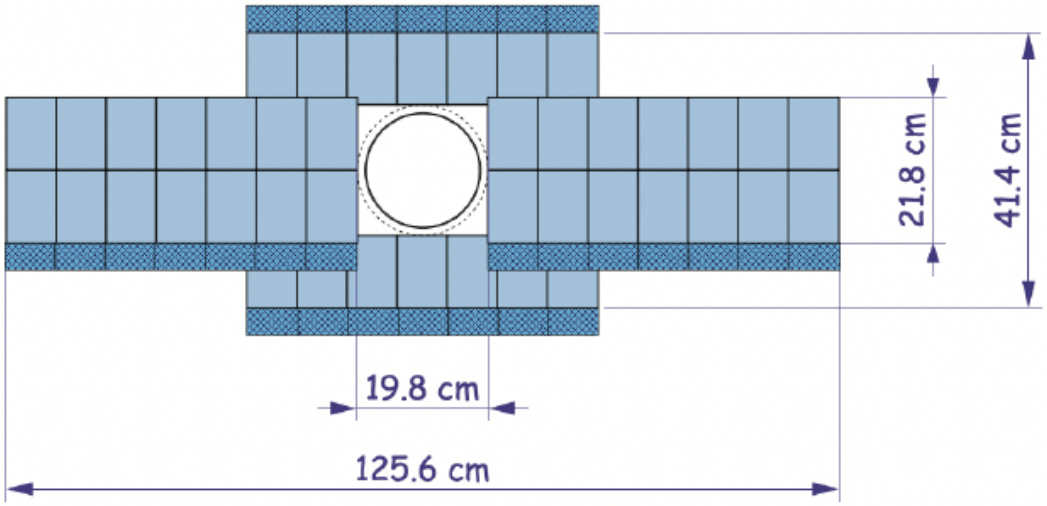

Figure 2.10. Schematic view of the x-layer of the IT detector.

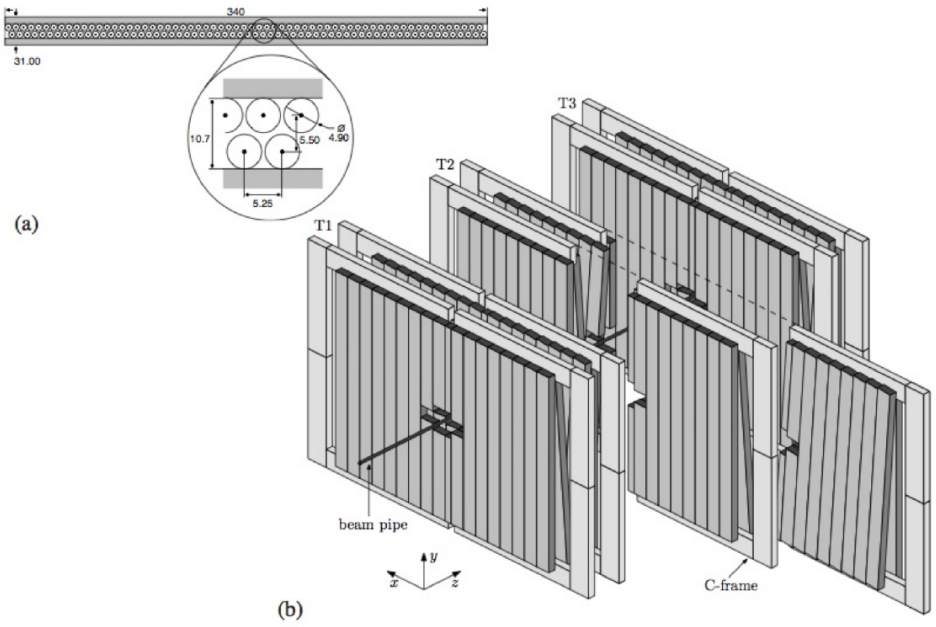

Figure 2.11. Section of a straw-tube in an OT module (a) and schematic view of the OT detector (b).

2.3.4 Tracking reconstruction and performance

Various algorithms are employed to reconstruct the LHCb tracks. In the initial phase of the track reconstruction, the pattern-recognition algorithms are used to detect the hits of the particles. This process involves the VELO tracking [85] and the T-seeding [86] algorithms to detect the hits in the VELO and the T-stations. For the reconstruction of long tracks, the forward tracking algorithm [87] and the matching algorithm [88] come also into play. In the second phase, the track fit tries to match a track model to the hits found by the pattern-recognition algorithms. These hits are fitted with a Kalman filter [89] and an estimation of the quantities defining the track, such as its charge and momentum, is performed. With the track fit, the quality of the track is decided and track candidates with poor quality are filtered out. In the final stage of the track reconstruction, track candidates with a bad fit quality are discarded. These tracks include *ghost* tracks [78], reconstructed with a random combination of hits, and clone tracks, reconstructed from a significant overlap of hits.

The efficiency of the track reconstruction for the LHCb tracks depends primarily on the particle kinematics and the count of charged particles within the event. On average, the track reconstruction efficiency is estimated to be $\sim 96\%$ in the momentum range 5 GeV/$c < p <$ 200 GeV/c. The relative uncertainty associated with the measured momentum ranges from 0.5% at lower values to 1.0% at 200 GeV/c [90]. The tracking efficiency as a function of the momentum is shown in Fig. 2.12 for the 2011 and 2012 LHCb data samples.

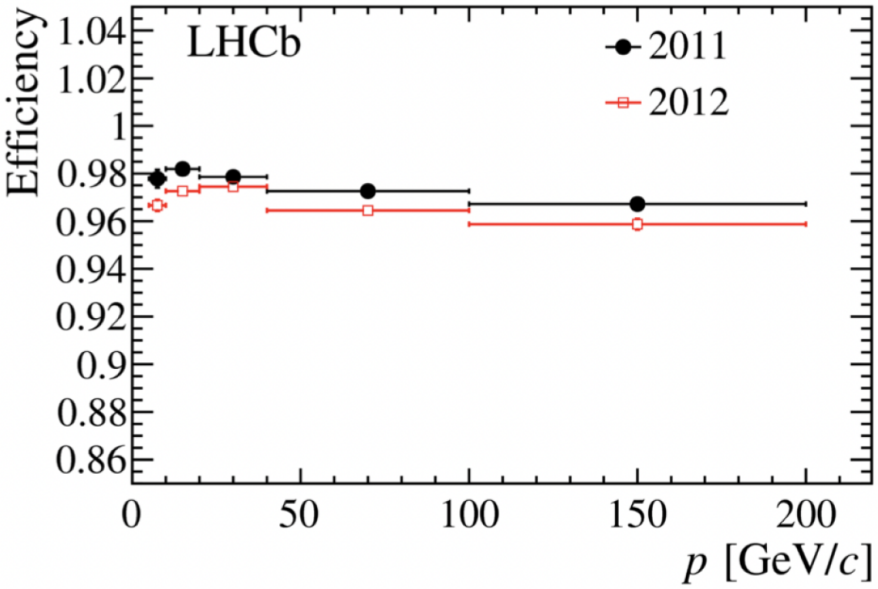

Figure 2.12. Tracking efficiency as a function of the momentum for the 2011 and 2012 LHCb data samples.

2.4 The particle identification system

In the analysis of rare decays with similar multiplicity and topology, contaminations due to particle misidentification are expected to become relevant sources of background. Therefore, particle identification (PID) emerges as a crucial prerequisite within the LHCb experiment.

The PID at LHCb is performed with the dual RICH detectors, the calorimeter and muon systems. These detectors contribute to evaluating the identity of charged particles, such as e, μ, π and K, within a momentum range from 2 to 450 GeV/c.

2.4.1 The Ring Imaging Cherenkov detectors

The main purpose of the Ring Imaging Cherekov (RICH) detectors [91] is the separation of charged hadrons, such as K, π and protons. The PID in the RICH system is based on the Cherenkov effect. This event occurs when a charged particle passes through a medium, referred to as radiator, exceeding the speed of light within it and generating a cone of Cherenkov light. The cone opening angle, denoted as Cherenkov angle θ_c, depends on both the refractive index n of the medium and the particle velocity v as $\cos\theta_c = 1/(\beta n)$, where $\beta = v/c$. Combining this information with the momentum p, provided by the tracking system, it is possible to evaluate the mass of the particle from the following equation:

$$\cos\theta_c = \frac{1}{n}\sqrt{1+\left(\frac{mc}{p}\right)^2}. \tag{2.2}$$

The LHCb RICH system is divided into two detectors: RICH1 and RICH2. The RICH1 detector, positioned between the VELO and the magnet, employs a C_4F_{10} gas mixture as a radiator, with a refractive index of $n = 1.0014$, covering the momentum range from 1 to 60 GeV/c. It has an angular acceptance from ±25 mrad to ±300 mrad horizontally and from ±25 mrad to ±250 mrad vertically. On the other hand, RICH2 is positioned downstream of the magnet and employs a CF_4 gas mixture as a radiator, with a refractive index of $n = 1.0005$, covering the momentum range from 10 to 100 GeV/c. In comparison to RICH1, its angular acceptance is more constrained, extending from ±15 mrad to ±120 mrad horizontally and from ±15 mrad to ±100 mrad vertically. A schematic view of both RICH1 and RICH2 is illustrated in Fig. 2.13. The combination of the two RICH detectors covers the entire range of momenta of the B and D meson decay products.

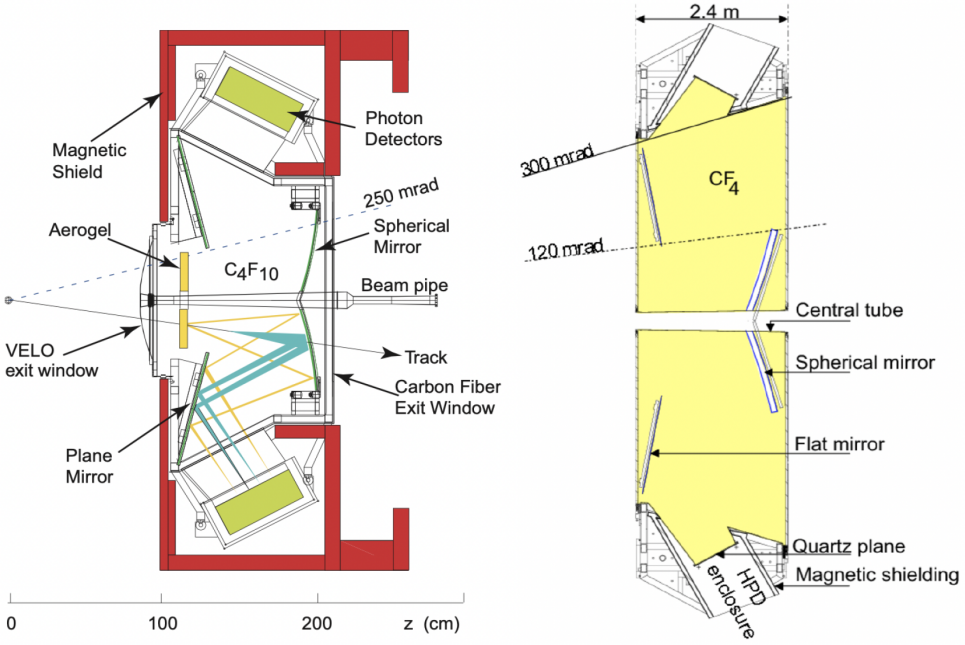

Figure 2.13. Schematic side views of the RICH1 (left) and RICH2 (right) detectors.

The photons emitted through the RICH radiators are reflected, using a system of plane and spherical mirrors, to the detection planes, where the Hybrid Photon Detectors (HPDs) are installed. The HPDs are position-sensitive sensors, designed to detect the Cherenkov rings and measure their radius and θ_c. The distribution of the Cherenkov angle as a function of the particle momentum for different RICH radiators is reported in Fig. 2.14 (left) while the same distribution for the C_4F_{10} gas mixture used as the radiator in Run 1 is shown in Fig. 2.14 (right) [92].

In the RICH system, the PID is performed by matching VELO and TT tracks with the hits in the detection planes and selecting the most likely candidate particle. Using the Cherenkov angle, the RICH pattern recognition technique aligns photon hits, corresponding to charged particle tracks, with the expected pattern of hits using a maximum likelihood approach. A typical LHCb event in RICH1 with the Cherenkov rings interpolation is illustrated in Fig. 2.15.

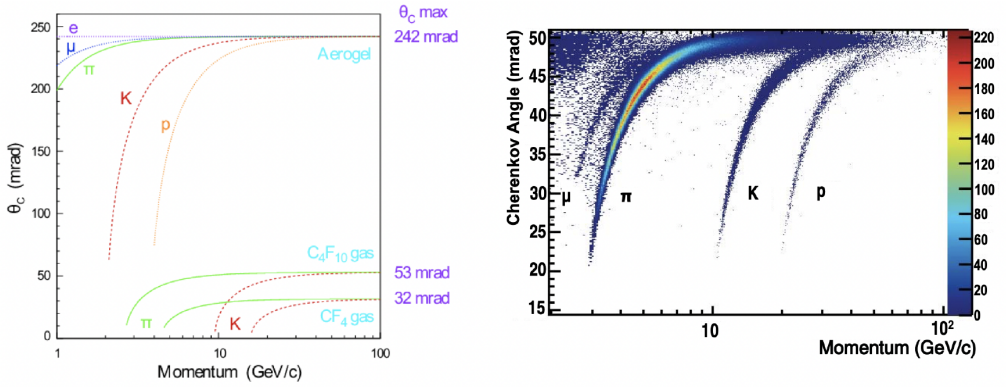

Figure 2.14. Cherenkov angle as a function of the particle momentum for different RICH radiators (left). Cherenkov angle as a function of the particle momentum for the C_4F_{10} gas mixture used as the radiator in Run 1 (right).

2.4.2 The calorimeter system

The calorimeter system [93] is positioned downstream of the RICH2 detector and provides measurements on the energies and the positions of clusters deposited by electrons, photons and hadrons. Candidates with high deposited transverse energy are selected from this system, which provides information for the hardware trigger level and for the PID. The system is made of four detectors: the Scintillating Pad Detector (SPD), the PreShower detector (PS) and the electromagnetic and hadronic calorimeters (ECAL and HCAL). Both ECAL and HCAL detect the hits of the particles with PhotoMultiplier Tubes (PMTs), while the SPD and the PS detectors use Multianode PMTs. A graphical representation of the particles deposited energies in the LHCb calorimeter system is illustrated in Fig. 2.16.

The SPD is employed to identify charged tracks, while the PS discriminates photons and pions from the electrons. Once this separation is achieved, the energies of these particles are measured by the ECAL. The ECAL is a heterogeneous sampling calorimeter, which measures the energies and the positions of clusters deposited by the electrons and the photons. It is made of shashlik cells, consisting of 66 alternating layers of 2 mm thick lead and 4 mm thick scintillator. The ECAL energy resolution is

$$\frac{\sigma_E}{E} = \frac{10\%}{\sqrt{E}} \oplus 1\%, \tag{2.3}$$

where the first 10% term is due to the statistical uncertainty on the energy deposit of the electromagnetic shower and the 1% term is a constant contribution due to the systematics effects. The upper limit for the observable transverse energy is set at 10 GeV, exceeding the usual energy deposits associated with the b and c hadron decays within the LHCb events [94].

The HCAL is responsible for measuring the energies and the positions of clusters deposited by neutral and charged hadrons. It is a sampling calorimeter, positioned after the ECAL detector, made of 16 mm thick iron tiles and 4 mm thick scintillator layers, for a total extension along the z-axis of 1.6 m.

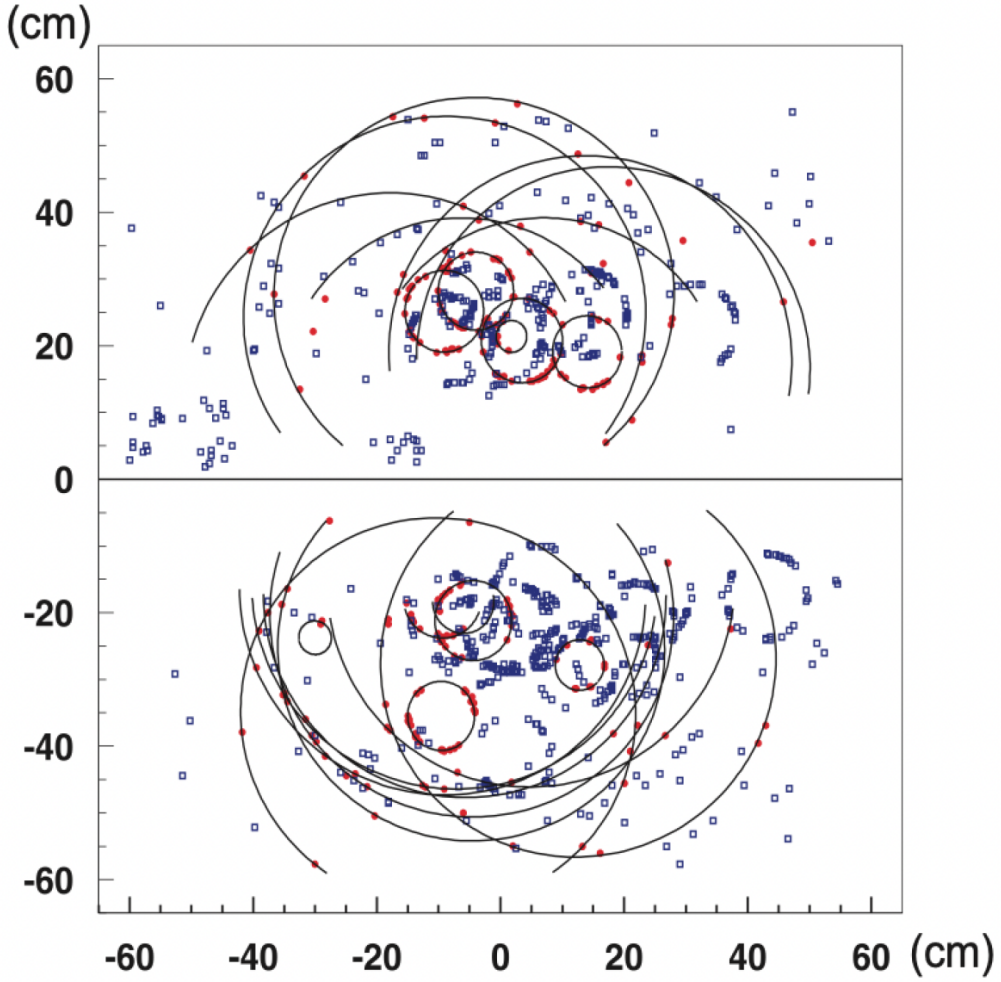

Figure 2.15. Typical LHCb event in RICH1 with the Cherenkov rings interpolation. The small (large) ring radii in RICH1 originate from the C_4F_{10} radiator. The solid red rings indicate the particles passing through the whole detector while the blue dotted rings denote the particles for which no match is found with the tracks in the VELO and TT detectors.

The HCAL energy resolution is

$$\frac{\sigma_E}{E} = \frac{70\%}{\sqrt{E}} \oplus 10\%, \tag{2.4}$$

where the first 70% term is due to statistical uncertainty on the energy deposit of the hadronic shower and the 10% term is a constant contribution due to systematics effects [95].

Due to the different occupancy of the detectors between the inner and outer regions, distinct segmentation patterns are employed in the calorimeter system. The SPD, PS, and ECAL detectors are divided into three regions, while only two regions are employed for the HCAL detector. The regions of different granularity for the ECAL and the HCAL subsystems are shown in Fig. 2.17.

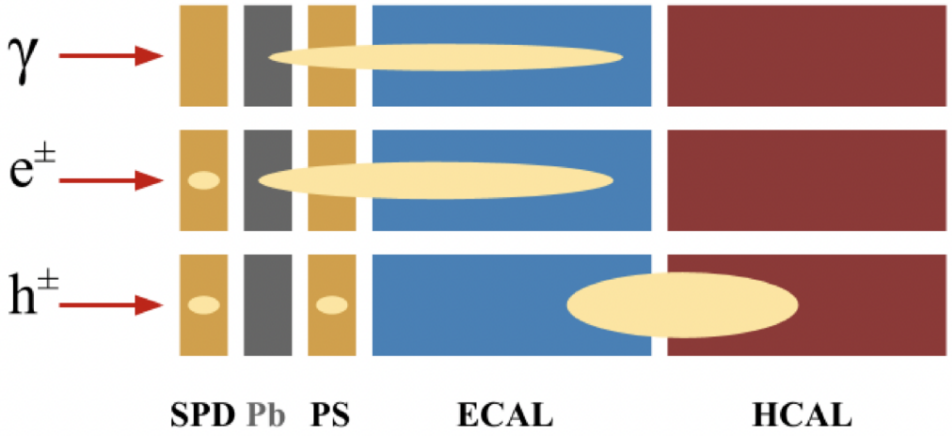

Figure 2.16. Graphical representation on the particles deposited energies in the LHCb calorimeter system.

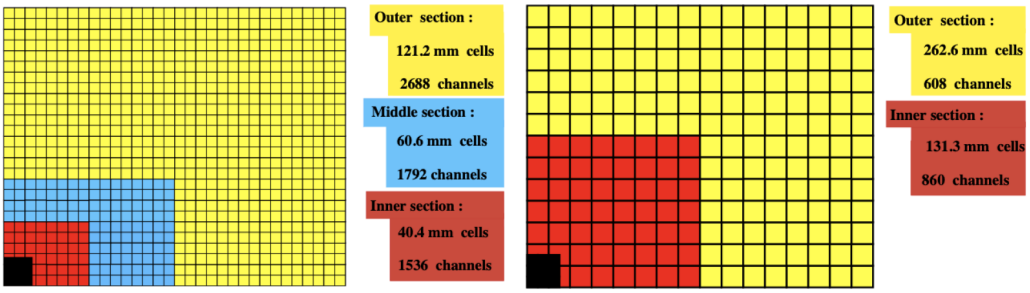

Figure 2.17. Regions of different granularity for the ECAL (left) and the HCAL (right) subsystems. The black area, corresponding to the beam pipe, is outside of the LHCb acceptance.

2.4.3 The muon system

The muon system [96] is positioned downstream of the calorimeters and it is able to identify and trigger the muons. The system is made of five progressively larger rectangular stations, denoted as M1-M5. The M1 station is located between RICH2 and the SPD detector, permitting a fast and accurate estimate of the muon traverse momentum, while the rest of the stations are positioned downstream of the HCAL. The last station, M5, has a dimension approximately of 10×9 m^2. Each station is divided into four regions, denoted R1-R4 with R1 being the innermost, with dimensions that increase as the distance from the z-axis increases. These regions have a finer segmentation closer to the beam pipe and coarser in the outer regions. Schematic side and front views of the muon system are illustrated in Fig. 2.18.

The stations are made of Multi Wire Proportional Chambers (MWPCs) [97], containing a gas mixture of Ar, CO_2 and CF_4. An exception is made for the M1 inner region, which is made of triple Gas Electron Multiplier (GEM) detectors [98], with the same mixture of gas.

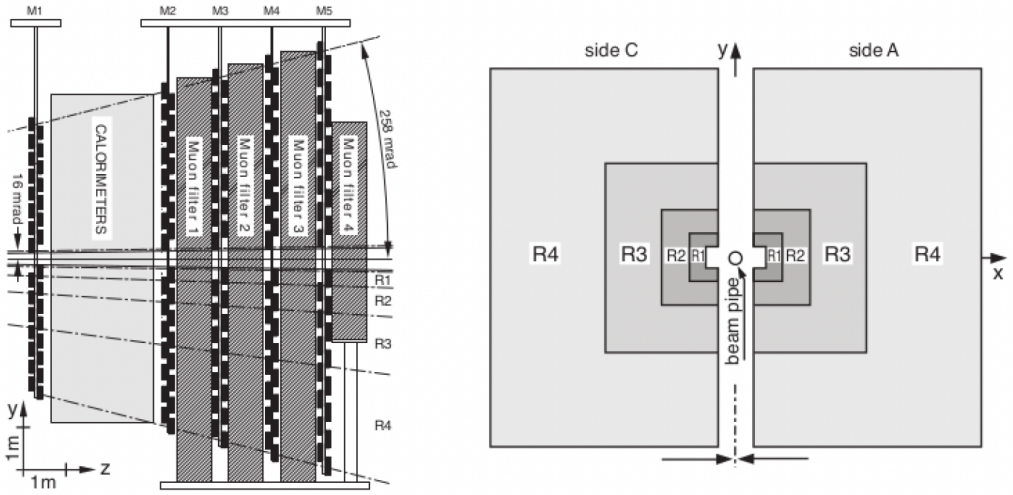

Figure 2.18. Schematic side (left) and front (right) views of the LHCb muon system.

In total, 1368 MWPCs and 12 triple GEM detectors are employed in the muon system. In particular, each station is equipped with 276 MWPCs: 12, 24, 48 and 192 in the R1, R2, R3 and R4 regions, respectively, with the exception of the M1R1 region, which uses 12 GEMs, as they allow a higher granularity and better responses for high particles occupancy, which is about 500 kHz/cm^2 in this region. Each station is separated by 80 cm of thick iron absorbers, acting as muon filters. In detail, only muons with a minimum momentum of 6 GeV/c can cross the whole system. These muons leave a signature in all of the five muon stations. Given the different geometries, resolutions and rate capability requirements, 20 types of chambers, with different sizes, segmentation and readout granularity are used in the muon system. Nevertheless, the internal geometry is practically the same for all the MWPCs. The readout electronics can be divided into two main categories, according to the position of the boards: the front-end electronics, mounted directly on the chambers, required to be highly radiation tolerant, and the off-detector electronics, mounted on racks close to the stations but already outside the acceptance. The angular acceptance of the system ranges from 20 to 306 mrad vertically and from 16 to 258 mrad horizontally, enabling approximately 20% of the muons from inclusive b semileptonic decays to pass through the system.

The muon system achieves an efficiency greater than 95% at a frequency of 10 MHz at the nominal luminosity of LHCb. This allows to use the muon detector information also for the hardware level trigger, for muons with a p_T above a given threshold, as well as to separate muons from hadrons in the software level trigger. This distinction is particularly significant for rare decays involving muons in the final state, given the significantly higher occurrence of purely hadronic decays with similar multiplicity and topology.

2.4.4 Particle identification and performance

The PID algorithms assign a mass hypothesis to the LHCb tracks, relying on the information collected by the RICH, the calorimeters and the muon systems [99]. The data from these detectors are gathered and combined to provide a PID likelihood for each track. Given a track that falls within a specific particle hypothesis k, defined by x_i variables such as the track parameters and energy deposit in the calorimeter cells, the following log-likelihood function is defined:

$$\ln \mathcal{L}^k = \sum_i^n \ln p_i^k(x_i). \tag{2.5}$$

where $p_i^k(x_i)$ are the probability distribution functions, extrapolated from simulations and/or data calibration samples.

Furthermore, the delta-log-likelihood (ΔLL or DLL) function is used to compare the different particles hypothesis:

$$\Delta LL(h_1) = \ln \mathcal{L}(h_1) - \ln \mathcal{L}(h_2) = \ln \left(\frac{\mathcal{L}(h_1)}{\mathcal{L}(h_2)} \right) \ , \tag{2.6}$$

where h_1 and h_2 denote the different mass hypotheses for the considered track.

A combined likelihood is expressed by multiplying the likelihoods from the RICH, the calorimeters and the muon systems, according to their respective mass hypothesis:

$$\begin{aligned} \mathcal{L}(K) &= \mathcal{L}^{\text{RICH}}\,(K) \cdot \mathcal{L}^{\text{Calo}}\,(K) \cdot \mathcal{L}^{\text{Muon}}\,(\bar{\mu}), \\ \mathcal{L}(\pi) &= \mathcal{L}^{\text{RICH}}\,(\pi) \cdot \mathcal{L}^{\text{Calo}}\,(\pi) \cdot \mathcal{L}^{\text{Muon}}\,(\bar{\mu}), \\ \mathcal{L}(\mu) &= \mathcal{L}^{\text{RICH}}\,(\mu) \cdot \mathcal{L}^{\text{Calo}}\,(\bar{h}, \bar{e}) \cdot \mathcal{L}^{\text{Muon}}\,(\mu), \end{aligned} \tag{2.7}$$

where the bar indicates the opposite hypothesis.

Using these methods, the global PID variables are assembled. The PID performances for the kaon, in terms of efficiency of correct identification and misidentification, are reported in Fig. 2.19 as a function of the momentum for both the 2015 data and simulated samples.

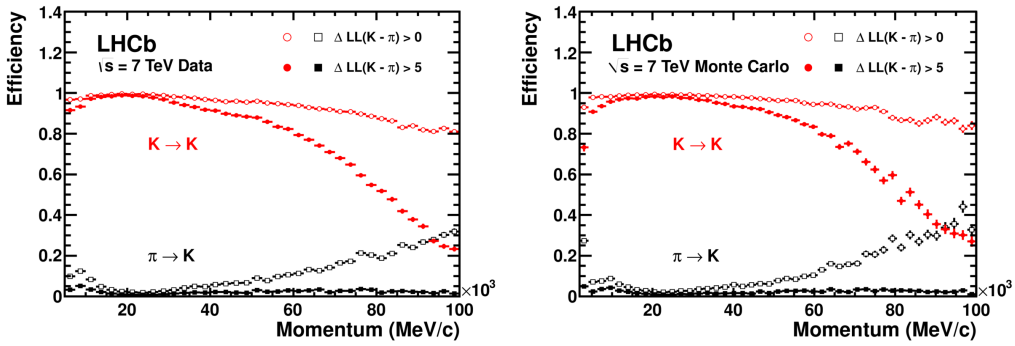

Figure 2.19. Kaon PID performances for the 2015 data (left) and simulated (right) samples. The kaon identification ($K \to K$) and misidentification ($\pi \to K$) are reported for two different ΔLL requirements.

2.5 The trigger system

The main goal of the trigger system is to select events of interest, according to the available bandwidth and storage capabilities. In LHCb, a dual-tiered system of triggers is employed, using both hardware and software components, to evaluate which events must be stored [100]. The LHCb trigger system, divided into two distinct stages [101], is shown in Fig. 2.20. The initial stage is a low-level hardware trigger, known as Level-0 (L0), which makes swift selections based on raw information. The final stage is the High Level Trigger (HLT), which uses software from CPU-based computer clusters to execute a comprehensive event reconstruction and selection. At nominal luminosity, the rate of observable interactions ranges from 15 to 40 MHz, while only 5 to 12.5 kHz of data can be stored for subsequent offline analyses [102].

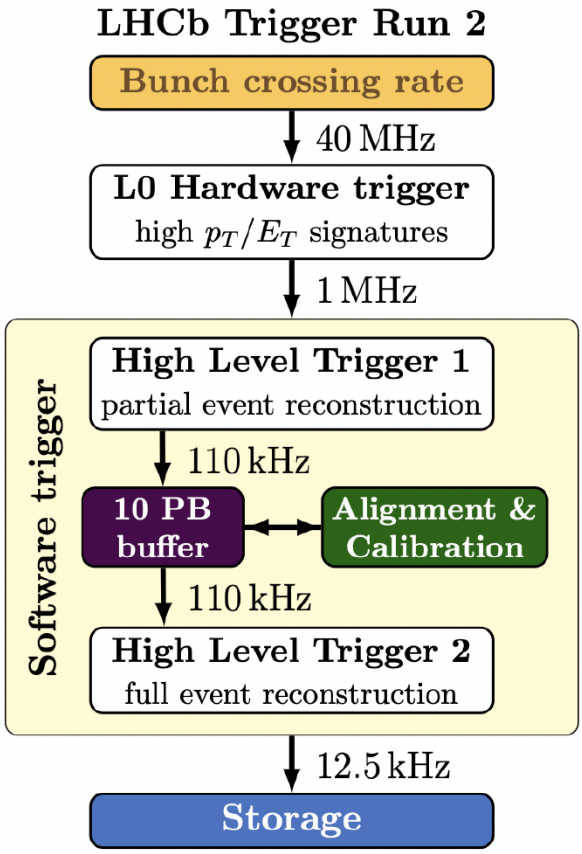

Figure 2.20. Scheme of the LHCb Run 2 trigger system. The event rate is reduced from 40 MHz to 12.5 kHz and saved in the disk storage.

The trigger classifications, denoted as trigger lines, are uniquely identified by a 32-bit hexadecimal code, known as Trigger Configuration Key (TCK), and implemented with different sets of requirements and adjustable rates.

2.5.1 The Level-0 trigger

The L0 trigger [103] is the hardware-based selection stage that reduces the event rate from 40 to 1 MHz by selecting events with high p_T tracks in the muon system or high E_T clusters in the calorimeters. In fact, events including heavy-flavour decays are characterised by high transverse momentum and energy signatures, compared to the QCD backgrounds. In order to take into account this information and process it, the L0 is divided into two independent sections, connected to their respective systems: the L0 calorimeter and muon. The final decision is the logical operator OR between these independent outputs.

The L0 calorimeter searches for high E_T clusters in 2×2 cell blocks in the ECAL and HCAL, defined as $E_T = \sum_{c=1}^{4} E_c \sin\theta_c$, with c being the cell index, E_c the energy deposit in each cell and θ_c the angle between the beam axis and the line joining the cell to the nominal detector interaction region. The event is accepted if contains at least one candidate with the transverse energy above the L0 threshold. Limited information is available in the L0 stage to separate the electrons from the photons. The object is flagged as "Photon", "Electron", or "Hadron" using the information coming from the SPD and PS detectors. The corresponding trigger lines are `L0Photon`, `L0Electron` and `L0Hadron`. The `L0Photon` trigger line working point is set to achieve high purity but relatively low efficiency. Many real photons are selected by the `L0Electron` line, which has a higher efficiency but a lower purity.

The L0 muon selects events with muon tracks with high p_T. The transverse momentum of each track is estimated assuming that the particle originates at the interaction point and crosses the entire muon system. The search algorithm starts from the logical pads fired in M3, which define the starting points to search for other hits in the remaining stations within a predefined Field of Interest (FoI). For each event with at least two muon candidates, the highest transverse momenta are used to form a trigger decision based on the highest one (`L0Muon`) or both (`L0DiMuon`). In order to boost the efficiency of finding the $B_s^0 \to \mu^+\mu^-$ decays, very loose occupancy requirements are used for the `L0DiMuon` decision.

In all the hardware triggers, except for the `L0DiMuon` line, events with a number of SPD hits > 450 are rejected to avoid saturation in the HLT processing farms. The L0 trigger lines thresholds, based on the muon p_T and the calorimeter E_T, are listed in Tab. 2.1 for each year of the Run 2 data-taking period [101].

Year	`L0Muon` [GeV/c]	`L0Electron` [GeV/c]	`L0Hadron` [GeV/c]
2015	$p_T > 2.80$	$E_T > 2.70$	$E_T > 3.60$
2016	$p_T > 1.80$	$E_T > 2.40$	$E_T > 3.70$
2017	$p_T > 1.35$	$E_T > 2.11$	$E_T > 3.46$
2018	$p_T > 1.75$	$E_T > 2.38$	$E_T > 3.75$

Table 2.1. L0 trigger lines thresholds for each year of the Run 2 data-taking period.

2.5.2 The High Level Trigger

Events passing the L0 trigger lines are processed by the HLT stage. The HLT is a software trigger, divided into the HLT1 and HLT2 sections. The HLT trigger lines are made of a set of reconstruction and selection steps, accessing the full detector information and allowing for more complex decisions, compared to the L0 trigger. This high computational effort is performed by the Event Filter Farm (EFF), a platform network-based with an overall disk space of 10 PB, consisting of $\sim$ 1800 nodes, each made from 24 to 32 logical processor cores. Between the HLT levels, a precise real time alignment and calibration of the detector is performed to improve the selection of rare decays [104].

At the HLT1 stage, a reduction in event rate from 1 MHz to 30 kHz is performed with a partial event reconstruction, using a sequence of algorithms designed for the reconstruction of vertices and tracks. This parametrization facilitates the evaluation of IPs with respect to the PV, SVs, invariant masses, and flight directions. Given this enriched set of parameters, simple multivariate classifiers contribute to an enhanced selection over basic requirements. This is particularly relevant for selecting one and two-track combinations with associated high-quality vertices [105]. For muons, a fast identification is executed by comparing VELO and T-station tracks with the hits in the muon system. This information is used to select displaced muons with large p_T and dimuon displaced vertices.

Events passing the HLT1 lines are eligible for further processing at the HLT2 stage. This level uses all the available information from the LHCb detectors to perform a full reconstruction. The HLT2 is made of selection algorithms, divided into inclusive topological lines, which accommodate partially reconstructed decays, and exclusive lines, dedicated to selecting specific final states. At HLT2, the output rate is further reduced to 5-12.5 kHz and the data is finally recorded into the disk storage. The HLT2 bandwidth allocation serves both the inclusive trigger lines, predominantly associated with topological b hadron, inclusive c hadron, and dimuon triggers, as well as the TURBO stream, encompassing exclusive trigger lines made for the reconstruction of specific rare decays.

During the Run 1 period, a configuration, denoted as "deferred HLT2", has been employed. With this software configuration, about 20% of the events accepted at the L0 stage were temporarily saved in the local unused EFF disks and processed during the LHC fills. This allowed a track reconstruction with less stringent selections, giving also an improvement in the selection performance of rare decays. During the Run 2 data-taking, the increased luminosity and multiplicity leads to more stringent selections. In this case, all the events before the HLT2 reconstruction are buffered to disk, while a precise real time alignment and calibration of the detector has been implemented between the HLT1 and HLT2 stages. This is critical to achieve the best possible reconstruction at HLT2 with the updated information from the detectors. The LHCb trigger schemes for the Run 1 and Run 2 data-taking periods are illustrated in Fig. 2.21.

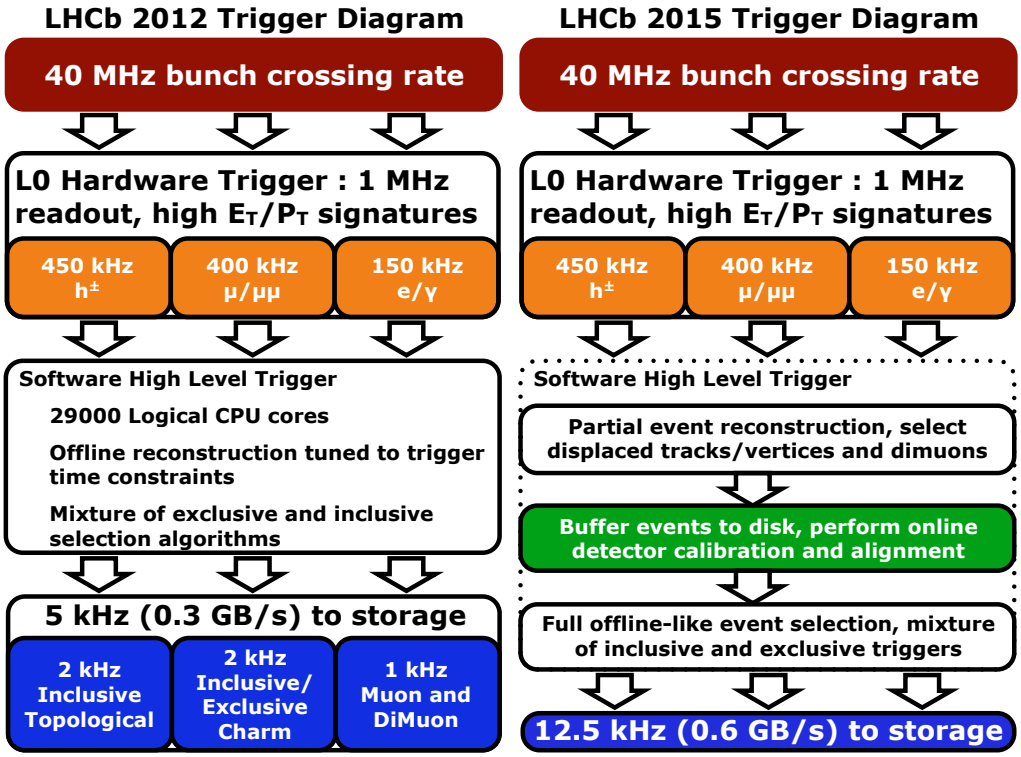

Figure 2.21. LHCb trigger schemes for the Run 1 (left) and Run 2 (right) data-taking periods.

2.6 The LHCb computing framework

The software used by the LHCb experiment [106] for both online and offline analyses is built within an object-oriented framework, known as Gaudi [107]. This framework is programmed in C++ and serves as a unified foundation and ecosystem for many software applications across all the data processing phases of LHCb. This includes activities such as simulating physics and detectors, executing high-level software triggers, conducting event reconstruction, performing physics analysis, and more.

The Monte Carlo (MC) simulated samples are produced by the Gauss application [108]. The simulation starts with Pythia [109], which reproduces the pp collisions, followed by EvtGen [110] for the generation of the particle decays. The QED final-state radiation is simulated by the Photos package [111]. The Geant4 toolkit [112] is also used to emulate the interaction of particles with the LHCb detector. The dimensions, materials and geometries of all the LHCb systems are fully reproduced. The simulation of the detector responses, based on the calibration data samples, is performed by the Boole digitization program [113]. This tool replicates the detector response, simulating the read-out electronics and the L0 trigger lines. The execution of the HLT lines is performed by Moore [114]. For a comprehensive event reconstruction, both real data and simulated samples are processed together by the Brunel application [113]. In the final phases of the analysis, the DaVinci software package [113] is used as the main framework.

Using the PID hypotheses and the track/vertex information coming from the reconstruction phase, DaVinci is able to build entire chains of decay, combining reconstructed particles to define B or D mesons or allowing manipulation of all the quantities available in the event. The LHCb data flow for the Run 2 data-taking period with the associated applications for both data and simulated samples is illustrated in Fig. 2.22.

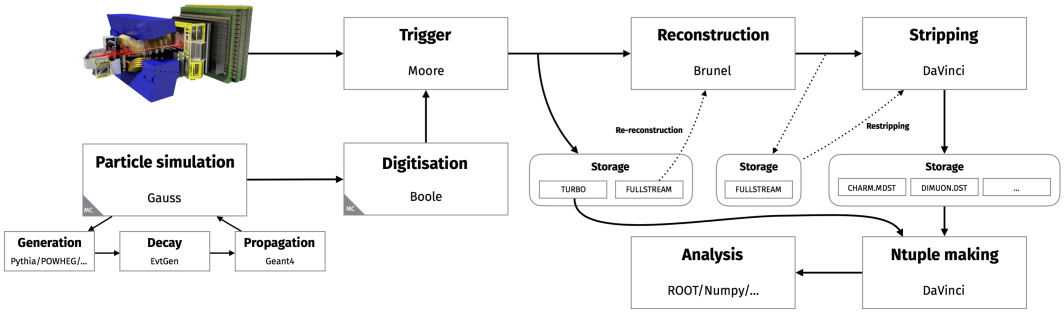

Figure 2.22. LHCb data flow for the Run 2 data-taking period with the associated applications for both data and simulated samples.

Real data coming from the data-taking periods are recorded in files, designated as RAW. Furthermore, the event reconstruction is conducted by Brunel with the analysed data being stored in other files, referred to as Data Summary Tape (DST). These DSTs contain all the event details, including the reconstructed objects and the raw data, and typically occupy around 150 kB of disk space. To reduce the amount of non-useful information for the data analysis and also to save disk space, a subsequent centralised procedure called stripping is implemented. This process involves a series of offline selection algorithms, denoted as stripping lines, characterized by loose selection criteria, similar to those applied at the HLT2 stage.

Since the stripping selection is applied to the offline samples, analysts had to take into account both the HLT and stripping selections, which usually concerned the same quantities but with different resolutions, due to the different reconstructions. Therefore, a considerable effort was undertaken before Run 2 to optimize the reconstruction algorithms both online, at the HLT stage, and offline, aligning these levels to be identical and opening the possibility of performing some physics studies directly after the HLT2 filtering. Starting from Run 2, candidates selected by specific stripping lines are stored in files presented in formats suitable to be analysed, such as DST or the reduced DST (μDST). The latter aims to conserve disk space by exclusively retaining information pertinent to the candidate of interest, discarding the raw event data, which takes around 10 kB per event. The stripping procedure is also able to automatically flag the candidate particle of interest as a signal candidate. Since this flag is applied at the offline level, it is interesting to retrieve the online objects at the trigger level and check if they are fired by the signal candidate or by the rest of the event.

2.7 The LHCb Upgrade 1

At the end of the Run 2 data-taking period, the primary constraint of the LHCb detector was attributed to the readout trigger system, imposing a limitation on the achievable luminosity. To facilitate the data operations under an elevated luminosity of 2×10^{33} cm^{-2}s^{-1}, LHCb underwent an upgrade, increasing the detector readout from 1 to 40 MHz, with the goal of collecting a minimum of 50 fb^{-1} of data by the end of the Run 3 campaign.

A fundamental modification within the LHCb upgrade includes the comprehensive overhaul of the existing readout and back-end electronics and the replacement of the front-end electronics. This upgrade removes the L0 trigger stage, replacing the hardware trigger component with a full software one, using information from the calorimeter and muon systems. The front-end electronics, therefore, operate autonomously, transmitting data synchronously at the 40 MHz rate to the back-end electronics with a fixed latency [115]. The acquired data is buffered as in the Run 2 data-taking period and a software-triggered process undertakes the initial selection and reconstruction steps. The ultimate result is an output rate from 2 to 5 GB/s. A scheme of the Run 3 trigger system of the LHCb experiment is illustrated in Fig. 2.23.

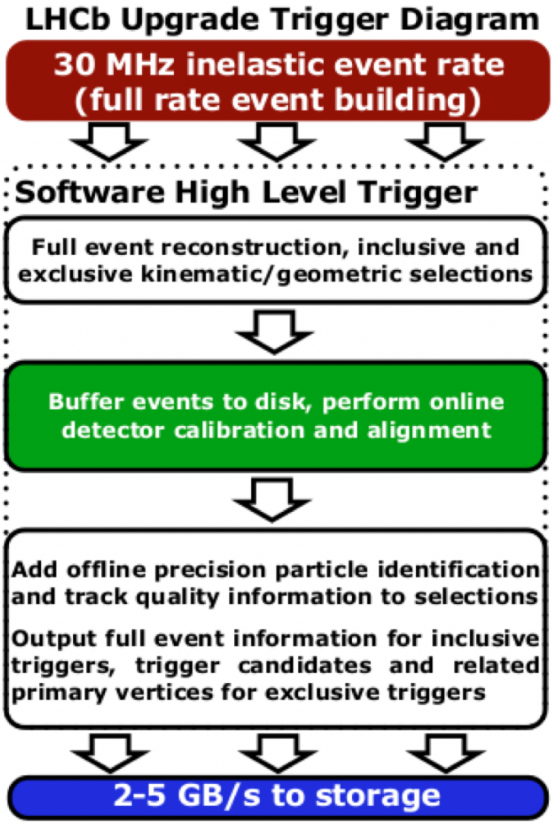

Figure 2.23. Scheme of the Run 3 trigger system of the LHCb experiment.

The LHCb subdetectors went also under major upgrades. The VELO [116] is relocated closer to the beam pipe, reducing its distance from the z-axis to 5.1 mm. Furthermore, the conventional strip technology is substituted with pixels of reduced thickness of 200 μm. This upgrade is projected to yield a 40% improvement in the IP resolution, with an amplified tracking efficiency for particles with low momentum and better decay time resolution. The tracking stations are replaced with the Upstream Tracker (UT), positioned upstream of the magnet, and the Scintillating Fiber Tracker (SciFi), situated downstream of the magnet [117]. The UT is configured with four tracking layers, using a silicon strip technology in the p^+-in-n and n^+-in-p configurations. The SciFi, on the other hand, is made of twelve detector layers, featuring plastic scintillating fibers 2.4 m long with a diameter of 250 μm. The new tracking systems will reduce the number of ghost tracks by a factor of 50-70%. For the RICH1 [118], modifications in the optical layout are implemented to handle the higher occupancy. The focal length of the spherical mirrors is increased by a factor of $\sqrt{2}$, coupled with a corresponding enlargement to the mirror curvature radius. These upgrades aim to enhance the Cherenkov angle resolution and mitigate the mirror aberrations. The readout mechanism for both RICH detectors is upgraded to multi-anode PMTs, operating at 40 MHz. While the calorimeter undergoes relatively minor alterations, the SPD and PS are removed for the Run 3 campaign, given their predominant role in the L0 trigger. The upgrades to the muon system [119] involve minimal alterations. The M1 station is removed, due to its previous role in enhancing the p_T resolution on muon tracks at L0. A schematic view of the upgraded LHCb experiment for the Run 3 data-taking period is illustrated in Fig. 2.24.

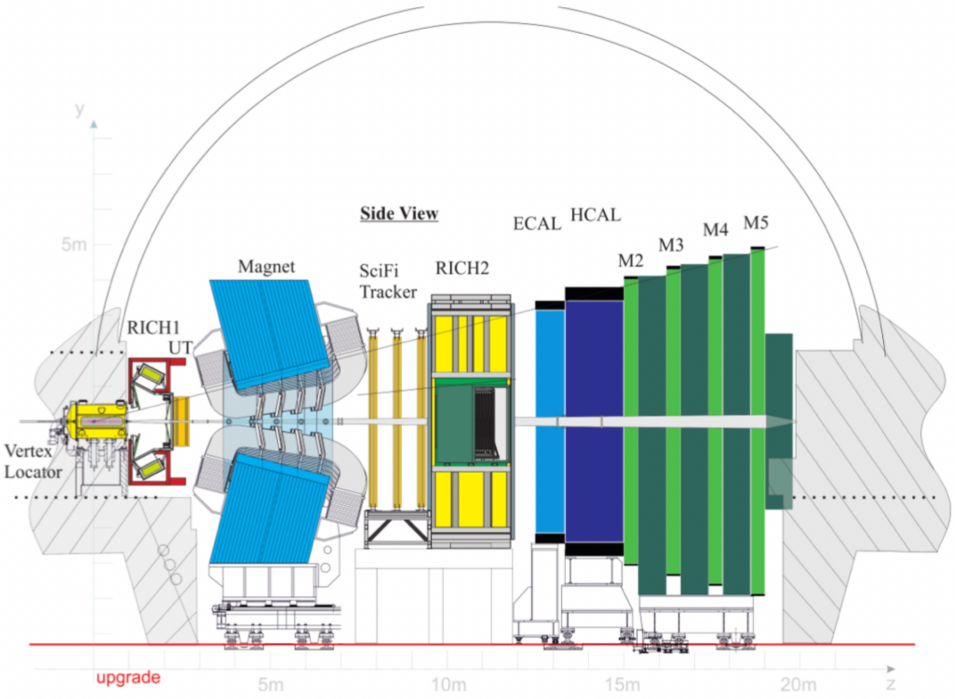

Figure 2.24. Schematic view of the upgraded LHCb detector in the non-bending y-z plane.

Chapter 3

Selection of the $\Sigma^+ \to p\mu^+\mu^-$ decay

The Run 2 analysis of the $\Sigma^+ \to p\mu^+\mu^-$ decay is similar to the previous one, performed with the Run 1 dataset at LHCb. However, several improvements have been implemented to increase the chances of observation and reduce the uncertainties in the branching fraction measurement.

In this chapter, the $\Sigma^+ \to p\mu^+\mu^-$ selection criteria are described. After a brief summary of the analysis strategy, the adopted trigger lines for both signal and normalisation modes and the Run 2 dataset are presented. The reconstruction of all the decay modes of interest is reported as well as the applied stripping and preselection requirements to the $\Sigma^+ \to p\mu^+\mu^-$ decay. Furthermore, the relevant sources of background of the signal decay and the employed multivariate analysis are illustrated. The variables used in the analysis are described in App. A.

3.1 Run 2 analysis strategy

The main goals of the Run 2 analysis of the $\Sigma^+ \to p\mu^+\mu^-$ decay are to observe for the first time the decay itself, make a precise branching fraction measurement and confirm or exclude the possible NP result from the HyperCP experiment [30].

The Σ^+ candidates are reconstructed through the $p\mu^+\mu^-$ final state and a first loose preselection is applied at the stripping level. Furthermore, a tight selection is performed with the use of a multivariate discriminant and PID variables to reject most of the relevant sources of background. After the optimisation of the selection strategy, a fit to the $m_{p\mu^+\mu^-}$ invariant mass distribution is performed to extract the signal final yield. Once the $\Sigma^+ \to p\mu^+\mu^-$ candidates are isolated, the $m_{\mu^+\mu^-}$ distribution is investigated for a possible resonant structure.

The second part of the analysis requires a normalisation mode to measure the signal branching fraction. The normalization to a known final state is far from trivial, due to the absence of any accessible fully charged final state of the Σ^+ particle [12]. Therefore, given its high branching fraction value, the $\Sigma^+ \to p\pi^0$ decay is exploited and the $\Sigma^+ \to p\mu^+\mu^-$ branching fraction is estimated as

$$\mathcal{B}\left(\Sigma^+ \to p\mu^+\mu^-\right) = \frac{\varepsilon_{\Sigma^+\to p\pi^0}}{\varepsilon_{\Sigma^+\to p\mu^+\mu^-}} \frac{\mathcal{B}\left(\Sigma^+ \to p\pi^0\right)}{N_{\Sigma^+\to p\pi^0}} N_{\Sigma^+\to p\mu^+\mu^-}, \tag{3.1}$$

where N and ε are the final yield and overall efficiency of the signal and normalisation decay modes, and $\mathcal{B}\left(\Sigma^+ \to p\pi^0\right) = (51.57 \pm 0.30)\,\%$ is the $\Sigma^+ \to p\pi^0$ branching fraction, taken from the PDG [12].

As for the previous Run 1 study [31], a blind analysis technique is implemented: from the full $\Sigma^+ \to p\mu^+\mu^-$ data sample, the invariant mass region $1173 < m_{p\mu^+\mu^-} < 1205$ MeV/c^2 is removed up to the final definition of the selection criteria, in order to avoid unconscious biases. This blind region corresponds to about 4 standard deviations from the expected signal mass peak.

Several improvements are available in the Run 2 analysis with respect to the previous one. In addition to the larger data sample, given the increased Run 2 luminosity and cross-section, as outlined in Sec. 2.1, about a factor 10 increase in trigger efficiency is expected due to the presence of new dedicated trigger lines. Furthermore, PID variables with better performances and larger MC samples are available.

In addition to the $\Sigma^+ \to p\mu^+\mu^-$ branching fraction, new measurements are expected to become accessible, such as the differential branching fraction with respect to the dimuon invariant mass and the forward-backward asymmetry in the decay. A "direct" CP asymmetry measurement is also possible as

$$\mathcal{A}_{CP} = \frac{\mathcal{B}\left(\Sigma^+ \to p\mu^+\mu^-\right) - \mathcal{B}\left(\bar{\Sigma}^+ \to \bar{p}\mu^+\mu^-\right)}{\mathcal{B}\left(\Sigma^+ \to p\mu^+\mu^-\right) + \mathcal{B}\left(\bar{\Sigma}^+ \to \bar{p}\mu^+\mu^-\right)}. \tag{3.2}$$

These measurements, however, are not investigated in this analysis as they will be subjects to future works.

3.2 Run 2 trigger improvements for strange hadron physics at LHCb

In view of the Run 2 data-taking, a great effort has been put to improve the trigger strategy for strange hadrons physics [120]. These improvements consist of new requirements at HLT1 and HLT2, designed to keep in mind the typical signature of strange hadron decays: low p_T for muons in the final state and a large lifetime for strange particles compared to the $b-$ and $c-$ hadrons, as illustrated in Fig. 3.1.

At HLT1, an initial momentum estimate is performed on all track segments reconstructed within the VELO and extended to the TT upstream of the magnet, known as VeloTT segments. The VeloTT segments corresponding to particles with a p_T larger than 500 MeV/c are passed to the forward tracking algorithm, which upgrades them to long tracks if they match hits in the other tracking stations downstream of the magnet. Tracks with p_T lower than 500 MeV/c, denoted as soft tracks, are not passed to the algorithm as their large number would make the online computing time consumption unsustainable. These tracks are fundamental for the analysis of strange hadron decays with muons in the final state, as shown in Fig. 3.1 (left). Therefore, a complementary reconstruction of muon tracks with $80 < p_T < 500$

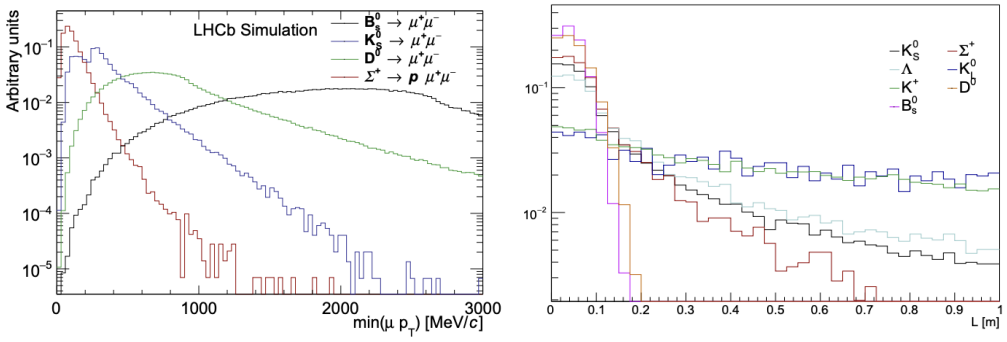

Figure 3.1. Simulated distribution of the minimum transverse momentum for muons in the $K_S^0 \to \mu^+\mu^-$, $D^0 \to \mu^+\mu^-$, $\Sigma^+ \to p\mu^+\mu^-$ and $B_s^0 \to \mu^+\mu^-$ decays (left) and distribution of the decay length in pp collisions for strange and heavy flavour hadrons (right).

MeV/c has been developed by matching VELO and VeloTT segments with hits in the muon chambers and passing only the matched candidates to the forward tracking algorithm [121]. This algorithm is exploited by the `Hlt1DiMuonNoL0` line, aiming to select inclusively strange decays with a dimuon pair in the final state. This trigger is also used to mitigate the inefficiencies of the `L0Muon` and `L0DiMuon` lines, which do not efficiently select soft muons due to their tight p_T requirements of $p_T(\mu^\pm) > 1.3$ GeV/c and $p_T(\mu_1) \cdot p_T(\mu_2) > (1.3\ \text{GeV}/c)^2$, respectively. In fact, `Hlt1DiMuonNoL0` takes as input all the events selected by L0, unlike the other HLT1 muon lines. This includes events selected by the hadron, electron, and photon L0 triggers, in addition to the muon and the dimuon L0 selections. The selection criteria of the `Hlt1DiMuonNoL0` line are summarised in Tab. 3.1. Here, the Global Event Cut (GEC) applies requirements on the maximum number of hits in the tracking detectors.

Variable	Cut
$Track\ \chi^2$	< 4
$\mu^\pm\ IP$	> 0.4 mm
$\mu^\pm\ IP\chi^2$	> 9
$\mu^\pm\ p$	> 3000 MeV/c
$\mu^\pm\ p_T$	> 80 MeV/c
$\mu^+\mu^-\ DOCA$	< 0.2 mm
$\mu^+\mu^-\ Vtx\chi^2$	< 25
$\mu^+\mu^-$ Mass	> 220 MeV/c^2
GEC (OT)	< 15000
GEC (IT)	< 3000
GEC (VELO)	< 3000

Table 3.1. Selection criteria of the `Hlt1DiMuonNoL0` trigger line.

At HLT2, soft dimuon pairs are selected by the inclusive `Hlt2DiMuonSoft` line. This line has no further p_T requirements on the muons, no request on the Impact

Parameter of the dimuon object and no rejection of short-lived decaying particles. The `Hlt2DiMuonSoft` selection criteria are summarized in Tab. 3.2. Here, ρ is defined as the radial coordinate of the dimuon vertex and $\theta_{\mu^+\mu^-}$ is the angle between the two muons in the laboratory frame. The request on the Secondary Vertex z position, SV_z, ensures that the parent particle decays within the VELO.

Variable	Cut
$\mu^\pm$ IP	> 0.3 mm
$Track$ $GhostProb$	< 0.4
$\mu^\pm$ $IP\chi^2$	>9
$ProbNN\mu^\pm$	>0.05
ρ	>3 mm
SV_z	< 650 mm
$\mu^+\mu^-$ Mass	< 1000 MeV/c^2
$\mu^+\mu^-$ $DOCA$	< 0.3 mm
$\mu^+\mu^-$ $Vtx\chi^2$	< 25
$\theta_{\mu^+\mu^-}$	> 2 mrad
$IP_{\mu\mu}/\Delta z$	$< 1/60$

Table 3.2. Selection criteria of the `Hlt2DiMuonSoft` trigger line.

In addition to the `Hlt2DiMuonSoft` line, the exclusive `Hlt2RareStrangeSigmaPMuMu` trigger line has been introduced for the $\Sigma^+ \to p\mu^+\mu^-$ decay. Its selection criteria are listed in Tab. 3.3.

Variable	Cut
$Track$ χ^2	< 3
$Track$ $GhostProb$	< 0.3
$\mu^\pm$ $IP\chi^2$	> 25
p $IP\chi^2$	> 25
Σ^+ $DOCA$	< 2 mm
Σ^+ p_T	< 500 MeV/c
Σ^+ $Vtx\chi^2$	< 25
Σ^+ $IP\chi^2$	< 36
Σ^+ $DIRA$	> 0.9
Σ^+ Decay time	> 6 ps
Σ^+ Mass	500 MeV/c^2

Table 3.3. Selection criteria of the `Hlt2RareStrangeSigmaPMuMu` trigger line.

The presented lines increase the HLT trigger efficiency on the $\Sigma^+ \to p\mu^+\mu^-$ decay by a factor $\sim$10 with respect to Run 1 [120].

3.2.1 Trigger strategy

Within LHCb, all the information used in the reconstruction process, such as the channels of the detectors, is defined by a distinct numerical identifier, known as LHCbID. Once the event has passed the HLT requests and the offline processing, the IDs are compared with those used by the trigger systems and various possibilities are verified: a specific trigger line could be fired by only signal candidates, by the rest of the event or by a combination of both. Therefore, three main trigger categories can be defined:

- Trigger On Signal (TOS) - The trigger line is verified by the particles belonging to the signal, regardless of the presence of the rest of the event. A candidate is classified as TOS with respect to a trigger line if the LHCbIDs of the trigger accepted decay overlap for more than 70% with the LHCbIDs of the selected signal candidate;

- Trigger Independent of Signal (TIS) - The trigger line is verified regardless of the presence of the signal. A candidate is classified as TIS with respect to a trigger line if, removing it from the event, the trigger continues to accept the event. In this scenario, another particle is present in the event that also satisfies the trigger requirements and the LHCbIDs of the triggered particles exhibit an overlap of less than 1% compared to those of the selected candidate;

- Trigger Decision (Dec) - The trigger line is verified by candidates that have passed the trigger requirements, but they are not classified either as TIS or TOS.

The TIS and TOS groups are not mutually exclusive, meaning that an event can be simultaneously TIS and TOS for a given trigger line. If a trigger line is fired by a partial combination of the signal and the rest of the event, the candidate is neither TIS nor TOS and falls under the Triggered On Both (TOB) group. These categories allow a direct trigger efficiency evaluation on data samples with the TISTOS method [122], which computes the efficiency of a TIS(TOS) selection within a TOS(TIS) sub-sample.

In view of what is described above, the trigger strategy for the signal channel, which is detailed in App. B, is chosen to have the highest possible efficiency. Further details on the efficiency will be given in Ch. 6. The chosen trigger lines are:

- L0 - The logical OR of `L0MuonDecision_Dec`, `L0DiMuonDecision_Dec`, `L0HadronDecision_Dec`, `L0PhotonDecision_TIS`, `L0ElectronDecision_TIS`;

- HLT1 - The logical OR of `Hlt1TrackMuonDecision_Dec`, `Hlt1SingleMuonHighPTDecision_Dec`, `Hlt1DiMuonLowMassDecision_Dec`, `Hlt1DiMuonHighMassDecision_Dec`, `Hlt1DiMuonNoL0Decision_Dec`, `Hlt1TrackMVADecision_Dec`, `Hlt1TwoTrackMVADecision_Dec`;

- HLT2 - The logical OR of `Hlt2DiMuonSoftDecision_Dec`, `Hlt2RareStrangeSigmaPMuMuDecision_Dec`.

On the other hand, the trigger strategy for the normalisation channel is chosen to be simpler. The following trigger lines are used:

- L0 - `L0HadronDecision_TOS`;
- HLT1 - `Hlt1TrackMVADecision_TOS`;
- HLT2 - `Hlt2PassThroughDecision_Dec`.

3.3 Dataset

The full dataset, recorded between 2016 and 2018, is used in this analysis. These samples were collected by recording pp collisions at a centre-of-mass energy of 13 TeV, corresponding to an integrated luminosity of 5.4 fb^{-1}. The 2015 sample is excluded due to the absence of the new dedicated trigger lines. Its analysis would have required a specific selection with low gain in terms of statistics. The integrated luminosity $\mathcal{L}$ of the used dataset, listed by year and magnet configuration, is reported in Tab. 3.4.

Year	Magnet	$\mathcal{L}$ [fb^{-1}]
2016	MagDown	0.842 ± 0.017
	MagUp	0.778 ± 0.016
	MagAll	1.620 ± 0.032
2017	MagDown	0.862 ± 0.017
	MagUp	0.820 ± 0.016
	MagAll	1.682 ± 0.034
2018	MagDown	1.024 ± 0.020
	MagUp	1.107 ± 0.022
	MagAll	2.131 ± 0.043
Run 2	MagDown	2.728 ± 0.055
	MagUp	2.705 ± 0.054
	MagAll	5.433 ± 0.108

Table 3.4. Integrated luminosity of the used dataset listed by year and magnet configuration.

Several MC samples were produced to perform and optimise the analysis, involving the software packages detailed in Sec. 2.6. The LHCb detector is simulated using the `Geant4` toolkit [112] [108] while the pp collisions are generated using PYTHIA [109] [123]. Each MC event contains at least one primary Σ^+ particle following the desired decay mode, while the remaining Σ^+ particles in the same event decay according to the measured branching fractions, as listed in the PDG [12]. The decay modes are described by EVTGEN [110], in which final state radiation is generated by PHOTOS [111].

The $\Sigma^+ \to p\mu^+\mu^-$ decay is generated with a flat three-body phase space, as the form factors need still to be measured. On the other hand, the $\Sigma^+ \to p\pi^0$ decay is generated as a standard two-body process, given that no Σ^+ polarisation is expected. Events for both decay modes are generated with a set of requirements, simulating

their presence within the LHCb acceptance. This selection criteria are listed in Tab. 3.5. Additional cuts on p_T are applied on the normalisation channel to save computational resources during the generation process.

Decay	Particle	Generation cut
$\Sigma^+ \to p\mu^+\mu^-$	p, μ^+, μ^-	$10 < \theta < 400$ mrad
$\Sigma^+ \to p\pi^0$	p	$10 < \theta < 400$ mrad $p_T > 900$ MeV/c
	π^0	$5 < \theta < 400$ mrad $p_T > 200$ MeV/c

Table 3.5. Selection criteria applied at generation level on the signal and normalisation decay modes.

All used MC samples are produced in *filtering mode*, whereby events that do not pass any trigger or stripping line are thrown away. This is done to emulate the typical LHCb data-taking scenario. The number of MC events, coming from stripping filtered samples, are listed by year and magnet configuration in Tab. 3.6 for both signal and normalisation modes.

Channel	Year	Magnet field	Stripping filtered events
$\Sigma^+ \to p\mu^+\mu^-$	2016	MagDown	205350
		MagUp	203428
	2017	MagDown	205750
		MagUp	204923
	2018	MagDown	209573
		MagUp	203513
$\Sigma^+ \to p\pi^0$	2016	MagDown	309444
		MagUp	297088
	2017	MagDown	299094
		MagUp	314938
	2018	MagDown	306877
		MagUp	308720

Table 3.6. Number of stripping filtered MC decay events listed by year and magnet configuration for both signal and normalisation modes.

3.4 Reconstruction

Both $\Sigma^+ \to p\mu^+\mu^-$ and $\Sigma^+ \to p\pi^0$ decays can be reconstructed with long and downstream tracks. In this analysis, only long tracks are used as they offer better tracking and vertex reconstruction performances and better momentum and mass resolutions. The only disadvantage is a shorter lifetime span as the long tracks belong only to those Σ^+ particles decayed inside the VELO.

The reconstruction of the signal and normalisation modes with long tracks is performed with DaVinci, already presented in Sec. 2.6. The standard long tracks requirements are:

- $Track\chi^2 < 3$;
- $GhostProb < 0.3$;
- $IP\chi^2 > 4.0$.

An additional p_T cut of 250 MeV is applied on the charged track compatible with being a proton. Proton candidates passing this condition are also required to have $ProbNNp > 0.05$. Neutral pions are reconstructed either with one or two clusters of photons in the electromagnetic calorimeter. These pions are known as "merged" and "resolved" [124], respectively. Resolved pions are reconstructed from photons with $p_T < 2$ GeV/c^2. At these values, photons coming from the π^0 disintegration form two well-separated clusters in the ECAL. Once the photon candidates are identified, their corresponding invariant mass is compared to the nominal mass value of the π^0 to reconstruct the neutral pion. A mass resolution of 8 MeV/c^2 is obtained for these pions. On the other hand, merged pions are reconstructed from photons with higher transverse momenta, which are detected as overlapping clusters in the electromagnetic calorimeter. These clusters are identified with a reconstruction algorithm, which splits each single cluster into two 3×3 subclusters, built around the two highest energy deposits of the original cluster. Furthermore, the energy of the common cells is distributed between the two subclusters by fitting the energy distribution with that of two photons, using the expected transverse profile from the simulated samples. As for resolved pions, the merged π^0 is finally reconstructed by comparing the invariant mass from the identified photons with its nominal mass value. A lower mass resolution of about 15 MeV/c^2 is found for merged pions.

3.5 Stripping and preselection

The $\Sigma^+ \to p\mu^+\mu^-$ candidates are selected at the stripping level by combining two good-quality opposite charged tracks, identified as muons, with a third track, identified as a proton. A Σ^+ candidate is required to have a proper decay time $\tau > 6$ ps, ensuring that the decay vertex is displaced from any pp interaction vertex. The Σ^+ decay vertex is fitted, and its quality is assessed by requiring $Vtx\chi^2 < 36$. The final state particles must originate from the Σ^+ decay vertex and not from any secondary decay. This is achieved by requesting $IP\chi^2 < 36$ and a $DIRA > 0.9$. An additional $minIP\chi^2 > 9$ request is applied for the muons. Only Σ^+ candidates with a transverse momentum $p_T > 500$ MeV/c and $DOCA < 2$ mm are considered to guarantee a good quality on the reconstructed quantities. Finally, a signal candidate is considered only if its invariant mass $m_{p\mu^+\mu^-}$ satisfies $|m_{p\mu^+\mu^-} - m_{\Sigma^+}| < 500$ MeV/c^2, where m_{Σ^+} is the known mass of Σ^+ particle from the PDG [12]. The signal stripping requirements presented above are summarised in Tab. 3.7.

Following the stripping level, a data cleaning preselection is applied before optimising the final requirements. The $m_{p\mu^+\mu^-}$ invariant mass is restricted to below

Particle	Stripping cut
μ^+, μ^-	$minIP\chi^2 > 9$
$p\mu^+\mu^+$	$\lvert m_{p\mu^+\mu^-} - m_{\Sigma^+}\rvert < 500$ MeV/c^2
	$DOCA < 2$mm
	$p_T > 500$ MeV/c
	$DIRA > 0.9$
	$IP\chi^2 < 36$
	$Vtx\chi^2 < 36$
	$\tau > 6$ ps

Table 3.7. Stripping requirements applied on the $\Sigma^+ \to p\mu^+\mu^-$ decay.

1400 MeV/c^2. This request creates a large enough sideband on the right side of the signal region and avoids complications from some background components, such as $K_S \to \pi^+\pi^-$ decays with both pions misidentified as muons and combined with an accidental proton. The Σ^+ decay vertex is restricted to be within 1 m from its generation point, to ensure that the decay vertex is located within the VELO. Loose PID cuts are also implemented on both proton and muons: $ProbNNp > 0.1$ and $ProbNNmu > 0.05$. A requirement on the opening angle between each pair of tracks $\alpha > 0.0025$ rad is set as well to remove the clone tracks. Two tracks are considered clones of each other if they share at least 70% of the hits in the VELO and at least 70% of the hits in the T-stations. This background component is shown in Fig. 3.2 after the stripping criteria in data as an accumulation at very small angles between two of the three tracks of the $\Sigma^+ \to p\mu^+\mu^-$ decay candidates. Each plot is zoomed towards very small angles and, therefore, the entire dataset is not shown.

The $\Sigma^+ \to p\mu^+\mu^-$ invariant mass distribution is shown in Fig. 3.3 after the stripping and preselection requirements for both data (left) and MC (right) samples. Note that while the data distribution is blinded, the signal region is not removed on MC.

3.6 Residual background

After applying the trigger strategy and the stripping and preselection requirements, only two main sources of background are expected to contribute to the $\Sigma^+ \to p\mu^+\mu^-$ invariant mass distribution, due to the extremely small phase space of the decay:

- Combinatorial - Random combinations of three tracks with correct or incorrect identification of the involved particles. This background is distributed along the whole invariant mass and increases as the phase space increases;

- $\Lambda \to p\pi^-$ decays - One negative pion is misidentified as a muon and combined with an accidental positive muon. This background is expected to appear on the right side of the Σ^+ mass value. The $p\mu^-$ invariant mass distribution, with the $p\pi^-$ mass hypothesis, is shown in Fig. 3.4 after the preselection requirements in data.

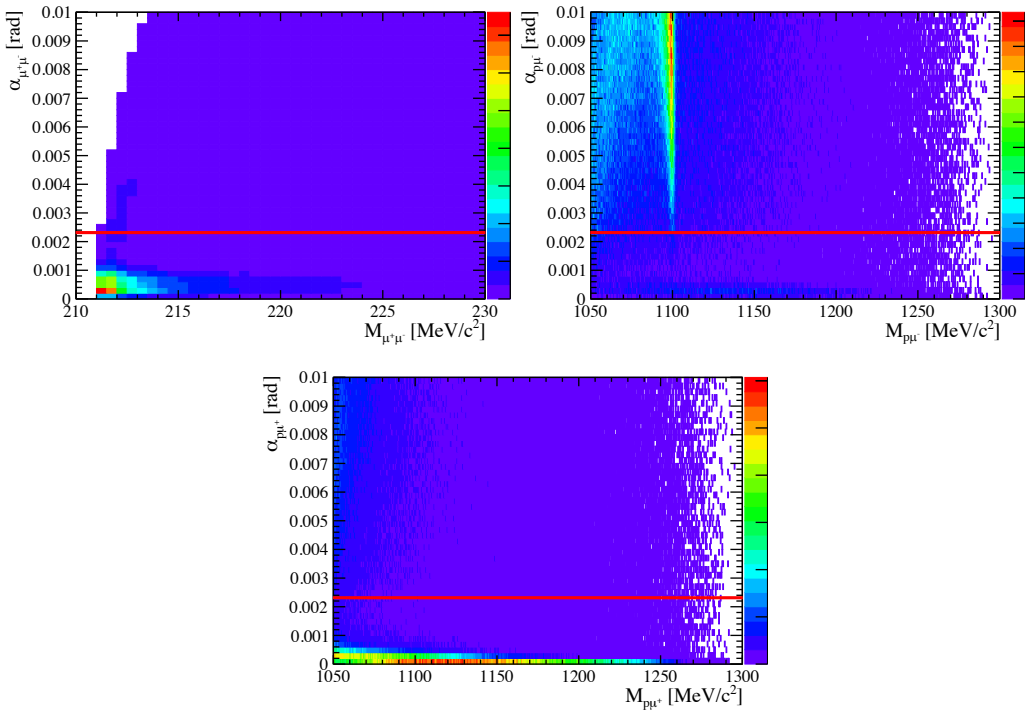

Figure 3.2. Distribution of the pairs invariant masses as a function of the opening angle for each pair of tracks after the stripping criteria in data. The chosen requirement is shown as a horizontal red line in each plot.

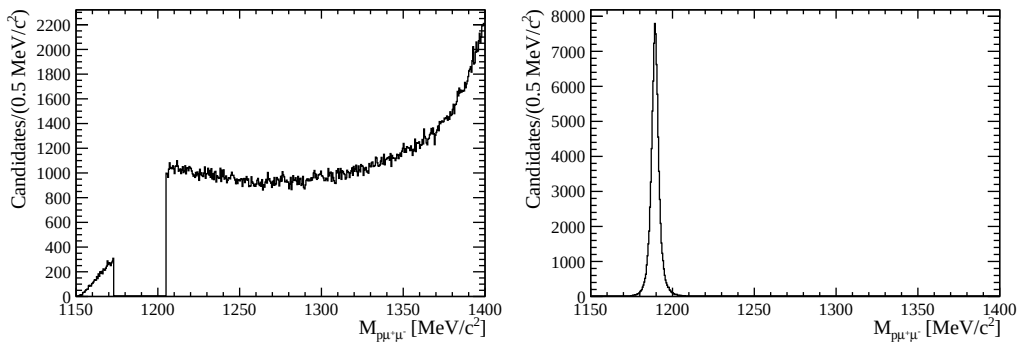

Figure 3.3. Distribution of the $\Sigma^+ \to p\mu^+\mu^-$ invariant mass after the stripping and preselection requirements for both data (left) and MC (right) samples.

The difference between the Σ^+ mass value and the sum of its final state particle masses is $(m_{\Sigma^+} - m_p - 2m_\mu) = (1189.37 - 938.27 - 2 \cdot 105.66) = 39.8$ MeV/c^2. This implies that very few decays can mimic the signal channel.

The $K^+ \to \pi^+\pi^-\pi^+$ decay is similar to the signal one as its final state is composed of three charged and very displaced tracks. It could mimic the signal mode if one pion is misidentified as a proton and the other two as muons. However, if the $p\mu^+\mu^-$ mass hypothesis is considered, as shown in Fig. 3.5 (left) in simulation, the K^+ expected peak, illustrated in Fig. 3.5 (right) in simulation, moves significantly

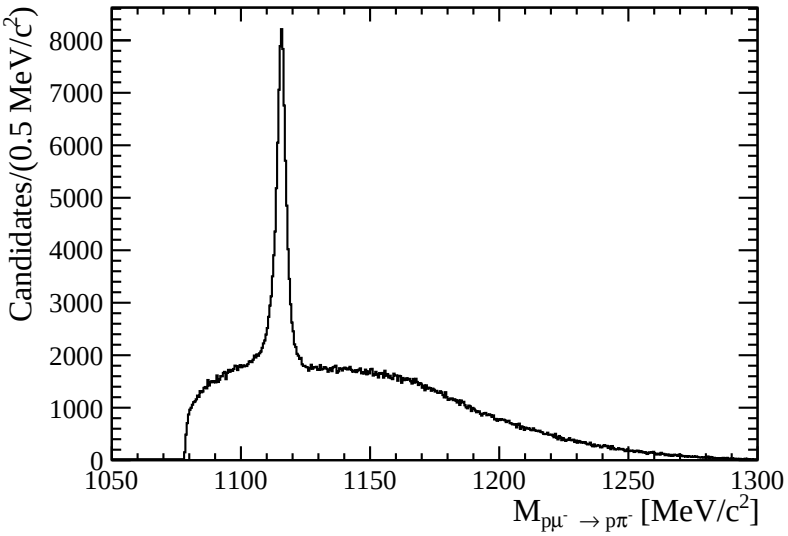

Figure 3.4. Distribution of the $p\mu^-$ invariant mass in the $p\pi^-$ mass hypothesis after the preselection requirements in data.

to the right respect to the $\Sigma^+ \to p\mu^+\mu^-$ signal region and only a small tail reaches it. This makes the $K^+ \to \pi^+\pi^-\pi^+$ decay a negligible source of background. Given this, the $K^+ \to \pi^+\mu^+\mu^-$ decay becomes also an irrelevant source of background due to its very small branching fraction with respect to the $K^+ \to \pi^+\pi^-\pi^+$ decay mode [12]. Decays of mesons with higher mass values are not considered important sources of background as they would be shifted to the right side of the signal region even more than the $K^+ \to \pi^+\pi^-\pi^+$ decay.

Concerning other Σ^+ modes, the $\Sigma^+ \to p\pi^+\mu^-\bar{\nu}_\mu$ and $\Sigma^+ \to p\mu^+\nu_\mu\mu^-\bar{\nu}_\mu$ decays can in principle contribute to the signal background. The $\Sigma^+ \to p\pi^+\mu^-\bar{\nu}_\mu$ decay is described by a tree-level weak diagram and the predicted branching fraction is 9×10^{-13} [12]. It has a very limited phase space, $(m_{\Sigma^+} - m_p - m_\pi - m_\mu) = (1189.37 - 938.27 - 139.57 - 105.66)$ MeV/c^2 = 5.87 MeV/c^2, and, therefore, it is strongly suppressed. The $\Sigma^+ \to p\mu^+\nu_\mu\mu^-\bar{\nu}_\mu$ decay is also significantly suppressed as proceeds through double-beta decay diagrams and does not have large long distance contributions [12]. Furthermore, the presence of the two neutrinos brings the $m_{p\mu^+\mu^-}$ mass below the one of the Σ^+ particle. Both decays have been simulated with the RapidSim software [125] and their invariant mass distributions are reported in Fig. 3.6, compared to the $\Sigma^+ \to p\mu^+\mu^-$ simulated one. Both distributions are well below the $\Sigma^+ \to p\mu^+\mu^-$ signal region as expected. Decays from other baryons with a real proton in the final state are not taken into account as relevant sources of background as they will have a reconstructed mass considerably larger with respect to the signal one.

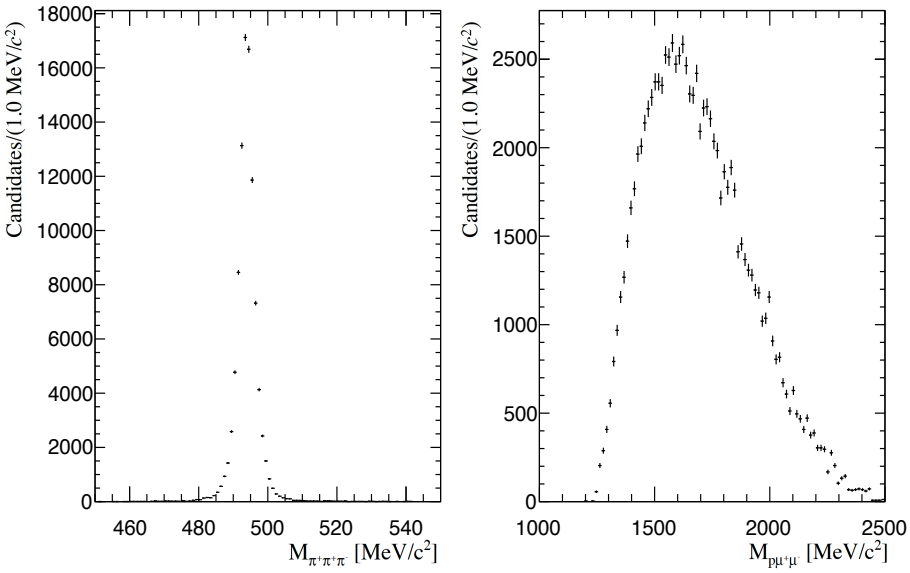

Figure 3.5. Simulated distribution of the $K^+ \to \pi^+\pi^-\pi^+$ invariant mass in the $\pi^+\pi^-\pi^+$ (left) and the $p\mu^+\mu^-$ (right) mass hypothesis.

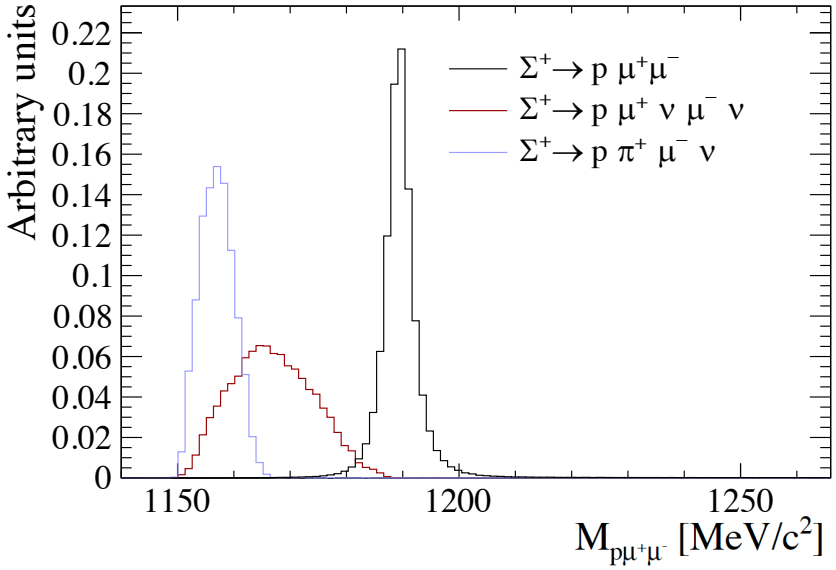

Figure 3.6. Simulated distributions of the $\Sigma^+ \to p\mu^+\nu_\mu\mu^-\bar{\nu}_\mu$ (red) and $\Sigma^+ \to p\pi^+\mu^-\bar{\nu}_\mu$ (blue) invariant masses compared to the signal one (black).

3.7 Multivariate operator

The final selection is based on a multivariate operator, built with the TMVA package in ROOT [126] and trained to distinguish the signal from the combinatorial background. A Boosted Decision Tree (BDT) has been trained with the signal

MC sample and two sideband regions in the data. These sidebands are chosen with the following ranges: $m_{p\mu^+\mu^-} < 1173$ MeV/c^2 and $m_{p\mu^+\mu^-} > 1205$ MeV/c^2. Both samples are preselected, as explained in Sec. 3.5. In addition, the background component due to $\Lambda \to p\pi^-$ decays is vetoed by discarding candidates having a $p\mu^-$ invariant mass, calculated with the $p\pi^-$ mass hypothesis, within 10 MeV/c^2 from the known Λ mass [12]. This requirement is implemented to train the operator only against the combinatorial background.

The following variables have been used as input to the multivariate training:

- $\log(1 - \Sigma^+\ DIRA)$ - The logarithm of one minus the cosine of the Σ^+ pointing angle;
- $\Sigma^+\ IP\chi^2$ - The χ^2 of the Impact Parameter of the Σ^+ with respect to the decay vertex;
- $p\ IP\chi^2$ - The χ^2 of the Impact Parameter of the proton with respect to the decay vertex;
- $min(\mu\ IP\chi^2)$ - The minimum χ^2 of the Impact Parameter of the two muons with respect to the decay vertex;
- $\Sigma^+\ DOCA$ - The minimum Distance Of Closest Approach between any pair of the three final state particles;
- $\Sigma^+\ FD\chi^2$ - The χ^2 of the Flight Distance of the Σ^+ from the decay vertex;
- $\Sigma^+\ Vtx\chi^2$ - The χ^2 of the Σ^+ fitted decay vertex;
- $min(\mu\ p_T)$ - The minimum transverse momentum of the two muons;
- $p\ p_T$ - The transverse momentum of the proton;
- $\mathrm{Iso} = \sum_i \mathrm{Iso_i}$ - The sum of the isolation variables of the three final state particles. In particular, the sum of the p_T of the three final state particles taken inside a cone with $\Delta R = \sqrt{\Delta\eta^2 + \Delta\phi^2} < 1$.

The distributions of the input variables are shown in Fig. 3.7 for the signal MC sample (red) and the combinatorial background of the sideband regions in data (black).

The BDT parameters have been optimised in order to always keep overtraining to a minimum. In addition, the *k-folding* method [127] has been used with 9 permutations. The distribution of the BDT output is shown in Fig. 3.8 (top) for the signal MC sample (red) and the combinatorial background of the sideband regions in data (black). The same output for a data sample without requesting the Λ veto is also illustrated (blue). It can be seen that the BDT distributions for the two background sources are very similar. This implies that a requirement in BDT will not only reject combinatorial background, for which it is trained, but also the Λ component. The same distribution under a bijective transformation, such that the signal is distributed uniformly between zero and one while the background peaks at zero, is reported in Fig. 3.8 (bottom).

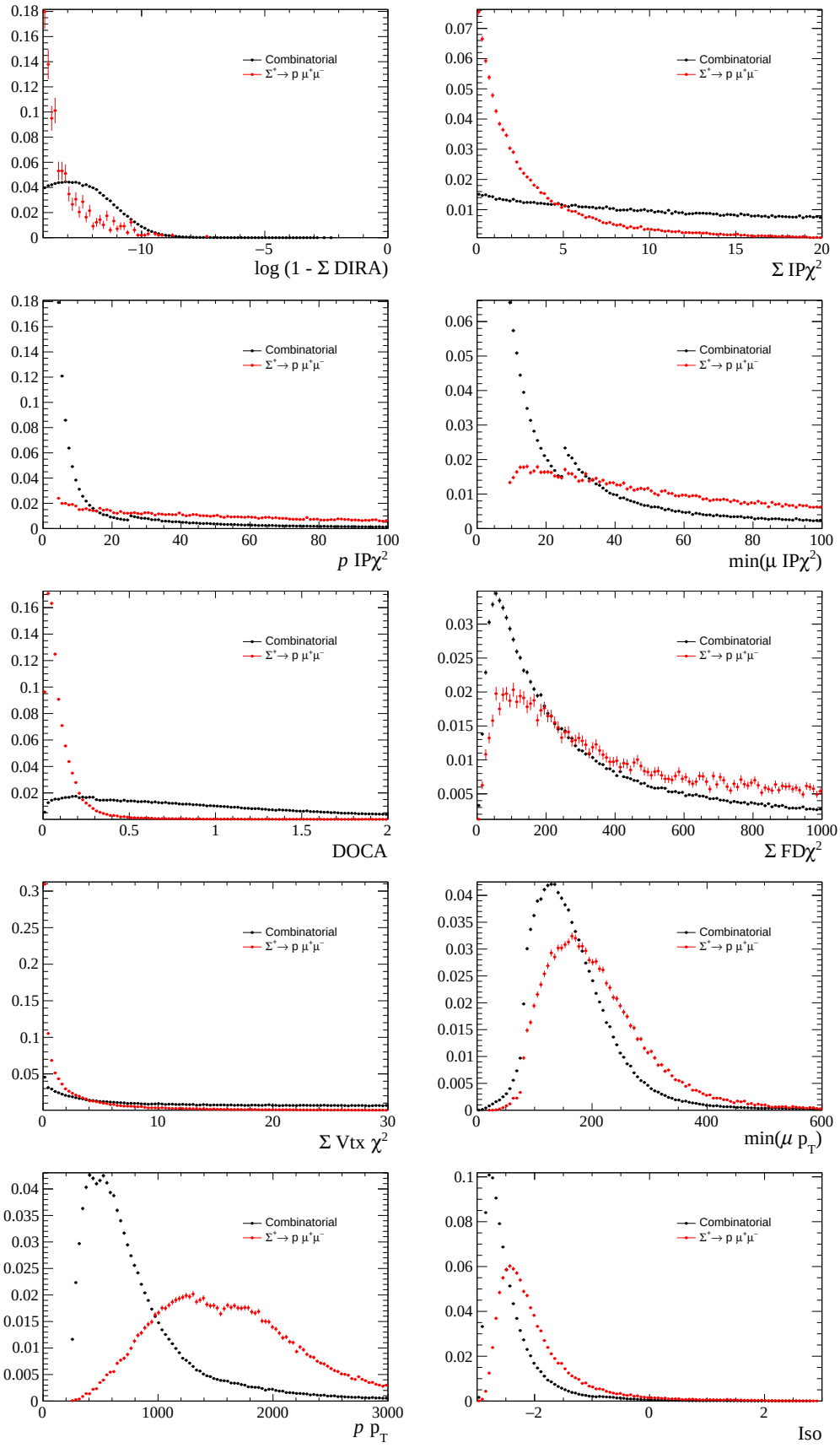

Figure 3.7. Normalised distributions of the input variables in the BDT for the signal MC sample (red) and the combinatorial background of the sideband regions in data (black).

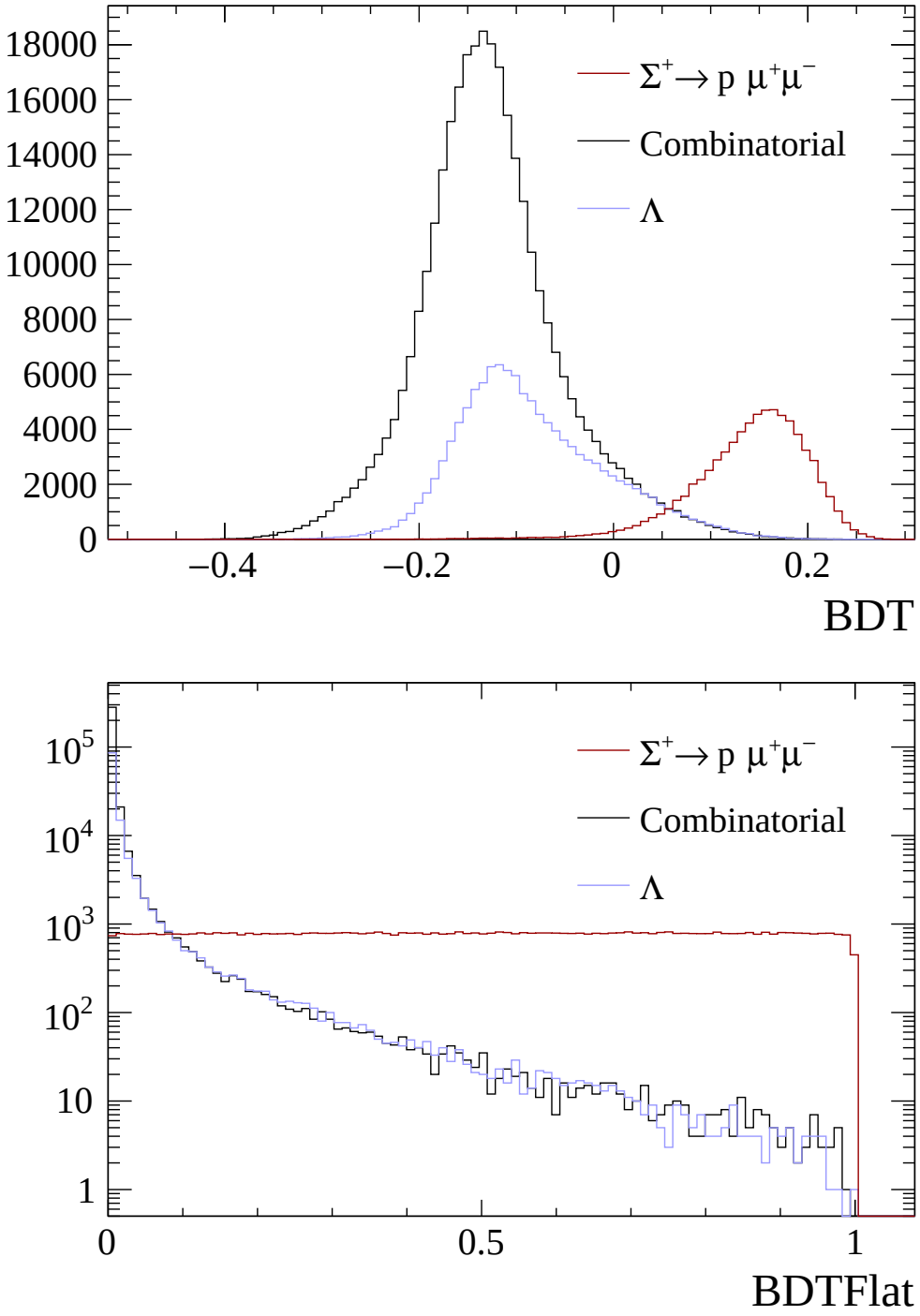

Figure 3.8. Distribution of the BDT output (top) for the signal MC sample (red), the combinatorial background (black) and the Λ component (blue) of the sideband regions in data. The same distribution is also reported under the bijective transformation explained in the text (bottom).

Chapter 4

Optimisations of the $\Sigma^+ \to p\mu^+\mu^-$ selection strategy

In order to have the best chances of observation, the $\Sigma^+ \to p\mu^+\mu^-$ selection strategy has been optimized.

In this chapter, two optimisations are presented. The first one is performed without unblinding the signal region. In this scenario, a first estimation of the $\Sigma^+ \to p\mu^+\mu^-$ final yield is reported. Given the nature of the obtained results, it was decided to perform a second optimisation post-unblinding to reduce uncertainties on the measured quantities of the analysis.

4.1 First optimisation

The first optimisation is performed with the Punzi Figure Of Merit (FOM) [128] using the formula:

$$\mathcal{P} = \frac{\varepsilon_{sig}}{\frac{a}{2} + \sqrt{N_{bkg}}}, \tag{4.1}$$

where ε_{sig} and N_{bkg} denote the signal efficiency and the total number of expected background candidates for a given selection requirement. The parameter a is the significance for which the analysis is being optimized, expressed in a number of standard deviations σ, and it is chosen to be $a = 3$. The optimisation is performed in two dimensions:

- μ $ProbNNmu$ - The minimum value between the PID variables of the two muons, within the range [0.10, 0.60] at 0.01 intervals;
- BDT - The BDT output, within the range [0.120, 0.205] at 0.005 intervals.

Both signal efficiency and background candidates are estimated for each combination of the selection requirements.

The signal efficiency ε_{sig} is evaluated from the MC sample by fitting the $m_{p\mu^+\mu^-}$ invariant mass distribution with an Hypatia function [129].

The number of background candidates N_{bkg} is obtained as the sum of the combinatorial and Λ candidates, referred to as N_{comb} and N_Λ. These are estimated

by fitting the sideband regions in data with an Argus function [130] and extrapolating the results in the signal region. To avoid overcounting the background candidates, N_Λ is evaluated by requiring $|m_{p\pi^-} - m_\Lambda| < 10$ MeV/c^2 to the data sample. The opposite request is applied for the evaluation of the combinatorial candidates.

The distribution of the $\mathcal{P}$ FOM is shown in Fig. 4.1 as a function of the two optimisation variables. The same distribution is illustrated in Fig. 4.2 as a function of the signal efficiency and background rejection. The ROC curve is also reported. The highest $\mathcal{P}$ values are marked in red.

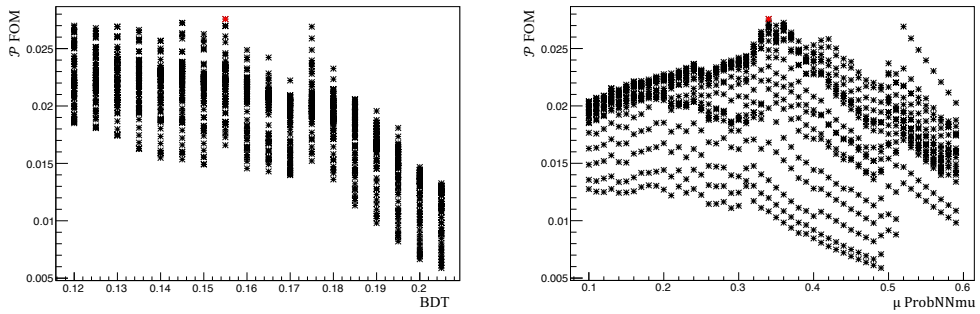

Figure 4.1. Distribution of the $\mathcal{P}$ FOM as a function of the BDT (left) and μ $ProbNNmu$ (right) variables. The highest $\mathcal{P}$ values are marked in red.

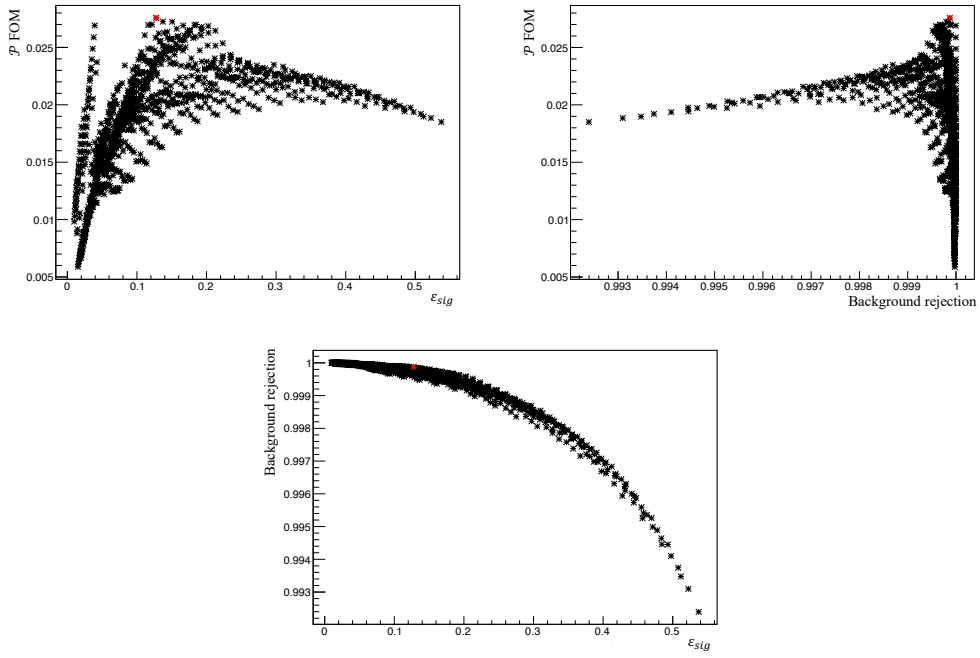

Figure 4.2. Distribution of the $\mathcal{P}$ FOM as a function of the signal efficiency (left) and the background rejection (right) and distribution of the ROC curve (bottom). The highest $\mathcal{P}$ values are marked in red.

The optimal point is chosen to be the one with the highest $\mathcal{P}$ value and corre-

sponds to the following selection:

- BDT > 0.15;
- μ $ProbNNmu > 0.34$.

The resulting blinded $\Sigma^+ \to p\mu^+\mu^-$ invariant mass distribution in data is shown in Fig. 4.3 (left). The $p\mu^-$ distribution in the $p\pi^-$ hypothesis in data is also reported with the same conditions in Fig. 4.3 (right).

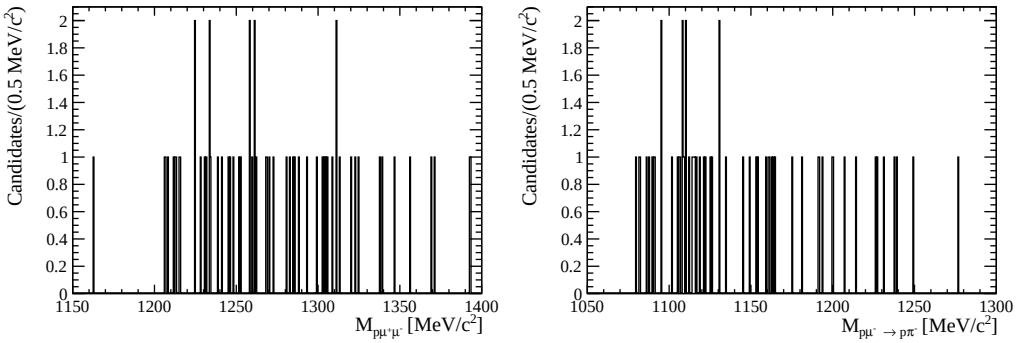

Figure 4.3. Distributions of the $m_{p\mu^+\mu^-}$ (left) and $p\mu^-$ in the $p\pi^-$ hypothesis (right) invariant masses after applying the optimised selection in data.

As shown, the Λ background component is almost completely removed. With this selection, the total amount of background candidates in the blinded signal region is expected to be $N_{bkg} = 13$.

4.1.1 Expected signal

The number of expected signal candidates is estimated by extrapolating the Run 1 final yield to the Run 2 dataset. This is done by multiplying the ratio between the Run 2 and Run 1 luminosities, cross-sections and efficiencies with the Run 1 number of signal candidates. The Run 2 efficiencies are taken from the signal MC sample and the cross-section is assumed to simply scale by the centre-of-mass energy. The calculation is reported in Tab. 4.1. The number of signal candidates is expected to be 118 ± 43, where the uncertainty is dominated by the statistics of the Run 1 signal candidates.

4.2 Unblinding of the signal region

Given the large number of expected signal candidates with respect to the small background, the signal region has been unblinded and a first estimation of the $\Sigma^+ \to p\mu^+\mu^-$ final yield has been performed.

The unblinded $\Sigma^+ \to p\mu^+\mu^-$ invariant mass distribution in data is shown in Fig. 4.4 after the optimised selection and superimposed with the fit (blue). The signal component is parametrised by an Hypatia function [129] (red) while the background is described by a modified Argus function [130] (green). Details on the fit strategy are given in Sec. 5.1.

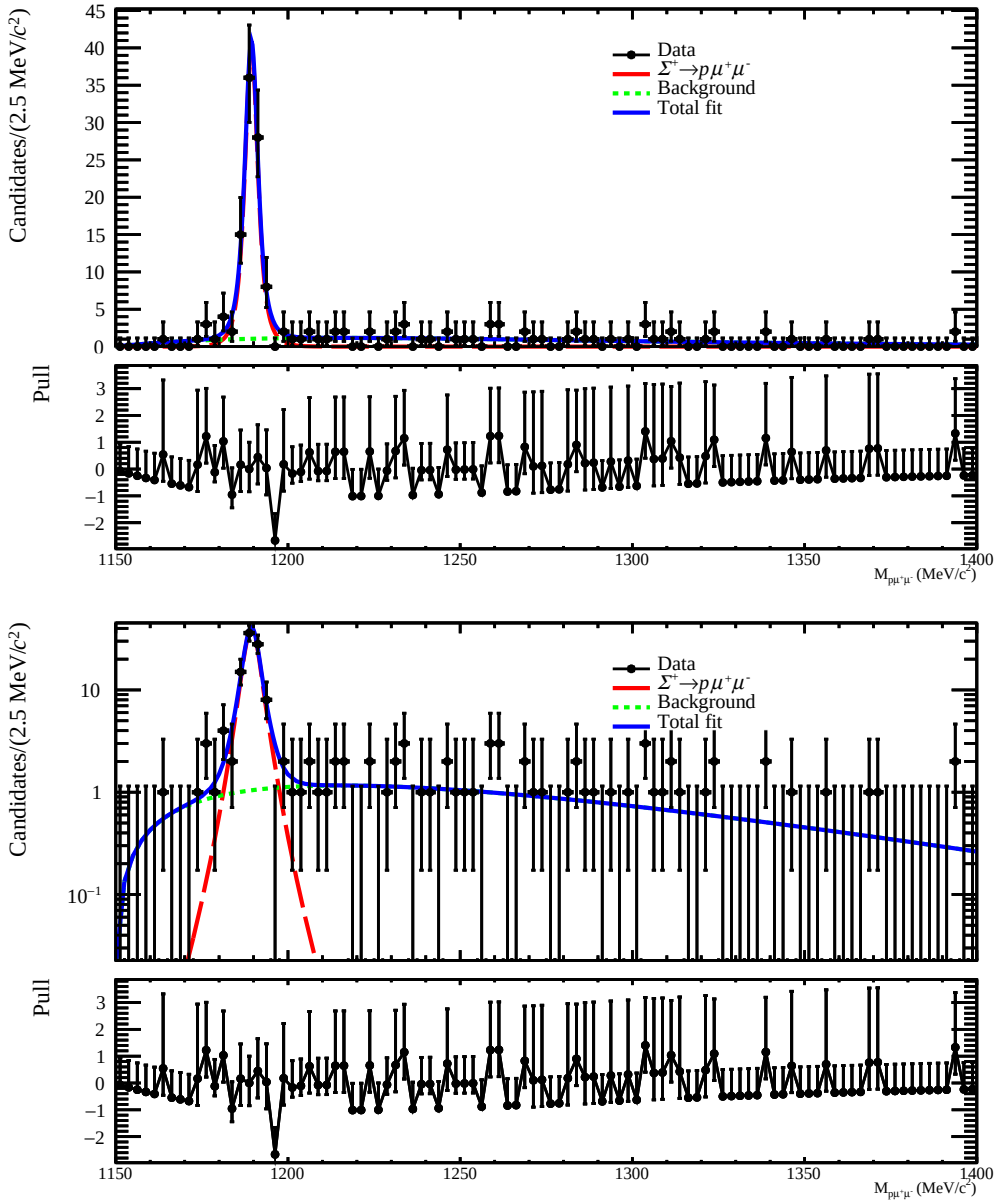

Figure 4.4. Distribution of the $m_{p\mu^+\mu^-}$ invariant mass in data after the optimised selection and superimposed with the fit (blue). The signal component is parametrised by an Hypatia function (red) while the background is described by an Argus function (green). The same distribution is reported in linear (top) and logarithmic scale (bottom). The pull distribution is also illustrated in the bottom panel.

	Run 1	Run 2	Ratio
ε_{Presel}	$(6.59 \pm 0.04) \times 10^{-3}$	$(8.322 \pm 0.012) \times 10^{-3}$	1.263 ± 0.010
ε_{Trig}	0.0143 ± 0.0005	0.1203 ± 0.0004	8.413 ± 0.322
ε_{Final}	0.3793 ± 0.0031	0.1270 ± 0.0004	0.335 ± 0.004
$\mathcal{L}$ [fb^{-1}]	3.0	5.4	1.80
σ [fb]			1.69
$N_{Obs/Exp}$	10.9 ± 3.3	118 ± 43.0	

Table 4.1. Relative normalisation of the Run 2 dataset to the one used in the Run 1 LHCb analysis, using only the signal information. The Run 2 efficiencies are taken from the signal MC sample and the cross-section is assumed to simply scale by the centre-of-mass energy.

The same distribution in MC is reported in Fig. 4.5. In this case, there is no need to include a function to describe the background component after the optimised selection.

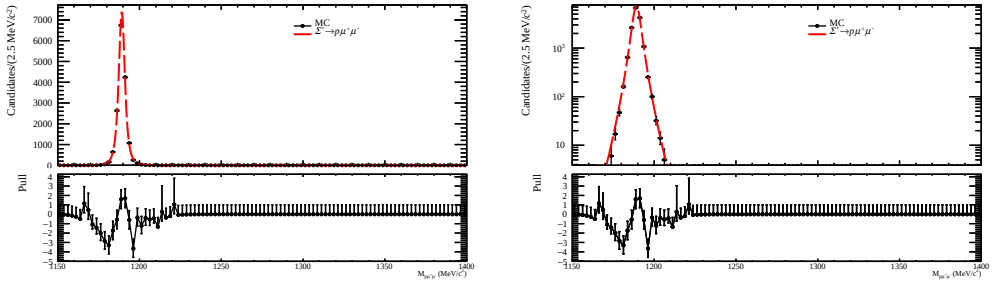

Figure 4.5. Distribution of the $m_{p\mu^+\mu^-}$ invariant mass in MC after the optimised selection and superimposed with the fit (red). Only the Hypatia function is used as there is no need to include a function to describe the background component after the optimised selection. The same distribution is reported in linear (left) and logarithmic scale (right). The pull distribution is also illustrated in the bottom panel.

The number of MC signal candidates is estimated to be $N^{MC}_{\Sigma^+\to p\mu^+\mu^-} = 15965 \pm 16$ with a resolution equal to $\sigma^{MC}_{\Sigma^+\to p\mu^+\mu^-} = 3.36 \pm 0.01$ MeV/c^2. In data, a large number of signal candidates is observed, estimated to be $N^{Data}_{\Sigma^+\to p\mu^+\mu^-} = 88 \pm 10$ with a resolution of $\sigma^{Data}_{\Sigma^+\to p\mu^+\mu^-} = 3.4 \pm 0.4$ MeV/c^2. In the signal region, the number of background candidates is measured to be $N_{bkg} = 13 \pm 2$. Both signal and background candidates are compatible with the expected values of the first optimisation.

The number of estimated signal candidates is 9 times larger than the reported error and the small fluctuation of the background does not explain the observed peak. Therefore, the result represents the first clear observation of the $\Sigma^+ \to p\mu^+\mu^-$ decay. Given the large signal and purity of the result, it was decided to optimise again the selection to reduce the uncertainties of the branching fraction measurement.

4.3 Second optimisation

For the second optimisation, the Punzi FOM has been discarded as it is meant to optimise the minimum visible cross-section with a given significance [128]. Therefore, different FOMs have been considered:

- Significance and Significance × Purity;
- Efficiency × Purity.

The second optimisation is performed in four dimensions:

- BDTFlat[1] - The BDT output after the bijective transformation presented in Sec. 3.7, within the range [0.0, 0.60] at 0.05 intervals;
- μ *ProbNNmu* - The minimum value between the PID variables of the two muons, within the range [0.1, 0.40] at 0.05 intervals;
- *ProbNNp* - The PID variable of the proton, within the range [0.1, 0.45] at 0.05 intervals;
- $|m_{p\pi^-} - m_\Lambda| > v$ MeV/c^2 - The Λ veto, with v equal to 6, 8, and 10 MeV/c^2.

The expected number of signal candidates $N_{exp}(x)$ for a given set of requirements x is evaluated as

$$N_{exp}(x) = N_{first}\frac{\varepsilon(x)}{\varepsilon(first)}, \tag{4.2}$$

where N_{first} and $\varepsilon(first)$ represent the number of expected signal candidates and the signal efficiency evaluated in the first optimisation. As in the first optimisation, the new signal efficiency $\varepsilon(x)$ is evaluated by fitting the MC sample.

The combinatorial background is estimated by fitting the sidebands in data with an Argus function [130], after applying the Λ veto to avoid overcounting the candidates. An example of this fit is shown in Fig. 4.6 (left). The background component from Λ decays is studied in data through a fit to the $m_{p\mu^-}$ mass distribution in the $p\pi^-$ mass hypothesis. An example of this fit is presented in Fig. 4.6 (right). Here, the signal component is parametrised by a double-sided Crystal Ball function (red) while a Chebyshev second degree polynomial function of the first kind [131] describes the background (green).

The Significance FOM is shown in Fig. 4.7 as a function of the background candidates and in Fig. 4.8 as a function of the BDT and PID requirements. The rest of the FOMs are shown in Fig. 4.9 as a function of the BDT variable.

The optimal points selected for different FOMs are shown in Tab. 4.2 with the corresponding requirements. Here, the number of expected signal, total and Λ background candidates in the signal region are also reported.

The Significance × Purity FOM with the Λ veto with $v = 10$ MeV/c^2 has been chosen, given the low number of expected Λ background candidates in the signal region, corresponding to the following selection:

[1] In the following, the variable BDTFlat will be denoted simply BDT.

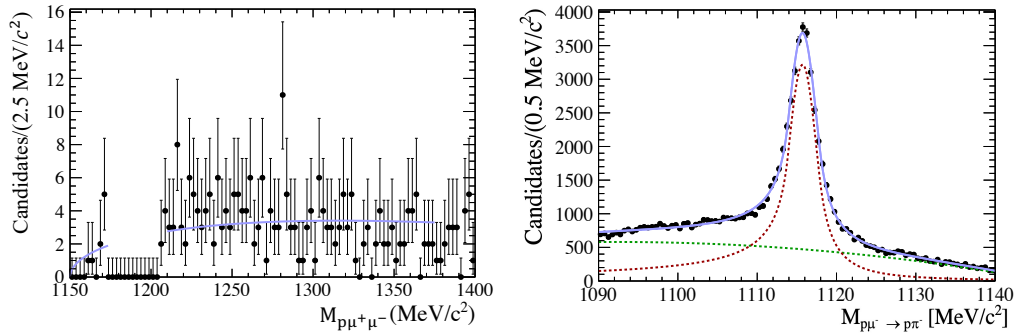

Figure 4.6. Distribution of the $m_{p\mu^+\mu^-}$ sidebands in data (left), superimposed with the fitted Argus function (blue) and distribution of the $m_{p\mu^-}$ invariant mass with the $p\pi^-$ mass hypothesis in data (right), superimposed with the fit (blue). The signal component is parametrised by a double-sided Crystal Ball function (red) while a Chebyshev second degree polynomial function of the first kind describes the background (green).

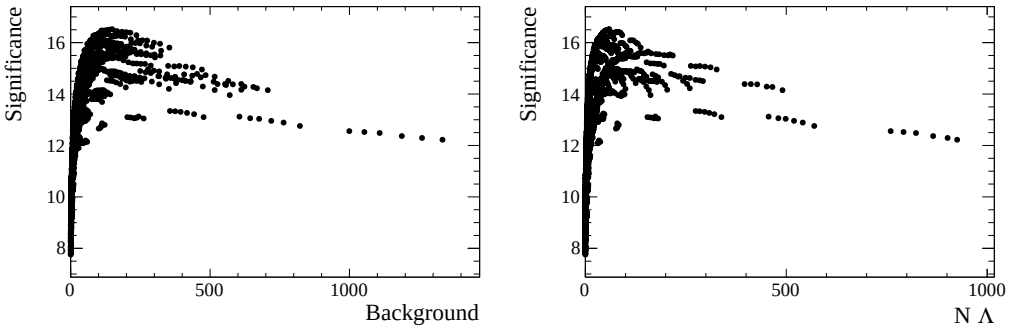

Figure 4.7. Distribution of the Significance FOM as a function of the expected total (left) and Λ (right) background candidates.

FOM	Optimal point	BDT	μ *ProbNNmu*	*ProbNNp*	v	N_S	N_B	N_Λ
Significance	15.9286	0.25	0.1	0.15	6	352.213	136.728	71.4679
Significance	14.233	0.4	0.15	0.15	8	228.633	29.4045	9.66182
Significance	13.6569	0.5	0.15	0.3	No veto	203.338	18.3454	9.57091
Significance	14.9432	0.3	0.15	0.15	No veto	309.286	119.096	86.4662
Significance × Purity	13.0175	0.35	0.15	0.35	6	243.993	31.5255	15.3475
Significance × Purity	12.7426	0.35	0.15	0.35	10	224.819	25.7569	9.57887
Significance × Purity	12.6017	0.5	0.2	0.2	No veto	177.726	6.79615	1.03789

Table 4.2. Optimal points for the different FOMs. The number of expected signal candidates, N_S, and the total and Λ background candidates, N_B and N_Λ, in the signal region are also reported.

- BDT > 0.35;
- μ *ProbNNmu* > 0.15;
- *ProbNNp* > 0.35;
- $|m_{p\pi^-} - m_\Lambda| > 10$ MeV/c^2.

In this configuration, the number of expected signal candidates in the signal

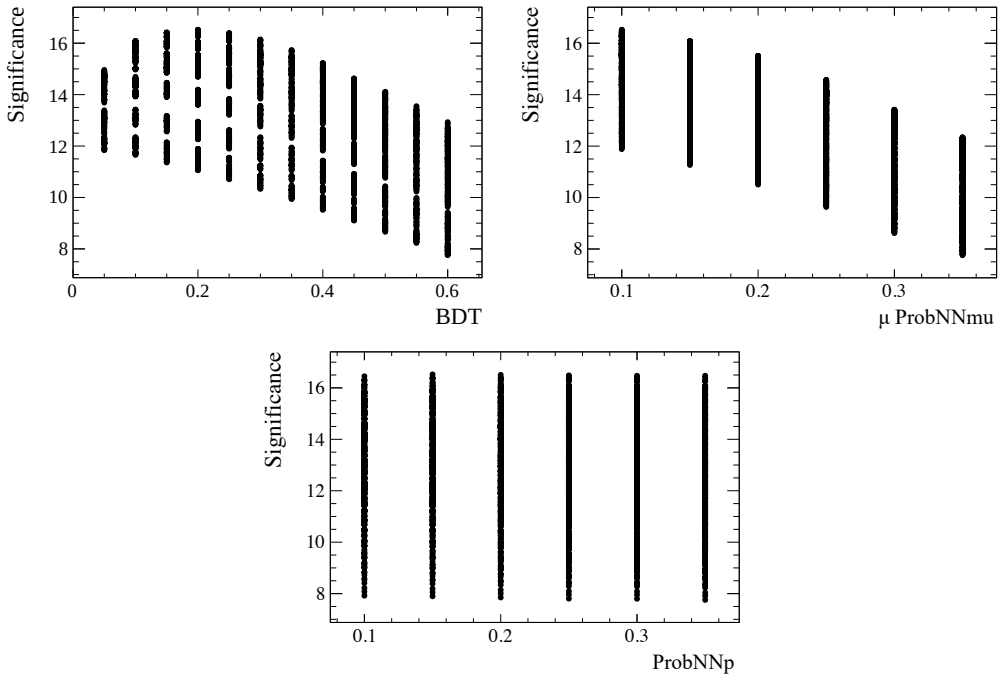

Figure 4.8. Distribution of the Significance FOM as a function of the BDT (left), the μ *ProbNNmu* (right) and the *ProbNNp* (bottom) variables.

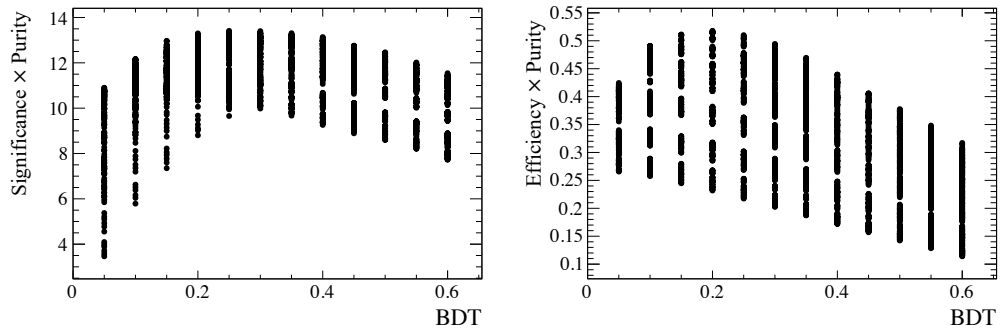

Figure 4.9. Distribution of the Significance × Purity (right) and Efficiency × Purity (right) FOMs as a function of the BDT variable.

region is estimated to be $N_{sig} = 225$ while the total amount of background candidates is expected to be $N_{bkg} = 26$, with 10 of them coming from the Λ decay.

4.3.1 Validation of the final selection

The efficiency of the final selection has been studied as a function of the $p\mu^+\mu^-$ and $\mu^+\mu^-$ invariant masses in the signal MC sample and using $\Sigma^+ \to \bar{p}\mu^+\mu^+$ candidates in data, as reported in Figs. 4.10. This decay consists of wrong-charged muons and, therefore, no signal is expected in data. The optimised selection prefers signal candidates closer to the correct mass as they are better reconstructed in that region. It does not create fake structures in the $\Sigma^+ \to \bar{p}\mu^+\mu^+$ distribution and it favours

larger dimuon masses without creating fake structures in the signal nor in the distribution of the $\Sigma^+ \to \bar{p}\mu^+\mu^+$ control sample. Therefore, the final selection is considered safe for the branching fraction measurement and studies of the dimuon mass.

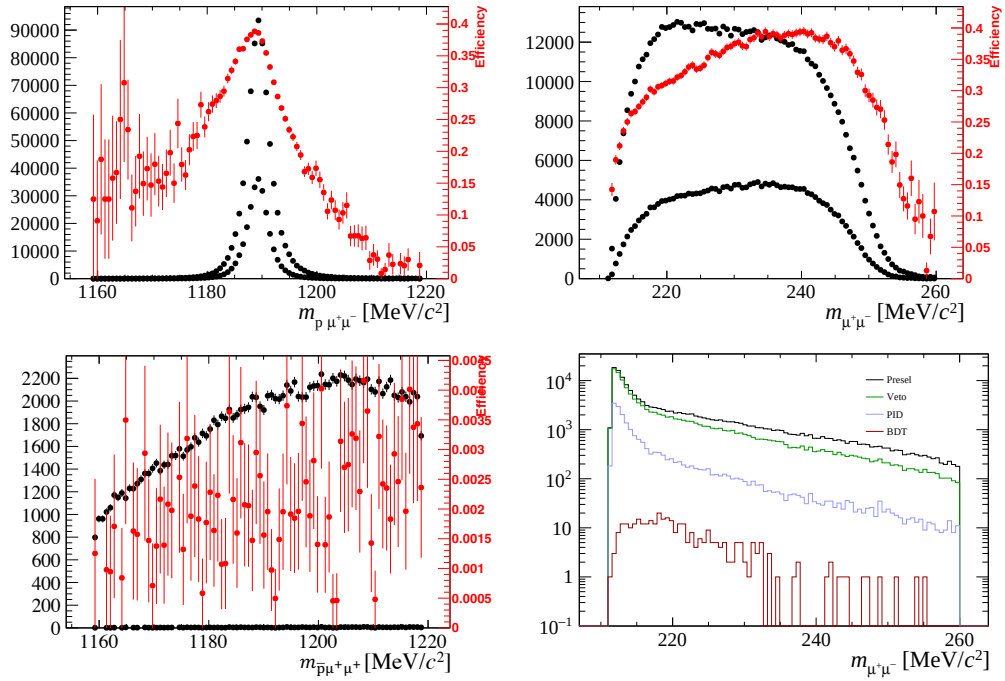

Figure 4.10. Distribution and efficiency of the simulated $\Sigma^+ \to p\mu^+\mu^-$ candidates before and after applying the final selection as a function of the $p\mu^+\mu^-$ (top-left) and the dimuon (top-right) masses. Distribution and efficiency of the $\Sigma^+ \to \bar{p}\mu^+\mu^+$ candidates before and after applying the final selection as a function of the $\bar{p}\mu^+\mu^+$ mass (bottom-left) and distribution of the dimuon mass after each selection requirement (bottom-right).

Chapter 5

Fit to the $\Sigma^+ \to p\mu^+\mu^-$ invariant mass distribution

In this chapter, the fit strategy to the $\Sigma^+ \to p\mu^+\mu^-$ invariant mass distribution is presented and the final yield is estimated. The fit is performed on both data and MC samples after applying the second optimisation, described in Sec. 4.3. The same fit strategy was applied to obtain the results reported in Sec. 4.2.

5.1 Signal final yield

The distribution of the signal invariant mass after applying the second optimisation is reported in Fig. 5.1 for both data (left) and MC (right) samples.

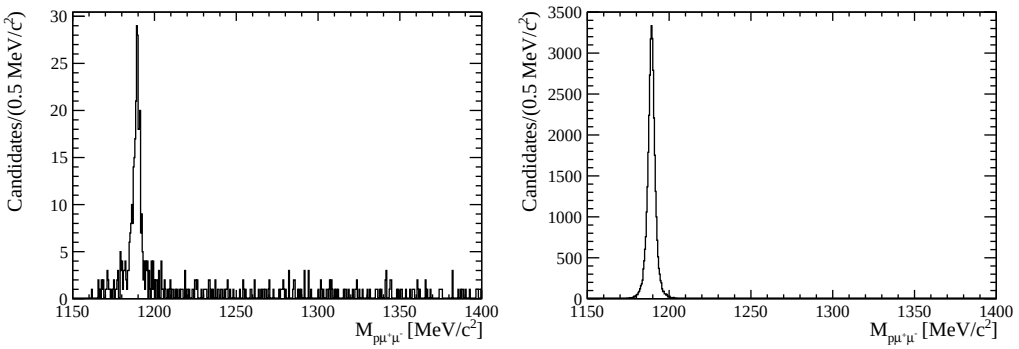

Figure 5.1. Distribution of the $m_{p\mu^+\mu^-}$ invariant mass in data (left) and MC (right) after applying the second optimisation.

An extended maximum likelihood fit is performed first on the simulated sample and then on the data one. The fit is performed in the range $1150 < m_{p\mu^+\mu^-} < 1400$ MeV/c^2, where the lower limit is chosen to be near the threshold value given by the sum of the proton and the muons masses. The signal component is described by an Hypatia function [129], defined as:

$$\mathrm{H}\left(x;\mu,\sigma,\lambda,\zeta,\beta,a_l,n_l,a_r,n_r\right) = \begin{cases} \frac{G(\mu-a_l\sigma,\mu,\sigma,\lambda,\zeta,\beta)}{\left(1-\frac{x}{n_l G(\ldots)/G'(\ldots)-a_l\sigma}\right)^{n_l}}, \text{ if } \frac{x-\mu}{\sigma} < -a_l \\ \left((x-\mu)^2 + A_\lambda^2(\zeta)\sigma^2\right)^{\frac{1}{2}\lambda-\frac{1}{4}} e^{\beta(x-\mu)} K_{\lambda-\frac{1}{2}}\cdot \\ \left(\zeta\sqrt{1+\left(\frac{x-\mu}{A_\lambda(\zeta)\sigma}\right)^2}\right) \equiv G(x,\mu,\ldots), \text{ otherwise} \\ \frac{G(\mu+a_r\sigma,\mu,\sigma,\lambda,\zeta,\beta)}{\left(1-\frac{x}{-n_r G(\ldots)/G'(\ldots)-a_r\sigma}\right)^{n_r}}, \text{ if } \frac{x-\mu}{\sigma} > a_r \end{cases} \tag{5.1}$$

Here, the hyperbolic core of the function is defined by a Crystal-Ball-like function G with two exponential tails, K_λ are the modified Bessel functions of the second kind and $A_\lambda^2(\zeta)$ is defined as:

$$A_\lambda^2(\zeta) = \frac{\zeta K_\lambda(\zeta)}{K_{\lambda+1}(\zeta)}. \tag{5.2}$$

In this function, the parameters are:

- λ and ζ - The shape parameters of the core;
- β - The asymmetry parameter, defining eventually asymmetries in the shape of the core. The symmetric case is defined by $\beta = 0$;
- μ - The mean value of the core;
- σ - The width of the core. If $\beta = 0$, this value represents the RMS width;
- a_l and a_r - The starting points of the left and right tails;
- n_l and n_r - The shape parameters of the left and right tails.

While λ and ζ are set at zero, the rest of the parameters are left free. The starting value of the mean is chosen to be the Σ^+ mass value, taken from the PDG. [12] and equal to 1189.37 MeV/c^2. As in Sec. 4.2, there is no need to include a function to describe the background in the MC after the chosen selection.

The fit to the full Run 2 MC sample is shown in Fig. 5.2. The number of MC signal candidates is estimated to be $N^{MC}_{\Sigma^+\to p\mu^+\mu^-} = 34288 \pm 345$ with a resolution equal to $\sigma^{MC}_{\Sigma^+\to p\mu^+\mu^-} = 3.41 \pm 0.02$ MeV/c^2.

When fitting the data sample, a modified version of the Argus function [130] is added to the *p.d.f.* to describe the small residual background. This function is expressed as follows:

$$f\left(x;m_0,p,c\right) = x\left(\frac{x^2}{m_0^2}-1\right)^p e^{c\frac{x}{m_0}}, \tag{5.3}$$

Here, m_0 is the threshold mass value and p and c define the shape of tails. In the fit, m_0 is set to the sum of the proton and muons mass values, which is equal

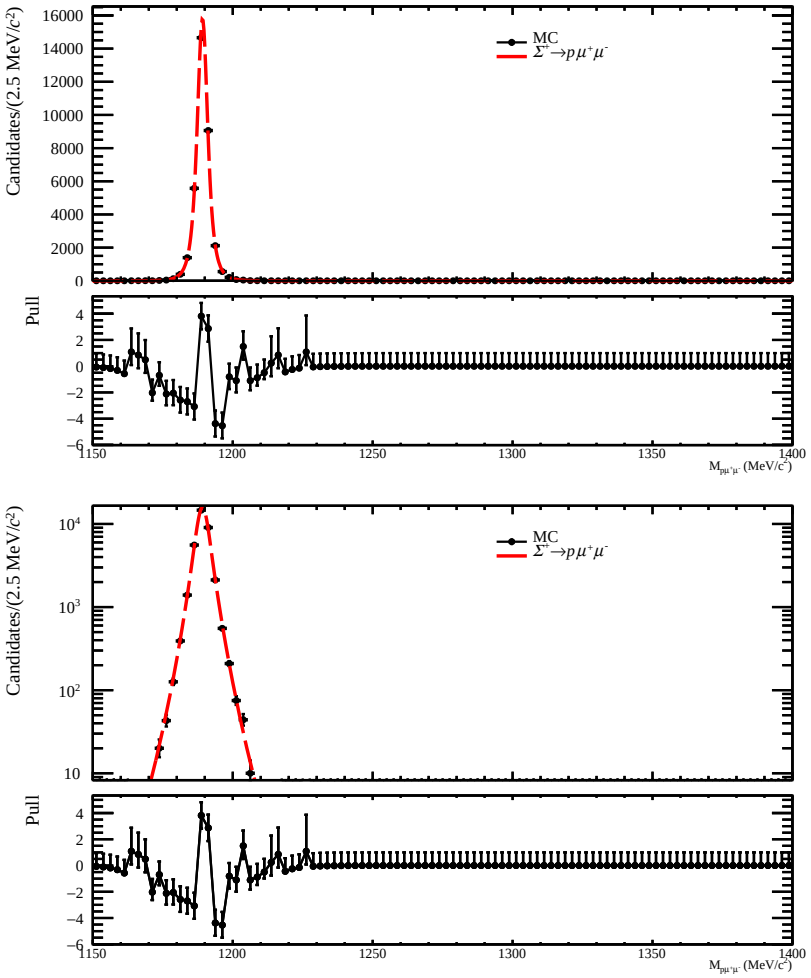

Figure 5.2. Distribution of the $m_{p\mu^+\mu^-}$ invariant mass in MC after the final selection and superimposed with the fit (red). Only the Hypatia function is used as there is no need to include a function to describe the background component after the final selection. The same distribution is reported in linear (top) and logarithmic scale (bottom). The pull distribution is also illustrated in the bottom panel.

to 1149.589 MeV/c^2, while p and c are left free. The parameters of the Hypatia function, on the other hand, are taken from the MC fit and fixed, with the exception of μ and σ. For these values, the MC fit parameters are used as starting points.

The fit to the full Run 2 data sample is shown in Fig. 5.3. The number of signal candidates in data is estimated to be $N^{Data}_{\Sigma^+\to p\mu^+\mu^-} = 273 \pm 18$ with a resolution equal to $\sigma^{Data}_{\Sigma^+\to p\mu^+\mu^-} = 3.91 \pm 0.13$ MeV/c^2. In the signal region, the total number of background candidates is measured to be $N^{Data}_{bkg} = 43 \pm 3$.

The measured final yield is ~ 3 times larger than the one reported in Sec. 4.2. Furthermore, a simple significance evaluation gives more than 10σ. Therefore, the result is confirmed to be the first clear observation of the $\Sigma^+ \to p\mu^+\mu^-$ decay and it will be used for the branching fraction measurement in Ch. 8.

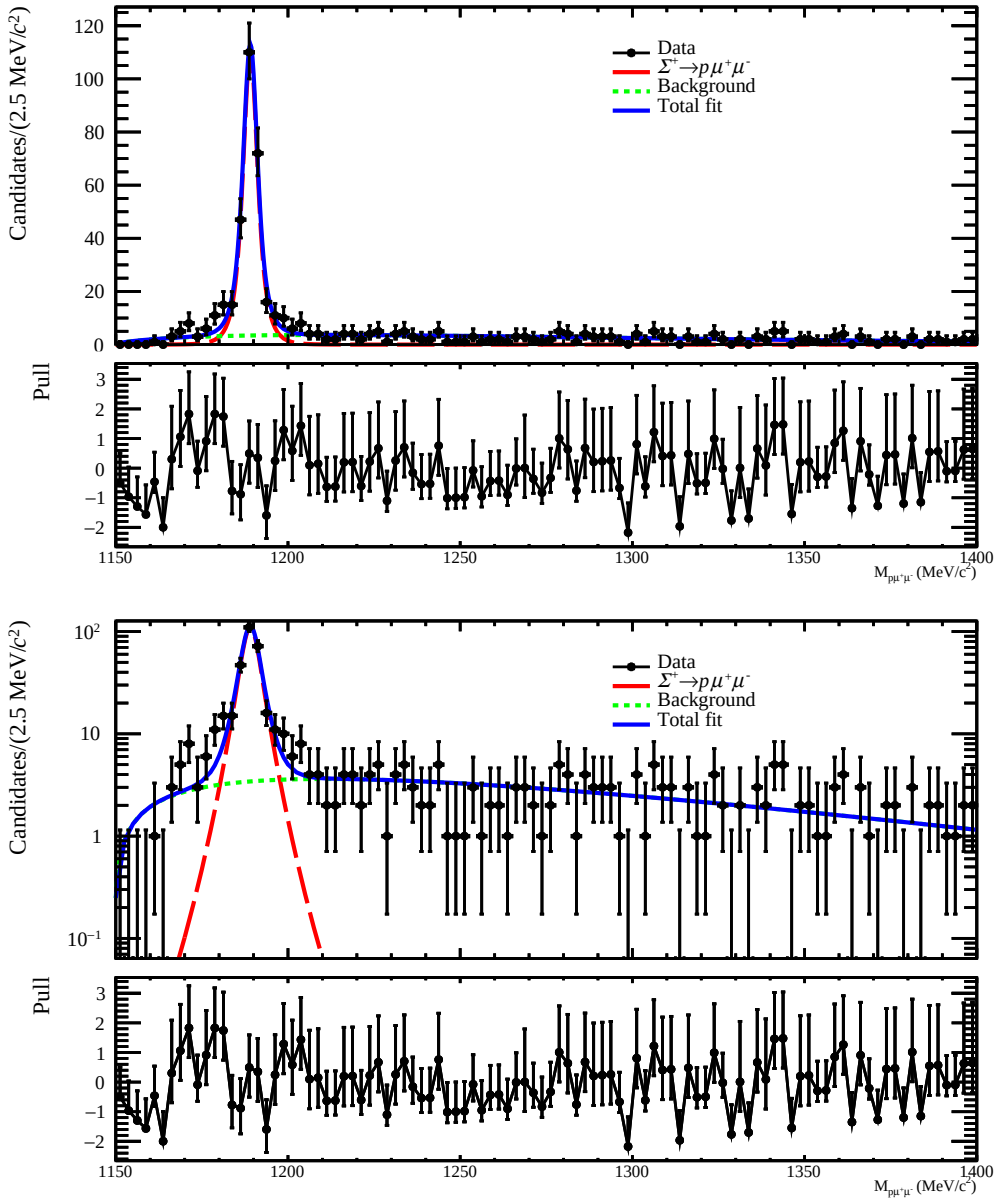

Figure 5.3. Distribution of the $m_{p\mu^+\mu^-}$ invariant mass in data after the final selection and superimposed with the fit (blue). The signal component is parametrised by an Hypatia function (red) while the background is described by a modified Argus function (green). The same distribution is reported in linear (top) and logarithmic scale (bottom). The pull distribution is also illustrated in the bottom panel.

Chapter 6

Normalisation

In order to measure the $\Sigma^+ \to p\mu^+\mu^-$ branching fraction, a normalisation mode is required. In this analysis, the normalisation is performed with the $\Sigma^+ \to p\pi^0$ decay. Following this, the signal branching fraction is estimated as

$$\begin{aligned} \mathcal{B}\left(\Sigma^+ \to p\mu^+\mu^-\right) &= \frac{\varepsilon_{\Sigma^+\to p\pi^0}}{\varepsilon_{\Sigma^+\to p\mu^+\mu^-}} \frac{\mathcal{B}\left(\Sigma^+ \to p\pi^0\right)}{N_{\Sigma^+\to p\pi^0}} N_{\Sigma^+\to p\mu^+\mu^-} \\ &= \alpha \cdot N_{\Sigma^+\to p\mu^+\mu^-}, \end{aligned} \tag{6.1}$$

where α denotes the single event sensitivity, ε and N represent the overall efficiency and final yield of the decay modes and $\mathcal{B}\left(\Sigma^+ \to p\pi^0\right) = (51.57 \pm 0.30)\,\%$ is the $\Sigma^+ \to p\pi^0$ branching fraction, taken from the PDG [12].

The total efficiency is evaluated as

$$\varepsilon = \varepsilon_{\text{Gen}} \cdot \varepsilon_{\text{Filter|Gen}} \cdot \varepsilon_{\text{Presel|Filter}} \cdot \varepsilon_{\text{FullSel|Presel}} \cdot \varepsilon_{\text{Trig|FullSel}}, \tag{6.2}$$

where

- ε_{Gen} is the generation efficiency, also known as the LHCb acceptance, including the applied selection in MC at generation level;
- $\varepsilon_{\text{Filter|Gen}}$ is the filtering efficiency, including the stripping selection;
- $\varepsilon_{\text{Presel|Filter}}$ is the preselection efficiency, including the PID requirements;
- $\varepsilon_{\text{FullSel|Presel}}$ is the efficiency of the final selection;
- $\varepsilon_{\text{Trig|FullSel}}$ is the trigger efficiency, evaluated after applying the full selection.

In this chapter, following a brief presentation on the chosen normalisation decay mode, all the efficiencies listed above are discussed. Furthermore, the fit strategy to the $\Sigma^+ \to p\pi^0$ invariant mass distribution is illustrated and the normalisation final yield $N_{\Sigma^+\to p\pi^0}$ is reported.

6.1 The $\Sigma^+ \to p\pi^0$ decay

Normalizing the $\Sigma^+ \to p\mu^+\mu^-$ candidates to compute the branching fraction is far from trivial as no fully charged final states of the Σ^+ are available. As a matter of fact, only the $\Sigma^+ \to p\gamma$ and $\Sigma^+ \to p\pi^0$ decays have reconstructible final states at LHCb. $\Sigma^+ \to p\pi^0$ candidates have the advantage of being reconstructed as a charged track, identified as a proton, plus a $\pi^0 \to \gamma\gamma$ decay with two photon clusters in the electromagnetic calorimeter [124]. Furthermore, the $\Sigma^+ \to p\pi^0$ decay has the highest branching fraction value among all the Σ^+ decay modes [12], meaning that a clean signal and a high yield are expected in data. For these reasons, the $\Sigma^+ \to p\pi^0$ decay is chosen to be the normalisation channel of the analysis[1].

6.1.1 Stripping and offline selection

The stripping criteria for the $\Sigma^+ \to p\pi^0$ decay are similar to the ones applied on the signal, reported in Tab. 3.7. Given the reconstruction of the decay being made only with one charged track and two photons, the main source of background is expected to be combinatorial. Therefore, tighter requirements with respect to the signal are applied on the transverse momenta of the final state particles. The normalisation stripping requirements are listed in Tab. 6.1.

Particle	Stripping cut
p	$ProbNNp > 0.6$, $p_T > 1000$ MeV/c
π^0	$p_T > 700$ MeV/c, $\pi^0 CL > 0.1$
$p\pi^0$	$\lvert m_{p\pi^0} - m_{\Sigma^+}\rvert < 150$ MeV/c^2
	$p_T > 500$ MeV/c
	$DIRA > 0.9$
	$IP\chi^2 < 36$
	$Vtx\chi^2 < 36$
	$\tau > 6$ ps

Table 6.1. Stripping requirements applied on the $\Sigma^+ \to p\pi^0$ decay.

To further reduce the combinatorial background, additional offline requirements on the proton and the neutral pion PID variables are applied. These criteria have been optimised to maximize the signal significance in data and are set at $ProbNNp > 0.9$ and $\pi^0 CL > 0.3$. The data and MC distributions of the proton and neutral pion PID variables are reported in Fig. 6.1 while the distribution of the normalisation invariant mass after applying the stripping and offline requirements is shown in Fig. 6.2 for both data (left) and MC (right) samples

Given the impossibility of reconstructing the Σ^+ decay vertex solely with the proton track, the momentum direction of the π^0 is calculated assuming its generation at the production vertex of the Σ^+ particle. This assumption deteriorates the resolution of the invariant mass distribution.

[1]The simulation takes into account all the possible π^0 decays and, therefore, there is no need to add the branching fraction of the $\pi^0 \to \gamma\gamma$ decay in Eq. 6.1.

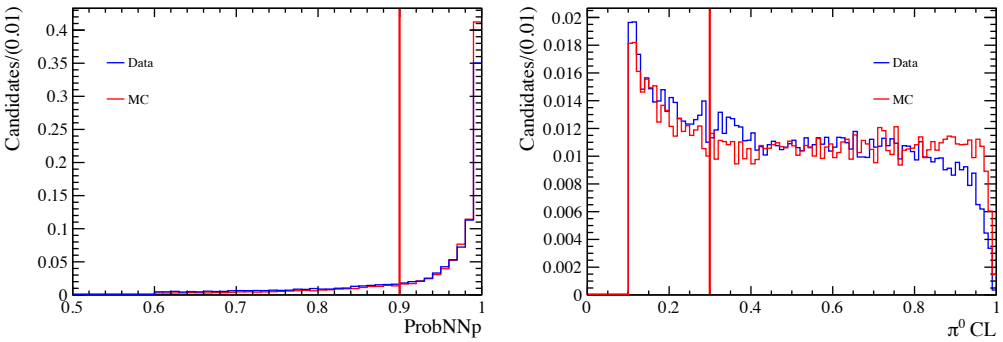

Figure 6.1. Data and MC distributions of the $ProbNNp$ (left) and $\pi^0 CL$ (right) variables. The chosen requirement is shown as a vertical red line in each plot.

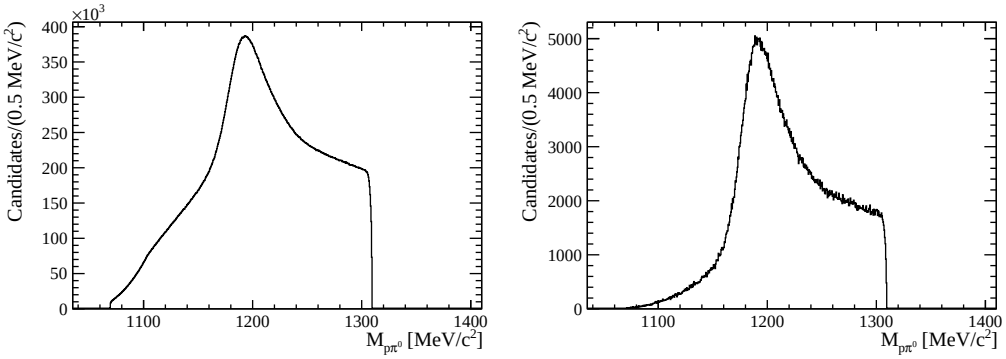

Figure 6.2. Distribution of the $m_{p\pi^0}$ invariant mass in data (left) and MC (right) after applying the stripping and offline requirements.

6.1.2 Correction to the invariant mass

A limited resolution on the $m_{\gamma\gamma}$ invariant mass becomes evident in data after applying the stripping selection, as shown in Fig. 6.3 (left). This is mainly due to the poor resolution of the two energy deposits of the photons in the electromagnetic calorimeter. The same distribution in MC is reported in Fig. 6.3 (right).

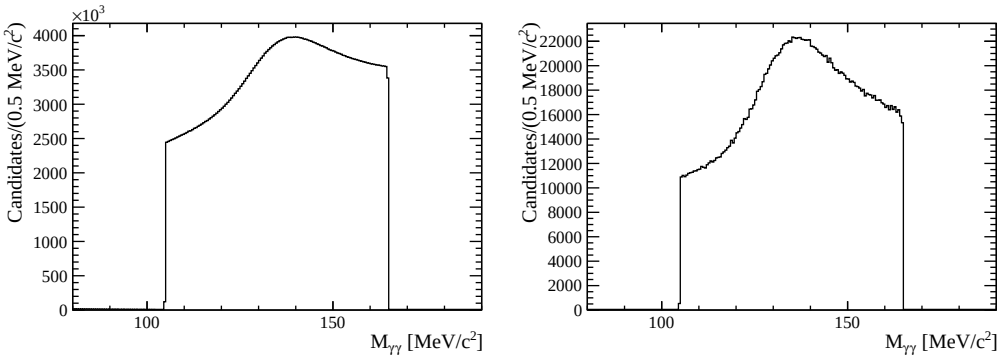

Figure 6.3. Distribution of the $m_{\gamma\gamma}$ invariant mass in data (left) and MC (right) after applying the stripping requirements.

To mitigate this effect, a correction is applied to the $m_{p\gamma\gamma}$[2] invariant mass. This correction involves adjusting the $\Sigma^+ \to p\pi^0$ reconstructed mass with the true mass value of the neutral pion, provided by the PDG [12], as follows:

$$M_{\Sigma}^{\text{Corr}} = m_{p\gamma\gamma} - m_{\gamma\gamma} + m_{\pi^0}^{PDG}, \tag{6.3}$$

where $m_{\gamma\gamma}$ is the reconstructed mass of the two photons and $m_{\pi^0}^{PDG} = 139.57$ Mev/c^2 is the mass value of the neutral pion from the PDG.

The corrected $\Sigma^+ \to p\pi^0$ invariant mass distribution after applying the stripping and offline requirements is shown in Fig. 6.4 for both data (left) and MC (right) samples. The normalisation mass peak becomes more evident as the resolution of the distribution greatly improves.

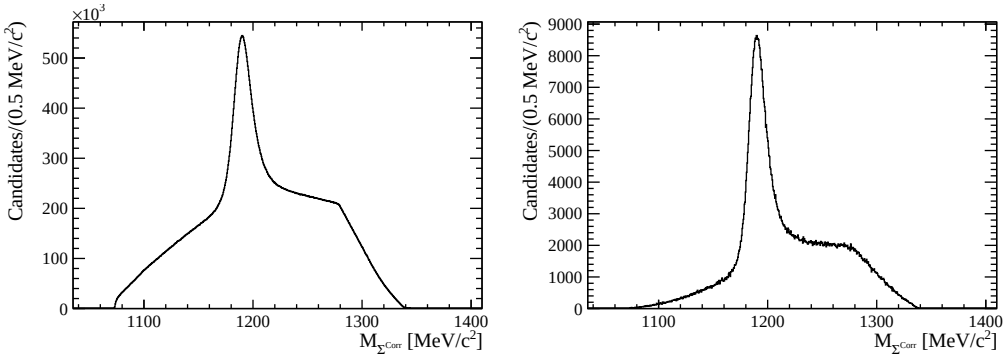

Figure 6.4. Corrected distribution of the $m_{p\pi^0}$ invariant mass in data (left) and MC (right) after applying the stripping and offline requirements.

6.2 Generation efficiency

The generation efficiency ε_{Gen} is estimated on MC for both signal and normalisation decay modes as

$$\varepsilon_{\text{Gen}} = \frac{N_{\text{Accepted}}}{N_{\text{Generated}}}, \tag{6.4}$$

where $N_{\text{Generated}}$ represents the generated number of decays in simulation and N_{Accepted} the number of generated decays passing the generation requests. These requirements are listed in Tab. 3.5 for both signal and normalisation modes.

The signal and normalisation generation efficiencies are listed by year and magnet polarity in Tab. 6.2. Absolute uncertainties are also reported.

6.3 Filtering efficiency

The filtering efficiency $\varepsilon_{\text{Filter|Gen}}$ is evaluated on MC for both signal and normalisation channels as

[2]The notations $m_{p\gamma\gamma}$ and $m_{p\pi^0}$ are used to denote the same reconstructed mass in this analysis.

Year	Magnet	$\varepsilon_{\text{Gen}}(\Sigma^+ \to p\mu^+\mu^-)$	$\varepsilon_{\text{Gen}}(\Sigma^+ \to p\pi^0)$
2016	MagDown	0.2158 ± 0.0004	0.04855 ± 0.00013
	MagUp	0.2167 ± 0.0004	0.04868 ± 0.00013
	MagAll	0.2162 ± 0.0003	0.04862 ± 0.00009
2017	MagDown	0.2154 ± 0.0005	0.04836 ± 0.00013
	MagUp	0.2149 ± 0.0005	0.04842 ± 0.00013
	MagAll	0.2152 ± 0.0003	0.04839 ± 0.00009
2018	MagDown	0.2158 ± 0.0005	0.04854 ± 0.00013
	MagUp	0.2161 ± 0.0005	0.04846 ± 0.00013
	MagAll	0.2160 ± 0.0003	0.04850 ± 0.00009
Run 2	MagDown	0.2157 ± 0.0003	0.04848 ± 0.00008
	MagUp	0.2159 ± 0.0003	0.04852 ± 0.00008
	MagAll	0.2158 ± 0.0002	0.04850 ± 0.00005

Table 6.2. Generation efficiencies for both signal and normalisation modes listed by year and magnet polarity.

$$\varepsilon_{\text{Filter|Gen}} = \frac{N_{\text{Filtered}}}{N_{\text{Accepted}}}, \tag{6.5}$$

where N_{Accepted} is the number of generated decays passing the generation requests and N_{Filtered} is the number of decays passing the stripping requirements. The stripping selections for both signal and normalisation modes are summarised in Tab. 3.7 and Tab. 6.1, respectively.

The filtering efficiencies for both signal and normalisation modes are listed by year and magnet polarity in Tab. 6.3. Absolute uncertainties are also reported.

Year	Magnet	$\varepsilon_{\text{Filter\|Gen}}(\Sigma^+ \to p\mu^+\mu^-)$	$\varepsilon_{\text{Filter\|Gen}}(\Sigma^+ \to p\pi^0)$
2016	MagDown	0.01134 ± 0.00003	$(5.585 \pm 0.011) \times 10^{-3}$
	MagUp	0.01130 ± 0.00003	$(5.637 \pm 0.011) \times 10^{-3}$
	MagAll	0.01132 ± 0.00002	$(5.611 \pm 0.008) \times 10^{-3}$
2017	MagDown	0.01166 ± 0.00003	$(5.383 \pm 0.011) \times 10^{-3}$
	MagUp	0.01165 ± 0.00003	$(5.739 \pm 0.011) \times 10^{-3}$
	MagAll	0.01166 ± 0.00002	$(5.561 \pm 0.008) \times 10^{-3}$
2018	MagDown	0.01164 ± 0.00003	$(5.097 \pm 0.010) \times 10^{-3}$
	MagUp	0.01156 ± 0.00003	$(5.247 \pm 0.010) \times 10^{-3}$
	MagAll	0.01160 ± 0.00002	$(5.172 \pm 0.007) \times 10^{-3}$
Run 2	MagDown	0.01154 ± 0.00002	$(5.355 \pm 0.006) \times 10^{-3}$
	MagUp	0.01151 ± 0.00002	$(5.541 \pm 0.006) \times 10^{-3}$
	MagAll	0.01152 ± 0.00001	$(5.448 \pm 0.004) \times 10^{-3}$

Table 6.3. Filtering efficiencies for both signal and normalisation modes listed by year and magnet polarity.

6.4 Selection efficiencies

The preselection efficiency $\varepsilon_{\text{Presel|Filter}}$ is estimated on MC for both signal and normalisation modes as

$$\varepsilon_{\text{Presel|Filter}} = \frac{N_{\text{Preselected}}}{N_{\text{Filtered}}}, \tag{6.6}$$

where N_{Filtered} is the number of decays filtered by the stripping requirements and $N_{\text{Preselected}}$ is the number of decays passing the PID criteria. In the signal MC samples, $N_{\text{Preselected}}$ is easily extracted by counting the remaining candidates after the PID requirements. This is not the case for the normalisation channel as a large combinatorial background component is present in the MC. Therefore, the normalisation $N_{\text{Preselected}}$ is estimated by fitting the corrected invariant mass distribution. More details on this fit strategy will be illustrated in Sec. 6.6.

The preselection efficiencies for both signal and normalisation modes are listed by year and magnet polarity in Tab. 6.4. Absolute uncertainties are also reported.

Year	Magnet	$\varepsilon_{\text{Presel\|Filter}}(\Sigma^+ \to p\mu^+\mu^-)$	$\varepsilon_{\text{Presel\|Filter}}(\Sigma^+ \to p\pi^0)$
2016	MagDown	0.7342 ± 0.0021	0.0849 ± 0.0006
	MagUp	0.7340 ± 0.0010	0.0838 ± 0.0006
	MagAll	0.7341 ± 0.0012	0.0843 ± 0.0004
2017	MagDown	0.7108 ± 0.0010	0.0847 ± 0.0006
	MagUp	0.7150 ± 0.0021	0.0840 ± 0.0006
	MagAll	0.7129 ± 0.0012	0.0843 ± 0.0004
2018	MagDown	0.7082 ± 0.0010	0.0850 ± 0.0006
	MagUp	0.7144 ± 0.0021	0.0841 ± 0.0006
	MagAll	0.7112 ± 0.0012	0.0846 ± 0.0004
Run 2	MagDown	0.7176 ± 0.0008	0.0849 ± 0.0004
	MagUp	0.7211 ± 0.0011	0.0840 ± 0.0004
	MagAll	0.7194 ± 0.0007	0.0844 ± 0.0003

Table 6.4. Preselection efficiencies for both signal and normalisation modes listed by year and magnet polarity.

No additional requirements are applied to the normalisation channel and, therefore, its $\varepsilon_{\text{Presel|Filter}}$ represents the efficiency of the full selection. This is not the case for the signal as a BDT requirement is applied. Given this, the full selection efficiency for the signal is estimated on MC as

$$\varepsilon_{\text{FullSel|Presel}} = \frac{N_{\text{Selected}}}{N_{\text{Preselected}}}, \tag{6.7}$$

where N_{Selected} denotes the number of signal decays passing the BDT request.

The signal full selection efficiencies are listed by year and magnet polarity in Tab. 6.5. Absolute uncertainties are also reported.

Year	Magnet	$\varepsilon_{\text{FullSel\|Presel}}(\Sigma^+ \to p\mu^+\mu^-)$
2016	MagDown	0.1239 ± 0.0008
	MagUp	0.1276 ± 0.0009
	MagAll	0.1257 ± 0.0006
2017	MagDown	0.1298 ± 0.0009
	MagUp	0.1305 ± 0.0009
	MagAll	0.1302 ± 0.0006
2018	MagDown	0.1302 ± 0.0009
	MagUp	0.1269 ± 0.0013
	MagAll	0.1286 ± 0.0008
Run 2	MagDown	0.1279 ± 0.0005
	MagUp	0.1283 ± 0.0006
	MagAll	0.1281 ± 0.0004

Table 6.5. $\Sigma^+ \to p\mu^+\mu^-$ full selection efficiencies listed by year and magnet polarity.

6.5 Trigger efficiency

The trigger efficiency $\varepsilon_{\text{Trig|Fullsel}}$ is evaluated as

$$\varepsilon_{\text{Trig|Fullsel}} = \varepsilon_{\text{L0}} \cdot \varepsilon_{\text{HLT1}} \cdot \varepsilon_{\text{HLT2}}, \tag{6.8}$$

depending on the efficiency at each level of the LHCb trigger system. The trigger strategies for both signal and normalisation modes are reported in Sec. 3.2.1.

MC samples are used to estimate the signal trigger efficiencies, as the chosen trigger strategy is well reproduced in simulation given that only charged particles are present in the final state. These are evaluated after applying the full selection requirements by counting the remaining candidates after each trigger level. The signal trigger efficiencies are listed by year and magnet polarity in Tab. 6.6. Absolute uncertainties are also reported. As expected and mentioned in Sec. 3.2, the Run 2 trigger efficiency is larger than the one of the previous analysis by almost a factor of ten. The Run 1 trigger efficiency is reported in Tab. 4.1.

The trigger efficiencies for the normalisation channel are estimated in different ways, depending on the level. The L0 efficiency is evaluated on data after the full selection with the TISTOS method [122] as

$$\varepsilon_{\text{L0}} = \frac{N_{\text{TISTOS}}}{N_{\text{TIS}}}, \tag{6.9}$$

where N_{TISTOS} is the number of normalisation candidates after both `L0HadronDecision_TIS` and `L0HadronDecision_TOS` lines are requested and N_{TIS} is the number of normalisation candidates after only the TIS line is applied.

The HLT1 efficiency is evaluated on MC after the full selection as

$$\varepsilon_{\text{HLT1}} = \frac{N_{\text{HLT1|FullSel}}}{N_{\text{FullSel!HLT1}}}, \tag{6.10}$$

$\Sigma^+ \to p\mu^+\mu^-$					
Year	Magnet	ε_{L0}	$\varepsilon_{\text{HLT1}}$	$\varepsilon_{\text{HLT2}}$	$\varepsilon_{\text{Trig\|FullSel}}$
2016	MagDown	0.2421 ± 0.0021	0.5878 ± 0.0049	0.9656 ± 0.0024	0.1374 ± 0.0017
	MagUp	0.2432 ± 0.0021	0.5964 ± 0.0049	0.9607 ± 0.0025	0.1394 ± 0.0017
	MagAll	0.2427 ± 0.0015	0.5921 ± 0.0034	0.9631 ± 0.0017	0.1384 ± 0.0012
2017	MagDown	0.2718 ± 0.0022	0.5984 ± 0.0046	0.9669 ± 0.0022	0.1573 ± 0.0018
	MagUp	0.2700 ± 0.0022	0.5900 ± 0.0047	0.9644 ± 0.0023	0.1536 ± 0.0018
	MagAll	0.2709 ± 0.0016	0.5942 ± 0.0033	0.9657 ± 0.0016	0.1554 ± 0.0013
2018	MagDown	0.2058 ± 0.0020	0.6064 ± 0.0053	0.9623 ± 0.0026	0.1201 ± 0.0016
	MagUp	0.2077 ± 0.0020	0.5924 ± 0.0054	0.9636 ± 0.0027	0.1185 ± 0.0016
	MagAll	0.2067 ± 0.0014	0.5995 ± 0.0038	0.9629 ± 0.0019	0.1193 ± 0.0011
Run 2	MagDown	0.2398 ± 0.0012	0.5971 ± 0.0028	0.9651 ± 0.0014	0.1382 ± 0.0010
	MagUp	0.2405 ± 0.0012	0.5929 ± 0.0029	0.9629 ± 0.0014	0.1373 ± 0.0010
	MagAll	0.2402 ± 0.0010	0.5950 ± 0.0020	0.9640 ± 0.0010	0.1378 ± 0.0007

Table 6.6. Signal trigger efficiencies listed by year and magnet polarity.

where $N_{\text{HLT1|FullSel}}$ and $N_{\text{FullSel!HLT1}}$ denotes the number of normalisation candidates in a sub-sample with HLT1 request and in a sub-sample without the HLT1 request.

At HLT2, the trigger request is a minimum bias line that takes as input all the events out of HLT1 and has a fixed prescale of 0.0001 in the full Run 2 data sample, which is taken as the HLT2 efficiency. No uncertainty is associated.

The normalisation trigger efficiencies are listed by year and magnet polarity in Tab. 6.7. Absolute uncertainties are also reported.

$\Sigma^+ \to p\pi^0$					
Year	Magnet	ε_{L0}	$\varepsilon_{\text{HLT1}}$	$\varepsilon_{\text{HLT2}}$	$\varepsilon_{\text{Trig\|FullSel}}$
2016	MagDown	0.0409 ± 0.0031	0.8157 ± 0.0088	0.0001	$(3.3 \pm 0.3) \times 10^{-6}$
	MagUp	0.0473 ± 0.0036	0.8423 ± 0.0085	0.0001	$(4.0 \pm 0.3) \times 10^{-6}$
	MagAll	0.0439 ± 0.0023	0.8283 ± 0.0061	0.0001	$(3.6 \pm 0.2) \times 10^{-6}$
2017	MagDown	0.0429 ± 0.0031	0.7941 ± 0.0081	0.0001	$(3.4 \pm 0.2) \times 10^{-6}$
	MagUp	0.0368 ± 0.0028	0.8318 ± 0.0073	0.0001	$(3.1 \pm 0.2) \times 10^{-6}$
	MagAll	0.0399 ± 0.0021	0.8130 ± 0.0055	0.0001	$(3.3 \pm 0.2) \times 10^{-6}$
2018	MagDown	0.0369 ± 0.0029	0.8161 ± 0.0092	0.0001	$(3.0 \pm 0.3) \times 10^{-6}$
	MagUp	0.0343 ± 0.0027	0.8321 ± 0.0088	0.0001	$(2.9 \pm 0.2) \times 10^{-6}$
	MagAll	0.0356 ± 0.0020	0.8245 ± 0.0064	0.0001	$(2.9 \pm 0.2) \times 10^{-6}$
Run 2	MagDown	0.0402 ± 0.0017	0.8073 ± 0.0050	0.0001	$(3.2 \pm 0.1) \times 10^{-6}$
	MagUp	0.0389 ± 0.0017	0.8349 ± 0.0047	0.0001	$(3.2 \pm 0.1) \times 10^{-6}$
	MagAll	0.0396 ± 0.0012	0.8211 ± 0.0034	0.0001	$(3.2 \pm 0.1) \times 10^{-6}$

Table 6.7. Normalisation trigger efficiencies listed by year and magnet polarity.

6.6 Normalisation final yield and summary

The distribution of the normalisation invariant mass after applying the selection requirements and the trigger strategy is reported in Fig. 6.5 for both data (left) and MC (right) samples.

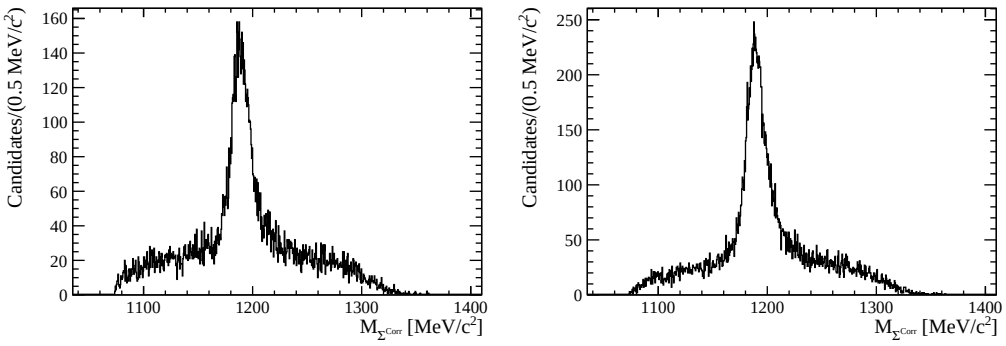

Figure 6.5. Corrected distribution of the $m_{p\pi^0}$ invariant mass in data (left) and MC (right) after applying the final selection.

The final yield is estimated with an extended maximum likelihood fit. The fit is performed in the range $1110 < M_{\Sigma}^{\mathrm{Corr}} < 1270$ MeV/c^2. This range is chosen to remove part of the remaining combinatorial background. The signal component is parametrized by a double-sided Crystal-Ball function. This function, which is a combination of a Gaussian and two exponential tails on both sides of the core, is defined as

$$\mathrm{C}\left(x;\mu,\sigma,\alpha_L,n_L,\alpha_R,n_R\right) == \begin{cases} A_L \cdot \left(B_L - \frac{x-m_0}{\sigma_L}\right)^{-n_L}, & \text{for } \frac{x-m_0}{\sigma_L} < -\alpha_L \\ \exp\left(-\frac{1}{2}\cdot\left[\frac{x-m_0}{\sigma_L}\right]^2\right), & \text{for } \frac{x-m_0}{\sigma_L} \leq 0 \\ \exp\left(-\frac{1}{2}\cdot\left[\frac{x-m_0}{\sigma_R}\right]^2\right), & \text{for } \frac{x-m_0}{\sigma_R} \leq \alpha_R \\ A_R \cdot \left(B_R + \frac{x-m_0}{\sigma_R}\right)^{-n_R}, & \text{otherwise,} \end{cases} \tag{6.11}$$

where

$$\begin{aligned} A_i &= \left(\frac{n_i}{|\alpha_i|}\right)^{n_i} \cdot \exp\left(-\frac{|\alpha_i|^2}{2}\right) \\ B_i &= \frac{n_i}{|\alpha_i|} - |\alpha_i| \end{aligned} \tag{6.12}$$

In this function, the parameters are:

- μ - The mean value of the Gaussian component;
- σ_L and σ_R - The width of both sides of the Gaussian component;
- α_L and α_R - The transition points to the exponential tails on the left and right side of the Gaussian core;
- n_L and n_R - The exponents of the exponential tails.

The background component is described by Chebyshev second degree polynomial function of the first kind [131].

The fit is performed first on the MC sample. Furthermore, the parameters of the tails from the signal MC fit are used as fixed values for the data fit. The data parameters for the background function are left free.

The fit to the full Run 2 sample is shown in Fig. 6.6 for both data (top) and MC (bottom). The normalisation final yields $N_{\Sigma^+\to p\pi^0}$ are listed by year and magnet polarity in Tab. 6.8.

Year	Magnet	$N_{\Sigma^+\to p\pi^0}$
2016	MagDown	1019 ± 42
	MagUp	935 ± 40
	MagAll	1955 ± 58
2017	MagDown	1161 ± 45
	MagUp	1021 ± 44
	MagAll	2182 ± 63
2018	MagDown	970 ± 42
	MagUp	1027 ± 44
	MagAll	1996 ± 60
Run 2	MagDown	3148 ± 75
	MagUp	2984 ± 73
	MagAll	6132 ± 105

Table 6.8. $\Sigma^+ \to p\pi^0$ final yields listed by year and magnet polarity.

The overall efficiencies for both signal and normalisation decay modes, estimated as in Eq. 6.2, are summarised in Tab 6.9, listed by year and magnet polarity. Before evaluating the $\Sigma^+ \to p\mu^+\mu^-$ branching fraction, corrections to these efficiencies need to be estimated. These corrections are presented in Ch. 7.

Year	Magnet	$\varepsilon(\Sigma^+ \to p\mu^+\mu^-)$	$\varepsilon(\Sigma^+ \to p\pi^0)$
2016	MagDown	$(3.06 \pm 0.04) \times 10^{-5}$	$(7.6 \pm 0.7) \times 10^{-11}$
	MagUp	$(3.20 \pm 0.05) \times 10^{-5}$	$(9.2 \pm 0.7) \times 10^{-11}$
	MagAll	$(3.13 \pm 0.03) \times 10^{-5}$	$(8.3 \pm 0.5) \times 10^{-11}$
2017	MagDown	$(3.64 \pm 0.05) \times 10^{-5}$	$(7.5 \pm 0.4) \times 10^{-11}$
	MagUp	$(3.59 \pm 0.05) \times 10^{-5}$	$(7.2 \pm 0.5) \times 10^{-11}$
	MagAll	$(3.62 \pm 0.04) \times 10^{-5}$	$(7.5 \pm 0.5) \times 10^{-11}$
2018	MagDown	$(2.78 \pm 0.04) \times 10^{-5}$	$(6.3 \pm 0.6) \times 10^{-11}$
	MagUp	$(2.69 \pm 0.05) \times 10^{-5}$	$(6.2 \pm 0.4) \times 10^{-11}$
	MagAll	$(2.73 \pm 0.03) \times 10^{-5}$	$(6.2 \pm 0.4) \times 10^{-11}$
Run 2	MagDown	$(3.16 \pm 0.03) \times 10^{-5}$	$(7.1 \pm 0.2) \times 10^{-11}$
	MagUp	$(3.16 \pm 0.03) \times 10^{-5}$	$(7.0 \pm 0.2) \times 10^{-11}$
	MagAll	$(3.16 \pm 0.02) \times 10^{-5}$	$(7.1 \pm 0.2) \times 10^{-11}$

Table 6.9. Total efficiencies for both signal and normalisation modes listed by year and magnet polarity.

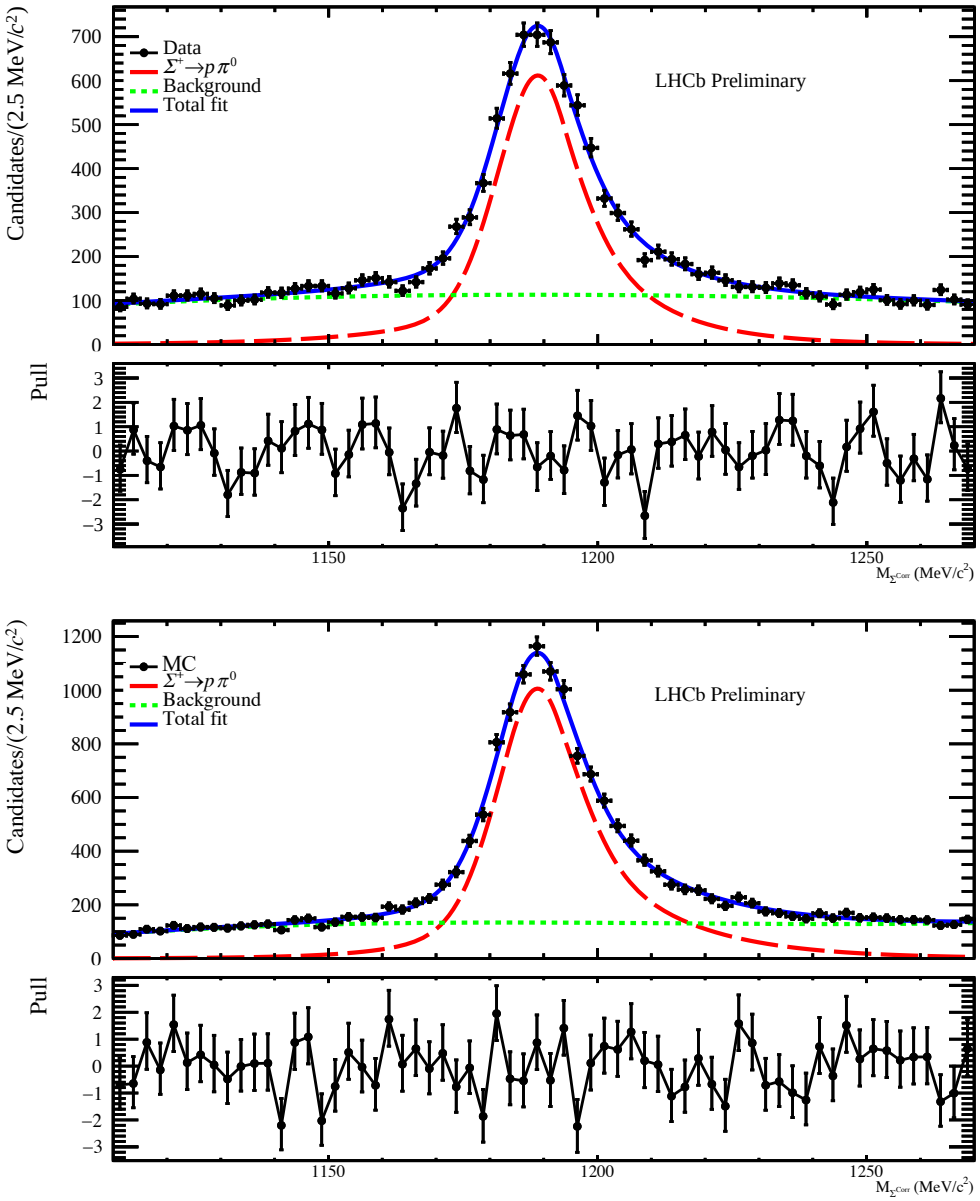

Figure 6.6. Distribution of the $M_{\Sigma}^{\mathrm{Corr}}$ corrected invariant mass in data (top) and MC (bottom) after the full selection and superimposed with the fit (blue). The signal component is parametrised by a double-sided Crystal-Ball function (red) while the background is described by a Chebyshev second degree polynomial function of the first kind (green). The pull distribution is also illustrated in the bottom panel.

Chapter 7

Systematic uncertainties

In this chapter, the systematic uncertainties related to the measured quantities of the analysis are presented. The systematic uncertainties can be divided into two groups:

- $\Sigma^+ \to p\mu^+\mu^-$ - Those affecting the observation of the decay, i.e. the signal final yield, including the systematics on the signal mass shape and the background knowledge;
- $\mathcal{B}\left(\Sigma^+ \to p\mu^+\mu^-\right)$ - Those affecting the normalisation and the branching fraction measurement, including the systematics on the corrections of the final efficiencies.

Most of them come from the latter group and do not affect the robustness of the observation.

In the next sections, only the most relevant systematics uncertainties are reported as the remaining ones are still under evaluation. The missing ones include the systematics affecting the tracking and the signal trigger efficiencies.

7.1 Correction to the phase space model

For branching fraction measurements, the evaluation of the absolute efficiencies integrated over multibody phase space requires *a priori* knowledge of the underlying physics model governing the decay, due to the non-uniformity in the detection efficiency across the phase space. The $\Sigma^+ \to p\mu^+\mu^-$ decay can, in principle, be described by both the relativistic [35] and heavy-baryon [36] χPT approaches. Both methods present four solutions for the branching fraction SM prediction, as explained in Sec. 1.6.3. Therefore, a correction, induced by the lack of knowledge on which model should be taken into account, must be applied.

A continuous model for the signal MC is first produced upon which corrections can subsequently be applied. The Kernel Density Estimate (KDE) algorithms [132] are used to handle the limited statistics available in the signal MC sample. A notorious issue with KDEs is their questionable performance along the event boundaries, which ideally should be hyper-rectangular. In three-body decays, this can be corrected using the square Dalitz plot,

$$
\begin{aligned}
m' &\equiv \frac{1}{\pi} \arccos\left(2\frac{m_{\mu^+\mu^-} - m^{\min}_{\mu^+\mu^-}}{m^{\max}_{\mu^+\mu^-} - m^{\min}_{\mu^+\mu^-}} - 1\right), \\
\theta' &\equiv \frac{1}{\pi}\theta_{\mu^+\mu^-},
\end{aligned}
\tag{7.1}
$$

where m' is an effective $m_{\mu^+\mu^-}$ mass scaled to lie within the closed interval $[0, 1]$, while θ' is the scaled helicity angle between the μ^- and the proton, estimated in the dimuon rest frame. The event distribution must represent an efficiency in the square Dalitz plot as it does in the phase space. Therefore, it must also be unweighted by the Jacobian of the coordinate transformation from the square Dalitz plot to physical phase space,

$$
|\det J| = 2\pi^2 pq m_{\mu^+\mu^-}(m^{\max}_{\mu^+\mu^-} - m^{\min}_{\mu^+\mu^-}) \sin(m'\pi)\sin(\theta'\pi), \tag{7.2}
$$

where p and q are the Σ^+ and μ^- momenta, respectively, evaluated in the dimuon rest frame. The resulting signal MC sample in the square Dalitz plot is shown in Fig. 7.1 (left), which is equivalent to an efficiency distribution in regular phase space. To determine the continuous efficiency model, these events are finally passed to a KDE software package `kalepy` [133]. The model is shown in Fig. 7.1 (right).

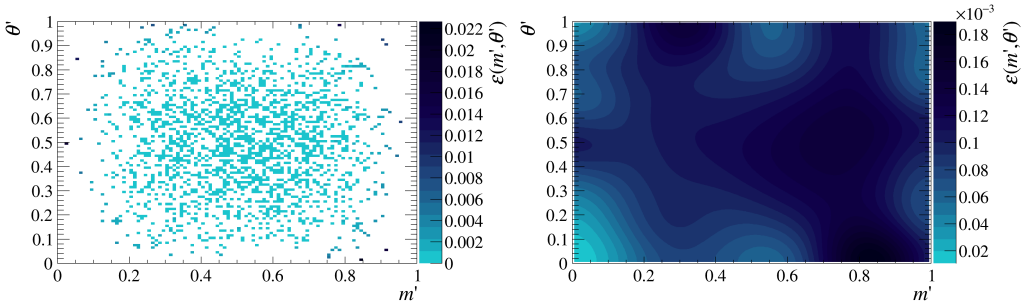

Figure 7.1. Distribution of signal MC sample in the square Dalitz plot (left) and the corresponding KDE model estimated from the same events (right).

At this point, it is possible to estimate a correction factor to the signal efficiency. This is achieved by evaluating the integrals of the KDE, subsequently weighted by each of the χPT approaches, relative to the raw KDE integral. The correction factor η_{Model} is equal to

$$
\eta_{\text{Model}} = 1.042 \pm 0.025, \tag{7.3}
$$

taken as the average value of the integrals with half the difference between the largest and smallest values as systematic uncertainty, due to the lack of knowledge of the correct physics model to obtain.

7.2 Correction for the $\Sigma^+ \to p\pi^0$ multiplicity at generation level

A large number of hyperon particles are produced in minimum bias events at LHCb. In particular, the probability of producing more than one Σ^+ particle in one pp

interaction is large. This is well observed for the $\Sigma^+ \to p\pi^0$ decay, which has a large branching fraction of about 50%. During the MC generation, the probability of having more than one candidate per event is enhanced by the fact that at least one Σ^+ particle is forced to decay in the normalisation mode.

To correctly evaluate the signal branching fraction, this effect must be taken into account, especially if it produces discrepancies in the decay multiplicity between unfiltered and filtered MC samples. The distribution of the generated $\Sigma^+ \to p\pi^0$ candidates per event from the MC filtered (red) and unfiltered (blue) samples is shown in Fig. 7.2.

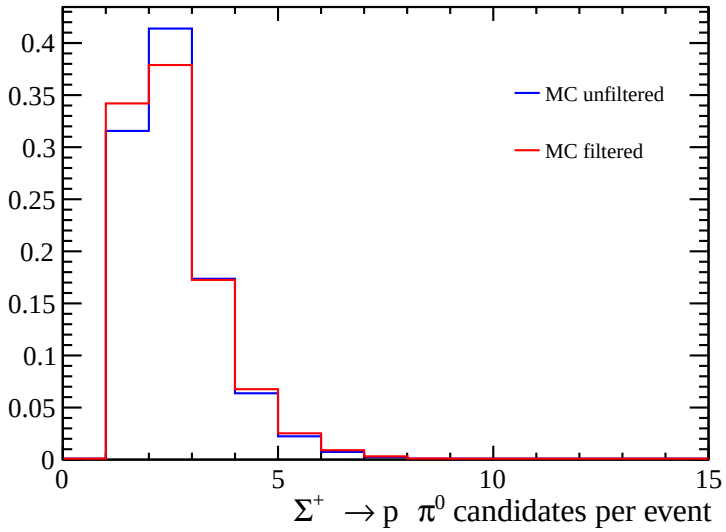

Figure 7.2. Distribution of the generated $\Sigma^+ \to p\pi^0$ candidates per event in simulation from the filtered (red) and unfiltered (blue) samples.

The stripping requirements affect the observed multiplicity, due to the presence of events with at least two candidates. To account for this discrepancy, a correction to the normalisation filtering efficiency $\eta_{\text{Filter|Gen}}$ is estimated as

$$\eta_{\text{Filter|Gen}} = \frac{\mathcal{M}_{\text{Unfiltered}}}{\mathcal{M}_{\text{Filtered}}}, \tag{7.4}$$

where $\mathcal{M}_{\text{Unfiltered}}$ and $\mathcal{M}_{\text{Filtered}}$ denote the normalisation multiplicity in the unfiltered and filtered samples. This correction is reported in Tab. 7.1, listed by year and magnet polarity. The related systematic uncertainty is evaluated as the propagation of the multiplicities absolute uncertainties.

7.3 Corrections to the proton and muons PID

Simulating the detectors dedicated to PID is a complex task. Reproducing their behaviours when particles pass through them requires knowledge of the kinematics, the occupancy of the detectors between events and their sensitivity to the beam condition variations. Additionally, experimental factors such as alignments, temperature, and gas pressure, which can alter the detector responses during the data

Year	Magnet	$\eta_{\text{Filter\|Gen}}(\Sigma^+ \to p\pi^0)$
2016	MagDown	1.0041 ± 0.0020
	MagUp	1.0023 ± 0.0020
	MagAll	1.0032 ± 0.0014
2017	MagDown	0.9973 ± 0.0020
	MagUp	0.9971 ± 0.0019
	MagAll	0.9972 ± 0.0014
2018	MagDown	0.9951 ± 0.0020
	MagUp	0.9967 ± 0.0019
	MagAll	0.9959 ± 0.0013
Run 2	MagDown	0.9988 ± 0.0011
	MagUp	0.9985 ± 0.0011
	MagAll	0.9986 ± 0.0008

Table 7.1. Corrections for the $\Sigma^+ \to p\pi^0$ multiplicity listed by year and magnet polarity.

acquisition, must also be considered. These problems have motivated the use of data-driven techniques to correct the efficiency of the PID variables used in various analyses.

The Particle IDentification Calibration (PIDCalib) package [134] is a set of LHCb tools which exploit data calibration samples to correct the PID efficiencies. This package produces the efficiencies of the calibration samples $\varepsilon_{\text{CalibSample}}$ in bins of momentum p, pseudorapidity η and number of hits in the SPD $N_{hits}(SPD)$. To obtain the same output, an analogue approach is employed for the evaluation of the efficiencies in the MC samples ε_{MC}. For each bin with at least 10 events in MC before the PID requirement and with $\varepsilon_{\text{CalibSample}} > 0$, a correction is defined as

$$\eta_{\text{bin}} = \frac{\varepsilon_{\text{CalibSample}}}{\varepsilon_{\text{MC}}}. \tag{7.5}$$

The average correction is calculated as

$$\eta_{\text{PID}} = \frac{\Sigma_{bin} N_{bin}(\text{MC, PID}) \cdot \eta_{\text{bin}}}{N_{tot}(MC)}, \tag{7.6}$$

where N_{bin}(MC, PID) represents the number of MC events in a specific bin, passing the PID requirement, and $N_{tot}(MC)$ is the total number of MC events.

Corrections to the PID variables of the $\Sigma^+ \to p\mu^+\mu^-$ decay are listed by year and magnet polarity in Tab. 7.2. To evaluate the systematic uncertainties on the corrections of the muon PIDs [1], an alternative binning scheme is introduced. The new values are compared with the ones calculated with the default binning scheme and the largest difference is taken as the systematic uncertainty. This is found to be 0.01 for each year and magnet polarity. For the proton PID, the momentum bins are kept unchanged while η and $N_{hits}(SPD)$ bins are rearranged to balance the bin-by-bin statistics. Its systematic uncertainty is found to be 0.05 for each year and magnet polarity.

[1] As both $\mu^\pm$ PID variables are used in the analysis, these corrections need to be applied twice.

Year	Magnet	η_{ProbNNp}	η_{ProbNNmu}
2016	MagDown	1.03 ± 0.05	1.03 ± 0.01
	MagUp	1.03 ± 0.05	1.03 ± 0.01
	MagAll	1.03 ± 0.05	1.03 ± 0.01
2017	MagDown	1.00 ± 0.05	1.03 ± 0.01
	MagUp	1.00 ± 0.05	1.04 ± 0.01
	MagAll	1.00 ± 0.05	1.04 ± 0.01
2018	MagDown	1.00 ± 0.05	1.03 ± 0.01
	MagUp	1.00 ± 0.05	1.04 ± 0.01
	MagAll	1.00 ± 0.05	1.04 ± 0.01
Run 2	MagDown	1.01 ± 0.05	1.03 ± 0.01
	MagUp	1.01 ± 0.05	1.04 ± 0.01
	MagAll	1.01 ± 0.05	1.04 ± 0.01

Table 7.2. Corrections to the signal proton and muon PID variables listed by year and magnet polarity.

The approach described above is also applied to the proton PID of the $\Sigma^+ \to p\pi^0$ decay mode. For each year and magnet polarity, the correction is found to be $\eta_{\text{ProbNNp}} = 1.02 \pm 0.04$.

7.4 Correction to the π^0 reconstruction efficiency

The reconstruction of photons and neutral pions has been studied at LHCb exploiting the $B \to J/\psi K^{*+}(\to K^+\pi^0(\to \gamma\gamma))$ and $B \to J/\psi K^+$ decays and using the Run 1 dataset collected in pp collisions at the centre-of-mass energies of 7 and 8 TeV [135] [136], corresponding to an integrated luminosity of 3.0 fb^{-1}. Correction factors to the π^0 reconstruction efficiency have been estimated, as reported in Tab. 7.3, depending on the π^0 transverse momentum. These corrections have small intrinsic uncertainties and a common irreducible systematic uncertainty of about 6% due to imprecise knowledge of the branching fractions of the B decays.

$\pi^0 p_T$[GeV/c]	η_{π^0}Rec[%]
$0.5 - 1.0$	$89.7 \pm 5.9 \pm 1.6 \pm 5.8$
$1.0 - 1.25$	$90.6 \pm 3.4 \pm 1.5 \pm 5.9$
$1.25 - 1.5$	$94.9 \pm 3.1 \pm 1.6 \pm 6.1$
$1.5 - 2.0$	$104.8 \pm 2.3 \pm 1.5 \pm 6.8$
> 2.0	$116.4 \pm 2.6 \pm 1.6 \pm 7.5$

Table 7.3. Correction factors for the Run 1 dataset in bins of π^0 transverse momentum. The first uncertainty is statistical, the second is systematic, and the third one is related to the knowledge of the branching fractions of the B decays.

Values from Tab. 7.3 have been used to estimate the proper corrections to be applied on the Run 2 analysis. Each event has been reweighted with the proper

correction in data, depending on the π^0 transverse momentum as shown in Fig. 7.3 after the full selection.

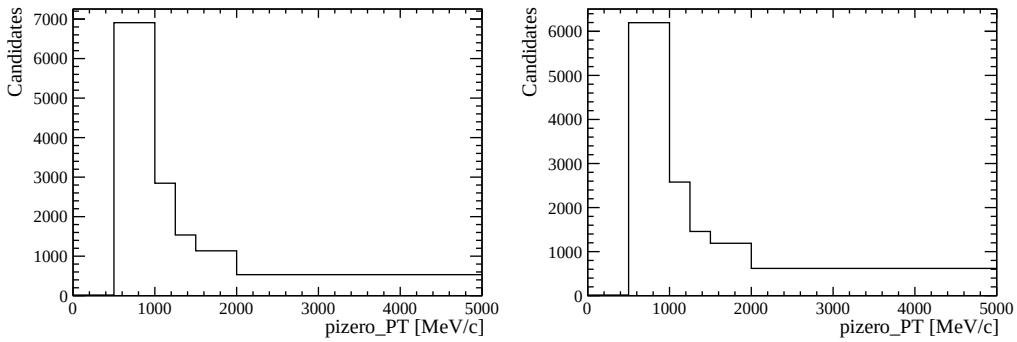

Figure 7.3. π^0 transverse momentum in data after the full selection with the same binning scheme illustrated in Tab. 7.3 unweighted (left) and reweighted (right).

The overall correction $\eta_{\pi^0\text{Rec}}$ is estimated as

$$\eta_{\pi^0\text{Rec}} = \frac{\sum_{bin=1}^{5} N(p_T^{bin}(w))}{\sum_{bin=1}^{5} N(p_T^{bin}(unw))}, \tag{7.7}$$

where $N(p_T^{bin}(unw))$ and $N(p_T^{bin}(w))$ represent the numbers of candidates before and after the reweighting.

The correction is found to be $\eta_{\pi^0\text{Rec}} = 0.93 \pm 0.08$ for each year and magnet polarity. The related systematic uncertainty is dominated by the external error, coming from the imprecise knowledge of the $B \to J/\psi K^{*+}(\to K^+\pi^0(\to \gamma\gamma))$ and $B \to J/\psi K^+$ branching fractions.

7.5 Correction to the BDT

A possible systematic effect due to the miscalibration of the BDT output variable between data and MC samples must be checked: the number of signal candidates has been estimated again from the signal fit for two variations of the final BDT requirement, around the nominal one. The efficiencies of these requirements have been evaluated from the MC samples and used to correct the newly evaluated yields, as reported in Tab. 7.4 for the full Run 2 sample. Based on Tab. 7.4, a systematic uncertainty for the BDT output of the signal selection is under evaluation.

Requirement	$N^{Data}_{\Sigma^+\to p\mu^+\mu^-}$	ε_{BDT}	$N^{Data}_{\Sigma^+\to p\mu^+\mu^-}/\varepsilon_{\text{BDT}}$
BDT > 0.30	316 ± 19	0.7214 ± 0.0020	438 ± 26
BDT > 0.35 (nominal value)	273 ± 18	0.6563 ± 0.0021	416 ± 28
BDT > 0.40	244 ± 18	0.6202 ± 0.0022	393 ± 29

Table 7.4. $\Sigma^+ \to p\mu^+\mu^-$ final yields as a function of the BDT requirement, efficiency of the BDT requirements and corrected signal yields.

7.6 Corrections to the $\Sigma^+ \to p\pi^0$ trigger efficiencies

In this section, corrections to the normalisation trigger lines are reported. Only studies on the HLT lines are shown as the corrections to the L0 trigger efficiency are still in development.

7.6.1 HLT1 trigger efficiency

The `Hlt1TrackMVA` line selects displaced tracks, applying requirements on the p_T, IP and $IP\chi^2$ variables. Therefore, a correction may be evaluated by comparing these two kinematic variables for the Σ^+ particle between data and MC samples.

The kinematic spectra of the `Hlt1TrackMVA` variables are studied using $\Sigma^+ \to p\pi^0$ and $\bar{\Sigma}^- \to \bar{p}\pi^0$ candidates in both data and MC samples. Each variable is considered over a signal and two sideband regions, defined as

- Signal region: $[1150; 1250]$ MeV/c^2;
- Left sideband region: $[1110; 1150)$ MeV/c^2;
- Right sideband region: $(1250; 1270]$ MeV/c^2.

The sidebands are merged and the resulting distribution is normalised with the number of background candidates in the signal region, estimated as the integral of the Chebyshev function. Furthermore, this normalised distribution is subtracted from the one in the signal region to obtain a kinematic spectrum background subtracted. The `Hlt1TrackMVA` kinematic spectra background subtracted are shown from Fig. 7.4 to Fig. 7.6 for both data and MC samples. A good agreement between data and simulation is found and, therefore, no corrections are applied to the HLT1 efficiency on the normalisation channel.

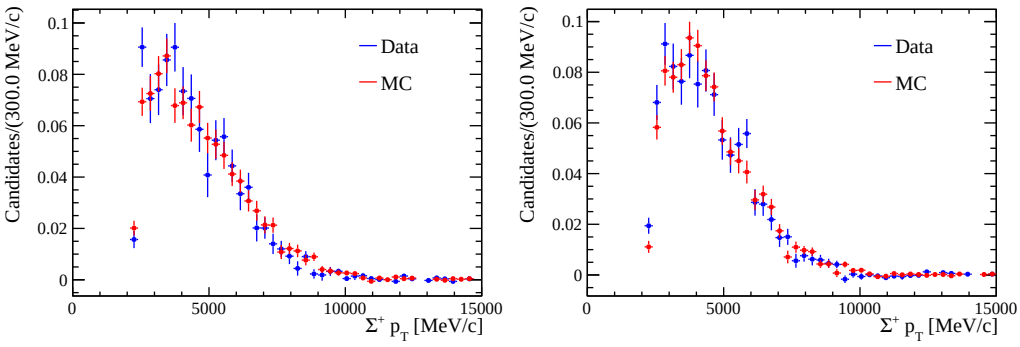

Figure 7.4. Σ^+ p_T for the $\Sigma^+ \to p\pi^0$ (left) and $\bar{\Sigma}^- \to \bar{p}\pi^0$ (right) decay modes in both data (blue) and MC (red).

This method has been extended to other kinematic variables to understand if a general reweight of the MC sample was necessary. The studied variables are: η for Σ^+, p_T, η, ϕ and $cos\theta$ for the proton, E and $cos\theta$ for the π^0. The distributions of these variables are shown from Fig. 7.7 to Fig. 7.13. No evidence of a need for reweighting is found.

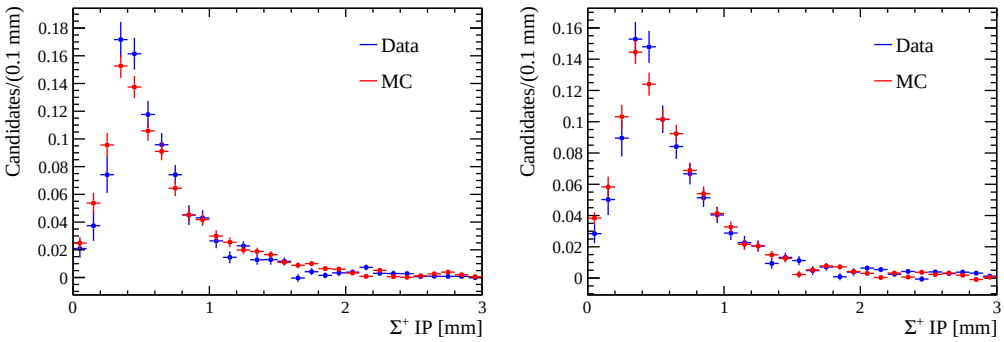

Figure 7.5. Σ^+ IP for the $\Sigma^+ \to p\pi^0$ (left) and $\bar{\Sigma}^- \to \bar{p}\pi^0$ (right) decay modes in both data (blue) and MC (red).

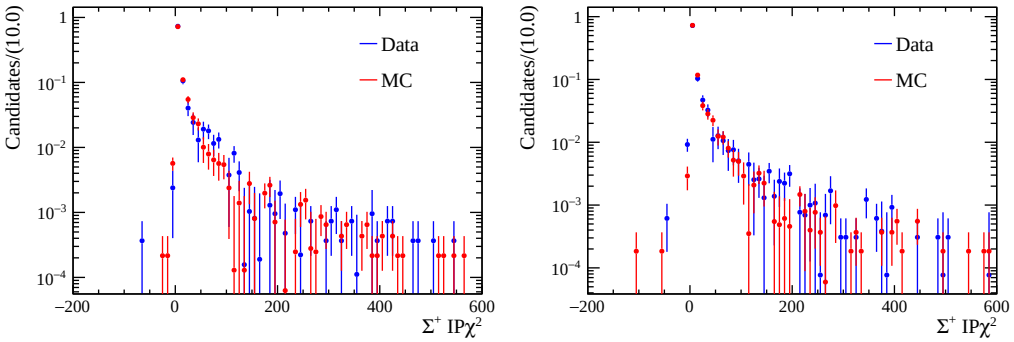

Figure 7.6. Σ^+ $IP\chi^2$ for the $\Sigma^+ \to p\pi^0$ (left) and $\bar{\Sigma}^- \to \bar{p}\pi^0$ (right) decay modes in both data (blue) and MC (red).

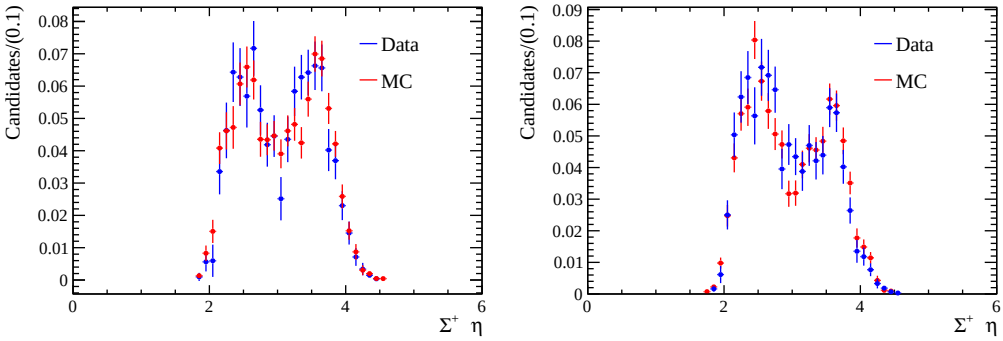

Figure 7.7. Σ^+ η for the $\Sigma^+ \to p\pi^0$ (left) and $\bar{\Sigma}^- \to \bar{p}\pi^0$ (right) decay modes in both data (blue) and MC (red).

7.6.2 HLT2 trigger efficiency

The `Hlt2PassThroughDecision` line takes as input all events out of the HLT1 and has a fixed prescale in data with negligible uncertainty. It has been checked that this prescale has been kept stable for the full Run 2 period, using all the other HLT2 lines as control triggers. Therefore, no corrections are assigned to this HLT2 efficiency.

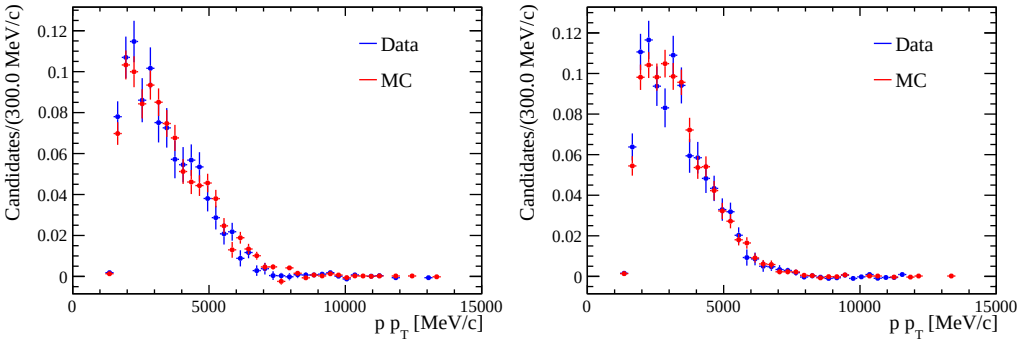

Figure 7.8. proton p_T for the $\Sigma^+ \to p\pi^0$ (left) and $\bar{\Sigma}^- \to \bar{p}\pi^0$ (right) decay modes in both data (blue) and MC (red).

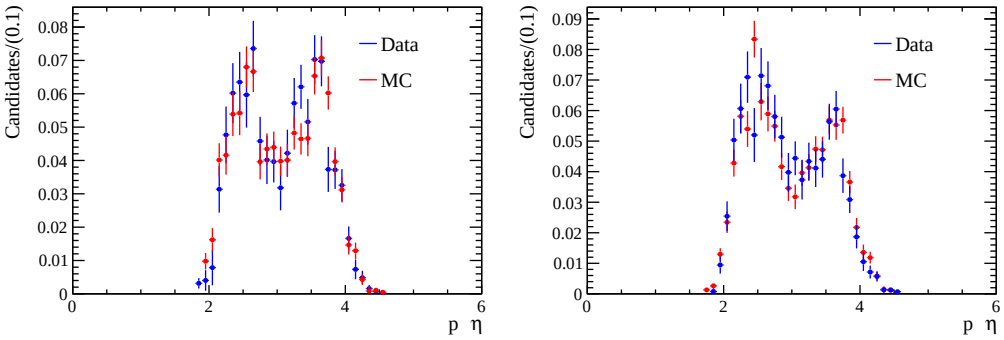

Figure 7.9. proton η for the $\Sigma^+ \to p\pi^0$ (left) and $\bar{\Sigma}^- \to \bar{p}\pi^0$ (right) decay modes in both data (blue) and MC (red).

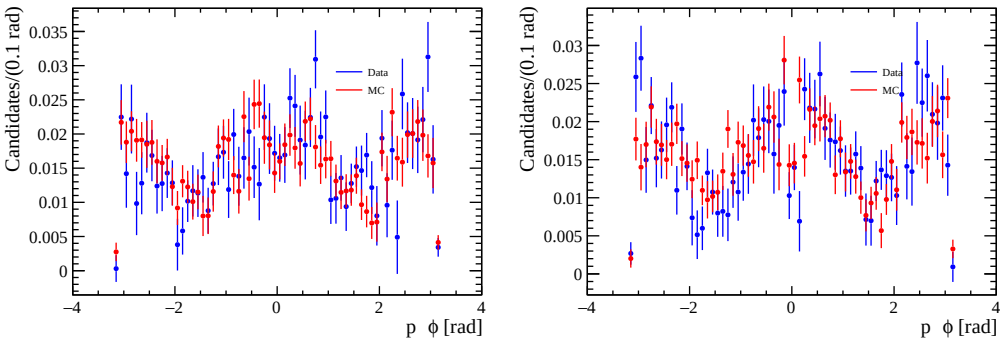

Figure 7.10. proton ϕ for the $\Sigma^+ \to p\pi^0$ (left) and $\bar{\Sigma}^- \to \bar{p}\pi^0$ (right) decay modes in both data (blue) and MC (red).

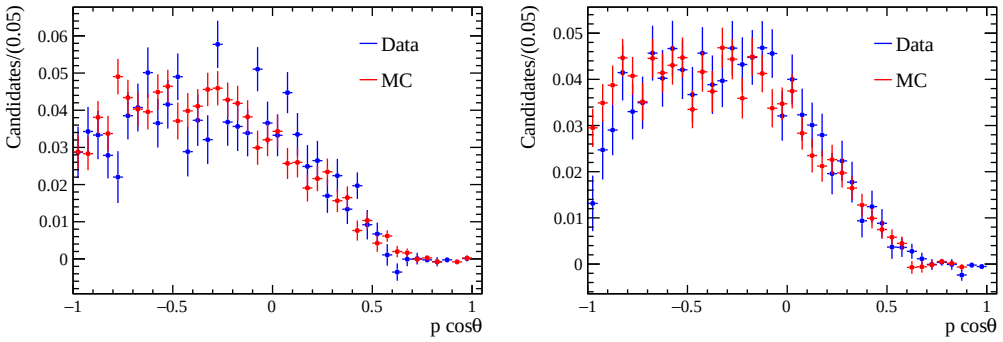

Figure 7.11. proton $\cos\theta$ for the $\Sigma^+ \to p\pi^0$ (left) and $\bar{\Sigma}^- \to \bar{p}\pi^0$ (right) decay modes in both data (blue) and MC (red).

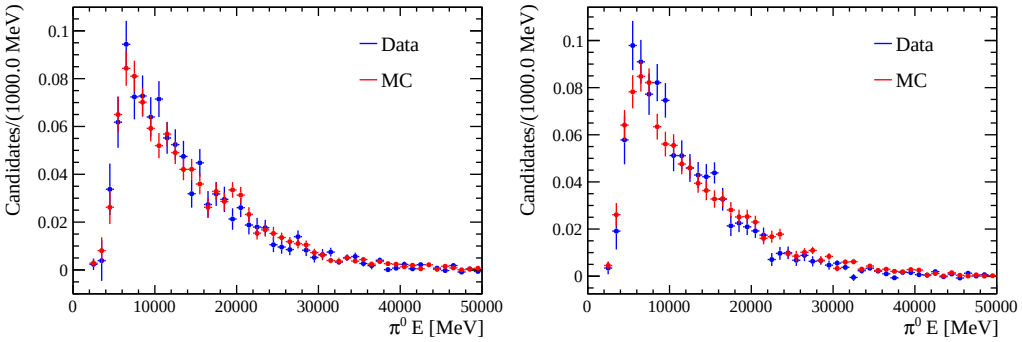

Figure 7.12. Neutral pion E for the $\Sigma^+ \to p\pi^0$ (left) and $\bar{\Sigma}^- \to \bar{p}\pi^0$ (right) decay modes in both data (blue) and MC (red).

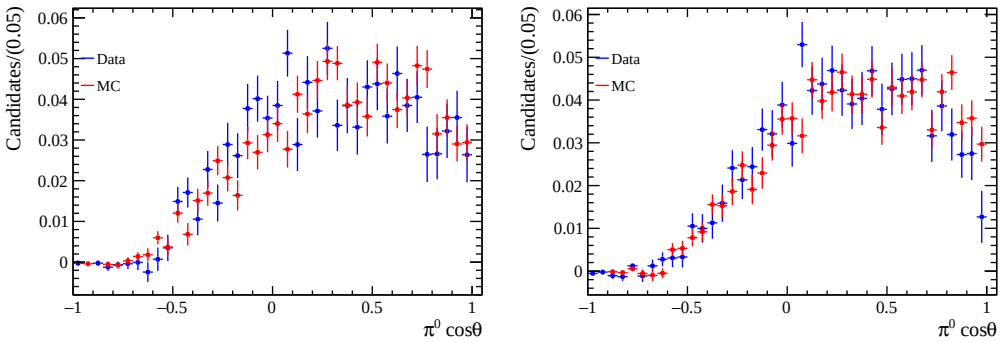

Figure 7.13. Neutral pion $\cos\theta$ for the $\Sigma^+ \to p\pi^0$ (left) and $\bar{\Sigma}^- \to \bar{p}\pi^0$ (right) decay modes in both data (blue) and MC (red).

7.7 Summary

The corrections to the $\Sigma^+ \to p\mu^+\mu^-$ and $\Sigma^+ \to p\pi^0$ efficiencies and their relative systematic uncertainties are summarised in Tab. 7.5 for the full Run 2 sample. These corrections are taken as multiplicative factors to their respective efficiencies.

A total relative systematic uncertainty for the branching fraction measurement is calculated by summing in quadrature each uncertainty in Tab. 7.5 and it is estimated to be 11%. The correction to the π^0 reconstruction efficiency is introducing the largest systematic error to the analysis. Even if some minor systematic uncertainties are still under development, this value is way below the relative systematic uncertainty reported in the Run 1 analysis, which was estimated to be 50% [31]. This great improvement comes mainly from the upgrades of the Run 2 analysis, already cited in Sec. 3.1.

Source	$\eta(\Sigma^+ \to p\mu^+\mu^-)$	$\eta(\Sigma^+ \to p\pi^0)$
Correction to the phase space model	1.042 ± 0.024	
Correction for multiplicity in generation		0.9986 ± 0.0008
Corrections to the particle identification	1.01 ± 0.05 (p) 1.04 ± 0.01 (μ^+) 1.04 ± 0.01 (μ^-)	1.02 ± 0.04 (p)
Correction to the π^0 reconstruction efficiency		0.93 ± 0.08
Total	1.14 ± 0.06	0.95 ± 0.09

Table 7.5. Corrections to the $\Sigma^+ \to p\mu^+\mu^-$ and $\Sigma^+ \to p\pi^0$ efficiencies and relative systematic uncertainties for the Run 2 sample.

Chapter 8

Measurement of the $\Sigma^+ \to p\mu^+\mu^-$ branching fraction and studies on the dimuon invariant mass

In this chapter, the measurement of the $\Sigma^+ \to p\mu^+\mu^-$ branching fraction is presented. The calculation is performed as

$$\begin{aligned}\mathcal{B}\left(\Sigma^+ \to p\mu^+\mu^-\right) &= \frac{\varepsilon_{\Sigma^+\to p\pi^0}}{\varepsilon_{\Sigma^+\to p\mu^+\mu^-}} \frac{\mathcal{B}\left(\Sigma^+ \to p\pi^0\right)}{N_{\Sigma^+\to p\pi^0}} N_{\Sigma^+\to p\mu^+\mu^-} \\ &= \alpha \cdot N_{\Sigma^+\to p\mu^+\mu^-},\end{aligned} \tag{8.1}$$

where α denotes the single event sensitivity, ε and N represent the overall efficiency and final yield of the decay modes and $\mathcal{B}\left(\Sigma^+ \to p\pi^0\right) = (51.57 \pm 0.30)\,\%$ is the $\Sigma^+ \to p\pi^0$ branching fraction, taken from the PDG [12].

All the quantities in Eq. 8.1 have already been estimated in the previous chapters. The total efficiencies and the normalisation final yield are summarised in Sec. 6.6 while the $\Sigma^+ \to p\mu^+\mu^-$ final yield is reported in Sec. 5.1. The corrections and the systematic uncertainties, affecting the branching fraction measurement, are discussed in Ch. 7.

In the first section of this chapter, the Σ^+ fluxes and absolute cross-sections of the Run 2 dataset are illustrated. Furthermore, the single event sensitivity is estimated and the $\Sigma^+ \to p\mu^+\mu^-$ branching fraction is calculated. Interpretations on the final result are also reported, considering the eight-fold ambiguity in the form factors and the corresponding SM predictions, already presented in Sec. 1.6.3.

At the end of this chapter, studies on the dimuon invariant mass are reported. The distribution is inspected in search of possible peaks, restricting to the signal region in the $\Sigma^+ \to p\mu^+\mu^-$ invariant mass distribution. A fit strategy is presented and the number of possible NP candidates is estimated. Furthermore, given that the distribution is compatible with the SM phase space, an upper limit on the fraction of decays in the considered HyperCP region is derived.

$\mathcal{B}(\Sigma^+ \to p\pi^0) = (51.57 \pm 0.30)\,\%$						
Year	Magnet	$N_{\Sigma^+\to p\pi^0}$	$\varepsilon_{\Sigma^+\to p\pi^0}$	$\Phi(pp \to \Sigma^+)$	$\mathcal{L}$ [fb^{-1}]	$\sigma(pp \to \Sigma^+)$ [fb]
2016	MagDown	1019 ± 42	$(7.2 \pm 0.7 \pm 0.6) \times 10^{-11}$	$(2.7 \pm 0.3 \pm 0.2) \times 10^{13}$	0.842 ± 0.017	$(3.2 \pm 0.4 \pm 0.3) \times 10^{13}$
	MagUp	935 ± 40	$(8.7 \pm 0.7 \pm 0.8) \times 10^{-11}$	$(2.1 \pm 0.2 \pm 0.2) \times 10^{13}$	0.778 ± 0.016	$(2.7 \pm 0.3 \pm 0.2) \times 10^{13}$
	MagAll	1955 ± 58	$(7.9 \pm 0.5 \pm 0.7) \times 10^{-11}$	$(4.8 \pm 0.3 \pm 0.4) \times 10^{13}$	1.620 ± 0.032	$(3.0 \pm 0.2 \pm 0.3) \times 10^{13}$
2017	MagDown	1161 ± 45	$(7.1 \pm 0.4 \pm 0.6) \times 10^{-11}$	$(3.2 \pm 0.2 \pm 0.3) \times 10^{13}$	0.862 ± 0.017	$(3.7 \pm 0.2 \pm 0.3) \times 10^{13}$
	MagUp	1021 ± 44	$(6.8 \pm 0.5 \pm 0.6) \times 10^{-11}$	$(2.9 \pm 0.2 \pm 0.3) \times 10^{13}$	0.820 ± 0.016	$(3.5 \pm 0.2 \pm 0.3) \times 10^{13}$
	MagAll	2182 ± 63	$(7.1 \pm 0.5 \pm 0.6) \times 10^{-11}$	$(6.1 \pm 0.5 \pm 0.5) \times 10^{13}$	1.682 ± 0.034	$(3.6 \pm 0.3 \pm 0.3) \times 10^{13}$
2018	MagDown	970 ± 42	$(5.9 \pm 0.6 \pm 0.5) \times 10^{-11}$	$(3.2 \pm 0.4 \pm 0.3) \times 10^{13}$	1.024 ± 0.020	$(3.1 \pm 0.4 \pm 0.3) \times 10^{13}$
	MagUp	1027 ± 44	$(5.8 \pm 0.4 \pm 0.5) \times 10^{-11}$	$(3.4 \pm 0.3 \pm 0.3) \times 10^{13}$	1.107 ± 0.022	$(3.1 \pm 0.3 \pm 0.3) \times 10^{13}$
	MagAll	1996 ± 60	$(5.8 \pm 0.4 \pm 0.5) \times 10^{-11}$	$(6.6 \pm 0.5 \pm 0.6) \times 10^{13}$	2.131 ± 0.043	$(3.1 \pm 0.2 \pm 0.3) \times 10^{13}$
Run 2	MagDown	3148 ± 75	$(6.7 \pm 0.2 \pm 0.6) \times 10^{-11}$	$(9.2 \pm 0.3 \pm 0.8) \times 10^{13}$	2.728 ± 0.055	$(3.4 \pm 0.1 \pm 0.3) \times 10^{13}$
	MagUp	2984 ± 73	$(6.6 \pm 0.2 \pm 0.6) \times 10^{-11}$	$(8.8 \pm 0.3 \pm 0.8) \times 10^{13}$	2.705 ± 0.054	$(3.3 \pm 0.1 \pm 0.3) \times 10^{13}$
	MagAll	6132 ± 105	$(6.7 \pm 0.2 \pm 0.6) \times 10^{-11}$	$(1.8 \pm 0.1 \pm 0.2) \times 10^{14}$	5.433 ± 0.108	$(3.31 \pm 0.02 \pm 0.29) \times 10^{13}$

Table 8.1. Flux $\Phi(pp \to \Sigma^+)$ and absolute cross-section $\sigma(pp \to \Sigma^+)$ for the Run 2 dataset listed by year and magnet polarity. Corrections to the normalisation efficiencies have already been applied. The first uncertainty is statistical and the second one is systematic.

8.1 Σ^+ flux and absolute cross-section

The Σ^+ flux $\Phi(pp \to \Sigma^+)$ is evaluated as

$$\Phi(pp \to \Sigma^+) = \frac{N_{\Sigma^+\to p\pi^0}}{\mathcal{B}(\Sigma^+ \to p\pi^0)\,\varepsilon_{\Sigma^+\to p\pi^0}}, \tag{8.2}$$

where $N_{\Sigma^+\to p\pi^0}$ is the normalisation final yield, $\varepsilon_{\Sigma^+\to p\pi^0}$ the corrected overall efficiency and $\mathcal{B}(\Sigma^+ \to p\pi^0) = (51.57 \pm 0.30)\,\%$ the $\Sigma^+ \to p\pi^0$ branching fraction, taken from the PDG [12]. From the flux, the absolute cross-section $\sigma(pp \to \Sigma^+)$ is calculated as

$$\sigma(pp \to \Sigma^+) = \frac{\Phi(pp \to \Sigma^+)}{\mathcal{L}}, \tag{8.3}$$

where $\mathcal{L}$ denotes the integrated luminosity, collected at LHCb between 2016 and 2018.

The Σ^+ fluxes and cross-sections of the Run 2 dataset are listed by year and magnet polarity in Tab. 8.1. The Run 2 flux is measured to be $\Phi(pp \to \Sigma^+) = (1.8 \pm 0.1 \pm 0.2) \times 10^{14}$ while the absolute cross-section is $\sigma(pp \to \Sigma^+) = (3.31 \pm 0.02 \pm 0.29) \times 10^{13}$ fb. The first uncertainty is statistical and the second one is systematic[1].

8.2 Single event sensitivity and signal branching fraction measurement

The single event sensitivity α, evaluated as in Eq. 8.1, is reported in Tab. 8.2. The corrected efficiencies and the final yields for the normalisation decay mode are also reported.

[1]The external and small error due to the knowledge of the $\Sigma^+ \to p\pi^0$ branching fraction has been included in the systematic uncertainty. This assumption will be also used for the branching fraction measurement.

$\mathcal{B}(\Sigma^+ \to p\pi^0) = (51.57 \pm 0.30)\,\%$				
Year	$\varepsilon_{\Sigma^+\to p\mu^+\mu^-}$	$\varepsilon_{\Sigma^+\to p\pi^0}$	$N_{\Sigma^+\to p\pi^0}$	α
2016	$(3.54 \pm 0.03 \pm 0.21) \times 10^{-5}$	$(7.9 \pm 0.5 \pm 0.7) \times 10^{-11}$	1955 ± 58	$(5.8 \pm 0.4 \pm 0.6) \times 10^{-10}$
2017	$(4.09 \pm 0.05 \pm 0.24) \times 10^{-5}$	$(7.1 \pm 0.5 \pm 0.6) \times 10^{-11}$	2182 ± 63	$(4.1 \pm 0.3 \pm 0.5) \times 10^{-10}$
2018	$(3.08 \pm 0.03 \pm 0.18) \times 10^{-5}$	$(5.8 \pm 0.4 \pm 0.5) \times 10^{-11}$	1996 ± 60	$(4.9 \pm 0.4 \pm 0.5) \times 10^{-10}$
Run 2	$(3.60 \pm 0.02 \pm 0.22) \times 10^{-5}$	$(6.7 \pm 0.2 \pm 0.6) \times 10^{-11}$	6132 ± 105	$(1.57 \pm 0.06 \pm 0.17) \times 10^{-10}$

Table 8.2. Single event sensitivity α for each year of the used Run 2 dataset. The corrected efficiencies and the final yields for the normalisation decay mode are also reported. The first uncertainty is statistical and the second one is systematic.

The single event sensitivity for the full Run 2 dataset is estimated to be $\alpha = (1.57 \pm 0.06 \pm 0.17) \times 10^{-10}$, where the first uncertainty is statistical and the second one is systematic. The single event sensitivity of the Run 1 analysis was measured to be $\alpha = (2.2 \pm 1.2) \times 10^{-9}$ [31], where the uncertainty was dominated by the systematic contribution. An improvement of factor 14 is obtained with respect to the previous analysis due to various elements, such as the dedicated trigger lines, increased statistics in the MC samples and better control of the systematics uncertainties.

Therefore, using the measured $\Sigma^+ \to p\mu^+\mu^-$ final yield, which is equal to $N_{\Sigma^+\to p\mu^+\mu^-} = 273 \pm 18$, the Run 2 signal branching fraction is estimated to be

$$\mathcal{B}\left(\Sigma^+ \to p\mu^+\mu^-\right) = (4.3 \pm 0.3 \pm 0.5) \times 10^{-8}, \tag{8.4}$$

where the first uncertainty is statistical and the second one is systematic.

8.2.1 Interpretation of the result

The measured $\Sigma^+ \to p\mu^+\mu^-$ branching fraction in Eq. 8.4 is compatible with the latest SM theoretical predictions, illustrated in Sec. 1.6.3. These are evaluated with the new BESIII inputs [58] in the relativistic [35] and heavy baryon [36] χPT approaches. In particular, each method gives four solutions, as listed in Tab. 8.3. Given the statistical and systematic uncertainties, the new result is compatible with Solution 3 of the relativistic χPT approach. Here, a discrepancy of 3σ from the measured branching fraction is observed with respect to Solution 2. Solutions 1 and 4 in the same method can be excluded, due to their 5σ discrepancy from the measured value. The same conclusions are extended to the heavy baryon χPT approach: Solutions 1 and 4 are excluded while Solutions 3 and 4 are compatible within 3σ from the reported value.

χPT approach	Solution 1	Solution 2	Solution 3	Solution 4
Relativistic baryon	1.2	2.5	4.3	7.9
Heavy baryon	1.7	3.4	3.4	6.5

Table 8.3. SM theoretical predictions of the $\Sigma^+ \to p\mu^+\mu^-$ branching fraction (10^{-8}) evaluated from the latest results of the BESIII collaboration in the relativistic and heavy baryon χPT approaches.

8.3 Studies on the dimuon invariant mass

The first evidence of the $\Sigma^+ \to p\mu^+\mu^-$ decay was reported by the HyperCP collaboration [30]. Three candidates were observed with almost the same dimuon invariant mass of $m_{X^0} = 214.3 \pm 0.5$ MeV/c^2, close to the lower kinematic limit. Such a result, if confirmed, would point towards a decay with an intermediate particle X^0 coming from the Σ^+ baryon and decaying in two muons, i.e. a $\Sigma^+ \to pX^0(\to \mu^+\mu^-)$ decay, which would constitute evidence for NP beyond the SM. The LHCb experiment repeated the search for this decay with the dataset collected during Run 1 [31] and no significant structure was observed in the dimuon invariant mass distribution, in contrast with the previous result.

In this section, new studies on the dimuon object are presented, using the Run 2 dataset. The distribution of the dimuon invariant mass, after the full section and requiring $|m_{p\mu^+\mu^-} - m^{PDG}_{\Sigma^+}| < 2\sigma(7.8)$ MeV/c^2 with σ taken from Sec. 5.1 and $m^{PDG}_{\Sigma^+}$ from the PDG [12], is shown in data in Fig. 8.1.

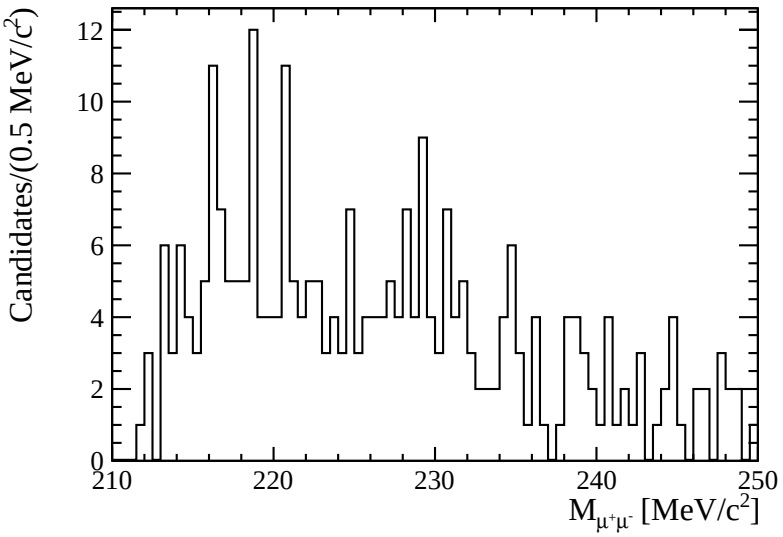

Figure 8.1. Distribution of the $m_{\mu^+\mu^-}$ invariant mass in data after applying the final selection and requesting $|m_{p\mu^+\mu^-} - m^{PDG}_{\Sigma^+}| < 7.8$ MeV/c^2.

An extended maximum likelihood fit is performed directly on data in two steps:

- Background only (B) - The distribution is fitted with only a function, describing the SM background component. This part is parametrised by a Chebyshev fourth degree polynomial function of the first kind [131];
- Signal + Background ($S + B$) - The fit is repeated by adding the component for the NP signal, described by a Gaussian function.

While the background parameters are fixed from the previous B fit, the signal mean is fixed at the hypothesis mass value of the NP particle, $\mu = 214.3$ MeV/c^2. The width σ, on the other hand, is decided by looking at $\Delta m_{\mu^+\mu^-}$, defined as the

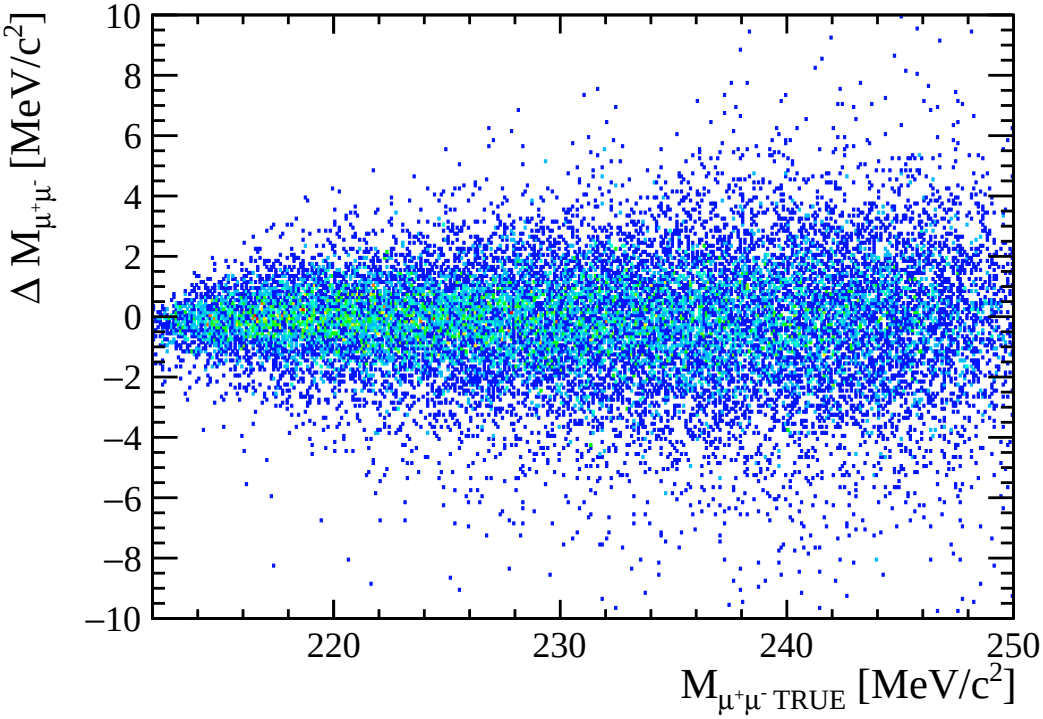

Figure 8.2. Distribution of the $\Delta m_{\mu^+\mu^-}$ mass as a function of the MC truth of the $m_{\mu^+\mu^-}$ invariant mass.

difference between the reconstructed and truth MC distributions. The distribution of $\Delta m_{\mu^+\mu^-}$ is reported in Fig. 8.2 as a function of the MC truth.

By looking at the vertical projection of the MC truth over the range $m_{\mu^+\mu^- TRUE} \in [214.3 \pm 0.5]$ MeV/c^2, a Gaussian-like distribution is found. The fitted distribution gives $\sigma = 0.55$ MeV/c^2, which represents the resolution of the LHCb experiment for two particles forming a decay vertex with an invariant mass value equal to the one reported by the HyperCP collaboration.

The $S+B$ fit to the selected data sample is shown in Fig. 8.3 (top) while the B fit is reported in Fig. 8.3 (bottom). The fit is performed in the range $212 < m_{\mu^+\mu^-} < 250$ MeV/c^2, where the lower limit is chosen to be near the threshold value given by the sum of the muons masses. No significant signal is found and a total of 3 ± 5 signal candidates have been fitted. Furthermore, the B fit gives a reduced χ^2 equal to $\chi^2/NDF(B) = 0.68$ while the $S+B$ one measures $\chi^2/NDF(S+B) = 0.67$. The difference between the two results confirms that adding a component to the *p.d.f.* to describe a HyperCP-like signal does not improve the quality of the fit.

In conclusion, a signal similar to the one observed by the HyperCP experiment can be completely excluded. An upper limit on the branching fraction of the resonant channel is set with the CL$_S$ method [137] at $\mathcal{B}\left(\Sigma^+ \to pX^0(\to \mu^+\mu^-)\right) < 8.5 \times 10^{-9}$ at 90% confidence level.

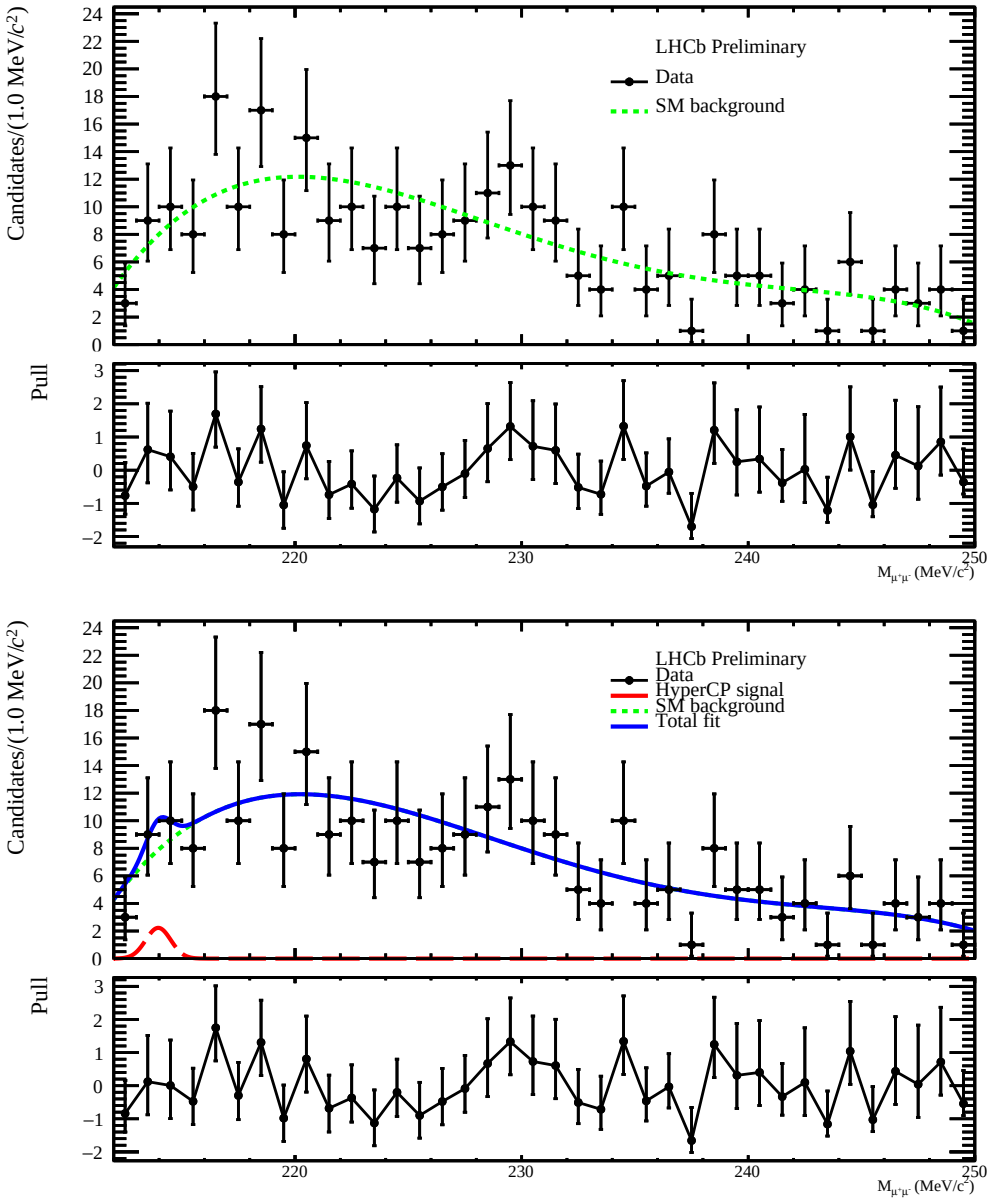

Figure 8.3. Distribution of the $m_{\mu^+\mu^-}$ invariant mass in data after the final selection and superimposed with the fit (blue). The HyperCP-like signal component is parametrised by a Gaussian function (red) while the SM background is described by a Chebyshev fourth degree polynomial function of the first kind (green). The same distribution is reported with the B (top) and $S + B$ (bottom) fit. The pull distribution is also illustrated in the bottom panel.

Conclusions

In this thesis, the first clear observation of the $\Sigma^+ \to p\mu^+\mu^-$ decay and a direct branching fraction measurement are presented.

The HyperCP experiment reported an evidence of this decay. The measured branching fraction was compatible with the SM prediction and the three observed candidates had almost the same dimuon invariant mass of $m_{X^0} = 214.3 \pm 0.5$ MeV/c^2, close to the lower kinematic limit. Such a result, if confirmed, would point towards a decay with an intermediate particle X^0 coming from the Σ^+ baryon and decaying in two muons, i.e. a $\Sigma^+ \to pX^0(\to \mu^+\mu^-)$ decay, which would constitute a sign of NP beyond the SM. Evidence for the $\Sigma^+ \to p\mu^+\mu^-$ decay was also observed at LHCb with the Run 1 dataset, collected by recording pp collisions at a centre-of-mass energy of 7 and 8 TeV, corresponding to an integrated luminosity of 3.0 fb^{-1}. A number of $10.2^{+3.9}_{-3.5}$ signal candidates has been measured, corresponding to a significance of 4.1σ. The spectrum of the dimuon invariant mass was compatible with the phase space distribution, i.e. no significant structure of a resonant contribution was observed.

The presented analysis is performed using pp collision data recorded by the LHCb experiment during Run 2 at centre-of-mass energies $\sqrt{s} = 13$ TeV, corresponding to an integrated luminosity of 5.4 fb^{-1}. Signal candidates are selected with a first loose preselection at the stripping level and a tight offline selection with a multivariate discriminant and PID variables to reject most of the relevant sources of background. Following the optimisations of the selection strategy, a fit to the $m_{p\mu^+\mu^-}$ invariant mass distribution is performed and the final $\Sigma^+ \to p\mu^+\mu^-$ yield is extracted. A number of 273 ± 18 signal candidates is observed with respect to the background expectation, marking the first clear observation of the decay. Furthermore, the result is normalised using the $\Sigma^+ \to p\pi^0$ decay and the branching fraction is measured to be

$$\mathcal{B}\left(\Sigma^+ \to p\mu^+\mu^-\right) = (4.3 \pm 0.3 \pm 0.5) \times 10^{-8}, \tag{8.5}$$

where the first uncertainty is statistical and the second one is systematic.

Recent results from the BESIII collaboration point to an eight-fold ambiguity in the form factors of the $\Sigma^+ \to p\mu^+\mu^-$ Lagrangian, which produce four SM branching fraction predictions in both the relativistic and heavy baryon χPT models. The measured result is compatible with two solutions of each theoretical model, having some tensions with the remaining ones.

Additionally, the dimuon invariant mass is inspected again for a possible HyperCP-like signal. A fit to the $m_{\mu^+\mu^-}$ invariant mass distribution is performed and no significant signal is found. An upper limit on the branching fraction of the resonant

channel is set with the CL_S method at $\mathcal{B}\left(\Sigma^+ \to pX^0(\to \mu^+\mu^-)\right) < 8.5 \times 10^{-9}$ at 90% confidence level, excluding the signal observed by the HyperCP experiment.

The analysis is currently under review and a paper is in preparation. The reported results in this thesis are preliminary at the time of writing. Minor systematic uncertainties, affecting the branching fraction measurement, are still under development. Given the large number of observed signal candidates, the differential branching fraction with respect to the dimuon invariant mass, the forward-backward asymmetry in the decay and the "direct" CP asymmetry measurement will be explored in the near future. Furthermore, a search of the $\mu^+\mu^-$ resonance as an intermediate state will be extended to all the $m_{\mu^+\mu^-}$ kinematic regions, even if no signal seems to be present.

Appendix A

Variables used in the analysis

In addition to the standard kinematic variables, such as the momentum p, the transverse momentum p_T, the mean lifetime τ and the mass m, many other variables are employed during the analysis. In this appendix, a detailed list of the used variables in the Run 2 analysis of the $\Sigma^+ \to p\mu^+\mu^-$ decay is illustrated.

- *Track* χ^2 - The χ^2 associated with a track, which is obtained by fitting the detector hits positions;
- IP and $IP\chi^2$ - The Impact Parameter, defined as the minimum distance between a reconstructed track and its Primary Vertex (PV). The $IP\chi^2$ is defined as the variation of the χ^2 per degree of freedom of the fit to the PV;
- $DOCA$ - The Distance Of Closest Approach, defined as the minimum distance between two tracks;
- $Vtx\chi^2$ - The χ^2 associated with the decay vertex of a particle, reconstructed by fitting the final state tracks;
- *GhostProb* - The probability that a track is a "ghost track". A ghost track is formed by the combinations of random hits that together are reconstructed as a real track;
- $ProbNN(i)$ - The particle identification variable of a particle i, generated by a neural network;
- $DIRA$ - The cosine of the pointing angle, defined as the angle between the particle flight and momentum directions;
- FD and $FD\chi^2$ -The distance between a particle decay vertex and its generation point. Its χ^2 is defined as

$$FD\chi^2 = (\vec{r}_{\mathrm{PV}} - \vec{r}_{\mathrm{DV}})^{\mathrm{T}}\, \Sigma^{-1}\, (\vec{r}_{\mathrm{PV}} - \vec{r}_{\mathrm{DV}})\,, \tag{A.1}$$

  where $\vec{r}_{\mathrm{PV}}$ and $\vec{r}_{\mathrm{DV}}$ are defined as the positions of the primary and decay vertices. Σ^{-1} is the inverse of the covariance matrix of their measurements;
- $(i)CL$ - The confidence level variable for the particle i. It is used to indicate the confidence that a chosen assignment of particle ID is correct.

Appendix B

Studies on the $\Sigma^+ \to p\mu^+\mu^-$ trigger strategy

The $\Sigma^+ \to p\mu^+\mu^-$ trigger strategy is decided to have the highest possible efficiency, despite the complexity of its calibration. The evaluation is done "backwards"' with respect to the order in which the trigger is processed in data to avoid optimising L0 on candidates that would not pass the dedicated HLT lines. Simulations are used to optimise the trigger strategy starting to evaluate HLT2 after the preselection. In a similar way, HLT1 has been optimised after the application of HLT2. The L0 lines have been chosen, after the application of the HLT lines, to maximise the number of signal candidates.

All the considered lines are expressed with the prefix "Sigma_", meaning that the trigger line is fired by events containing three tracks compatible with the $\Sigma^+ \to p\mu^+\mu^-$ decay. The suffixes "TOS", "TIS" and "Dec" define the trigger categories, already presented in Sec. 3.2.1. Various trigger strategies are formulated to understand the HLT and L0 tradeoff between efficiency and complexity In each strategy, the logical operation OR is considered between the lines.

The HLT2 trigger strategies are listed in Tab. B.1. The strategy "Dedi" denotes the dedicated trigger lines, "DiMu" the ones fired by two muons while "SMu" the trigger lines fired by a single muon in the final state. The trigger strategy "Phys" includes all the trigger lines related to physics studies, excluding calibration and minimum bias lines. The "Phys" collection is not reliable in simulation as it includes lines that are heavily prescaled in data. Efficiencies for each trigger strategy are reported in Tab. B.2. The "Dedi" strategy reaches 91% efficiency and the addition of other lines does not increase it. Therefore, only the "Dedi" family is chosen as the HLT2 trigger strategy for the $\Sigma^+ \to p\mu^+\mu^-$ decay.

Concerning HLT1, the new line `Hlt1DiMuonNoL0` has the largest efficiency by design, as it is customised to the signal, but small contributions from other lines are expected. As for HLT2, different trigger strategies are tested, as presented in Tab. B.3. The corresponding efficiencies, evaluated after the HLT2 requirement, are listed in Tab. B.4. Here, "Mu" is a combination of the "SMu" and "DiMu" trigger strategies while "MVA" represents the trigger lines fired by all the events passing a loose multivariate analysis designed to select generic B and D decays. In this case, the most inclusive selection still has an acceptable efficiency. Therefore, the

"Mu+MVA Dec" family is chosen to be the HLT1 trigger strategy.

For L0 the same approach used for HLT2 and HLT1 is applied. Different trigger strategies are devised, as listed in Tab. B.5, and their efficiency, evaluated after the HLT2 and HLT1 requirements, are listed in Tab. B.6. Here, "H" denotes the trigger strategy for the lines fired by hadrons while "Global" represents all the L0 lines available. Since the L0 is not designed for strange hadrons the best strategy is to keep everything. Therefore, the "Mu"+"HDec"+"TIS" strategy is chosen to be the signal L0 trigger strategy.

Strategy	Trigger line
PhysDec	Sigma_Hlt2Phys_Dec
PhysTOS	Sigma_Hlt2Phys_TOS
Dedi	Sigma_Hlt2RareStrangeSigmaPMuMuDecision_Dec
	Sigma_Hlt2DiMuonSoftDecision_Dec
Dedi+DiMu	Sigma_Hlt2RareStrangeSigmaPMuMuDecision_Dec
	Sigma_Hlt2DiMuonSoftDecision_Dec
	Sigma_Hlt2DiMuonDetachedDecision_TOS
	Sigma_Hlt2DiMuonLowMassDecision_TOS
Dedi+DiMu+SMu	Sigma_Hlt2RareStrangeSigmaPMuMuDecision_Dec
	Sigma_Hlt2DiMuonSoftDecision_Dec
	Sigma_Hlt2DiMuonDetachedDecision_TOS
	Sigma_Hlt2DiMuonDetachedDecision_TOS
	Sigma_Hlt2DiMuonLowMassDecision_TOS
	Sigma_Hlt2SingleMuonDecision_TOS
	Sigma_Hlt2SingleMuonHighPTDecision_TOS
	Sigma_Hlt2SingleMuonRareDecision_TOS

Table B.1. HLT2 trigger strategies studied for the signal mode.

Strategy	Efficiency
PhysDec	1.0000 ± 0.0000
PhysTOS	0.9227 ± 0.0015
Dedi	0.9136 ± 0.0015
Dedi+DiMu	0.9147 ± 0.0015
Dedi+DiMu+SMu	0.9148 ± 0.0015

Table B.2. Efficiency in simulation of the considered HLT2 trigger strategies.

Strategy	Trigger line
PhysDec	Sigma_Hlt1Phys_Dec
PhysTOS	Sigma_Hlt1Phys_TOS
SMuTOS	Sigma_Hlt1TrackMuonDecision_TOS
	Sigma_Hlt1SingleMuonHighPTDecision_TOS
DiMuTOS	Sigma_Hlt1DiMuonLowMassDecision_TOS
	Sigma_Hlt1DiMuonHighMassDecision_TOS
	Sigma_Hlt1DiMuonNoL0Decision_TOS
MuTOS	Sigma_Hlt1TrackMuonDecision_TOS
	Sigma_Hlt1SingleMuonHighPTDecision_TOS
	Sigma_Hlt1DiMuonLowMassDecision_TOS
	Sigma_Hlt1DiMuonHighMassDecision_TOS
	Sigma_Hlt1DiMuonNoL0Decision_TOS
Mu+MVA TOS	Sigma_Hlt1TrackMuonDecision_TOS
	Sigma_Hlt1SingleMuonHighPTDecision_TOS
	Sigma_Hlt1DiMuonLowMassDecision_TOS
	Sigma_Hlt1DiMuonHighMassDecision_TOS
	Sigma_Hlt1DiMuonNoL0Decision_TOS
	Sigma_Hlt1TrackMVADecision_TOS
	Sigma_Hlt1TwoTrackMVADecision_TOS
MuTOS+MVA TIS+TOS	Sigma_Hlt1TrackMuonDecision_TOS
	Sigma_Hlt1SingleMuonHighPTDecision_TOS
	Sigma_Hlt1DiMuonLowMassDecision_TOS
	Sigma_Hlt1DiMuonHighMassDecision_TOS
	Sigma_Hlt1DiMuonNoL0Decision_TOS
	Sigma_Hlt1TrackMVADecision_TOS
	Sigma_Hlt1TwoTrackMVADecision_TOS
	Sigma_Hlt1TrackMVADecision_TIS
	Sigma_Hlt1TwoTrackMVADecision_TIS
Mu+MVA Dec	Sigma_Hlt1TrackMuonDecision_Dec
	Sigma_Hlt1SingleMuonHighPTDecision_Dec
	Sigma_Hlt1DiMuonLowMassDecision_Dec
	Sigma_Hlt1DiMuonHighMassDecision_Dec
	Sigma_Hlt1DiMuonNoL0Decision_Dec
	Sigma_Hlt1TrackMVADecision_Dec
	Sigma_Hlt1TwoTrackMVADecision_Dec
	Sigma_Hlt1TrackMuonDecision_Dec
	Sigma_Hlt1SingleMuonHighPTDecision_Dec

Table B.3. HLT1 trigger strategies studied for the signal mode.

Strategy	Efficiency
PhysDec	0.99361 ± 0.00032
PhysTOS	0.8802 ± 0.0013
SMuTOS	$(8.6 \pm 1.2) \times 10^{-4}$
DiMuTOS	0.3219 ± 0.0018
MuTOS	0.3222 ± 0.0018
Mu+MVATOS	0.4366 ± 0.0020
MuTOS+MVATIS+MVATOS	0.5005 ± 0.0020
Mu+MVADec	0.5303 ± 0.0020

Table B.4. Efficiency in simulation of the considered HLT1 trigger strategies.

Strategy	Trigger line
L0Global	Sigma_L0Global_Dec
MuTOS	Sigma_L0MuonDecision_TOS
	Sigma_L0DiMuonDecision_TOS
MuTOS+MuTIS	Sigma_L0MuonDecision_TOS
	Sigma_L0DiMuonDecision_TOS
	Sigma_L0MuonDecision_TIS
	Sigma_L0DiMuonDecision_TIS
MuTOS+HTIS	Sigma_L0MuonDecision_TOS
	Sigma_L0DiMuonDecision_TOS
	Sigma_L0HadronDecision_TIS
MuTOS+TIS	Sigma_L0MuonDecision_TOS
	Sigma_L0DiMuonDecision_TOS
	Sigma_L0HadronDecision_TIS
	Sigma_L0MuonDecision_TIS
	Sigma_L0DiMuonDecision_TIS
MuTOS+TIS2	Sigma_L0MuonDecision_TOS
	Sigma_L0DiMuonDecision_TOS
	Sigma_L0HadronDecision_TIS
	Sigma_L0ElectronDecision_TIS
	Sigma_L0PhotonDecision_TIS
MuTOS+TIS3	Sigma_L0MuonDecision_TOS
	Sigma_L0DiMuonDecision_TOS
	Sigma_L0HadronDecision_TIS
	Sigma_L0ElectronDecision_TIS
	Sigma_L0PhotonDecision_TIS
	Sigma_L0MuonDecision_TIS
	Sigma_L0DiMuonDecision_TIS
MuDec+TIS	Sigma_L0MuonDecision_Dec
	Sigma_L0DiMuonDecision_Dec
	Sigma_L0HadronDecision_TIS
	Sigma_L0ElectronDecision_TIS
	Sigma_L0PhotonDecision_TIS
Mu+HDec+TIS	Sigma_L0MuonDecision_Dec
	Sigma_L0DiMuonDecision_Dec
	Sigma_L0HadronDecision_Dec
	Sigma_L0ElectronDecision_TIS
	Sigma_L0PhotonDecision_TIS

Table B.5. L0 trigger strategies studied for the signal mode.

Strategy	Efficiency
L0Global	0.2861 ± 0.0009
MuTOS	0.0620 ± 0.0005
MuTOS+MuTIS	0.1095 ± 0.0006
MuTOS+HTIS	0.1827 ± 0.0008
MuTOS+TIS	0.2199 ± 0.0008
MuTOS+TIS2	0.2281 ± 0.0008
MuTOS+TIS3	0.2622 ± 0.0009
MuDec+TIS	0.2639 ± 0.0009
Mu+HDec+TIS	0.2835 ± 0.0009

Table B.6. Efficiency in simulation of the considered L0 trigger strategies.

Appendix C

Studies of photon sensors for the upgrade of the LHCb RICHs

Particle identification usually involves Ring Imaging Cherenkov detectors. These detectors typically include a Cherenkov radiator, an optical system, and single-photon sensors. Enhancing the performance of PID systems, particularly under conditions of high track multiplicity and pile-up of events, may be achieved through the use of sub-nanosecond time resolutions, obtained with appropriate photon sensors coupled with high performance readout chain [138]. This appendix presents studies on the time resolution within the context of the RICH upgrades for the LHCb experiment. An upgrade of the photon sensors and the readout chain of the RICH is foreseen in the next decade to adapt the two detectors to the high luminosity phase of LHC.

Fig. C.1 illustrates the timeline of the RICH upgrades while a schematic evolution of the LHCb RICH optoelectronic readout chain is shown in Fig. C.2. During the LHC Run 3 and Run 4 data-taking, multi-anode photomultiplier tubes (MaPMTs) will be used for single-photon detection [139]. At the end of Run 4, the front-end will be equipped with a new ASIC known as the FastRICH [140]. The FastRICH improves the ability to timestamp photons with a bin size of 25 ps, alongside advanced data compression features and the coverage of a wide input signal dynamic range [141]. As part of the LHCb Upgrade II programme, which will prepare the experiment for a factor 7.5 increase in luminosity during Run 5, a comprehensive overhaul of the detector will be necessary [142]. The Run 4 electronics readout chain is designed to be compatible with new sensor types for Run 5. However, a substantial increase in channel density would necessitate a revision of the front-end layout.

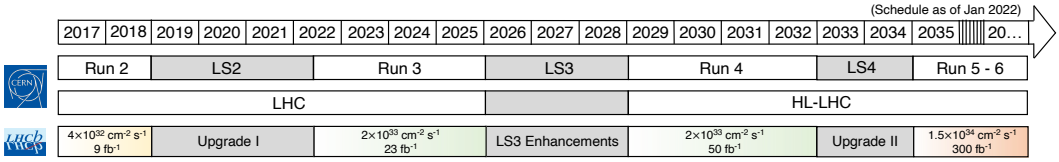

Figure C.1. Timeline of the LHCb RICH upgrade programme at the LHC.

In this appendix, the single-photon time resolution (SPTR), studied during the dedicated test beam campaigns between 2022 and 2023 at the charged particle beam

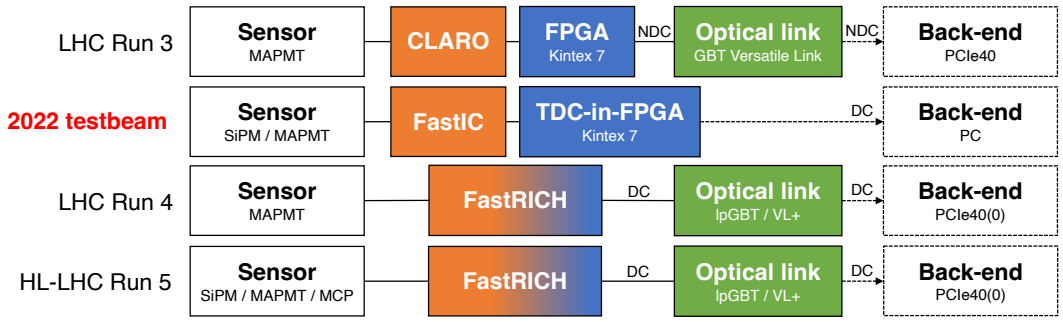

Figure C.2. Schematic evolution of the LHCb RICH optoelectronic readout chain from Run 3 to the high-luminosity Run 5.

facility of the CERN SPS, is discussed. A new readout front-end ASIC, called Fast Integrated Circuit (FastIC) [143], has been tested. It is the predecessor of the FastRICH and has an expected SPTR of $\sigma \sim$150/200 ps. Much like the FastRICH, the FastIC can be easily coupled to various sensor candidates for the LHCb Upgrade II, thanks to its wide input signal dynamic range. The test beam experimental setup is illustrated in Sec. C.1 while preliminary results on the SPTR, derived from a new advanced Cherenkov ring fitting algorithm, are reported in Sec. C.2. The analysis is currently under review and a technical paper is in preparation.

C.1 Experimental setup

The test beam campaigns were conducted at the CERN SPS beam facility [65], which provided charged hadron beams made of protons and pions with 180 GeV/c momentum. A schematic overview of the testbeam experimental setup is shown in Fig. C.3. The beam passed through the centre of a borosilicate lens, with 150 mm diameter and 300 mm focal length, emitting Cherenkov photons. The photons are then reflected to a vertical plane where a 1-inch-pixel MaPMT, a 2-inch-pixel MaPMT, and a SiPM are mounted. Half of the channels of each photon sensor are coupled to the FastIC readout chain to provide the photon timing information, as in Fig. C.4. The FastIC is operated in single-ended non-linear time-over-threshold (ToT) mode and it is DC-coupled to an FPGA. A TDC-in-FPGA was developed with a nominal bin size of 150 ps [144] to capture the FastIC output. A front-view picture of the experimental vertical plane is shown in Fig. C.5. In the photo, the orange-dotted ring represents the typical sensors illuminated by the Cherenkov photons.

The tested MaPMTs are the same ones that are used in the LHCb Run 3: the 1-inch R11265-103-M64 model and the 2-inch R12699-406-M64293 [145], both with 64 pixels. The 1-inch MaPMT contains 12 dynodes with a nominal signal transit time of 5.1 ns and nominal transit-time spread (TTS) of $\sim$ 150 ps. The 2-inch MaPMT has 10 dynodes resulting in 5.3 ns transit time and $\sim$ 120 ps TTS. Both sensors are mounted on a PCB with custom sockets which provide a bias voltage of around -1 kV to the photo-cathode and the dynodes through a resistor-divider chain. Additionally, it connects the MaPMT anodes to the FEBs [146].

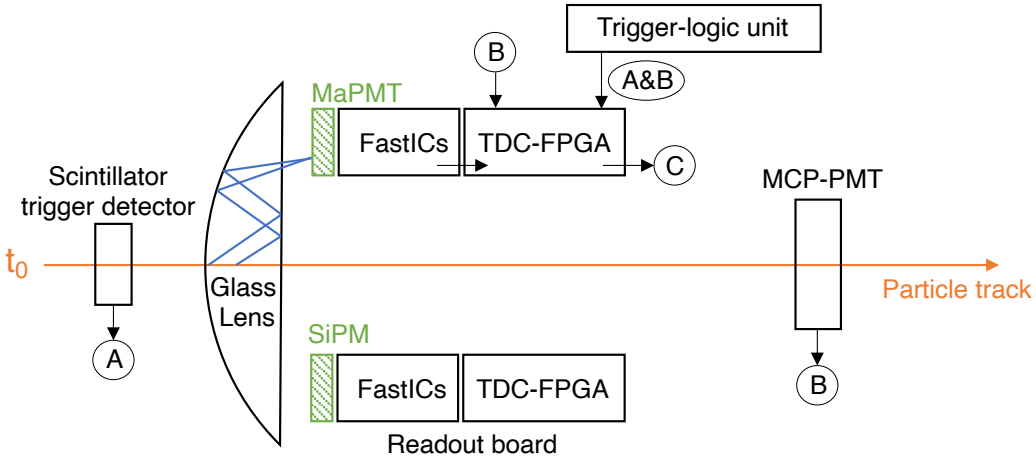

Figure C.3. Schematic overview of the testbeam experimental setup.

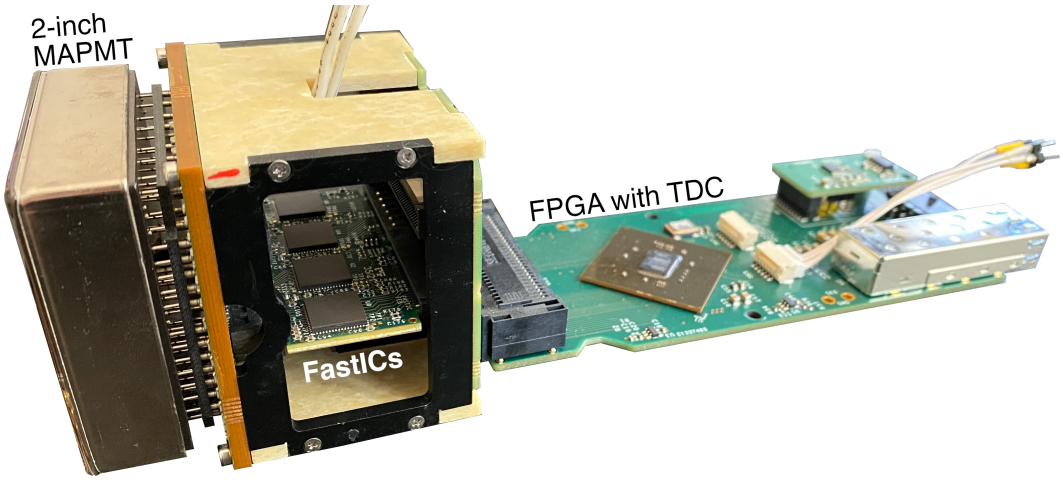

Figure C.4. The 2-inch MaPMT coupled to the FastIC ASIC.

During the test beam campaigns, two different Hamamatsu SiPM arrays with 64 pixels were tested:

- S13361-2050AE-08 with 2.0 mm channel dimensions and 50 μm cell pitch. At the suggested operating voltage of 54.1 V, the nominal gain is 1.7×10^6 M with 0.06 μA dark current per channel [147];
- S14161-3050HS-08 with 3.0 mm channel dimensions and 50 μm cell pitch. At the suggested operating voltage of 40.6 V the nominal gain is 2.5×10^6 M with 0.36 μA dark current per channel [148].

The signal is read from the SiPM anodes with a common cathode. At the rear-side of the SiPM boards, edge connectors are mounted to plug into up to four FEBs in an EC arrangement. The bias voltage to the SiPMs is provided through

the board from a DT8031M CAEN power supply. The current measured from the power supply was used to monitor the SiPM stability and approximate dark-count, thereby serving as a proxy for the operating temperature, which was around room temperature.

The experimental setup includes two scintillators, before and after the lens, marked as A and B in Fig. C.3. They are traversed by the charged beam and give the triggers to the acquisition system. Together, they are also used as a reference for the time measurement, given their combined time resolution below 100 ps.

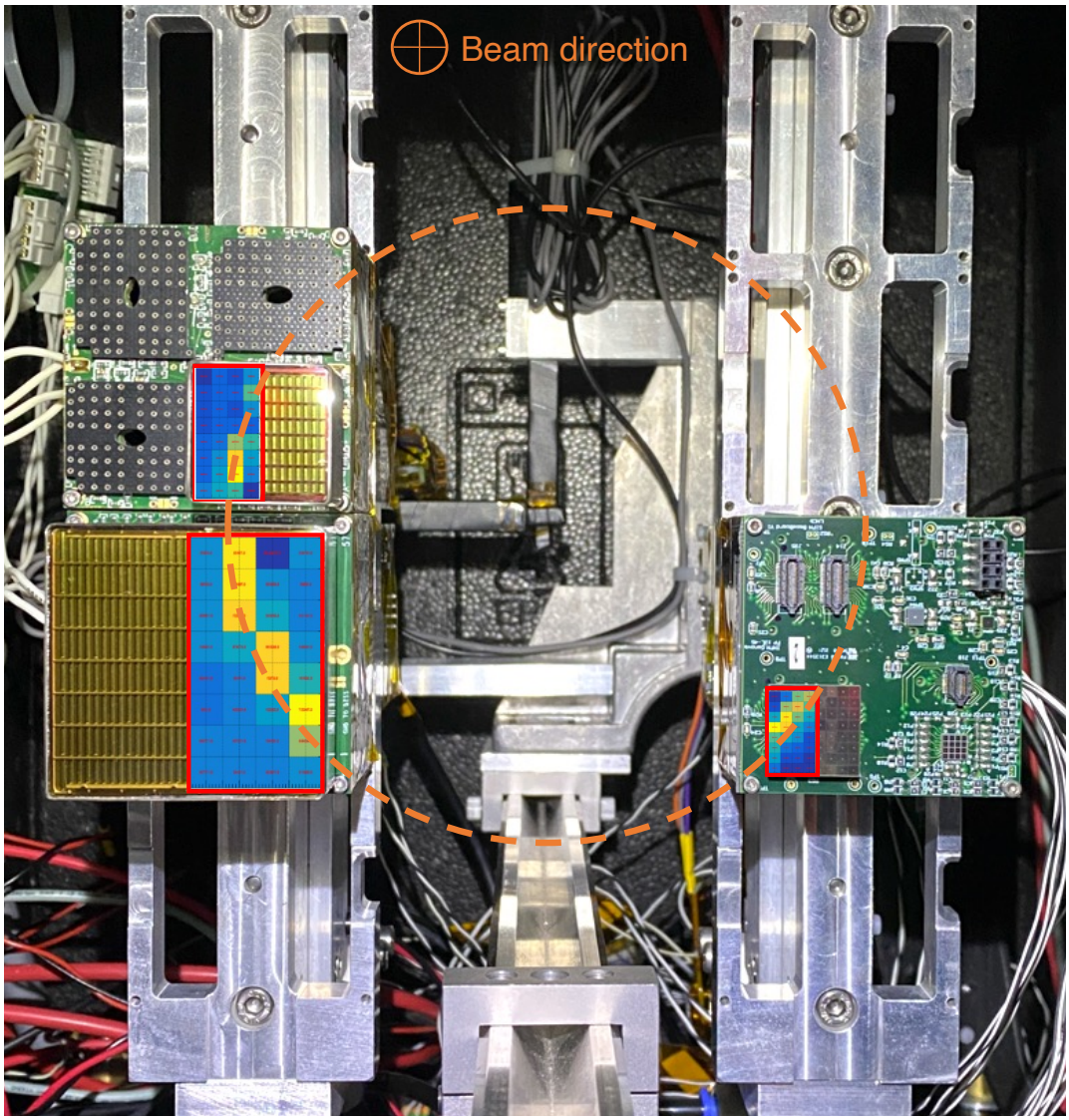

Figure C.5. Front-view picture of the experimental vertical plane with the 1-inch MaPMT (top-left), 2-inch MaPMT (bottom-left) and SiPM (right).

C.2 Cherenkov ring fit and ring time resolution

My contributions to the test beam campaigns were the participation in the data-taking periods (setup of the experimental apparatus and shifts) and the development of the Cherenkov ring-fitting algorithm. The algorithm can extract the geometrical variables of a Cherenkov ring, such as its centre coordinates and radius, and reject accidental photons which could deteriorate such measurement. Furthermore, the algorithm is used to estimate the ring time resolution as a function of the number of illuminated pixels. Indeed, due to the complexity of the geometry of the radiator lens and the lack of a full simulation of the experimental setup, my study primarily focuses on the extraction of the time resolution of the fitted rings more than on the measurement of the Cherekonv angle resolution.

The Cherenkov ring-fitting algorithm is applied on a trigger-by-trigger basis. Each trigger is associated with an event, which is characterized by several illuminated pixels on the three sensors. To find the best fit, a minimization process has been employed with the TMinuit class from CERN ROOT [149]. The formula R_f minimized in this process is

$$R_f = \Sigma_i w \left[\sqrt{(x_i - x_{\text{centre}})^2 + (y_i - y_{\text{centre}})^2} - R \right]. \tag{C.1}$$

Here, x_i and y_i denote the hit position, meaning the centre coordinates of the illuminated pixels i. The variables x_{centre} and y_{centre} represent the centre coordinates of the fitted ring while R corresponds to its radius. Each hit in Eq. C.1 is weighted with a factor w, taken as the inverse of the illuminated pixel size. Only Cherenkov rings with a number of illuminated pixels between 5 and 20 across all the sensors are considered. This range has been chosen by taking into account the distribution shown in Fig. C.6, representing the number of illuminated pixels per trigger on the three sensors.

The centre coordinates and radius distributions are illustrated in Fig. C.7. A typical Cherenkov ring, reconstructed by the fit, is shown in Fig. C.8.

The ring time resolution is estimated once accidental hits are rejected. This is done by requesting that the distance between the position of the illuminated pixel and the fitted ring is smaller than the pixel size. This distance D is defined as

$$D = \sqrt{(x_{ch} - x)^2 + (y_{ch} - y)^2} - R, \tag{C.2}$$

where x_{ch} and y_{ch} are the centre coordinates of the illuminated pixel and (x, y, R) are the parameters estimated from the ring-fitting algorithm. The distribution of the ring Time of Arrival (ToA), with respect to the trigger sensor, is shown in Fig. C.7 (bottom-right). This distribution is fitted in the center region with a Gaussian function for different numbers of illuminated pixels. In this way, a trend of the ring time resolution as a function of the number of hits is obtained. This trend is reported in Fig. C.9 for the 1-inch MaPMT. The ring time resolution improves as a function of the square root of the number of illuminated pixels on-ring, saturating around 200 ps.

The Cherenkov ring-fitting algorithm proves to be effective in removing accidental hits and estimating the ring time resolution.

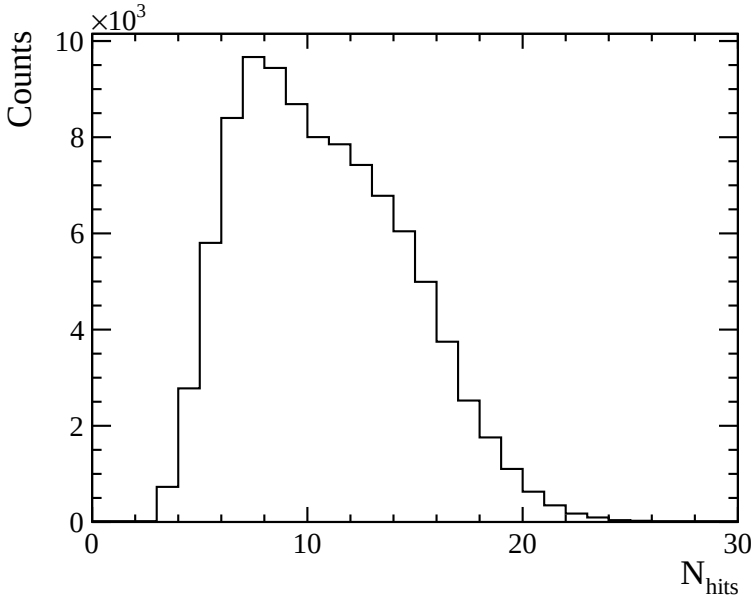

Figure C.6. Number of illuminated pixels per trigger on the three sensors.

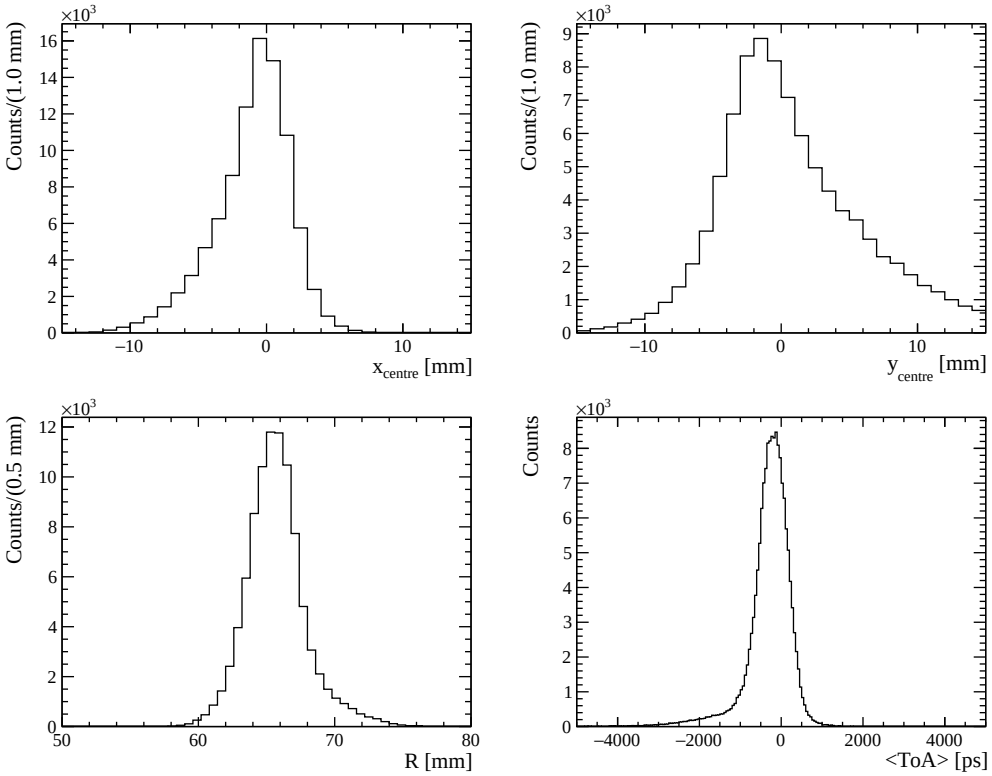

Figure C.7. Centre coordinates (top) and radius (bottom-left) distributions from the ring-fitting algorithm. Distribution of the ring ToA with respect to the trigger system for the 1-inch MaPMT (bottom-right).

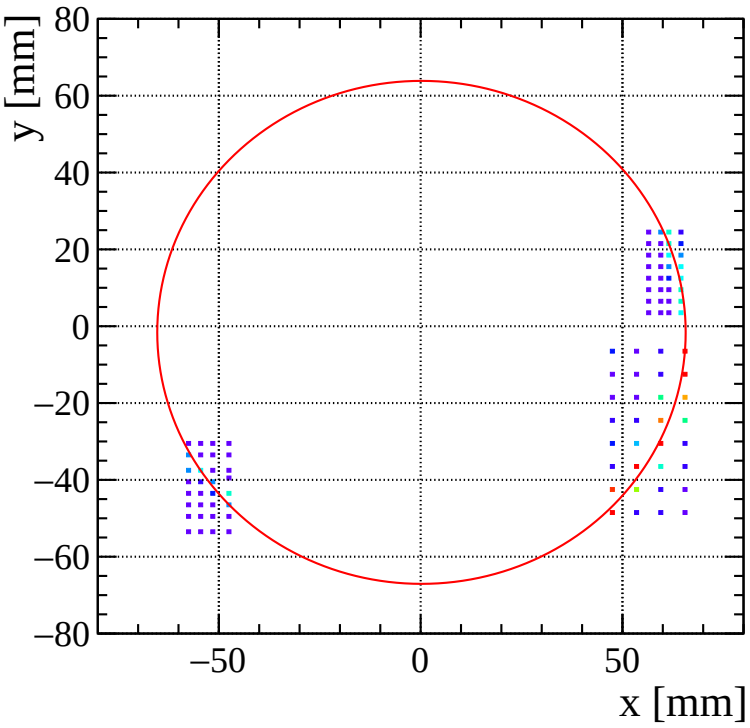

Figure C.8. Tipical Cherenkov ring reconstructed by the ring-fitting algorithm.

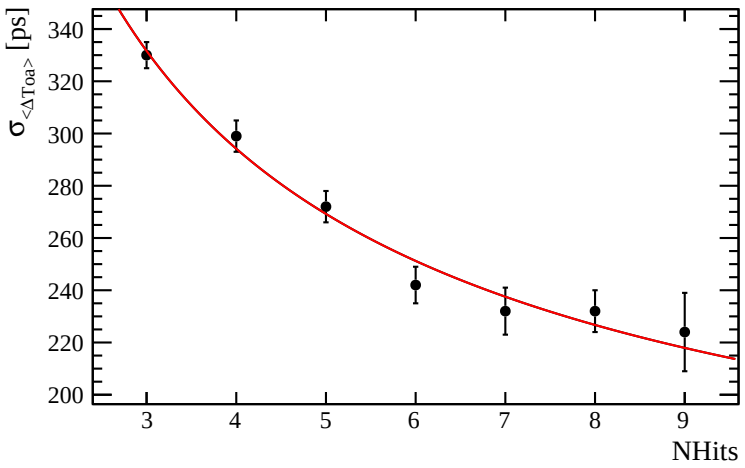

Figure C.9. Trend of the ring time resolution for the 1-inch MaPMT.

Bibliography

[1] J. J. Thomson, M.A., F.R.S., "XL. Cathode Rays," *The London, Edinburgh, and Dublin Philosophical Magazine and Journal of Science*, vol. 44, no. 269, pp. 293–316, 1897. [Online]. Available: https://doi.org/10.1080/14786449708621070

[2] E. Rutherford, F.R.S., "LXXIX. The scattering of α and β particles by matter and the structure of the atom," *The London, Edinburgh, and Dublin Philosophical Magazine and Journal of Science*, vol. 21, no. 125, pp. 669–688, 1911. [Online]. Available: https://doi.org/10.1080/14786440508637080

[3] E. Fermi, "Tentativo di una Teoria Dei Raggi β," *Il Nuovo Cimento (1924-1942)*, vol. 11, no. 1, pp. 1–19, 1934. [Online]. Available: https://doi.org/10.1007/BF02959820

[4] S. L. Glashow, "Partial-symmetries of weak interactions," *Nuclear Physics*, vol. 22, no. 4, pp. 579–588, 1961. [Online]. Available: https://doi.org/10.1016/0029-5582(61)90469-2

[5] A. Salam and J. Ward, "Electromagnetic and weak interactions," *Physics Letters*, vol. 13, no. 2, pp. 168–171, 1964. [Online]. Available: https://doi.org/10.1016/0031-9163(64)90711-5

[6] S. Weinberg, "A Model of Leptons," *Phys. Rev. Lett.*, vol. 19, pp. 1264–1266, 1967. [Online]. Available: https://link.aps.org/doi/10.1103/PhysRevLett.19.1264

[7] M. Gell-Mann, "A Schematic Model of Baryons and Mesons," *Resonance*, vol. 24, no. 8, pp. 923–925, 2019. [Online]. Available: https://doi.org/10.1007/s12045-019-0853-x

[8] G. Zweig, "An SU(3) model for strong interaction symmetry and its breaking. Version 2," *Developments in the Quark Theory of Hadrons. Vol. 1. (1964 -1978)*, pp. 22–101, 1964. [Online]. Available: http://doi.org/10.17181/CERN-TH-412

[9] P. W. Higgs, "Broken Symmetries and the Masses of Gauge Bosons," *Phys. Rev. Lett.*, vol. 13, pp. 508–509, 1964. [Online]. Available: https://link.aps.org/doi/10.1103/PhysRevLett.13.508

[10] G. Aad et al., "Observation of a new particle in the search for the Standard Model Higgs boson with the ATLAS detector at the LHC,"

Physics Letters B, vol. 716, no. 1, pp. 1–29, 2012. [Online]. Available: https://doi.org/10.1016/j.physletb.2012.08.020

[11] S. Chatrchyan et al., "Observation of a new boson at a mass of 125 GeV with the CMS experiment at the LHC," *Physics Letters B*, vol. 716, no. 1, pp. 30–61, 2012. [Online]. Available: https://doi.org/10.1016/j.physletb.2012.08.021

[12] Particle Data Group et al., "Review of Particle Physics," *Progress of Theoretical and Experimental Physics*, vol. 2022, no. 8, p. 083C01, 2022. [Online]. Available: https://doi.org/10.1093/ptep/ptac097

[13] G.'t Hooft and M. Veltman, "Regularization and renormalization of gauge fields," *Nuclear Physics B*, vol. 44, no. 1, pp. 189–213, 1972. [Online]. Available: https://doi.org/10.1016/0550-3213(72)90279-9

[14] F. Englert and R. Brout, "Broken Symmetry and the Mass of Gauge Vector Mesons," *Phys. Rev. Lett.*, vol. 13, pp. 321–323, 1964. [Online]. Available: https://link.aps.org/doi/10.1103/PhysRevLett.13.321

[15] G. S. Guralnik, C. R. Hagen, and T. W. B. Kibble, "Global Conservation Laws and Massless Particles," *Phys. Rev. Lett.*, vol. 13, pp. 585–587, 1964. [Online]. Available: https://link.aps.org/doi/10.1103/PhysRevLett.13.585

[16] N. Cabibbo, "Unitary Symmetry and Leptonic Decays," *Phys. Rev. Lett.*, vol. 10, pp. 531–533, 1963. [Online]. Available: https://link.aps.org/doi/10.1103/PhysRevLett.10.531

[17] S. L. Glashow, J. Iliopoulos, and L. Maiani, "Weak Interactions with Lepton-Hadron Symmetry," *Phys. Rev. D*, vol. 2, pp. 1285–1292, 1970. [Online]. Available: https://link.aps.org/doi/10.1103/PhysRevD.2.1285

[18] J. E. Augustin et al., "Discovery of a Narrow Resonance in e^+e^- Annihilation," *Phys. Rev. Lett.*, vol. 33, pp. 1406–1408, 1974. [Online]. Available: https://link.aps.org/doi/10.1103/PhysRevLett.33.1406

[19] J. J. Aubert et al., "Experimental Observation of a Heavy Particle J," *Phys. Rev. Lett.*, vol. 33, pp. 1404–1406, 1974. [Online]. Available: https://link.aps.org/doi/10.1103/PhysRevLett.33.1404

[20] J. H. Christenson, J. W. Cronin, V. L. Fitch, and R. Turlay, "Evidence for the 2π Decay of the K_2^0 Meson," *Phys. Rev. Lett.*, vol. 13, pp. 138–140, 1964. [Online]. Available: https://link.aps.org/doi/10.1103/PhysRevLett.13.138

[21] M. Kobayashi and T. Maskawa, "CP-Violation in the Renormalizable Theory of Weak Interaction," *Progress of Theoretical Physics*, vol. 49, no. 2, pp. 652–657, 1973. [Online]. Available: https://doi.org/10.1143/PTP.49.652

[22] L. Wolfenstein, "Parametrization of the Kobayashi-Maskawa Matrix," *Phys. Rev. Lett.*, vol. 51, pp. 1945–1947, 1983. [Online]. Available: https://link.aps.org/doi/10.1103/PhysRevLett.51.1945

[23] E. Aprile et al., "Physics reach of the XENON1T dark matter experiment." *Journal of Cosmology and Astroparticle Physics*, vol. 2016, no. 04, p. 027, 2016. [Online]. Available: https://dx.doi.org/10.1088/1475-7516/2016/04/027

[24] Aalseth, C. E. et al., "DarkSide-20k: A 20 tonne two-phase LAr TPC for direct dark matter detection at LNGS," *The European Physical Journal Plus*, vol. 133, no. 3, p. 131, 2018. [Online]. Available: https://doi.org/10.1140/epjp/i2018-11973-4

[25] Y. Suzuki, "The Super-Kamiokande experiment," *The European Physical Journal C*, vol. 79, no. 4, p. 298, 2019. [Online]. Available: https://doi.org/10.1140/epjc/s10052-019-6796-2

[26] W. Heinrich, "First observation and precision measurement of direct CP violation: the experiments NA31 and NA48," *Physics Reports*, vol. 403-404, pp. 19–25, 2004. [Online]. Available: https://doi.org/10.1016/j.physrep.2004.08.007

[27] A. Alavi-Harati et al., "Observation of Direct CP Violation in $K_{S,L} \to \pi\pi$ Decays," *Phys. Rev. Lett.*, vol. 83, pp. 22–27, 1999. [Online]. Available: https://link.aps.org/doi/10.1103/PhysRevLett.83.22

[28] I. Belyaev, G. Carboni, N. Harnew, C. Matteuzzi, and F. Teubert, "The history of LHCb," *The European Physical Journal H*, vol. 46, no. 1, p. 3, 2021. [Online]. Available: https://doi.org/10.1140/epjh/s13129-021-00002-z

[29] E. Kou et al., "The Belle II Physics Book," *Progress of Theoretical and Experimental Physics*, vol. 2019, no. 12, p. 123C01, 2019. [Online]. Available: https://doi.org/10.1093/ptep/ptz106

[30] H. K. Park et al., "Evidence for the Decay $\Sigma^+ \to p\mu^+\mu^-$," *Phys. Rev. Lett.*, vol. 94, p. 021801, 2005. [Online]. Available: https://link.aps.org/doi/10.1103/PhysRevLett.94.021801

[31] R. Aaij et al., "Evidence for the Rare Decay $\Sigma^+ \to p\mu^+\mu^-$," *Phys. Rev. Lett.*, vol. 120, p. 221803, 2018. [Online]. Available: https://link.aps.org/doi/10.1103/PhysRevLett.120.221803

[32] X.-G. He, J. Tandean, and G. Valencia, "Decay $\Sigma^+ \to p\ell^+\ell^-$ within the standard model," *Phys. Rev. D*, vol. 72, p. 074003, 2005. [Online]. Available: https://link.aps.org/doi/10.1103/PhysRevD.72.074003

[33] ——, "Implications of a new particle from the HyperCP data on $\Sigma^+ \to p\mu^+\mu^-$," *Physics Letters B*, vol. 631, no. 3, pp. 100–108, 2005. [Online]. Available: https://doi.org/10.1016/j.physletb.2005.10.005

[34] ——, "Decay rate and asymmetries of $\Sigma^+ \to \mu^+\mu^-$," *Journal of High Energy Physics*, vol. 2018, no. 10, p. 40, 2018. [Online]. Available: https://doi.org/10.1007/JHEP10(2018)040

[35] R. Baur and J. Kambor, "Generalized heavy baryon chiral perturbation theory," *The European Physical Journal C - Particles and Fields*, vol. 7, no. 3, pp. 507–524, 1999. [Online]. Available: https://doi.org/10.1007/s100529801024

[36] R. P. Springer, "Heavy baryon chiral perturbation theory and the weak nonleptonic p-wave decays of the baryon octet," *Physics Letters B*, vol. 461, no. 3, pp. 167–174, 1999. [Online]. Available: https://doi.org/10.1016/S0370-2693(99)00714-5

[37] J. F. Donoghue, E. Golowich, and B. R. Holstein, *Dynamics of the Standard Model*, ser. Cambridge Monographs on Particle Physics, Nuclear Physics and Cosmology. Cambridge University Press, 2023. [Online]. Available: https://doi.org/10.1017/CBO9780511803512

[38] A. A. El-Hady and J. Tandean, "Hyperon nonleptonic decays in chiral perturbation theory reexamined," *Phys. Rev. D*, vol. 61, p. 114014, 2000. [Online]. Available: https://link.aps.org/doi/10.1103/PhysRevD.61.114014

[39] R. A. Burnstein et al., "HyperCP: A high-rate spectrometer for the study of charged hyperon and kaon decays," *Nuclear Instruments and Methods in Physics Research Section A: Accelerators, Spectrometers, Detectors and Associated Equipment*, vol. 541, no. 3, pp. 516–565, 2005. [Online]. Available: https://doi.org/10.1016/j.nima.2004.12.031

[40] G. J. Feldman and R. D. Cousins, "Unified approach to the classical statistical analysis of small signals," *Phys. Rev. D*, vol. 57, pp. 3873–3889, 1998. [Online]. Available: https://link.aps.org/doi/10.1103/PhysRevD.57.3873

[41] R. D. Cousins and V. L. Highland, "Incorporating systematic uncertainties into an upper limit," *Nuclear Instruments and Methods in Physics Research Section A: Accelerators, Spectrometers, Detectors and Associated Equipment*, vol. 320, no. 1, pp. 331–335, 1992. [Online]. Available: https://doi.org/10.1016/0168-9002(92)90794-5

[42] X.-G. He, J. Tandean, and G. Valencia, "Does the HyperCP Evidence for the Decay $\Sigma^+ \to p\mu^+\mu^-$ Indicate a Light Pseudoscalar Higgs Boson?" *Phys. Rev. Lett.*, vol. 98, p. 081802, 2007. [Online]. Available: https://link.aps.org/doi/10.1103/PhysRevLett.98.081802

[43] ——, "Light Higgs production in hyperon decay," *Phys. Rev. D*, vol. 74, p. 115015, 2006. [Online]. Available: https://link.aps.org/doi/10.1103/PhysRevD.74.115015

[44] D. S. Gorbunov and V. A. Rubakov, "Sgoldstino interpretation of HyperCP events," *Phys. Rev. D*, vol. 73, p. 035002, 2006. [Online]. Available: https://link.aps.org/doi/10.1103/PhysRevD.73.035002

[45] S. V. Demidov and D. S. Gorbunov, "More about the sgoldstino interpretation of HyperCP events," *JETP Letters*, vol. 84, no. 9, pp. 479–484, 2007. [Online]. Available: https://doi.org/10.1134/S0021364006210028

[46] C. Q. Geng and Y. K. Hsiao, "Constraints on the new particle in $\Sigma^+ \to p\mu^+\mu^-$," *Physics Letters B*, vol. 632, no. 2, pp. 215–218, 2006. [Online]. Available: https://doi.org/10.1016/j.physletb.2005.10.056

[47] N. G. Deshpande, G. Eilam and J. Jiang, "On the possibility of a new boson X0(214MeV) in $\Sigma^+ \to p\mu^+\mu^-$," *Physics Letters B*, vol. 632, no. 2, pp. 212–214, 2006. [Online]. Available: https://doi.org/10.1016/j.physletb.2005.10.050

[48] C.-H. Chen, C.-Q. Geng, and C.-W. Kao, "U-boson and the HyperCP exotic events," *Physics Letters B*, vol. 663, no. 5, pp. 400–404, 2008. [Online]. Available: https://doi.org/10.1016/j.physletb.2008.04.053

[49] G. Xiangdong, C. S. Li, Z. Li, and H. Zhang, "Contributions from SUSY-FCNC couplings to the interpretation of the HyperCP events for the decay $\Sigma^+ \to p\mu^+\mu^-$," *The European Physical Journal C*, vol. 55, no. 2, pp. 317–324, 2008. [Online]. Available: https://doi.org/10.1140/epjc/s10052-008-0580-z

[50] M. L. Mangano and P. Nason, "Radiative Quarkonium Decays and the NMSSM Higgs Interpretation of the HyperCP $\Sigma^+ \to p\mu^+\mu^-$ events," *Modern Physics Letters A*, vol. 22, no. 19, pp. 1373–1379, 2007. [Online]. Available: https://doi.org/10.1142/S0217732307023729

[51] W. Love et al., "Search for Very Light CP-Odd Higgs Boson in Radiative Decays of $\Upsilon(1S)$," *Phys. Rev. Lett.*, vol. 101, p. 151802, 2008. [Online]. Available: https://link.aps.org/doi/10.1103/PhysRevLett.101.151802

[52] B. Aubert et al., "Search for Dimuon Decays of a Light Scalar Boson in Radiative Transitions $\Upsilon \to \gamma A^0$," *Phys. Rev. Lett.*, vol. 103, p. 081803, 2009. [Online]. Available: https://link.aps.org/doi/10.1103/PhysRevLett.103.081803

[53] H. J. Hyun et al., "Search for a Low Mass Particle Decaying into $\mu^+\mu^-$ in $B^0 \to K^{*0}X$ and $B^0 \to \rho^0 X$ at Belle," *Phys. Rev. Lett.*, vol. 105, p. 091801, 2010. [Online]. Available: https://link.aps.org/doi/10.1103/PhysRevLett.105.091801

[54] M. Ablikim et al., "Search for a light CP-odd Higgs boson in radiative decays of J/ψ," *Phys. Rev. D*, vol. 93, p. 052005, 2016. [Online]. Available: https://link.aps.org/doi/10.1103/PhysRevD.93.052005

[55] R. Aaij et al., "Search for Rare $B^0_{(s)} \to \mu^+\mu^-\mu^+\mu^-$ Decays," *Phys. Rev. Lett.*, vol. 110, p. 211801, 2013. [Online]. Available: https://link.aps.org/doi/10.1103/PhysRevLett.110.211801

[56] ——, "Search for Hidden-Sector Bosons in $B^0 \to K^{*0}\mu^+\mu^-$ Decays," *Phys. Rev. Lett.*, vol. 115, p. 161802, 2015. [Online]. Available: https://link.aps.org/doi/10.1103/PhysRevLett.115.161802

[57] ——, "Search for Dark Photons Produced in 13 TeV pp Collisions," *Phys. Rev. Lett.*, vol. 120, p. 061801, Feb 2018. [Online]. Available: https://link.aps.org/doi/10.1103/PhysRevLett.120.061801

[58] M. Ablikim et al., "Precision Measurement of the Decay $\Sigma^+ \to p\gamma$ in the Process $J/\psi \to \Sigma^+\overline{\Sigma}^-$," *Phys. Rev. Lett.*, vol. 130, p. 211901, 2023. [Online]. Available: https://link.aps.org/doi/10.1103/PhysRevLett.130.211901

[59] L. Evans and P. Bryant, "LHC Machine," *Journal of Instrumentation*, vol. 3, no. 08, p. S08001, 2008. [Online]. Available: https://dx.doi.org/10.1088/1748-0221/3/08/S08001

[60] T. Taylor and D. Treille, "The Large Electron Positron Collider (LEP): Probing the Standard Model," *Adv. Ser. Direct. High Energy Phys.*, vol. 27, pp. 217–261, 2017. [Online]. Available: https://doi.org/10.1142/9789814749145_0007

[61] E. Lopienska, "The CERN accelerator complex, layout in 2022. Complexe des accélérateurs du CERN en janvier 2022," *CERN-GRAPHICS-2022-001*, 2022, General Photo. [Online]. Available: https://cds.cern.ch/record/2800984

[62] M. Vretenar et al., "Linac4 design report," *CERN Yellow Reports: Monographs*, vol. 6, 2020. [Online]. Available: https://cds.cern.ch/record/2736208

[63] K. Hanke, "Past and present operation of the CERN PS Booster," *International Journal of Modern Physics A*, vol. 28, no. 13, p. 1330019, 2013. [Online]. Available: https://doi.org/10.1142/S0217751X13300196

[64] E. Regenstreif, "The CERN Proton Synchrotron," *CERN Yellow Reports: Monographs*, 1962. [Online]. Available: https://cds.cern.ch/record/278715

[65] N. Doble et al., "The Super Proton Synchrotron (SPS): A Tale of Two Lives," *Adv. Ser. Direct. High Energy Phys.*, vol. 27, pp. 135–177, 2017. [Online]. Available: https://doi.org/10.1142/9789814749145_0005

[66] The ATLAS Collaboration, "The ATLAS Experiment at the CERN Large Hadron Collider," *Journal of Instrumentation*, vol. 3, no. 08, p. S08003, 2008. [Online]. Available: https://dx.doi.org/10.1088/1748-0221/3/08/S08003

[67] The CMS Collaboration, "The CMS experiment at the CERN LHC," *Journal of Instrumentation*, vol. 3, no. 08, p. S08004, 2008. [Online]. Available: https://dx.doi.org/10.1088/1748-0221/3/08/S08004

[68] The ALICE Collaboration, "The ALICE experiment at the CERN LHC," *Journal of Instrumentation*, vol. 3, no. 08, p. S08002, 2008. [Online]. Available: https://dx.doi.org/10.1088/1748-0221/3/08/S08002

[69] T. Schörner-Sadenius, "The Large Hadron Collider: Harvest of Run 1," *Springer*, 2015. [Online]. Available: https://doi.org/10.1007/978-3-319-15001-7

[70] J. T. Boyd, "LHC Run-2 and future prospects," *Proceedings of the 2019 European School of High-Energy Physics*, vol. 5, 2021. [Online]. Available: https://doi.org/10.23730/CYRSP-2021-005.247

[71] R. Aaij et al., "Measurement of the b-Quark Production Cross Section in 7 and 13 TeV pp Collisions," *Phys. Rev. Lett.*, vol. 118, p. 052002, 2017, [Erratum: Phys. Rev. Lett. 119, no. 16, 169901 (2017)]. [Online]. Available: https://link.aps.org/doi/10.1103/PhysRevLett.118.052002

[72] ——, "Measurements of prompt charm production cross-sections in pp collisions at $\sqrt{s} = 13$ TeV," *Journal of High Energy Physics*, vol. 2016, no. 3, p. 159, 2016, [Erratum: JHEP05, 074 (2017)]. [Online]. Available: https://doi.org/10.1007/JHEP03(2016)159

[73] The LHCb Collaboration, "The LHCb Detector at the LHC," *Journal of Instrumentation*, vol. 3, no. 08, p. S08005, 2008. [Online]. Available: https://dx.doi.org/10.1088/1748-0221/3/08/S08005

[74] R. Antunes-Nobrega et al., "LHCb reoptimized detector design and performance: Technical Design Report," *LHCb technical design report*, 2003. [Online]. Available: https://cds.cern.ch/record/630827

[75] M. P. Altarelli and F. Teubert, "B physics at LHCb," *International Journal of Modern Physics A*, vol. 23, no. 32, pp. 5117–5136, 2008. [Online]. Available: https://doi.org/10.1142/S0217751X08042791

[76] H. Burkhardt and P. Grafström, "Absolute Luminosity from Machine Parameters," *CERN-LHC-PROJECT-Report-1019*, 2007. [Online]. Available: http://cds.cern.ch/record/1056691

[77] F. Follin and D. Jacquet, "Implementation and experience with luminosity levelling with offset beam," *ICFA Mini-Workshop on Beam-Beam Effects in Hadron Colliders*, pp. 183–187, 2014. [Online]. Available: http://cds.cern.ch/record/1955354

[78] The LHCb Collaboration, "LHCb detector performance," *International Journal of Modern Physics A*, vol. 30, no. 07, p. 1530022, 2015. [Online]. Available: https://doi.org/10.1142/S0217751X15300227

[79] P. R. Barbosa-Marinho et al., "LHCb VELO (VErtex LOcator): Technical Design Report," *LHCb technical design report*, 2001. [Online]. Available: https://cds.cern.ch/record/504321

[80] R. Aaij et al., "Performance of the LHCb Vertex Locator," *Journal of Instrumentation*, vol. 9, no. 09, p. P09007, 2014. [Online]. Available: https://dx.doi.org/10.1088/1748-0221/9/09/P09007

[81] S. Amato et al., "LHCb magnet: Technical Design Report," *LHCb technical design report*, 2000. [Online]. Available: https://cds.cern.ch/record/424338

[82] P. R. Barbosa-Marinho et al., "LHCb inner tracker: Technical Design Report," *LHCb technical design report*, 2002. [Online]. Available: https://cds.cern.ch/record/582793

[83] J. Luisier, "Performance of LHCb Silicon Tracker Detector in the LHC," *Physics Procedia*, vol. 37, pp. 851–858, 2012. [Online]. Available: https://doi.org/10.1016/j.phpro.2012.04.097

[84] R. Arink et al., "Performance of the LHCb Outer Tracker," *Journal of Instrumentation*, vol. 9, no. 01, p. P01002, 2014. [Online]. Available: https://dx.doi.org/10.1088/1748-0221/9/01/P01002

[85] O. Callot, "FastVelo, a fast and efficient pattern recognition package for the Velo," *LHCb technical report*, 2011. [Online]. Available: https://cds.cern.ch/record/1322644

[86] O. Callot and M. Schiller, "PatSeeding: A Standalone Track Reconstruction Algorithm," *LHCb technical report*, 2008. [Online]. Available: https://cds.cern.ch/record/1119095

[87] O. Callot and S. Hansmann-Menzemer, "The Forward Tracking: Algorithm and Performance Studies," *LHCb technical report*, 2007. [Online]. Available: https://cds.cern.ch/record/1033584

[88] M. Needham, "Performance of the Track Matching," *LHCb technical report*, 2007. [Online]. Available: https://cds.cern.ch/record/1060807

[89] R. Frühwirth, "Application of Kalman filtering to track and vertex fitting," *Nuclear Instruments and Methods in Physics Research Section A: Accelerators, Spectrometers, Detectors and Associated Equipment*, vol. 262, no. 2, pp. 444–450, 1987. [Online]. Available: https://doi.org/10.1016/0168-9002(87)90887-4

[90] R. Aaij et al., "Selection and processing of calibration samples to measure the particle identification performance of the LHCb experiment in Run 2," *EPJ Techniques and Instrumentation*, vol. 6, no. 1, p. 1, 2019. [Online]. Available: https://doi.org/10.1140/epjti/s40485-019-0050-z

[91] S. Amato et al., "LHCb RICH: Technical Design Report," *LHCb technical design report*, 2000. [Online]. Available: https://cds.cern.ch/record/494263

[92] M. Adinolfi et al., "Performance of the LHCb RICH detector at the LHC," *The European Physical Journal C*, vol. 73, no. 5, p. 2431, 2013. [Online]. Available: https://doi.org/10.1140/epjc/s10052-013-2431-9

[93] S. Amato et al., "LHCb calorimeters: Technical Design Report," *LHCb technical design report*, 2000. [Online]. Available: https://cds.cern.ch/record/494264

[94] C. Abellán Beteta et al., "Calibration and performance of the LHCb calorimeters in Run 1 and 2 at the LHC," *LHCb technical report*, 2020. [Online]. Available: https://cds.cern.ch/record/2729028

[95] C. Coca et al., "The hadron calorimeter prototype beam-test results," *LHCb technical report*, 2000. [Online]. Available: https://cds.cern.ch/record/691519

[96] P. R. Barbosa-Marinho et al., "LHCb muon system: Technical Design Report," *LHCb technical design report*, 2001. [Online]. Available: http://cds.cern.ch/record/504326

[97] F. Sauli, "Principles of operation of multiwire proportional and drift chambers," *LHCb technical report*, 1977. [Online]. Available: https://cds.cern.ch/record/117989

[98] G. Bencivenni et al., "A triple GEM detector with pad readout for high rate charged particle triggering," *Nuclear Instruments and Methods in Physics Research Section A: Accelerators, Spectrometers, Detectors and Associated Equipment*, vol. 488, no. 3, pp. 493–502, 2002. [Online]. Available: https://doi.org/10.1016/S0168-9002(02)00515-6

[99] C. Marin Benito, "PID strategy and performance at LHCb in Run 2," *PoS*, vol. ICHEP2018, p. 687, 2019. [Online]. Available: https://cds.cern.ch/record/2702461

[100] R. Antunes-Nobrega et al., "LHCb trigger system: Technical Design Report," *LHCb technical design report*, 2003. [Online]. Available: https://cds.cern.ch/record/630828

[101] R. Aaij et al., "Design and performance of the LHCb trigger and full real-time reconstruction in Run 2 of the LHC," *Journal of Instrumentation*, vol. 14, no. 04, p. P04013, 2019. [Online]. Available: https://dx.doi.org/10.1088/1748-0221/14/04/P04013

[102] F. Dordei, "LHCb detector and trigger performance in Run II," *EPJ Web Conf.*, vol. 164, p. 01016, 2017. [Online]. Available: https://cds.cern.ch/record/2310660

[103] S. Akar et al., "Review Document: Low Level Trigger (LLT)," *LHCb technical report*, 2014. [Online]. Available: https://cds.cern.ch/record/1700272

[104] G. Dujany and B. Storaci, "Real-time alignment and cali bration of the LHCb Detector in Run II," *Journal of Physics: Conference Series*, vol. 664, no. 8, p. 082010, 2015. [Online]. Available: https://dx.doi.org/10.1088/1742-6596/664/8/082010

[105] T. Likhomanenko et al., "LHCb Topological Trigger Reoptimization," *Journal of Physics: Conference Series*, vol. 664, no. 8, p. 082025, 2015. [Online]. Available: https://dx.doi.org/10.1088/1742-6596/664/8/082025

[106] G. Corti et al., "Software for the LHCb experiment," *IEEE Transactions on Nuclear Science*, vol. 53, no. 3, pp. 1323–1328, 2006. [Online]. Available: https://doi.org/10.1109/TNS.2006.872627

[107] G. Barrand et al., "GAUDI - A software architecture and framework for building HEP data processing applications," *Computer Physics Communications*, vol. 140, no. 1, pp. 45–55, 2001. [Online]. Available: https://doi.org/10.1016/S0010-4655(01)00254-5

[108] M. Clemencic et al., "The LHCb Simulation Application, Gauss: Design, Evolution and Experience," *Journal of Physics: Conference Series*, vol. 331, no. 3, p. 032023, 2011. [Online]. Available: https://dx.doi.org/10.1088/1742-6596/331/3/032023

[109] T. Sjöstrand et al., "An introduction to PYTHIA 8.2," *Computer Physics Communications*, vol. 191, pp. 159–177, 2015. [Online]. Available: https://doi.org/10.1016/j.cpc.2015.01.024

[110] D. J. Lange, "The EvtGen particle decay simulation package," *Nuclear Instruments and Methods in Physics Research Section A: Accelerators, Spectrometers, Detectors and Associated Equipment*, vol. 462, no. 1, pp. 152–155, 2001. [Online]. Available: https://doi.org/10.1016/S0168-9002(01)00089-4

[111] N. Davidson, T. Przedzinski and Z. Was, "Photos interface in c++: Technical and physics documentation," *Computer Physics Communications*, vol. 199, pp. 86–101, 2016. [Online]. Available: https://doi.org/10.1016/j.cpc.2015.09.013

[112] S. Agostinelli et al., "Geant4 - a simulation toolkit," *Nuclear Instruments and Methods in Physics Research Section A: Accelerators, Spectrometers, Detectors and Associated Equipment*, vol. 506, no. 3, pp. 250–303, 2003. [Online]. Available: https://doi.org/10.1016/S0168-9002(03)01368-8

[113] R. Antunes-Nobrega et al., "LHCb computing: Technical Design Report," *LHCb technical design report*, 2005. [Online]. Available: https://cds.cern.ch/record/835156

[114] M. Frank et al., "Optimization of the HLT Resource Consumption in the LHCb Experiment," *Journal of Physics: Conference Series*, vol. 396, no. 1, p. 012021, 2012. [Online]. Available: https://dx.doi.org/10.1088/1742-6596/396/1/012021

[115] The LHCb Collaboration, "LHCb Trigger and Online Upgrade Technical Design Report," *LHCb technical design report*, 2014. [Online]. Available: https://cds.cern.ch/record/1701361

[116] ——, "LHCb VELO Upgrade Technical Design Report," *LHCb technical design report*, 2013. [Online]. Available: https://cds.cern.ch/record/1624070

[117] ——, "LHCb Tracker Upgrade Technical Design Report," *LHCb technical design report*, 2014. [Online]. Available: https://cds.cern.ch/record/1647400

[118] ——, "LHCb PID Upgrade Technical Design Report," *LHCb technical design report*, 2013. [Online]. Available: https://cds.cern.ch/record/1624074

[119] A. Cardini, "The LHCb Muon Upgrade," *Journal of Instrumentation*, vol. 9, no. 02, p. C02014, 2014. [Online]. Available: https://dx.doi.org/10.1088/1748-0221/9/02/C02014

[120] F. Dettori, D. Martinez Santos, and J. Prisciandaro, "Low-p_T dimuon triggers at LHCb in Run 2," *LHCb technical report*, 2017. [Online]. Available: https://cds.cern.ch/record/2297352

[121] R. Aaij et al., "Optimization of the muon reconstruction algorithms for LHCb Run 2," *LHCb technical report*, 2017. [Online]. Available: https://cds.cern.ch/record/2253050

[122] S. Tolk, J. Albrecht, F. Dettori and A. Pellegrino, "Data driven trigger efficiency determination at LHCb," *LHCb technical report*, 2014. [Online]. Available: https://cds.cern.ch/record/1701134

[123] I. Belyaev et al., "Handling of the generation of primary events in Gauss, the LHCb simulation framework," *Journal of Physics: Conference Series*, vol. 331, no. 3, p. 032047, 2011. [Online]. Available: https://dx.doi.org/10.1088/1742-6596/331/3/032047

[124] O. Deschamps, F. P. Machefert, M. H. Schune, G. Pakhlova and I. Belyaev, "Photon and neutral pion reconstruction," *LHCb technical report*, 2003. [Online]. Available: https://cds.cern.ch/record/691634

[125] G. A. Cowan, D. C. Craik and M. D. Needham, "Rapidsim: An application for the fast simulation of heavy-quark hadron decays," *Computer Physics Communications*, vol. 214, pp. 239–246, 2017. [Online]. Available: https://doi.org/10.1016/j.cpc.2017.01.029

[126] J. Therhaag, "TMVA Toolkit for multivariate data analysis in ROOT," *PoS*, vol. ICHEP2010, p. 510, 2010. [Online]. Available: https://doi.org/10.48550/arXiv.physics/0703039

[127] A. Blum, A. Kalai, and J. Langford, "Beating the Hold-out: Bounds for K-Fold and Progressive Cross-Validation," *Proceedings of the Twelfth Annual Conference on Computational Learning Theory*, p. 203–208, 1999. [Online]. Available: https://doi.org/10.1145/307400.307439

[128] G. Punzi, "Sensitivity of searches for new signals and its optimization," *Proceedings of PHYSTAT2003: Statistical Problems in Particle Physics, Astrophysics, and Cosmology*, vol. C030908, p. MODT002, 2003. [Online]. Available: https://arxiv.org/abs/physics/0308063

[129] D. Martínez Santos and F. Dupertuis, "Mass distributions marginalized over per-event errors," *Nuclear Instruments and Methods in Physics Research Section A: Accelerators, Spectrometers, Detectors and Associated Equipment*, vol. 764, pp. 150–155, 2014. [Online]. Available: https://doi.org/10.1016/j.nima.2014.06.081

[130] H. Albrecht et al., "Search for hadronic b→u decays," *Physics Letters B*, vol. 241, no. 2, pp. 278–282, 1990. [Online]. Available: https://doi.org/10.1016/0370-2693(90)91293-K

[131] T.J. Rivlin, "Chebyshev Polynomials," *Dover Books on Mathematics*, 2020. [Online]. Available: https://books.google.it/books?id=3s0mygEACAAJ

[132] M. Rosenblatt, "Remarks on Some Nonparametric Estimates of a Density Function," *The Annals of Mathematical Statistics*, vol. 27, no. 3, pp. 832–837, 1956. [Online]. Available: https://doi.org/10.1214/aoms/1177728190

[133] L. Z. Kelley, "kalepy: a Python package for kernel density estimation, sampling and plotting," *Journal of Open Source Software*, vol. 6, no. 57, p. 2784, 2021. [Online]. Available: https://doi.org/10.21105/joss.02784

[134] L. Anderlini et al., "The PIDCalib package," *LHCb technical report*, 2016. [Online]. Available: https://cds.cern.ch/record/2202412

[135] I. M. Belyaev, E. M. Govorkova, V. Yu. Egorychev and D. V. Savrina, "Study of $\pi 0/\gamma$ reconstruction and selection efficiency in the LHCb experiment," *Moscow University Physics Bulletin*, vol. 70, no. 6, pp. 497–503, 2015. [Online]. Available: https://doi.org/10.3103/S0027134915060077

[136] E. Govorkova, "Study of $\pi 0/\gamma$ efficiency using B meson decays in the LHCb experiment," *Physics of Atomic Nuclei*, vol. 79, no. 11, pp. 1474–1476, 2016. [Online]. Available: https://doi.org/10.1134/S1063778816100070

[137] A. L. Read, "Presentation of search results: the CLs technique," *Journal of Physics G: Nuclear and Particle Physics*, vol. 28, no. 10, p. 2693, 2002. [Online]. Available: https://dx.doi.org/10.1088/0954-3899/28/10/313

[138] F. Keizer, "Sub-nanosecond Cherenkov photon detection for LHCb particle identification in high-occupancy conditions and semiconductor tracking for muon scattering tomography," *CERN-THESIS-2019-203*, 2020. [Online]. Available: https://doi.org/10.17863/CAM.45822

[139] R. Aaij et al., "The LHCb upgrade I," *LHCb-DP-2022-002*, 2022. [Online]. Available: https://doi.org/10.48550/arXiv.2305.10515

[140] F. Keizer, "A novel fast-timing readout chain for LHCb RICH LS3 and prototype beam tests," *Nuclear Instruments and Methods in Physics Research Section A: Accelerators, Spectrometers, Detectors and Associated Equipment*, vol. 1055, p. 168475, 2023. [Online]. Available: https://doi.org/10.1016/j.nima.2023.168475

[141] R. Ballabriga, C. D'Ambrosio, S. Easo, F. Keizer, A. Petrolini, and S. W. (Eds.), "Proposal for LHCb RICH detector enhancements during LHC Long Shutdown 3," *CERN-LHCb-PUB-014*, 2021. [Online]. Available: https://cds.cern.ch/record/2798273

[142] R. Aaij et al., "Framework TDR for the LHCb Upgrade II: Opportunities in flavour physics, and beyond, in the HL-LHC era," *LHCb technical report*, 2021. [Online]. Available: https://cds.cern.ch/record/2776420"

[143] S. Gómez et al., "FastIC: a fast integrated circuit for the readout of high performance detectors," *Jinst*, vol. 17 C05027, 2022. [Online]. Available: https://doi.org/10.1088/1748-0221/17/05/C05027

[144] L. N. Cojocariu, D. Foulds-Holt, F. Keizer, V. M. Placinta and S. Wotton, "A multi-channel TDC-in- FPGA with 150 ps bins for time-resolved readout of Cherenkov photons," *NIMA*, vol. 1055, p. 168483, 2022. [Online]. Available: https://doi.org/10.1016/j.nima.2023.168483

[145] Hamamatsu Photonics, "R11265-103-M64 and R12699-406-M64 datasheets." [Online]. Available: https://www.hamamatsu.com/eu/en/product/optical-sensors/pmt/pmt_tube-alone/metal-package-type/

[146] M. Ameri et al., "Design of a Base-Board for arrays of closely packed Multi-Anode Photo-Multipliers," *Nuclear Instruments and Methods in*

Physics Research Section A: Accelerators, Spectrometers, Detectors and Associated Equipment, vol. 550, no. 3, pp. 559–566, 2005. [Online]. Available: https://doi.org/10.1016/j.nima.2005.05.063

[147] Hamamatsu Photonics, "S13361-2050AE-08." [Online]. Available: https://www.hamamatsu.com/content/dam/hamamatsu-photonics/sites/documents/99_SALES_LIBRARY/ssd/s13361-2050_series_kapd1055e.pdf

[148] ——, "S14161-3050HS-08." [Online]. Available: https://www.hamamatsu.com/content/dam/hamamatsu-photonics/sites/documents/99_SALES_LIBRARY/ssd/s14160_s14161_series_kapd1064e.pdf

[149] R. Brun and F. Rademakers, "ROOT — An object oriented data analysis framework," *Nuclear Instruments and Methods in Physics Research Section A: Accelerators, Spectrometers, Detectors and Associated Equipment*, vol. 389, no. 1, pp. 81–86, 1997. [Online]. Available: https://doi.org/10.1016/S0168-9002(97)00048-X